Citation: Akanni, S. (2002). Air Jet Vortex Generator Flow Control Applied to the Rear Multi-Element High Downforce Wing of a Formula One Racing Car. (Unpublished Doctoral thesis, City, University of London)

Air Jet Vortex Generator Flow Control Applied to the Rear Multi-Element High Downforce Wing of a Formula One Racing Car

Saïf-Deen Akanni

Thesis submitted for the degree of
Doctor of Philosophy
in the School of Engineering and Mathematical Sciences
City University

Centre for Aeronautics
School of Engineering and Mathematical Sciences
City University
Northampton Square
London EC1V 0HB
England

May 2002

Acknowledgements

My thanks and love to my Ma, Mrs. Viola Small and Daï, Mr. Cuthbert Small for putting me in the position to arrive at this point in my life. May you rest in peace.

I would also like to thank my mother, Ermine Atwell for her never ending patience and support. The same goes for Jeanette Ekdahl, friend and mother of my child.

To my daughter Sanna Liv Akanni who inspires me and always keeps me focused on what is important. I love you much and much and much.

Thanks to Natalie Macwilliam for being there when I was soul searching.

This effort would not have been possible without the guidance, patience and support of my supervisor, Dr. Frank Henry and thank you Professor David Peake for efforts and suggestions on the experimental side.

To Willem Toet, then Head of Aerodynamics at La Scuderia Ferrari, thank you for providing the technical and financial resources that made these investigations possible.

To the late Albrecht Honnecker, ICEM-CFD mesher extraordinaire and Reimund Steberl also of ICEM-CFD for all your support.

Thanks to Kevin Fox of Silicon Graphics UK and to Ian Jones of CFX International for the advice and hardware and software resources you made available.

Also to Neil Lewington and Christoph Küpper, it was a privilege to work with you both.

Declaration

I grant powers of discretion to the University Librarian to allows this thesis to be copied in whole or in part without further reference to the author and according to the legally binding confidentiality agreement between The Department of Mechanical Engineering and Aeronautics at City University and *Il Gestione Sportiva, Ferrari.* This permission only covers single copies made for study purposes, subject to normal conditions of acknowledgement.

Abstract

Numerical and experimental and investigations have been conducted on a full-scale, high downforce rear wing from a Ferrari Formula One racing car. The wing comprised a mainplane, vane and flap elements incorporating substantial aft camber and for the first time, air jet vortex generators. This study focuses on the wing performance at 19^o incidence.

Original numerical investigations were conducted using the CFX-4.2 finite volume, Navier-Stokes, fluid flow solver using non-orthogonal, body-fitted grids. All flows were modelled as steady state, incompressible and fully turbulent using the standard $k - \epsilon$ turbulence model for closure of the Navier-Stokes equations.

Two-dimensional numerical studies capture the performance trends of the high downforce wing. When compared with the experiments, the downforce is generally overpredicted by up to 28%. In the three-dimensional numerical studies performed, flow separation is predicted on the suction surface of the mainplane. The application of air jets is predicted to reduce the amount of flow separation through an enhancement of the skin friction above that seen on the model without air jets. An increase in downforce is also predicted for the air jet equipped wing.

Some modifications were made to the wing to facilitate its testing in the City University Low Speed T2 Wind Tunnel at 35 and 40 m/s. These were the installation of the air jets, static pressure orifices, and the fitting of endplates. Boundary-layer control was not applied to the endplates.

In the experiments, at high angles of incidence, the wing experiences incipient flow separation on the suction surface of the mainplane. The application of air jets reduces this flow separation and also increases the downforce generated by the wing over that of the wing without air jets.

The interactions of the experimental and numerical solutions reveal the mechanisms by which the air jets enable the wing to generate more downforce. Nevertheless, additional work is needed to address issues such as the degree of two dimensionality of the flow fields in the experiments and grid sensitivity of the numerical results.

Nomenclature

English

A	Reference area of the high downforce wing asembly
C	Chord of aerofoil or high downforce wing assembly
C_f	Skin friction coefficient, $[\sqrt{(\tau_x^2+\tau_y^2+\tau_z^2)}/\frac{1}{2}\rho V_\infty^2](-\tau_x/\lvert\tau_x\rvert)$
C_h	Hydraulic diameter, $4A/P$, where P is the inlet perimeter
c_l	Two-dimensional lift coefficient, $L/\frac{1}{2}\rho V_\infty^2 C$
c_d	Two-dimensional drag coefficient, $D/\frac{1}{2}\rho V_\infty^2 C$
C_n	Normal force coefficient, $\int_0^1 (C_{pu}-C_{pl})\, d\left(\frac{x}{c}\right)$
C_x	Axial force coefficient, $\int_{\frac{y1}{c}}^{\frac{y2}{c}} C_p d\left(\frac{y}{c}\right)$
C_L	Three-dimensional lift coefficient, $L/\frac{1}{2}\rho V_\infty^2 A$
C_D	Three-dimensional drag coefficient, $D/\frac{1}{2}\rho V_\infty^2 A$
C_p	Pressure coefficient, $(P-P_\infty)/\frac{1}{2}\rho V_\infty^2$
C_1	Turbulence model constant, 1.44, see Equation 2.27
C_2	Turbulence model constant, 1.92, see Equation 2.27
C_3	Turbulence model constant, 0.00, see Equation 2.27
C_μ	Turbulence model constant, 0.09, see Equation 2.27
d	Wingspan of high downforce model
D	Aerodynamic drag
e	Eastern face of finite volume, see Figure 2.6
E	Centre of eastern finite volume, see Figure 2.6
E	A constant used in the calculation of near wall, streamwise velocity, see Equation 2.29
E_{ajvg}	Skin friction enhancement, $\frac{d}{z}\int_{\frac{z}{d}=0}^{\frac{z}{d}=1} (C_{f\,ajvg}-C_{f\,Clean\,Wing})\left(\frac{z}{d}\right)$
f	Body force acting on a control volume
G	Turbulent production due to body forces
H	Height of fluid domain
k	Turbulent kinetic energy
k_{inlet}	Turbulent kinetic energy at the domain inlet
L	Aerodynamic downforce
$\frac{l}{d}$	Two-dimensional lift to drag ratio
$\frac{L}{D}$	Three-dimensional lift to drag ratio

x/c	Non-dimensional chordwise position on aerofoil
x, y, z	Cartesian coordinate space
y/d	Non-dimensional y-coordinate
z/d	Non-dimensional spanwise position on wing
n	Northern face of finite volume, see Figure 2.6
N	Centre of northern finite volume, see Figure 2.6
P	Static pressure as measured or predicted about the high lift system
P	The centre of a finite volume, see Figure 2.6
P_{atm}	Atmospheric pressure, taken as 1.01 x 10^5 N/m^2 for numerical models
P_{ajvg}	Blowing pressure at air jet pressure boundary referenced to P_{atm}
Re	Reynolds number, $\rho V_\infty C/\mu$
s	Southern face of finite volume, see Figure 2.6
S	Centre of southern finite volume, see Figure 2.6
S	Source term
t	time
u_τ	Streamwise friction velocity, $\sqrt{\tau_w/\rho}$
u^+	Non-dimensional streamwise velocity
u	x-component of velocity
v	y-component of velocity
w	z-component of velocity
w	Western face of finite volume, see Figure 2.6
W	Centre of western finite volume, see Figure 2.6
V_∞	Freestream velocity
y^+	Non-dimensional distance from a wall, yu_τ/ν

Greek

α	Angle of incidence of high downforce system with respect to global coordinate axis
β	Under-relaxation factor, see Section 2.6.2
δ	Streamwise boundary layer thickness
ϵ	Turbulence kinetic dissipation
ϵ_{inlet}	Turbulence kinetic dissipation at domain inlet, $k_{inlet}^{\frac{3}{2}}/0.3C_h$
ξ, η, ζ	Curvilinear coordinate system

κ	von Kármán's constant, 0.4, see Equation 2.29
λ	Second viscosity coefficient, $-\frac{2}{3}\mu$
μ	Molecular viscosity
μ_t	Turbulent viscosity, $C_\mu \rho \frac{k^2}{\epsilon}$
μ_{eff}	Effective viscosity, $\mu + \mu_t$
ϕ	Skew angle of air jet with respect to the global x-axis
Φ	Generic transport equation variable, see Equation 2.20
ρ	Density of fluid
$\tau_{xx}, \tau_{yy}, \tau_{zz}$	Normal components of shear stress
$\tau_{xy}, \tau_{xz}, \tau_{yz}$	Tangential components of shear stress
τ_w	Wall shear stress in the local flow direction
θ	Pitch angle of air jet with respect to the local surface tangent

Subscripts

f	Parameter pertaining to the flap
i, j, k	Unit vectors in the x, y and z-directions
x, y, z	Subscripts in orthogonal directions
l	Lower aerofoil surface
m	Parameter pertaining to the mainplane
u	Upper aerofoil surface
v	Parameter pertaining to the vane

Superscripts

*	Initial guess for calculation of pressure in SIMPLEC algorithm, see Section 2.5
'	Correction to initial guess in the SIMPLEC algorithm, see Section 2.5
'	Fluctuating component as defined in Reynolds averaging, see Equation 2.20
-	Mean component as defined in Reynolds averaging, see Equation 2.20

Definitions

Clean Wing(s)	High downforce model with the air jets absent from the mainplane or quiescent
ajvg, AJVG(s)	Concerning the high downforce model with the air jets active
SV	Denotes experiments using the scanivalve system to measure pressures
AM	Denotes experiments using the alcohol manometer system to measure pressures

Contents

List of Figures

List of Tables

Introduction

The research discussed in this doctoral thesis was performed at City University between 1994 and 1998. This research was part of an on-going programme by *La Scuderia Ferrari*, the Ferrari Formula One, (F-1) racing team, to increase the downforce capability of their racing cars. It is the intent of the research programme to investigate the use of air jet vortex generators on some components of a Ferrari F-1 high downforce rear wing.

The focus of the investigations was three components of an upper rear wing configuration which has the Ferrari designation B5. A typical high downforce rear wing system has a minimum of five wing elements and some have sported as many as eight. Many designs at the time tended to have the higher number. Changes to the regulations in the year 2000 mandate a maximum of three upper rear wing elements and one lower rear wing element.

The B5 configuration has five wings as its major lifting components and these are arranged in a lower tier, double element system and an upper, triple element system. In view of the preliminary nature of these investigations and physical constraints of the wind tunnel used, the triple element arrangement was chosen as the basis of the investigations. This triple element system possessed the relevant physical qualities of camber and separated flow that would test the viability of applying an air jet vortex generator array.

The isolated nature of the numerical and experimental tests was considered a valid approach despite the very different on-set flow conditions experienced by the full rear wing configuration operating behind the car. The reason for this is the air jet vortex generators act locally on the boundary layer to delay or eliminate flow separation. A cursory examination of the nature of the full car geometry flows would suggest that air jet vortex generators would be an unnecessary addition to an F-1 high downforce system because the flows on the rear wing are attached. The fact that the flow on these types of highly cambered, multi-element systems can be attached is discussed in work by Katz (1995*a*), Katz (1995*b*) and Katz & Dykstra (1989). Personal communications from F-1 aerodynamicists Mullarkey (1998), Hamidy (1998) and Toet (1998) also confirm that this is possible on F-1 cars. Generally, F-1 teams adjust the rear wings on the cars to produce the maximum downforce with the constraint of attached flow at up to 5^o yaw. Air jet vortex generators would be useful in extending the attached flow range of existing wing designs at all yaw angles while increasing the downforce they produce. The effect would be similar to that found by Liebeck (1978) in his investigations on the aerodynamics of rear wings incorporating Gurney flaps as used on the Eagle Indiannapolis open wheel race car. It was observed that the use of Gurney flaps on the flap of a single slotted, rear wing decreased the likelihood of flow separation on the rear wings in zero yaw conditions and crossflows.

Innes (1995) suggests that there is even greater potential in designing a future family of wings where air jet vortex generators are an integral part of the design from the concept stage. The author envisions wing designs that would exploit significant increased camber and thickness to such an extent that it would be impossible to use them effectively or efficiently without the application of air jets.

A study has been undertaken into the application of air jet vortex generators to an F-1 style multi-element high downforce system. The majority of the work was numerical in nature with two and three-dimensional, Navier Stokes calculations performed on models that were representative of the wings. Experimental investigations were also undertaken on a model in the City University Low Speed T2 Wind Tunnel. These experiments were performed to provide data for the validation of the numerical calculations. Both the numerical and experimental results are promising despite problems encountered. The results are the subject of discussion in this thesis.

Chapter 1

History of Problem

1.1 Review of Previous Work

Since 1969, with the debut of winged cars, the development of Formula One aerodynamics has been inspired to a certain extent by the progress made in aviation high lift systems. This is true of both the aerodynamic devices and techniques of research and development. Examples of technology that has been adapted for use in motor sports are multi-element wings, materials such as carbon fibre, electronic data acquisition and numerical methods in structural engineering and fluid dynamics.

The following discussion will briefly relate some of the experimental and numerical work previously done on high lift systems and vortex generators. A brief history of F-1 aerodynamics is also given. The extent to which F-1 is affected by aerodynamic development in the aerospace industry is also discussed. It is due to this extensive borrowing that a discussion of aircraft high lift systems is necessary.

1.1.1 High Lift Systems in Aviation

The origin of aircraft high lift systems seems to lay with trailing edge flaps and British Aeronautical Research Council Report and Memoranda No. 110, published in 1914. One section of this document is titled, *Experiments on Wings Having a Hinged Rear Portion.* The concept of leading edge devices is attributed to German pilot, Gustav V. Lachmann and British aeronautical engineer, Sir Frederick Handley Page, during World War One. The former developed the leading edge slot in 1918 and the later was independently responsible for the leading edge slat in 1919. They did collaborate at a later date. These systems were developed to eliminate leading edge flow separation on thin biplanes wings, thus maximising manoeuvrability during dogfights. A maximum lift coefficient, $C_{L_{max}}$ of

3.9 was quoted for these designs.

Research and development did continue on such systems and some very significant progress was achieved during World War Two. As war planes became heavier, it was necessary to address the increases in takeoff and landing speeds that mandated longer runways. Trailing edge plain and split flaps made their operational appearance at this time. From the simplicity of the designs of Lachmann and Handley Page, high lift configurations were created by the mechanical alteration of the wings. These alterations, for the most part, created lifting sections with increased camber. Nowadays, increased camber and effective chord are typical features of high lift systems while boundary layer control by virtue of multiple close form elements is common as well. Such systems are found on every heavy transport aircraft and most military aircraft throughout the world. Figure 1.1 shows the evolution of high lift devices from the simple systems of yesteryear to the complex devices used on heavy transports today. Figure 1.2 depicts an eight element aerofoil based on a highly modified RAF 19 wing section. It was created by Handley Page during ten years of high lift research and was presented to the Royal Aeronautical Society on the 17^{th} February 1921. The model is shown at 42^o angle of incidence, the angle for maximum lift. The pressure distributions are theoretical and were made at $\alpha = 36^o$ to correspond to the local angle of incidence of the wind tunnel model which had an aspect ratio (AR) of 6. The theoretical C_L of the configuration is 4.33. This system bears a remarkable resemblance to contemporary multi-element high lift configurations. The fact that this design made such an early appearance suggests that the theory of multi-element high lift wings was well understood at a very early stage.

Alston (1935) and Duddy (1949) published work that discussed the principles governing high lift flows and various flap systems in particular. Abbott & Von Doenhoff (1959) of the National Aeronautics and Space Administration (NASA), had published *The Theory of Wing Sections* which remains a popular reference for high lift research. This text clearly demonstrates that the solution to all high lift problems is not addressed by using the most complex systems available or those which produce the highest lift coefficient, $C_{L_{max}}$. Some of the simpler systems mentioned in their book can still be found on modern aircraft. It is the more complex multi-element designs, that found their way on to F-1 racing cars, and it is these that are examined in this review and later on in this thesis.

Foster, Irwin & Williams (1970) are among those researchers who performed extensive experiments on wings with single slotted flaps. They concluded that the changes in lift were more dependent on size of the gap between the elements than the amount of overlap. The

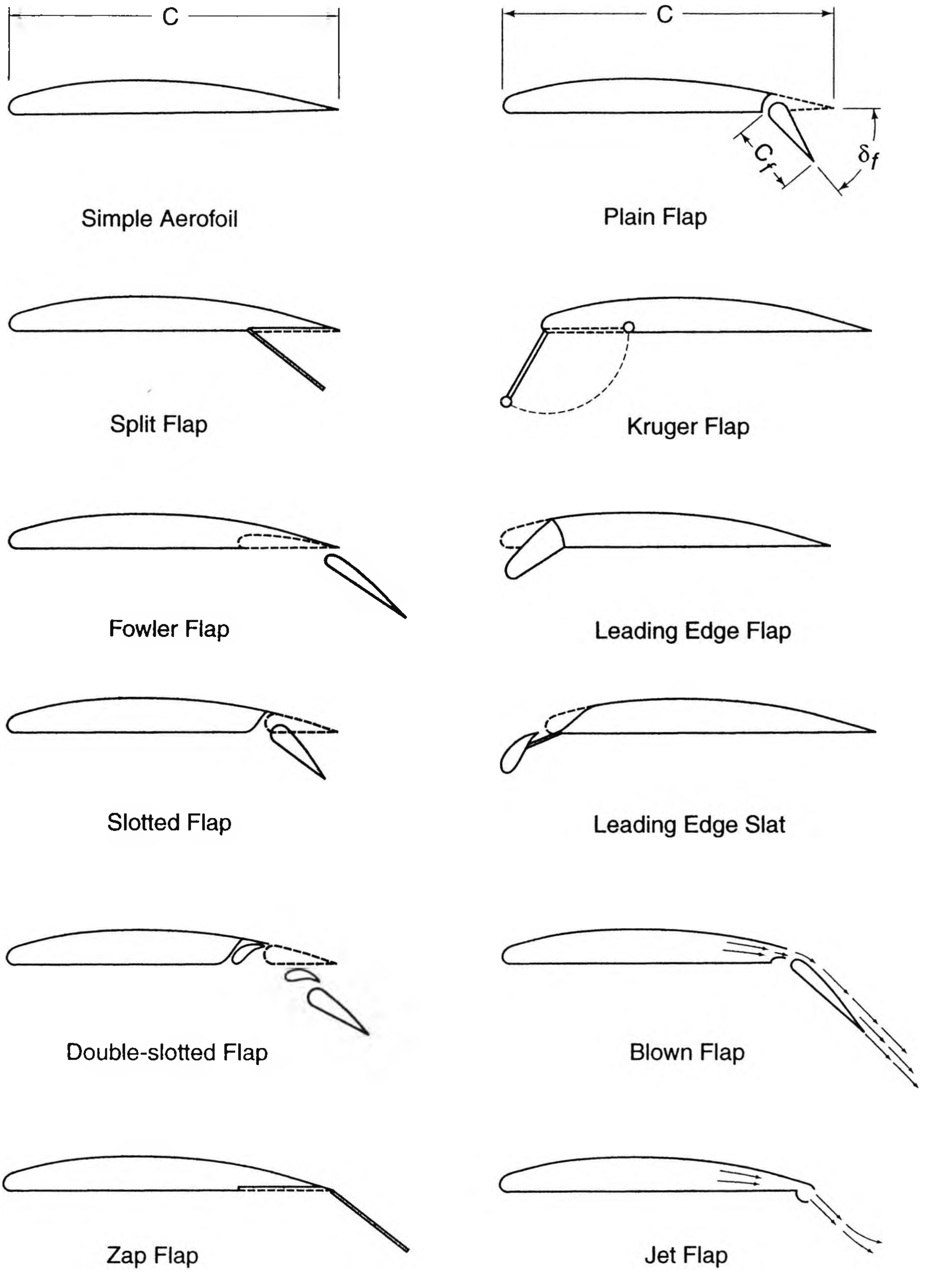

Figure 1.1: Various High Lift Concepts. (Shevell, R. S. (1989))

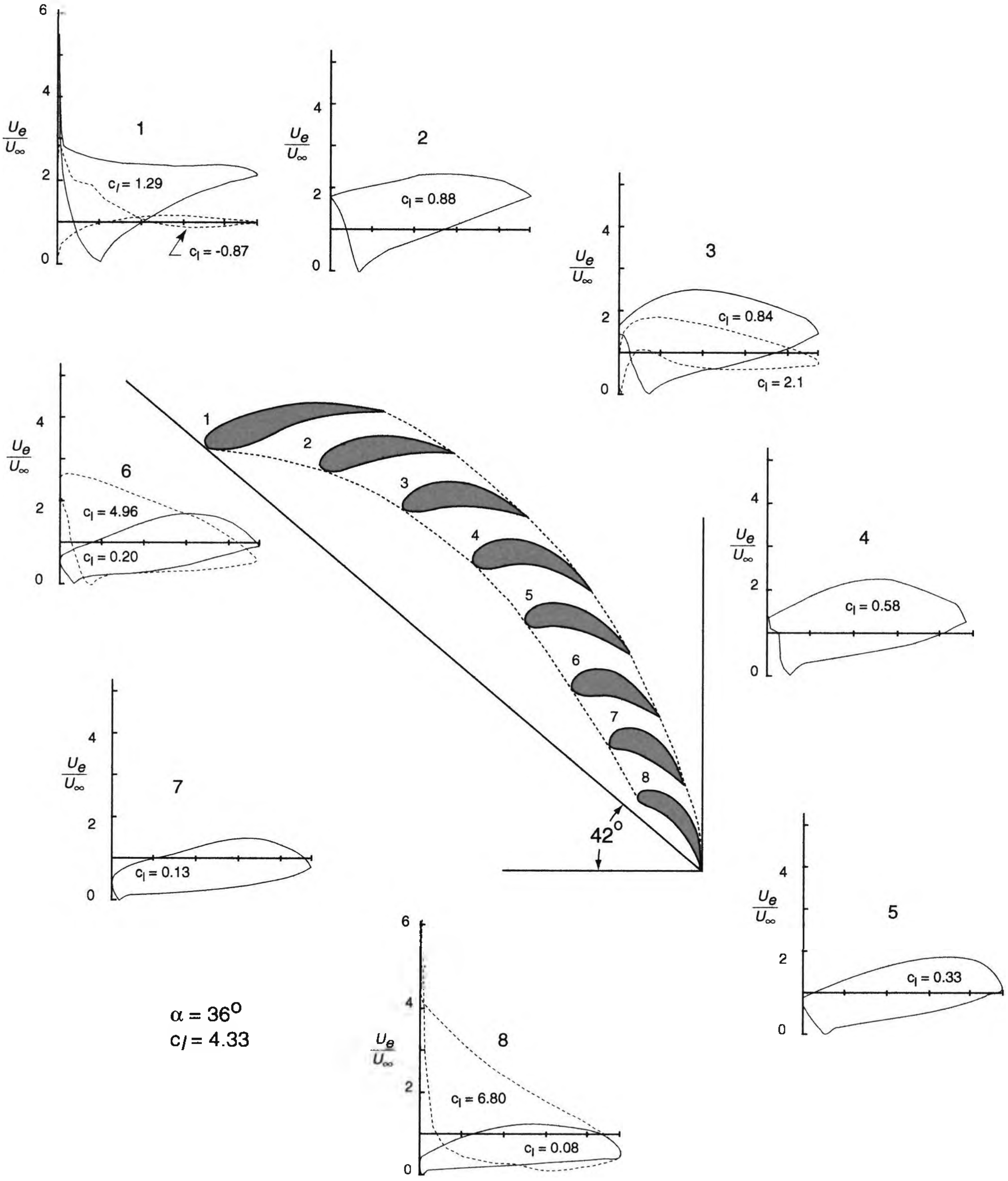

Figure 1.2: Handley Page's eight-element aerofoil. (Smith (1975))

interaction between the wakes and boundary layers of the elements and Reynolds number effects on the gap size were also noted. The results compared well with inviscid theory and showed that the optimum flap position occurred when there was a weak interaction between the wake of the mainplane and the flap boundary layer. Ljungstrom (1972) carried on in a similar vein, but with two-dimensional experiments on a triple element high lift model comprising a leading edge slat, mainplane and trailing edge flap. Again the importance of the interaction between the wakes of the preceding elements and the boundary layers of the downstream elements was noted. Ljungstrom (1972) also found that the skin friction coefficient bore a direct relation to increases in the gap between the slat and the mainplane as well as the angle of the elements.

Smith (1975) clarified some of the more important mechanisms governing high lift flows in his paper entitled, *High-Lift Aerodynamics.* Among the points he emphasised was the inability of a single aerofoil, however well designed, to produce more lift than an equally well designed multi-element system. He was in agreement with Handley Page, concluding that the maximum lift increased with the number of elements. The possibility of semantics at play was also discussed with regards to the effect of slots in a multi-element system. It is often said that slotted systems work by directing higher energy air from the high-pressure side of the multi-element aerofoil to the low-pressure side, thus re-energising the boundary layer. This is not possible given that the total energy contained in the flow around the aerofoils is no greater than that contained in the freestream. Smith (1975) explains that multi-element systems generate higher lift than single element designs through five important mechanisms. These are as follows:

1. **Peak Suction Suppression** - One effect of an upstream lifting element is to suppress the peak suction pressure experienced on its downstream neighbour, thus reducing the adverse pressure gradients to which the boundary layers on that element are subjected.

2. **Increased Circulation** - By virtue of being adjacent to the low pressure region of the downstream element, the trailing edge region of the upstream element experiences higher velocity. The local velocity vectors are inclined to the mean camber line thus inducing higher circulation about the forward element.

3. **The Dumping Effect** - The trailing edges of the upstream elements are located in regions with velocities that are significantly higher than the freestream velocity. The boundary layers from these upstream elements are *dumped* at higher velocities. This

dumping reduces the effects of the on-surface momentum loss experienced by these boundary layers due to the adverse pressure gradients to which they were subjected. The result is that flow separation on these elements is delayed.

4. **Off Surface Pressure Recovery** - The boundary layers from the forward elements in a high lift system are *dumped* at velocities significantly higher than freestream. The deceleration to the freestream occurs without contact with any wing surface. This pressure recovery is far more efficient than is possible with any on-surface pressure recovery.

5. **Separate Boundary Layers** - As the flow field is incident on each lifting element, a new boundary layer is formed at the leading edge of each downstream element. These thinner boundary layers are more tolerant of adverse pressure gradients and are less likely to separate from the wing surface. The total pressure recovery from the peak suction of the first element to the trailing edge of the last is achieved in a number of stages equal to the number of elements in the system.

While providing a significant aerodynamic benefit, it is the slots and the resulting boundary layers that make high lift systems very difficult to analyse and design. This is especially true if the wake from an upstream element merges with the boundary layer of a downstream element to form a confluent boundary layer. Nakayama, Kreplin & Morgan (1990) showed the complexity of these flows through measurements of the mean flow and turbulence quantities on a triple element high lift system consisting of a slat, mainplane and a flap. In that particular series of experiments, it was found that there was not a significant merging or intense interaction between the slat wake and the mainplane boundary layer. However, the turbulence data did show that the turbulence levels in the slat wake did have a profound effect on the mainplane boundary layer. This is in keeping with the findings of Smith (1975) and his recommendations for a well designed high lift systems. Such a system would be one where the interaction of the upstream wakes with the boundary layers of the downstream elements is minimal.

1.1.2 Numerical Studies of High Lift Systems

High lift flows are characterised by strongly coupled inviscid, and viscous flows, the latter having multiple boundary layers, which are sometimes confluent. There is almost always some sort of flow separation with re-attachment occurring on occasion to form separation bubbles. The effects of unsteadiness, compressibility, streamline curvature and laminar to turbulent flow transition compound the difficulty. All of the numerical and experimental work reviewed encountered these problems.

Potential flow theory has been used for some time now in calculating high lift flows. VSAERO is one of the more popular CFD codes to be used for this type of problem. It is a first order accurate panel method with singularity elements. It uses the Dirichlet boundary condition for thick bodies and the Neumann condition for thin surfaces. The boundary layer calculations are addressed by the lag entrainment method as described by Nash & Hicks (1968). Maskew (1983) demonstrated the suitability of VSAERO to calculate high lift flows.

Papadakis & Miller (1992) in their experimental and computational efforts showed that using the measurements made during experiments to set up boundary conditions for the numerical calculations greatly improved the correlation between experimental and computational results. This emphasises the need to accurately specify the onset flow and boundary conditions when a direct comparison is to be made. Rumsey, Gatski, Ying & Bertelrud (1998) and Ying & Spaid (1998) performed more in-depth studies of similar systems and concluded that the transition location was crucial to the computation of accurate boundary layer profiles because inaccuracies are propagated downstream and lead to increasingly inaccurate wake profile calculations. The selection of an appropriate turbulence model is also discussed. Ying & Spaid (1998) and Valarezo & Mavriplis (1993) independently concluded that more work is needed to increase the accuracy of turbulence models.

The Menter, Spalart-Allmaras and Baldwin-Barth low Reynolds number turbulence models are currently the most popular models used in the prediction of high lift flows. These are more capable of addressing the flows in the near wall regions than the standard k-ϵ model because the latter is limited by the use of wall functions. Another drawback of the standard k-ϵ model is the possibility of excessive numerical diffusion as discussed by Kim & Benson (1992) in their work on circular jets in crossflow using a multiple time scale turbulence model.

Two-dimensional CFD calculations have been shown to provide useful insight into the behaviour of more complex three-dimensional high downforce systems. Such studies of high lift systems have been carried out by Fritz (1993) on multi-element aircraft high lift systems where a Navier-Stokes solver in conjunction with the Baldwin-Lomax turbulence model and the Lam-Bremhost, two equation, Low Reynolds number k-ϵ turbulence model, to predict the behaviour of multiple element high lift systems at low and high angles of incidence. The study concluded that this approach permitted the analysis of these configurations up to maximum lift despite the fact that the calculation of drag was not very accurate.

The Navier-Stokes calculations presented in this thesis are based on a solver using structured, multiblock grids. However there is a trend at the moment which sees chimera grids [1] and unstructured hexahedral and tetrahedral grids being the most popular basis for discretisation. Bartsch, Nitsche & Britsch (1993) use block-structured, hexahedral meshes in their investigations. In doing so, they share some of the same experiences as the author, namely the difficulty in achieving an economy of cells and a smooth grid. It can be especially difficult to achieve these two grid qualities if the guidelines of a twenty percent cell size increase in any direction as laid out by Castro & Jones (1987) are followed. Highly cambered high lift geometries with their multiple elements in rectangular sectioned wind tunnel test sections make it very difficult to follow these guidelines.

Unstructured grids offer an ease of problem discretisation for high lift geometries that is unmatched by any other method with the exception of some flows calculated using panel methods. Anderson & Bonhaus (1993) used a two dimensional unstructured Navier Stokes code to compute the flow field around a multi-element high downforce model in landing and take off configurations. Grid dependence studies were also carried out in the course of these investigations. It was found that further refinement was needed to resolve the velocity profiles at the high angles of incidence. They also found that the trends arising from variations in flap positions and Reynolds numbers were well predicted. However, the angle of incidence for maximum downforce was overpredicted.

The work of Habashi, Dompierre, Bourgault, Fortin & Vallet (1998) demonstrates that adaptive, unstructured grid refinement based on the calculation of flow gradients offer an objective way forward to producing accurate grid independent solutions. It is much easier to achieve grid refinement with an unstructured grid that with one that is structured.

1.1.3 Vortex Generators

Despite the fact that multi-element high lift systems produce lift more effectively than single element systems, they do have limitations and at some point are subject to flow separation and stalling as one or more of the boundary layers separate. Additional elements could be the solution but this is not always practical or possible. It is the inability to use additional elements that sets the scene for lift enhancement through the application of

---

[1] Gridding configurations in which blocks overlap.

vortex generators.

A study of previous work on vortex generators as a form of boundary layer control begins with Fage & Sargent (1944), who used the method of air jets issuing from small circular holes to fix boundary layer transition in experiments on the leading edges of single element wings. Brunes and Taylor of the United Aircraft Corporation were the first to use vane vortex generators to control separation on aircraft wings in 1947. Rodi (1952), Wallis (1956) and Wallis & Stuart (1958) are on record as being the first to use air jets that were pitched and skewed to the freestream flow to eliminate laminar separation on the leading edges of thin wings. Pearcey (1961) also initiated a parametric study of vortex generator arrays which built on this philosophy. It is evident that there was an appreciation that the mixing effect of vortices could aid in maintaining attached flow of boundary layers subjected to adverse pressure gradients. However, a review of the research conducted at this time and the practical applications arising from this research, shows that the majority of boundary layer control through vortex generation was and still is achieved through the use of vanes. The reason for this is that vanes are easy to manufacture and install, are robust and therefore inexpensive. It is worthy of note that wings which make use of vane vortex generators have a stigma of not being properly designed. Vane vortex generators are viewed by some in the aviation industry as a 'fix'. By contrast, air jets are seen as an intelligent solution to boundary layer control on high lift systems because their performance can be actively altered.

Vane vortex generators have seen numerous applications since their initial discovery. They have been used near the base of the windscreen of the Gulfstream GV aircraft to suppress Mach rumble caused by shock induced flow separation. They are also popular in heat transfer applications where they are used to enhance turbulent mixing of flows. Drag reduction on bluff bodies such as crash helmets and articulated lorries is another area where vanes are seeing increased use. The Wheeler wishbone type vortex generator, designed by Dr. Gary Wheeler, is very well known in these types of applications. The problem of separated inlet and diffuser flows has also been subjected to the application of vane vortex generators.

By contrast, air jet vortex generators have been relegated primarily to being a novel research concept. It is possible that the increased complexity of this type of system was prohibitive. This attitude is changing. Pearcey (1961) conducted a series of experiments on using air jets to reduce shock induced separation. Compton & Johnston (1992) have also examined the use of the effect of circular air jets issuing into a turbulent, zero adverse pressure gradient boundary layer. More recently, Henry & Pearcey (1994) conducted a numerical and experimental study of air jets on a flat plate with various pressure gradients. Innes (1995) has also investigated the use of pitched and skewed rectangular air jets on a multi-element high lift system with very promising results. The nature of co-rotating and counter-rotating AJVG arrays was one of the focal points of this discussion. Higher skin friction coefficients were recorded for both types of arrays over and above those calculated for the cases without jets. In keeping with previous findings, the slightly lower values of C_f calculated for the counter-rotating cases were more persistent downstream than those of the co-rotating geometries.

Innes (1995) concluded that the improvement in the performance of high lift systems is not merely due to the mixing effect of the vortices in the boundary layers of the wings as is the case with vanes. There is evidence to show that the interaction of the jets with the wakes of the upstream elements and consequently with the boundary layers of the downstream elements is also responsible for the improvement. Another factor which encourages the use of air jets is that they could be activated on high lift systems during the take-off and landing phases of flight but concealed during the cruising phase. There would be no parasite drag penalty as a result. Lin, Robinson, McGhee & Valarezo (1994) in their work on micro-vortex generators, have suggested trying to achieve concealment of an array of vanes. It would be easier to do this with an air jet array. There are other reasons to argue the increasing viability of using air jets on aviation high lift systems.

If implemented, the findings of Innes (1995) could have a positive impact on the *time-to-climb* for passenger aircraft.[2] At present the climb phase of flight accounts for a disproportionate amount of the fuel consumed because jet engines operate less efficiently at lower altitudes. The climb rate of an aircraft is limited by the maximum lift coefficient, $C_{L_{max}}$. An increase in $C_{L_{max}}$ also has positive implications for takeoff and landing performance.

Contemporary Navier-Stokes codes are better able to model real world flows and this has the potential to aid in achieving a better understanding of air jet vortex generators. In the last few years, some studies using Navier-Stokes CFD codes and large multiprocessor computers have allowed the modelling of realistic flows. Johnston & Nishi (1989) and Claus & Vanka (1992) are among those who have undertaken complex numerical investigations into the effect of air jets and mixing. Henry & Pearcey (1994) and Akanni & Henry (1995) have also performed a series of numerical calculations on rectangular air jets issuing into and otherwise undisturbed boundary layer. This work helped to confirm some of the

---

[2] The time taken for an aircraft to climb to a given altitude.

characteristics of the vortex system produced by pitched and skewed air jets. Figure 1.3 shows one of the grids used in the study. Figure 1.4 shows one of the main differences between the vortex system of an air jet and a that of a vane (not shown). The efflux of the air jet occupies the inner circulatory region of the vortex. There is no such efflux associated with vane generated vortices because they are momentum deficient. Figure 1.5 shows that two vortices of unequal strength are produced. The smaller vortex is seen on the right side of the vortex sheet. The smaller vortex is quickly overwhelmed by the larger system as the flow develops downstream.

The experience gained from this work served as the basis for investigating the more complex air jet vortex generators on an F-1 style high downforce wing. At City University, the work carried out by Peake, Henry, Lush & Pearcey (1998), Küpper (1999) and Lewington (2002) also provided a measure to assess whether Navier-Stokes CFD codes could accurately capture the phenomena of vortex generation. They also provided an appreciation of the software and hardware requirements. Their experiences showed that the most difficulty lay with finding a computer large enough to model realistic problems. Mesh generation has advanced to the point where complex, real world geometries, can be easily meshed thereby reserving the greatest effort to analyse the problem at hand.

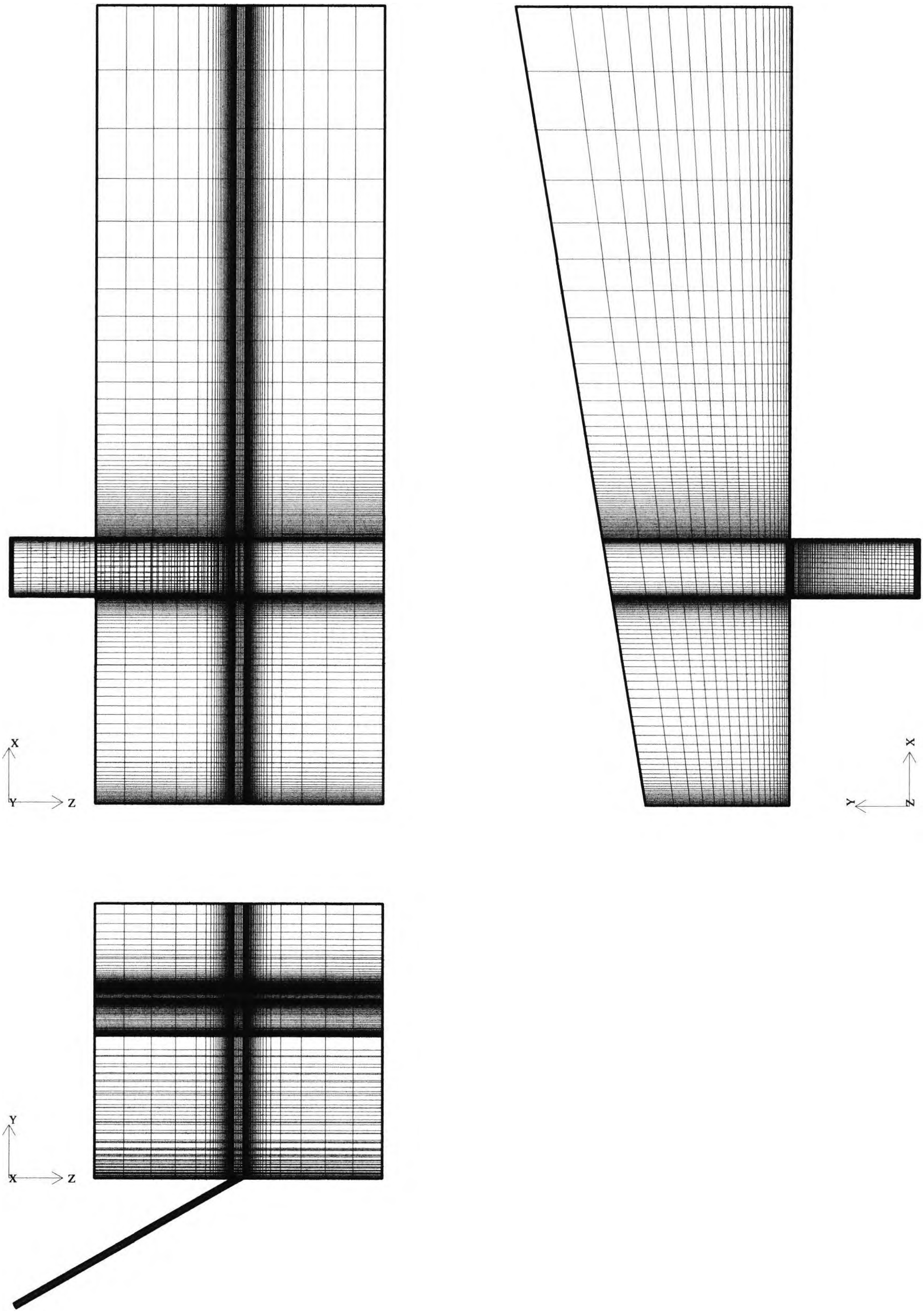

Figure 1.3: Solution domain with jet exiting from flat plate. (Akanni and Henry (1995))

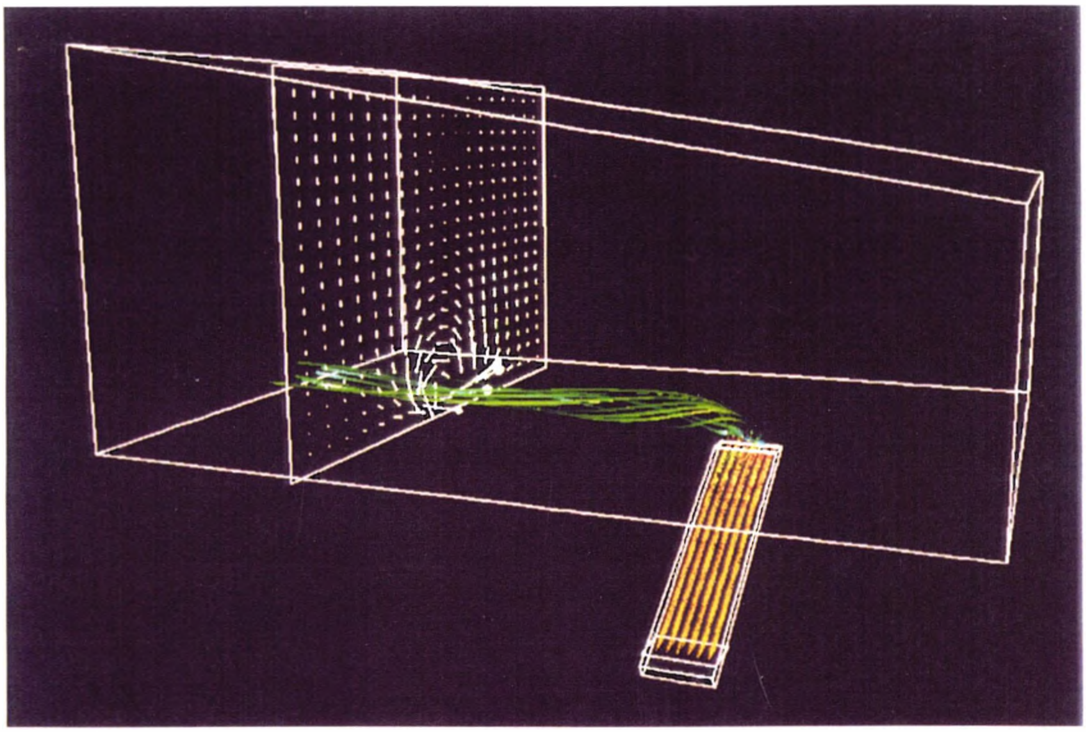

Figure 1.4: Isometric view of air jet mixing with freestream. (Akanni and Henry (1995))

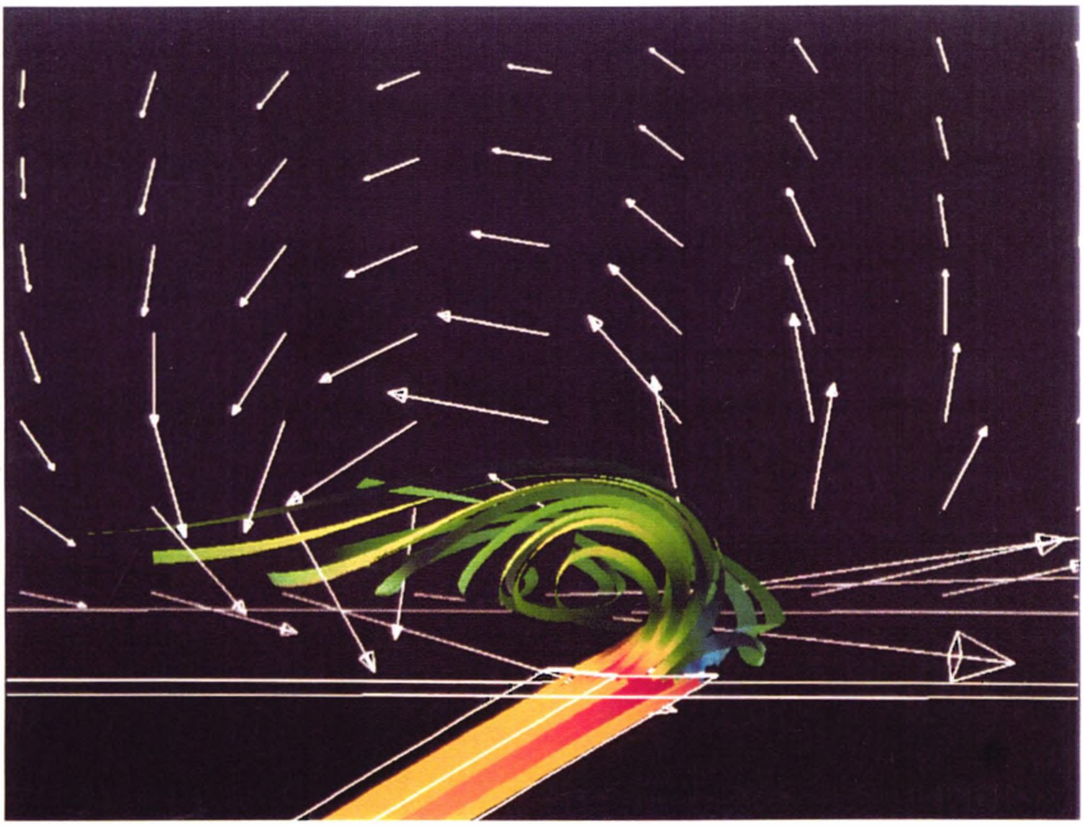

Figure 1.5: View downstream of two unequal strength vortices. (Akanni and Henry (1995))

1.2 Formula One

The Formula One World Championship is the world's premier automotive racing series where open wheel motor cars, optimised for sprints of approximately 300 to 400 Kilometres, are raced against each other on closed, road courses. It was created in 1950 as a drivers championship by the Fédération Internationale du Automobile (FIA). Eight years later, the Formula One Constructors Championship was created. Since 1958, the Formula One World Championship has comprised the Formula One Drivers Championship and the Formula One Constructors Championship being simultaneously disputed at several international venues, but mainly in Western Europe.

Despite the dual nature of the championship, it is the drivers championship which captures most of the publicity. Be that as it may, the automotive manufacturers involved view the championship in a very different manner. To them, it is a proving ground for their latest automotive technology and they attempt to do this by providing the Formula One (F-1) teams with their latest engine technology. Success in the championship is paramount because it implies that the company possesses a technical capability superior to that of its rivals. Having achieved this success, ideally by winning both championships, the automotive company in question attempts to make as strong an association as possible between the technology used in its racing cars and that of its road going motor cars with the goal of increased sales of the latter.

Given this sentiment, the only path to an increased market share is to win races and if this is done consistently, then the victory in the championship is the result. Over the years, this need to win has been the motivation behind the never ending research and development programmes that Formula One teams and their automotive partners have employed to extract the maximum performance from their cars. The research for this thesis is a small part of that effort.

1.2.1 Effect of Negative Lift on F-1 Car Performance

Until 1965, the aerodynamic philosophy was one of streamlining to effect a reduction in drag. According to Harvey (1980), a driver called Michael May driving a Type 500 Porsche at the Nürburgring 1000 Kilometres race in 1956 was the first to make use of aerodynamic downforce on a racing car with inverted wings to extremely good effect. Unfortunately he was not allowed to race it because the embarrassed Porsche factory team conspired to have it banned for use in the race. It is strange that nobody pursued this line of development for over a decade.

In 1966, Frank Winchell oversaw the implementation of a wing on a racing car for the first time in regular competition. A driver adjustable, inverted, single element wing was mounted on the Chaparral Canadian American (CANAM) 2E with the intent of producing downforce so that the tyres could produce higher cornering forces. This car is shown in Figure 1.6. The greater the downforce, the greater the cornering ability of the car. These increased vertical forces also had positive effects on the braking and to a lesser extent, the acceleration. Figure 1.7 depicts these forces on a single tyre. For an average, road going car, the forces could be represented in the form of a traction circle and under normal operation, the maximum acceleration in any direction could never exceed 1.0 g. On racing cars, the tyre performance and downforce transform this circle to produce an elliptical capability depicted in Figure 1.8. In 1968, inverted wings made their debut on F-1 cars in various guises. The Lotus 49 F-1 car shown in Figure 1.9 is one example. For the most part, these wings were mounted high above the car in the undisturbed airflow and attached to the front and rear suspension members. They were mounted directly to the unsprung parts of the front and rear suspension so as not to change the sprung/unsprung ratio of the suspension and chassis ride height as the car's speed varied. At the time, the forces involved were not well understood and some of these wing designs were under engineered. Several spectacular and sometimes tragic failures resulted. The governing body reacted by mandating that all wings be mounted directly to the sprung portion of the car's chassis the following year.

The period that followed has characterised technical development and the FIA response to it as it threatens what is perceived to be the welfare of the sport. Quite often, the performance of the cars is reigned in through restrictive changes in the rules. An appreciation of what could be achieved with downforce has resulted in some novel designs with and without the use of wings.

Shortly after the appearance of wings, the Chaparral team developed another CANAM racing car, the Chaparral 2J, also called "Sucker Car". This car, pictured in Figure 1.11, used a fan system to evacuate the air from a sealed floor. This demonstrated the first time that there was an appreciation for what was possible through the use of a modest pressure drop acting on the large surface area under a racecar. In 1977, the ground-effect era was born.

The Lotus Type 79 F-1 car shown in Figure 1.10 was developed by Peter Wright. It made use of underbody venturis and front and rear wings to create downforce. These venturis or tunnels functioned by allowing the air to flow under the car and directing it

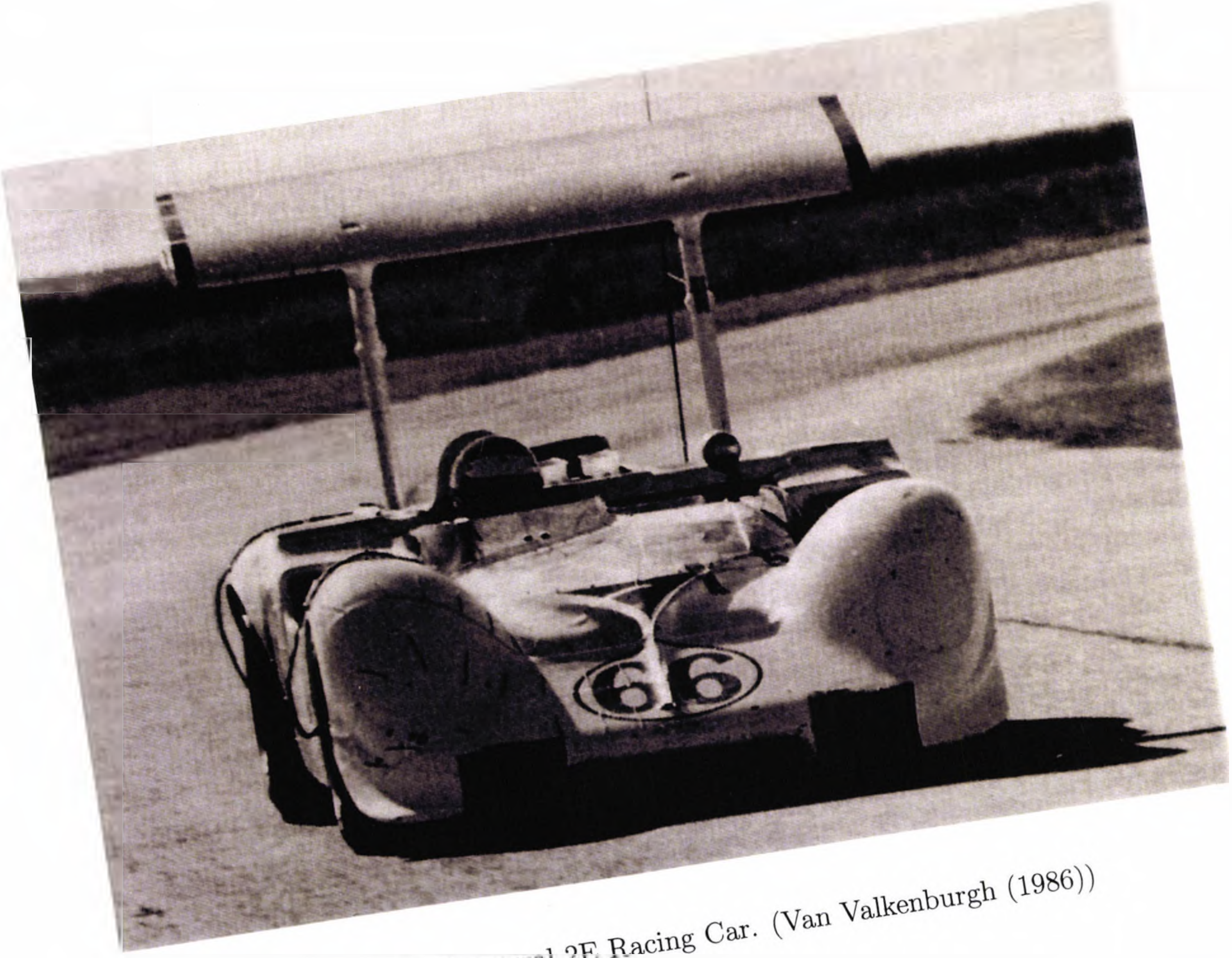

Figure 1.6: Chaparral 2E Racing Car. (Van Valkenburgh (1986))

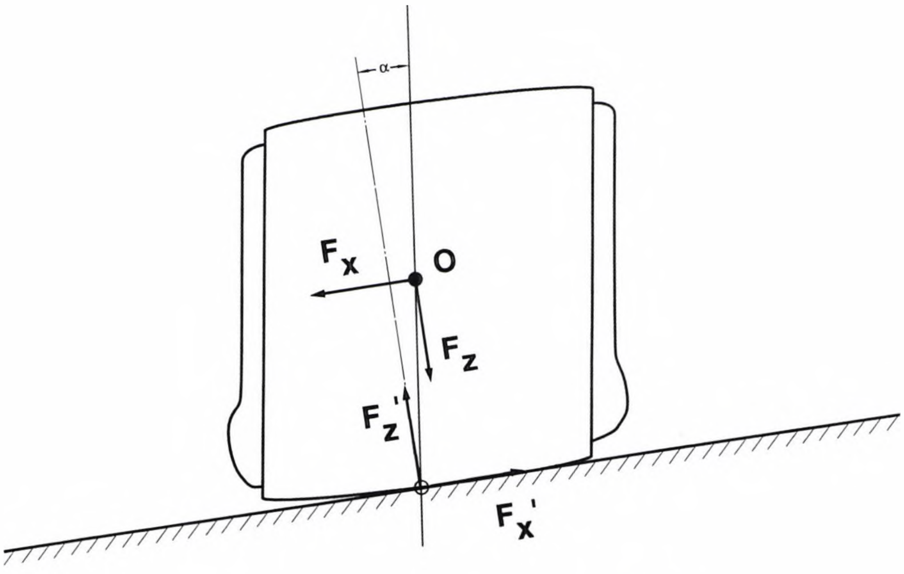

Figure 1.7: Forces on single tyre.

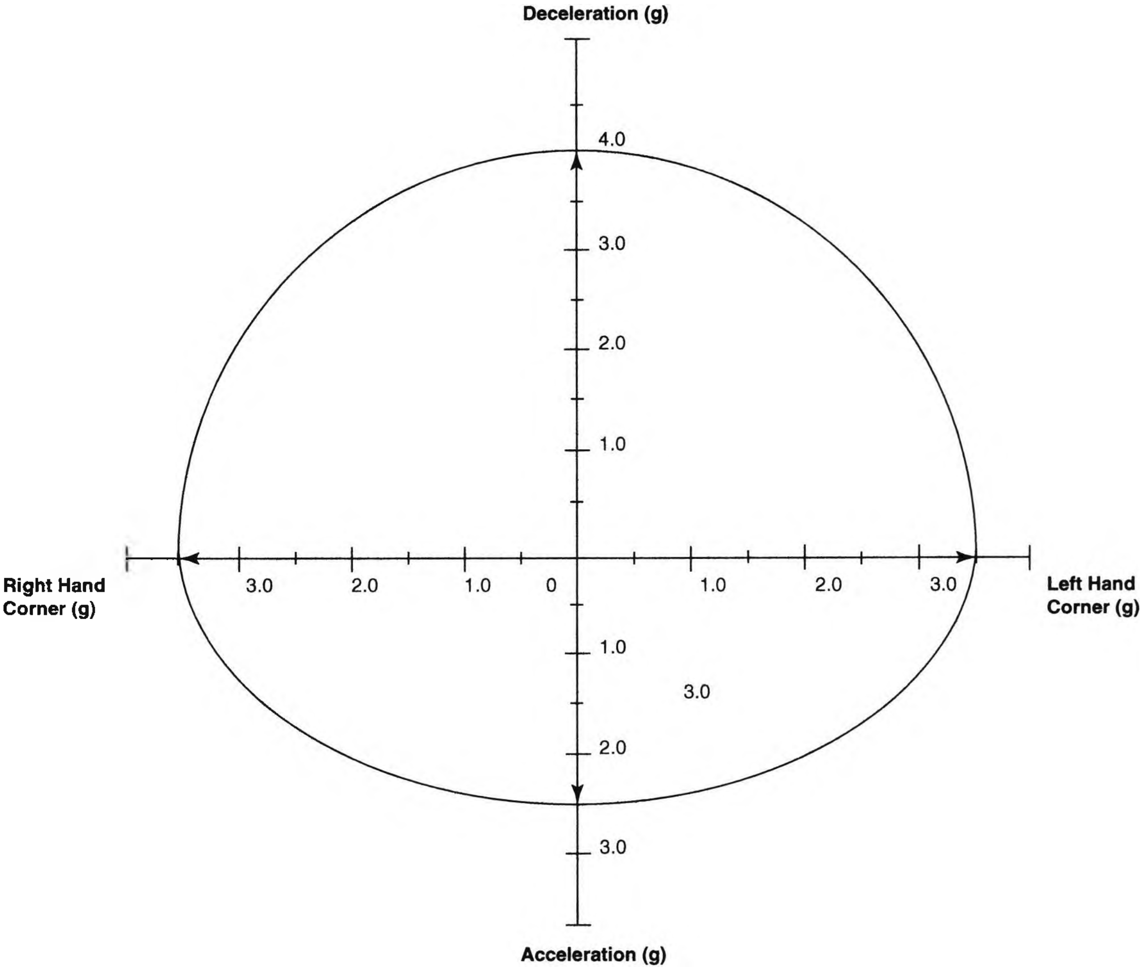

Figure 1.8: Capabilities of contemporary F-1 race car.

through a nozzle, thus lowering the pressure. This resulting pressure drop created a level of downforce that in certain configurations, exceeded the weight of the car by a factor of 2.

One radical design was the Brabham BT-46B design, presided over by Gordon Murray and depicted in Figures 1.12 and 1.13. This car, another exercise in vacuum assisted traction, used a large fan at the rear to evacuate air from its underbody venturis. It was quite successful in the 1978 Swedish Grand Prix. In one weekend, it took pole position, went on to win the race and was immediately banned. According to Wright (1982), this period saw cars capable of steady state cornering loads of 3.5 g at a velocity of 240 km/h and transient loads exceeding 4.0 g/sec. Not wanting or being able to stand still, the progress made by the tyre companies was evidenced by tyres that had a rolling coefficient of friction greater than 1.5. This led the teams in the direction of even greater aerodynamic downforce in order to exploit the capability of the tyres. The progress made by engine manufacturers in terms of increasing specific and maximum power also allowed the teams to focus on increasing the achievable downforce while addressing the increased attendant profile and induced drag with increased engine power.

This period saw a class of F-1 cars that were spectacular to watch but very unpleasant to drive. To achieve the performance required to minimise the lap times at any given track, the car were engineered with very high spring and damping rates in the pitching mode with the result that the cars were over damped in roll. Indeed, Wright (1982) and Milliken & Milliken (1995) cite frequencies of 5 Hz, 8 Hz and 15 Hz for the heave, pitch and roll modes respectively. These modes are also representative of contemporary F-1 cars. Ground effect aerodynamics and turbocharged engines capable of producing 1500 Horsepower were banned since the late 1980's and the performance level was reduced for a short period. However, Figure 1.14 shows what a tireless battle it is to keep the car performance in check. The back and forth nature of performance increases and rules derived restriction is endemic to the racing world and will not end in the foreseeable future. Aerodynamics will continue to be targeted by the FIA as a means of reducing car performance because of the potential significant impact.

1.2.2 Contemporary F-1 Car and Air Flow about it

Current F-1 cars have single seats and open cockpits. They can be powered by a 3.0 Litre engine, which can have any number of cylinders, up to a maximum of ten. The cars must have four wheels (some have had up to six) and they, along with the suspension

[redacted]

Figure 1.9: Winged Lotus 49 F-1 Car. (Katz (1995))

[redacted]

Figure 1.10: Lotus 78, first race car to use ground effect aerodynamics. (Katz (1995))

[redacted]

Figure 1.11: Chaparral 2J with vacuum assisted traction. (Katz (1995))

[redacted]

Figure 1.12: Frontal view of fan assisted Brabham BT-46B. (Katz (1995))

[redacted]

Figure 1.13: Brabham BT-46B and its controversial fan. (Katz (1995))

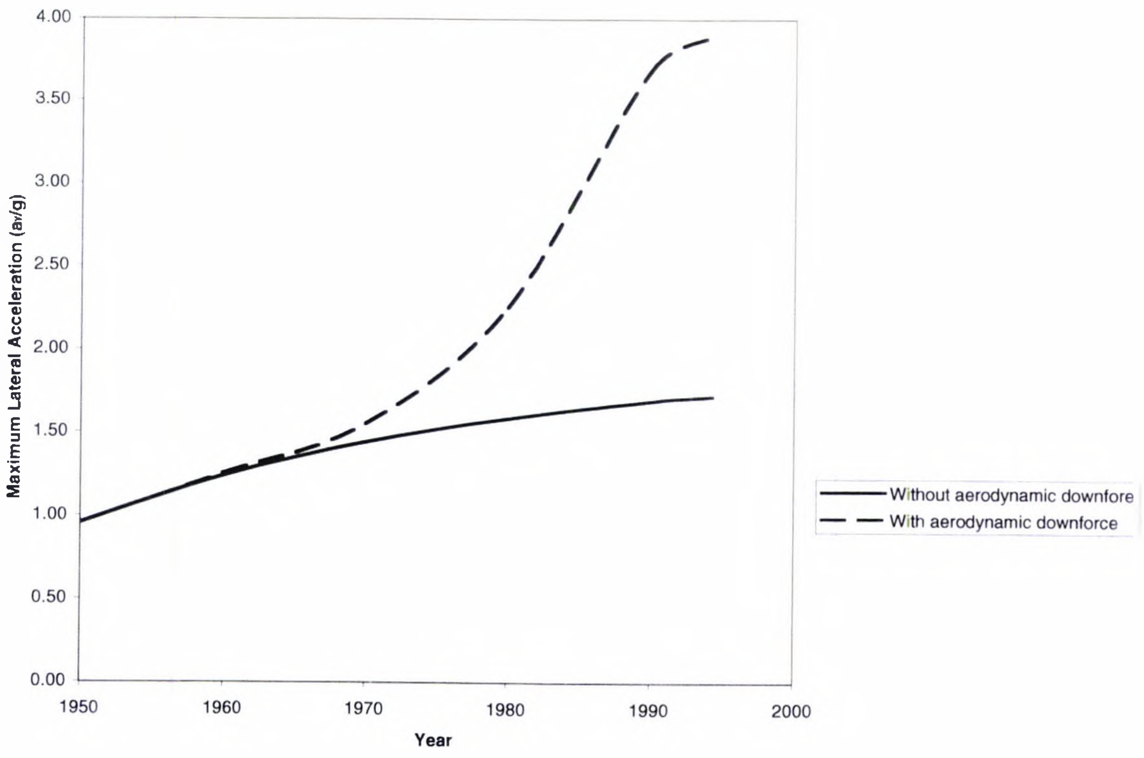

Figure 1.14: Performance over fifty years. (Katz (1995))

components must be uncovered and therefore exposed to the airstream, thus creating one of the single largest sources of drag on the car.

The downforce is provided by a winged high nose, a flat bottom floor with a diffuser and a rear wing assembly. The front wing produces downforce that acts ahead of the front wheel centreline. The high nose allows a greater air mass flow to the car's floor. This airflow accelerates as it flows into the decreasing volume created by the car's floor and the ground plane. The air pressure decreases according to Bernoulli's Law and the modest reduction in pressure over the generous surface area of the floor creates most of the downforce. At the rear wheel centreline, where the flat bottom ends as dictated by the rules, the diffuser begins as a sharp ramp. Typical angles that the diffuser makes with the plane of the floor are 10^o to 15^o. The flow can separate at the transition between the floor and the diffuser. If engineered properly, the flow can reattach forming a separation bubble that produces a region of low pressure on the underside of the car. This low pressure created by the diffuser provides a favourable pressure gradient downstream of the nose and the floor.

The rear wing assembly in turn, provides a favourable pressure gradient for the flow on the diffuser. Adjustment of the wings is not permitted while the car is in motion. Figure 1.15 shows a typical F-1 car with some key components labelled.

Wind tunnel tests by the author and others have shown that the behaviour of all the aerodynamic components on an F-1 car are intimately linked. Changes in the rear wing angle of incidence can propagate upstream causing significant changes in pressure on the front wings. Thus any isolated aerodynamics study of an F-1 car must be carefully conducted with this behaviour in mind. In addition, the flow around the car is dominated by interacting vortices, wakes and flow separation. The vortical flows are produced by the wings and other appendages such as the turning vanes. There are wakes shed by the wheels which are exposed to the airstream as well as every other component similarly exposed. Significant separated flows occur on the wheels. Figure 1.16 shows some features of the airflow about a generic open wheel racecar. The rear wheels, diffuser and the lower tier of the rear wing assembly produce an upwash which reduces the local angle of incidence of the flow about the upper rear wing tiers. The wakes generated by the rear wheels flow towards the car's centreline. The blockage produced in the near ground plane region by these wakes, imposes an upwash angle into the oncoming flow. The low aspect ratio of the rear wings, approximately 2.5 to 3.0 for an F-1 triple element rear wing assembly, produce strong vortical flows which despite the presence of endplates, also induce an upwash angle.

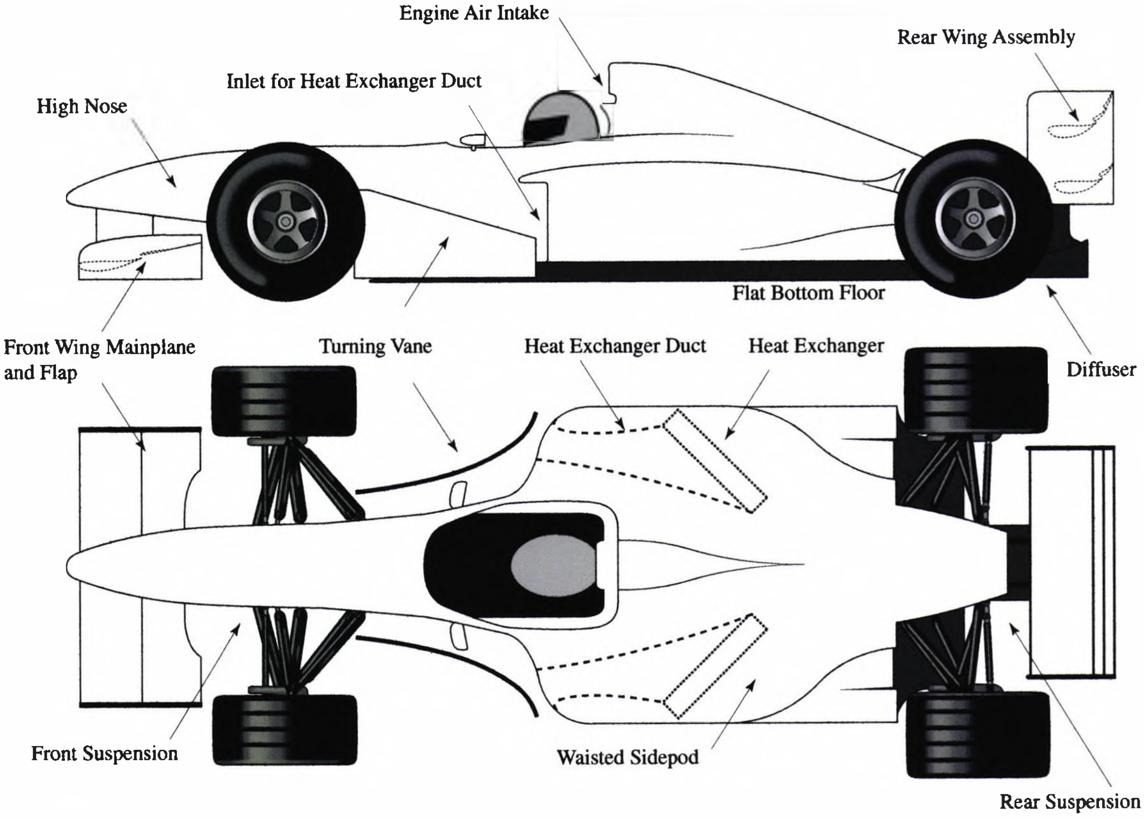

Figure 1.15: Some components on contemporary F-1 car.

The diffuser by virtue of its positive angle orientation and the resultant upward flow also induce an upwash angle. It is because of these three factors that the possibility of flow separation on the wings is reduced over the angle of incidence range. The same wings tested in isolation would demonstrate flow separation over a larger range of angles. It is possible to have flow separation on such wings at the highest angles on a racecar. The upwash induced by the rear wheels, diffuser and the lower wing elements and its action to reduce separation is not well documented due to the secrecy in Formula One.

A typical F-1 car with the aforementioned aerodynamic devices can produce a C_L of -2.5 to -3.5. The C_D of an F-1 car can vary from 0.9 to 1.1. A C_D greater than unity is possible because of the rotating wheels exposed to the airflow. The C_L and C_D will vary depending on whether low, high or medium downforce configuration is used which in turn depends on the track on which the car is run.

1.2.3 Rear Wings, Region of Focus

With the deaths of Roland Ratzenberger and Ayrton Senna in 1994, the FIA instituted a series of rules aimed at reducing downforce. One of the areas targeted was the diffuser.

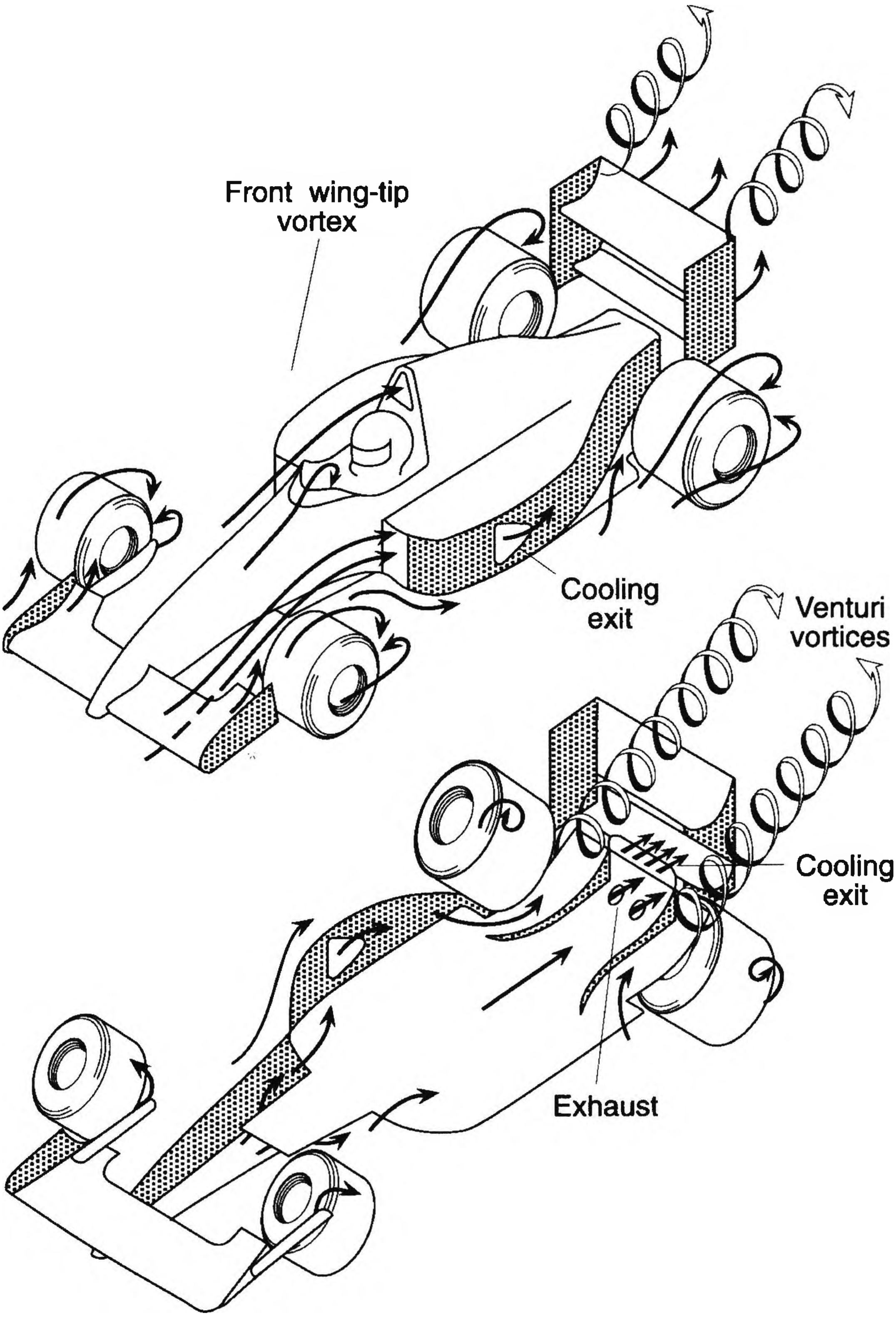

Figure 1.16: Flows around generic open wheel racecar. (Katz (1995))

Its length was significantly reduced and the size of any separation bubble that could be created on it. Most of the downforce generated by a moving F-1 car still comes from the floor, but it was immediately obvious that the rear wings would be called upon to decrease the downforce deficit. One of the early solutions was to use more elements in the rear wing assembly with some teams sporting rear wing assemblies with as many as twelve. But this new innovation was quickly addressed by the FIA with a new rule stating that the rear wings be able to fit in a volume that is defined by a width of 1000 mm, length of 350 mm and a height of 210 mm. The high downforce wings used by all the teams fill this volume. It is now more difficult and in some cases impossible to get the high level of downforce required at tracks for which it would be ideal. Given that the front wing is essentially a trimming device and that for the time being, the floor is producing the maximum possible downforce, the only way to increase downforce is to increase the contribution of the rear wings. Considering the rules, this can only be achieved through an increase in wing loading. It is for this reason that the high downforce rear wing assembly is the focal point of this research.

In the experimental work of Innes (1995) and the experimental and numerical work conducted by Lewington (2002), the application of an AJVG array to aviation high lift systems was used to increase lift and decrease drag. In these systems, the array was powered by pressurised air. The use of AJVGs on an F-1 high downforce system would most likely depend on a ram air system. It was the intention of this research to establish whether a ram AJVG system could produce a similar improvement in lift and drag on F-1 high downforce rear wings.

A study of isolated rear wings constitutes a valid approach because AJVGs act locally on the boundary layers about the high downforce system. Therefore, the nature of the onset flow is irrelevant. This includes the very different onset flows experienced by the wings in situ behind the car and the same wings as used in the wind tunnel experiments. If the boundary layer on any of these wings is separated, then based on theory and previous work, AJVGs should be able to delay or eliminate this separation and at the same time increase the downforce.

The ability of AJVGs to effect improvements has been well demonstrated in the experiments where three-dimensional flow fields persisted despite attempts made to create nominal two-dimensional flows. The ability of the AJVGs to reduce the size of these highly three-dimensional separated regions and increase downforce bodes well for their application to the highly three-dimensional flows experienced about a racing car.

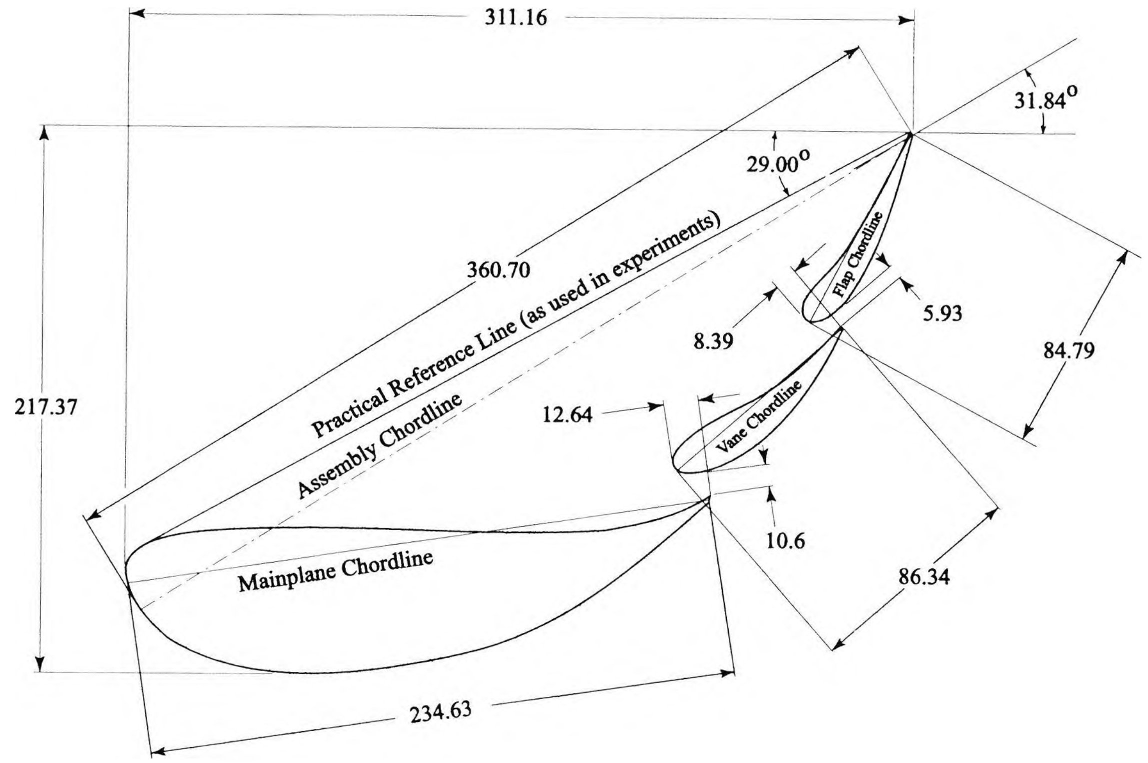

Figure 1.17: High downforce model dimensioned in millimetres.

1.2.4 Resolving Aerodynamic Forces

In order to compute the measured and predicted aerodynamic forces acting on the high downforce models, numerical integrations of C_p versus $\frac{x}{c}$ were performed based on the experimental and predicted pressures. This procedure involved the definition of element and assembly chords and their orientation with respect to the global co-ordinate system. Figure 1.18 shows the individual wings with their respective chords and relevant co-ordinate axes. Assuming a two-dimensional pressure distribution, we can define the normal and axial force coefficients C_n and C_x acting on an aerofoil that are perpendicular and parallel to its chord line. They can be expressed as follows

$$C_n = \int_0^1 (C_{pu} - C_{pl})\, d\left(\frac{x}{c}\right) \tag{1.1}$$

and

$$C_x = \int_{\frac{y1}{c}}^{\frac{y2}{c}} C_p d\left(\frac{y}{c}\right) \tag{1.2}$$

where C_{pu} and C_{pl} are the upper and lower surface pressure coefficients measured or predicted on the aerofoil. The lift and drag coefficients c_l and c_d are referred to the freestream direction. The c_l is perpendicular to the freestream direction and the c_d is parallel to the freestream direction. Figure 1.18 shows that for each element and the high downforce system as a whole we can write

$$c_l = C_n \cos\alpha - C_x \sin\alpha \tag{1.3}$$

$$c_d = C_x \cos\alpha + C_n \sin\alpha \tag{1.4}$$

Referring to Figure 1.18, we sum the normal and axial forces on the mainplane, vane and flap elements to arrive at the lift and drag forces for the assembly. This gives the following equations where the subscripts “m”, “v”,“f” and “a” represent the mainplane, vane, flap elements and the assembly parameters. A_a represents the assembly area which in the two-dimensional case is simply the assembly chord.

$$\begin{aligned} c_l = [&C_{nm}A_m \cos\alpha_m - C_{xm}A_m \sin\alpha_m \\ &+C_{nv}A_v \cos\alpha_v - C_{xv}A_v \sin\alpha_v \\ &+C_{nf}A_f \cos\alpha_f - C_{xf}A_f \sin\alpha_f]/A_a \end{aligned} \tag{1.5}$$

$$\begin{aligned} c_d = [&C_{xm}A_m \cos\alpha_m + C_{nm}A_m \sin\alpha_m \\ &+C_{xv}A_v \cos\alpha_v + C_{nv}A_v \sin\alpha_v \\ &+C_{xf}A_f \cos\alpha_f + C_{nf}A_f \sin\alpha_f]/A_a \end{aligned} \tag{1.6}$$

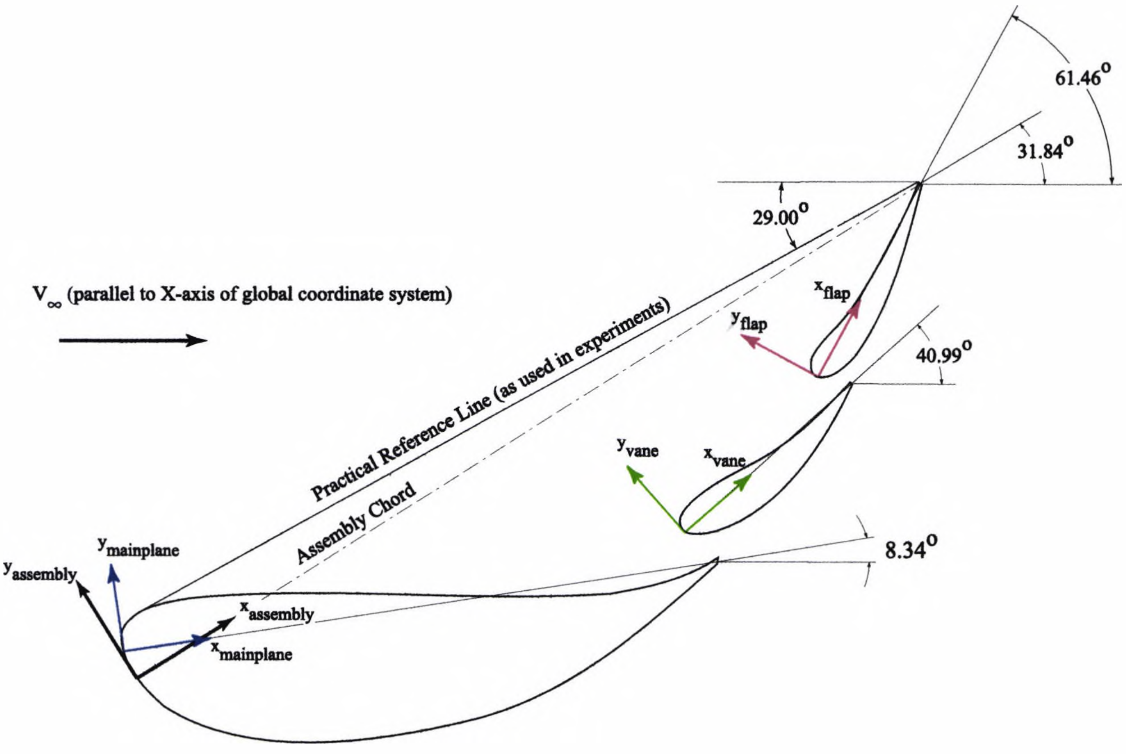

Note: All angles are measured with respect to global coordinate system

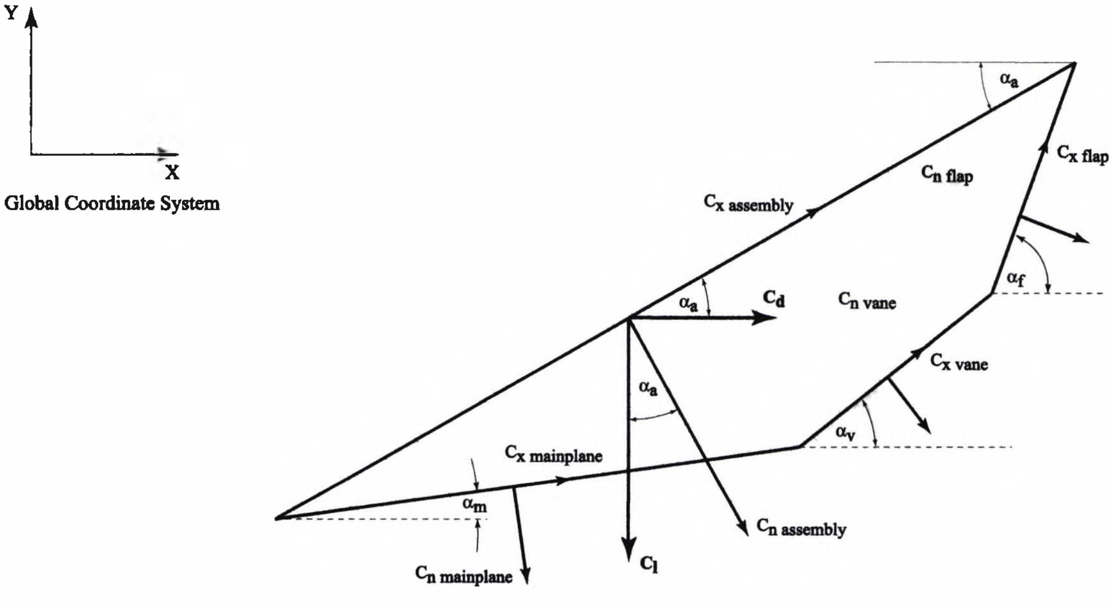

Figure 1.18: Basis for aerodynamic force resolution.

In their numerical and experimental work on high lift aerofoils, Larsson & Arlinger (1997) found that the computation of drag through the integration of surface pressures can be in error by as much as 50% even though both the predicted pressure and skin friction distributions can show excellent agreement with experiments. In performing an integration, small errors in the surface pressure can produce relatively large errors in C_x and c_d. This is especially true of the leading and trailing edge areas where the pressure gradients are highest.

Measurements with the wake rake would have allowed the estimation of drag through the integration of the momentum loss downstream of the high downforce model. In their work on high lift models Innes (1995) and Lewington (2002) successfully used the wake integration technique to estimate C_d. During the experiments conducted with the high downforce wing, it was not possible to use the wake rake provided because it was subjected to severe buffeting at most angles of incidence. It is highly unlikely that the instrument would have survived any prolonged testing. Due to a lack of time, it was not possible to make the necessary modifications required to increase the stiffness of the wake rake structure.

Innes (1995) and Lewington (2002) used C_n as determined by Equation 1.1 as an estimate of the useful aerodynamic force generated by the high lift systems in their work. C_n is less affected by numerical errors than C_x. c_l was not used because C_x terms derived from the integration of surface pressures are involved in its calculation. Nevertheless, the author includes the terms of C_x and c_d as they provide some insight into the performance trends of the high downforce wing.

1.2.5 Objectives

The aim of this research was to investigate the use of a air jets on a Formula One high downforce wing and to effect an improvement in its performance through an increase in the lift coefficient. The research focused on the angles of incidence where the lift coefficient, C_L, began to decrease due to flow separation. This angle was determined to be approximately 19^o through numerical models and experiments. The high downforce model used in this research differs significantly from those discussed in most of the aviation high lift research in that it has no leading edge slat. It consists of a mainplane, vane and trailing edge flap and is illustrated in Figure 1.17.

The secondary objectives of this research were to establish the suitability of the pre-processing software, Navier-Stokes CFD code and post-processing software for analysing the flows about these wings. Suitability was determined by the accuracy, userfriendliness, speed and how well the various software packages handled the large data sets. Valuable experience was also gained in the use of super computers for the calculation and post processing phases of the numerical effort.

Chapter 2

Mathematical Model

2.1 Grid Generation

In order to perform a numerical simulation of a fluid flow, one needs to be able to calculate the velocity and pressure by solving the algebraic form of the Navier-Stokes equations at discrete points within the confines of the flow domain. It is the concept of a grid and grid generation which will be the focus of this section. It is the grid that provides a description of the extent of the fluid domain, the boundary conditions and the level of discretisation. A numerical fluid flow simulation cannot be posed without these three items.

ICEM-CFD 3.3.2, a Graphic User Interface (GUI) based, dedicated suite of mesh generators, was used to create all the meshes presented. ICEM-CFD 3.3.2 is written and supported by ICEM Systems. There are two main reasons for the decision to choose ICEM-CFD 3.3.2 as the pre-processor. First, ICEM-CFD 3.3.2 can produce grids with unmatched ease. Initially, the panel method from Analytical Methods Incorporated, VSAERO, was to be used in conjunction with a Navier-Stokes code. After trials, CFX-4.2 was chosen. CFX-4.2 is written and supported by CFX International. Both these codes possessed their own pre-processors the use of which would have created a double workload. One of the virtues of ICEM-CFD 3.3.2 is that it can create grids for several codes thus decreasing the workload. Eventually, it was decided to forego the use of VSAERO because it could not model the air jets but even with just one code being used, ICEM-CFD 3.3.2 was still the pre-processing tool of choice.

Four modules within ICEM-CFD 3.3.2 were used to create the grids for the various cases. They were DDN, P-Cube, Leo and the CFX-4.2 translator. DDN is the computer aided design (CAD) package, P-Cube is an object oriented, parametric block modelling tool which performs functions on the CAD geometry supplied by DDN or other CAD software. Leo is a grid analysis tool where the user is able to view, diagnose and modify structured and unstructured grids produced by P-Cube and other grid generation modules in ICEM-CFD 3.3.2. The grids created by P-Cube and those modified by Leo are written in a proprietary binary format. The CFX-4.2 translator converts this ICEM format to one that is readable by the CFX-4.2 software.

2.1.1 ICEM-CFD DDN Computer Aided Design Software

The grid generation process originates with a digital copy of the wing geometry in the Initial Graphics Exchange Specification (IGES). The IGES standard is used to transfer product definition data, such as drawings, between different Computer Aided Design / Computer Aided Manufacturing (CAD/CAM) systems. It is maintained by the United States Product Data Association. The IGES files used for the transfer conformed to the 1993 IGES 5.2 USPRO/IPO-100 standard. This file was copied into the DDN CAD software where the aerofoils themselves were present as non-uniform rational B-splines (NURBS). These were used as the basis for creating any NURB surfaces that were required to represent the wings. The wings in situ in the wind tunnel experiment were measured and these data were used to create a virtual turntable analogous to the turntable used in the experiments. This turntable facilitated any changes in angle of incidence, α. Close Range Photogrammetry was employed to locate the static pressure orifices on the wing. These data were also input from an IGES file. Finally, DDN was used to create the walls of the wind tunnel test section. All of the above were performed to a more than adequate four decimal places with highly refined NURBS splines and surfaces.

2.1.2 ICEM-CFD P-Cube Meshing Software

P-Cube was used to dynamically build the block structures with reference to the CAD geometry produced by DDN. The topology produced is based on the following hierarchy; vertices, edges, faces and blocks. Two vertices can be used to create an edge, a minimum of two edges are needed to create a face and a minimum of two faces are required to create a block. In the last two instances, the remaining edges and faces are created by the software to have the necessary four edges for a face and six faces for a block.

The Eriksson or Hermite Orthogonal transfinite interpolation schemes are available in P-Cube for the creation of facial and domain grids. These schemes are further discussed in Thompson, Warsi & Mastin (1985) and the Wehner (1998). In addition Laplacian and Thomas-Middlecoff schemes are available for facial and domain grid relaxation. Any of the grid creation and relaxation options can be combined. With these techniques, P-Cube automatically generates the surface mapped grids from the user-defined edge distributions. The user has a significant amount of control over the final result. The interior domain nodes were created according to the default Eriksson scheme that is analogous to the default Eriksson interpolation scheme used for the faces.

With the exception of periodic boundaries, all types of boundaries used in CFX-4.2 could be assigned by P-Cube, namely inlets, outlets, pressure boundaries, symmetry planes and walls. This step was as simple as selecting the relevant face and assigning a name and boundary type to it.

2.1.3 Leo

Leo was used to examine the quality of the grids generated by P-Cube and in a few rare cases to actually improve it. For the most part, it was used to verify the grid quality through the examination of the determinants, aspect ratios and skewness of the grid cells. Leo was usually used to permute and align the **i**, **j**, **k** orientation of the grids to produce a right handed co-ordinate system with the **i**, **j**, **k** vectors parallel to the x, y and z axes. Finally, this module was used to verify the boundary conditions. The following sections discuss some features of Leo and how they were used in the grid generation process. The definitions of the parameters used to analyse the grid quality are for the most part, discussed in terms of hexahedral elements as they are the only type of element used in the calculations presented.

Element Jacobian

ICEM-CFD uses a non-standard mathematical definition of the Jacobian that is a normalised measure of an element's volume. It is used to analyse the metrics of linear hexahedral elements in structured volume meshes or linear quadrilateral elements in surface meshes. The algorithm is as follows:

Calculate the Jacobians A(**j**, **k**, **l**) of the 27 canonical points of the tri-linear hexahedron element for j, k and l = 1, 2, 3. Given the matrix A=$[A_1, A_2, A_3]$, its metric or inner product is:

$$\begin{aligned} \parallel A \parallel &= max\left(\mid A_1 \mid^2, \mid A_2 \mid^2, \mid A_3 \mid^2\right) \\ &= max(a_{11}^2 + a_{21}^2 + a_{31}^2, a_{12}^2 + a_{22}^2 + a_{32}^2, a_{13}^2 + a_{23}^2 + a_{33}^2) \end{aligned} \tag{2.1}$$

The value m is determined such that:

$$m = \frac{max \mid A_i\left(j,k,l\right) - A_i\left(j_{mx},k_{mx},l_{mx}\right) \mid^2}{max \mid A_i\left(j,k,l\right) \mid^2, \mid A_i\left(j_{mx},k_{mx},l_{mx}\right) \mid^2} \quad \text{for i=1, 2, 3} \tag{2.2}$$

The maximum is taken over the canonical points such that:

$$mx = \parallel A\left(j_{mx},k_{mx},l_{mx}\right) \parallel \tag{2.3}$$

The Jacobian is then defined as $100\left(1-m\right)$.

Element Determinant

ICEM-CFD uses a non-standard mathematical definition of the determinant that is a normalised measure of an element's volume and is computed at each corner node. It is derived from the element's Jacobian matrix. For an ideal mesh element, the determinant of the Jacobian is the same at all four corners.

If we consider the sub-region of a brick element to be an inner mesh volume, then the sign of any inner volume is determined by the sign of the determinant of the Jacobian. In the case of an element with all sides parallel to each other, the determinant is 100. A positive determinant corresponds to a cell that has no negative inner volume. A non-zero negative determinant is given by a cell that possesses negative internal volume. This can occur when a cube is deformed by moving one corner towards the centre until the volume is no longer convex. The equations and algorithm for calculating the determinant are as follows:

Calculate the Jacobian for 27 canonical points of a tri-linear hexahedron, $A\left(j,k,l\right)$, for j, k = 1, 2, 3. Find the point (j,k,l) where the value $\mid det \quad A\left(j,k,l\right) \mid$ achieves a maximum. The quantity mx, is then defined as $mx = max\left[det \quad A\left(j,k,l\right)\right]$. If mx = 0, then the cell is empty and the determinant is zero as well. The value m is defined as:

$$m = max\left[\frac{\mid A\left(j,k,l\right) - mx \mid}{mx}\right] \tag{2.4}$$

The determinant is given by the quantity $100\left(1-m\right)$ and is invariant under translation, scaling and rotation of the cell. Two-dimensional cells are analysed by a similar algorithm where mx is defined as:

$$mx = max \mid N\left(j,k\right) \mid^2 \tag{2.5}$$

The quantity $\mid N\left(j,k\right) \mid^2$ is the squared norm of the normal vector to the point $\left(j,k\right)$ for j and k = 1, 2, 3. Two-dimensional elements also differ from three-dimensional cells with regards to the quantity m given by:

$$m = max \left[\frac{N(j,k) \cdot N(j_{mx}, k_{mx})}{mx} \right] \tag{2.6}$$

The maximum is taken over the canonical points such that $mx = \mid N(j_{mx}, k_{mx}) \mid^2$. The two-dimensional determinant is then defined as 100m.

Element Aspect Ratio

The aspect ratio is defined to be the ratio between diagonally opposite vertices of hexahedral and quadrilateral elements. It is the ratio (shorter diagonal/longer diagonal).

Skewness

In the case of hexahedral elements, the skewness is calculated by taking all pairs of adjacent faces and computing the normals. The maximum value is then used to normalise all other values so that a value of zero corresponds to perpendicular faces and a value of one corresponds to parallel faces.

2.1.4 CFX-Meshimport

CFX-Meshimport was used to reblock the grids created by ICEM-CFD for some of the two-dimensional calculations and all of the three-dimensional calculations that were run in parallel. The parallel coding of CFX-4.2 demanded the use of CFX-Meshimport for domain optimisation.

The code creates the largest blocks possible to reduce the number of blocks and it orients these blocks in such a way that the first direction is the longest. This makes for improved computational efficiency in the solution process especially in the case of machines with a vector architecture. The algorithm also tries to create blocks with the same number of cells as this helps in maintaining an even balance between the processors in a multiprocessor solution run.

The conversion process creates a connected, structured, multi-block domain. The size and shape of each block is model specific and depends on the geometry. Each block is created by starting with Block 1 from the cell with the (**i**, **j**, **k**) label (1, 1, 1) and then cells are examined in the **i**, **j** and **k** directions. If an obstruction is encountered in a particular direction, then the code stops growing cells in that direction. Obstructions to growth could be the end of a block, or a wall. A new block is started when cell growth in all three directions has been completed in the previous block. The cell location and structure in unaffected by the reblocking procedure.

With the completion of the blocking procedure, the connectivity information is created to specify the connectivity of the new blocks. The secondary information such as boundary conditions, solid or porous regions and regions of different material properties is then transferred to the reblocked model. This information is stored as a list of elements belonging to a specific group. The new optimised grid is then written to disk. An original cell and block structure created with ICEM-CFD 3.3.2 is shown in Figures 2.1 and 2.2 respectively for the high lift model at 29^o incidence. It comprises fifty blocks. The reblocked grid, as modified by CFX-Meshimport comprises fourteen blocks and is shown in Figure 2.3.

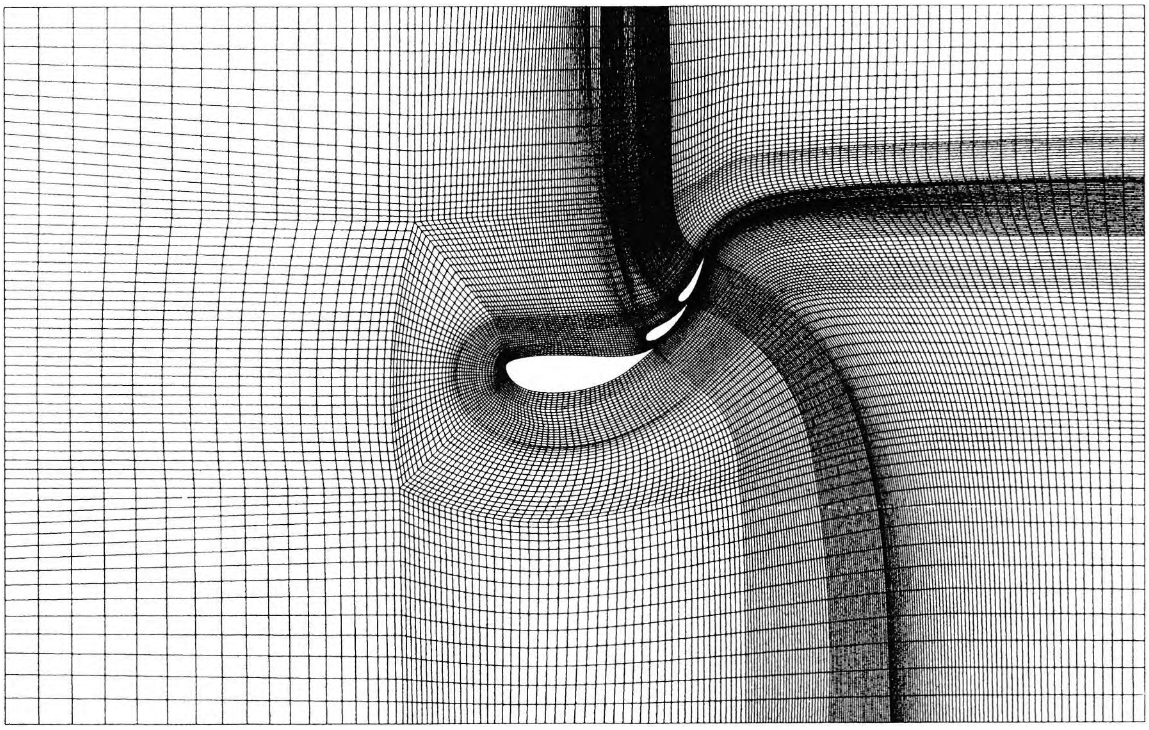

Figure 2.1: Cell structure and distribution, $\alpha = 29^o$.

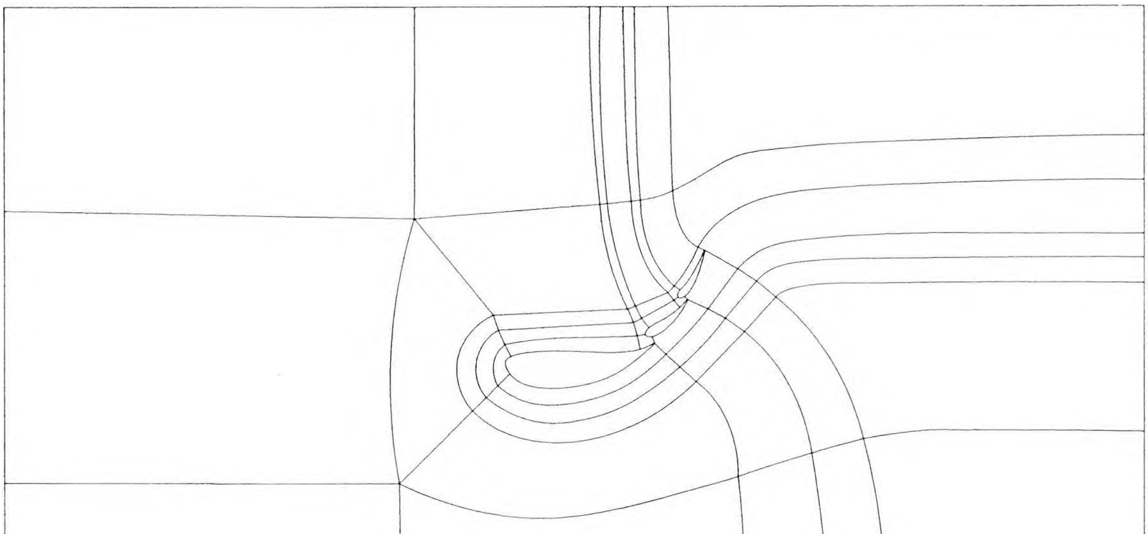

Figure 2.2: Block structure created in ICEM-CFD 3.3.2, $\alpha = 29^o$.

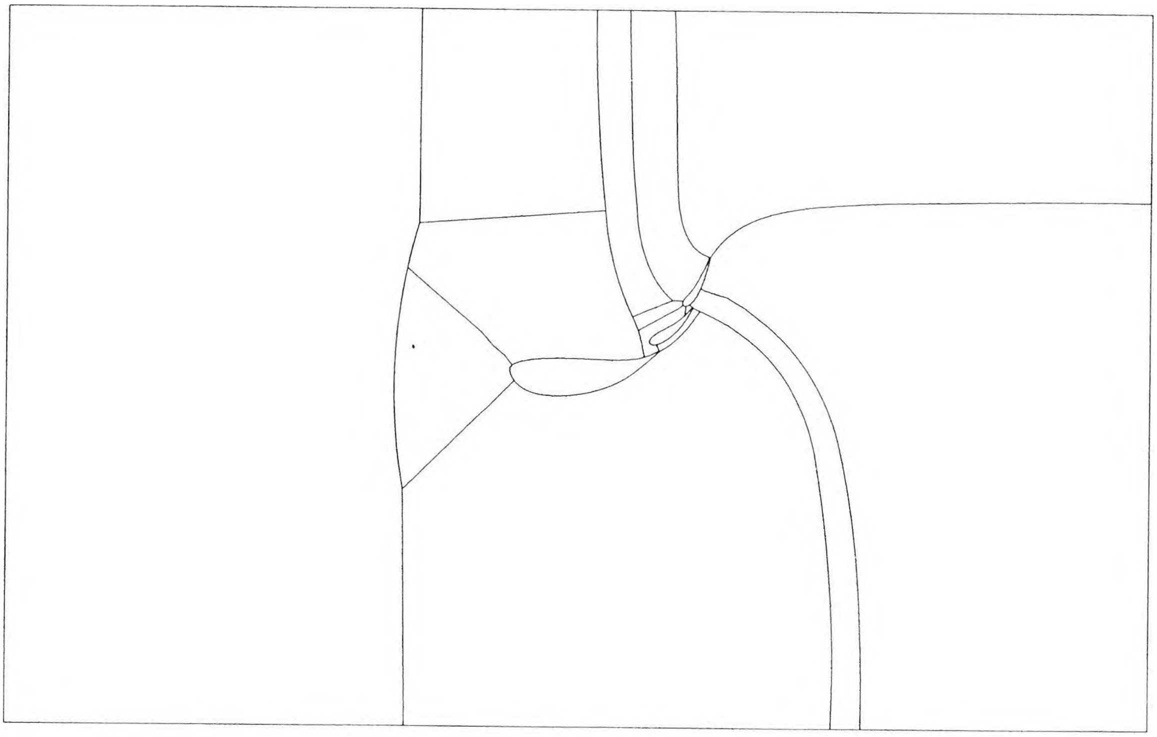

Figure 2.3: Domain reblocked by CFX-Meshimport, $\alpha = 29^o$.

2.2 Governing Equations

The flows considered in these investigations were modelled as steady state, single phase and incompressible with air as the fluid. They are Newtonian, turbulent and isothermal and as such can be described mathematically by the Navier-Stokes equations. The popular definition of the Navier-Stokes equations encompasses the momentum equations for viscous flow as well as the continuity and energy equations. Initially, only the momentum equations were so named as discussed in Anderson, J. D. Jr. (1995). The more strict definition, where the Navier-Stokes Equations are the viscous momentum equations is used in this thesis. This is done because the flows presented here are considered to be isothermal. The three-dimensional conservation form of the Navier-Stokes Equations is presented in Equations 2.7 to 2.9. They describe the conservation of linear momentum in three dimensions. u, v and w are the x, y and z components of velocity. The pressure is denoted by p. τ represents the normal and shear stress terms, depending on the suffix. The terms τ_{xx}, τ_{yy} and τ_{zz} are normal stresses. The terms τ_{xy}, τ_{xz} and τ_{yz} represent the shear stresses. ρ is density and f_x, f_y and f_z are the body forces on the fluid element in the x, y and z directions. Time is denoted by t.

$$\frac{\partial(\rho u)}{\partial t} + \nabla \cdot (\rho u V) = -\frac{\partial p}{\partial x} + \frac{\partial \tau_{xx}}{\partial x} + \frac{\partial \tau_{yx}}{\partial y} + \frac{\partial \tau_{zx}}{\partial z} + \rho f_x \tag{2.7}$$

$$\frac{\partial(\rho v)}{\partial t} + \nabla \cdot (\rho v V) = -\frac{\partial p}{\partial y} + \frac{\partial \tau_{xy}}{\partial x} + \frac{\partial \tau_{yy}}{\partial y} + \frac{\partial \tau_{zy}}{\partial z} + \rho f_y \tag{2.8}$$

$$\frac{\partial(\rho w)}{\partial t} + \nabla \cdot (\rho w V) = -\frac{\partial p}{\partial z} + \frac{\partial \tau_{xz}}{\partial x} + \frac{\partial \tau_{yz}}{\partial y} + \frac{\partial \tau_{zz}}{\partial z} + \rho f_z \tag{2.9}$$

Equations 2.10, 2.11 and 2.12 relate the normal stresses in the fluid to the velocity gradients and therefore the rate of shearing in the flow. Equations 2.13, 2.14 and 2.15 relate the shear stress to the viscosity and the cross component velocity gradients. They follow from experiments performed by Stokes (1845) on *Newtonian* fluids.

$$\tau_{xx} = \lambda(\nabla \cdot V) + 2\mu\frac{\partial u}{\partial x} \tag{2.10}$$

$$\tau_{yy} = \lambda(\nabla \cdot V) + 2\mu\frac{\partial v}{\partial y} \tag{2.11}$$

$$\tau_{zz} = \lambda(\nabla \cdot V) + 2\mu\frac{\partial w}{\partial z} \tag{2.12}$$

$$\tau_{xy} = \tau_{yx} = \mu\left[\frac{\partial v}{\partial x} + \frac{\partial u}{\partial y}\right] \tag{2.13}$$

$$\tau_{xz} = \tau_{zx} = \mu \left[\frac{\partial u}{\partial z} + \frac{\partial w}{\partial x} \right] \tag{2.14}$$

$$\tau_{yz} = \tau_{zy} = \mu \left[\frac{\partial w}{\partial y} + \frac{\partial v}{\partial z} \right] \tag{2.15}$$

μ is the molecular viscosity coefficient and λ is the second viscosity coefficient. Stokes made the hypothesis that $\lambda = -\frac{2}{3}\mu$. Substituting Equations 2.10 to 2.15 in Equations 2.7 to 2.9 yields the complete Navier-Stokes equations in conservation form. They are presented in Equations 2.16 to 2.18.

$$\begin{aligned} \frac{\partial(\rho u)}{\partial t} + \frac{\partial(\rho u^2)}{\partial x} + \frac{\partial(\rho uv)}{\partial y} + \frac{\partial(\rho uw)}{\partial z} &= -\frac{\partial p}{\partial x} \\ +\frac{\partial}{\partial x}\left(\lambda \nabla \cdot V + 2\mu \frac{\partial u}{\partial x}\right) &+ \frac{\partial}{\partial y}\left[\mu\left(\frac{\partial v}{\partial x} + \frac{\partial u}{\partial y}\right)\right] \\ &+\frac{\partial}{\partial z}\left[\mu\left(\frac{\partial u}{\partial z} + \frac{\partial w}{\partial x}\right)\right] + \rho f_x \end{aligned} \tag{2.16}$$

$$\begin{aligned} \frac{\partial(\rho v)}{\partial t} + \frac{\partial(\rho uv)}{\partial x} + \frac{\partial(\rho v^2)}{\partial y} + \frac{\partial(\rho vw)}{\partial z} &= -\frac{\partial p}{\partial y} \\ +\frac{\partial}{\partial x}\left[\mu\left(\frac{\partial v}{\partial x} + \frac{\partial u}{\partial y}\right)\right] &+ \frac{\partial}{\partial y}\left(\lambda \nabla \cdot V + 2\mu \frac{\partial v}{\partial y}\right) \\ &+\frac{\partial}{\partial z}\left[\mu\left(\frac{\partial w}{\partial y} + \frac{\partial v}{\partial z}\right)\right] + \rho f_y \end{aligned} \tag{2.17}$$

$$\begin{aligned} \frac{\partial(\rho w)}{\partial t} + \frac{\partial(\rho uw)}{\partial x} + \frac{\partial(\rho vw)}{\partial y} + \frac{\partial(\rho w^2)}{\partial z} &= -\frac{\partial p}{\partial z} \\ +\frac{\partial}{\partial x}\left[\mu\left(\frac{\partial u}{\partial z} + \frac{\partial w}{\partial x}\right)\right] &+ \frac{\partial}{\partial y}\left[\mu\left(\frac{\partial w}{\partial y} + \frac{\partial v}{\partial z}\right)\right] \\ &+\frac{\partial}{\partial z}\left(\lambda \nabla \cdot V + 2\mu \frac{\partial w}{\partial z}\right) + \rho f_z \end{aligned} \tag{2.18}$$

Equation 2.19 below, is the continuity equation which describes the conservation of mass and is used as a constraint on any Navier-Stokes fluid flow solution.

$$\frac{\partial \rho}{\partial t} + \nabla \cdot (\rho V) = 0 \tag{2.19}$$

These equations represent the necessary transport equations. The energy equation is not solved because the flow is modelled as isothermal. A process known as the Reynolds averaging of the Navier-Stokes equations introduces additional unknown variables. The concept of a turbulence model, which is discussed in the next section addresses these additional terms.

2.2.1 Turbulence Modelling

In theory, a direct solution of the Navier-Stokes equations is possible. Unfortunately, due to the limitations of modern computers, this is not yet achievable for any relevant flows because the amount of computer memory and disk space is too large. Even if these two limitations did not exist, the envisioned problem still could not be solved in anything approaching a reasonable time. Direct numerical simulations (DNS) are possible for low Reynolds number flows with simple geometries but such flows are of academic interest only. The root of this inability lies with discretisation of the flow domain which needs to be extremely dense to capture the nature of the flow in its entirety. Typical turbulence length scales can be 10^{-3} times smaller than the characteristic length of the flow domain. To resolve the features of the turbulent eddies of this scale in three dimensions would require at minimum 10^9 grid points. For the time being, turbulence models are used to address this issue and they arise from analytical methods that were first put forward many years ago.

Adopting a statistical approach, Osborne Reynolds proposed that the equations describing turbulent flows be considered in terms of mean and fluctuating components. The mean components are averaged over a time scale, $t_2 - t_1$, that is long when compared to the turbulent fluctuations but small relative to time scale of interest. Equation 2.20 shows the generic variable, ϕ expressed in terms of its mean and fluctuating components. ϕ could be a vector or scalar quantity and in so being it is representative of any of the vectors or scalars which appear in the governing equations. Equation 2.21 shows the definition of Reynolds time averaging for the quantity ϕ.

$$\phi = \overline{\phi} + \phi' \tag{2.20}$$

where the mean quantity is defined as

$$\overline{\phi} = \frac{1}{t_2 - t_1} \int_{t_1}^{t_2} \phi \, dt \tag{2.21}$$

Reynolds averaging has the following properties:

1. $\overline{\overline{\phi}} = \overline{\phi}, \quad \overline{\phi'} = 0.$

2. $\overline{a\phi + b\psi} = a\overline{\phi} + b\overline{\psi}$, where a and b are constants.

3. $\overline{\phi\psi} = \overline{\phi}\,\overline{\psi} + \overline{\phi'\psi'}$.

4. $\overline{\frac{\partial \phi}{\partial t}} = \frac{\partial \overline{\phi}}{\partial t}, \quad \overline{\frac{\partial \phi}{\partial x_i}} = \frac{\partial \overline{\phi}}{\partial x_i}$ where x_i = x, y, z.

For any general case, the time averaged expressions, for the three velocity components, pressure, temperature and species, when substituted into Equation 2.16 to 2.19, give the distribution of mean quantities in the flow. These are the quantities of greatest engineering interest. However, by using this statistical approach, the system of equations no longer constitute a closed system because of extra terms called Reynolds stresses, e.g. $-\rho\ \overline{uv}$ that represent the transport of mean momentum due to turbulence. Terms called Reynolds fluxes, e.g. $-\rho\ \overline{u\phi}$, also appear. They represent the transport of mass and heat by turbulent motion.

The Reynolds Averaged Momentum Equations can only be solved after the turbulence correlations such as, $\overline{uv}$ and $\overline{u\phi}$ are determined. Exact equations for these terms do exist, but these terms increase complexity of the problem because they contain even higher order correlations. Some form of empirical correlation is needed to provide values for these terms and this is provided by a turbulence model. The concept of a turbulence model is based on hypotheses about turbulent processes and they in turn require empirical input in the form of constants or functions. It is also necessary to note that they do not model turbulent processes directly, only their effects on the mean flow field.

2.2.2 k-ϵ Turbulence Model

The k-ϵ turbulence model is a two equation turbulence model based on the eddy-viscosity hypothesis first posed by Boussinesq. It presumes that an effective turbulent viscosity can be defined which is proportional to the fluctuating velocity of the turbulent motion and the typical length scale of this motion. In this model, it is assumed that the turbulent viscosity is given by

$$\mu_t = C_\mu \rho \frac{k^2}{\epsilon} \tag{2.22}$$

The transport equations for turbulent kinetic energy, k, and the rate of dissipation of turbulent energy, ϵ are

$$\frac{\partial\left(\rho k\right)}{\partial t} + \nabla \cdot \left(\rho V k\right) - \nabla \cdot \left[\left(\mu + \frac{\mu_T}{\sigma_k}\right) \nabla k\right] = P + G - \rho\epsilon \tag{2.23}$$

and

$$\frac{\partial\left(\rho \epsilon\right)}{\partial t} + \nabla \cdot \left(\rho V \epsilon\right) - \nabla \cdot \left[\left(\mu + \frac{\mu_T}{\sigma_\epsilon}\right) \nabla \epsilon\right] = C_1 \frac{\epsilon}{k}\left[P + C_3 max(G,0)\right] - C_2 \rho \frac{\epsilon^2}{k} \tag{2.24}$$

P is the shear production given by

$$P = \mu_{eff} \nabla V \cdot \left(\nabla V + (\nabla V)^T\right) - \frac{2}{3} \nabla \cdot V (\mu_{eff} \nabla \cdot V + \rho k) \tag{2.25}$$

where

$$\mu_{eff} = \mu + \mu_t \tag{2.26}$$

P is the turbulent production due to body forces. The constants appearing in Equation 2.22 to 2.25 of the model were left at their default values for all calculations. These values are, C_1 = 1.44, C_2=1.92, C_3=0.0, and C_μ=0.09. The turbulent Prandtl number for k, σ_k = 1.0 while the turbulent Prandtl number for ϵ, σ_ϵ is given by

$$\sigma_\epsilon = \frac{k^2}{(C_2 - C_1)\sqrt{C_\mu}} \tag{2.27}$$

It is the k-ϵ model described by these equations that was used in the numerical calculations.

2.2.3 Boundary Conditions

In order for a numerical problem to be well posed, the boundary conditions must be applied to the fluid domain. Among the conditions that can be imposed are inlets, outlets, pressure boundaries, symmetry and periodic boundaries.

Walls

At solid boundaries, a no-slip condition is imposed on the flow so that the mean and fluctuating velocities are zero but the rate of turbulent dissipation, ϵ, is finite. If the boundary conditions are specified to the wall, then the governing equations must be integrated through the viscous sub-layer and two problems arise from this approach. First, there are very high fluid flow gradients present in this region and a direct solution would require a disproportionately dense grid to resolve the effects. This is computationally expensive and therefore prohibitive. Second, the viscous effects are dominant in this region and the k-ϵ model, being a high Reynolds number turbulence model is not suited to resolving the flow fields.

An empirical relationship, known as The Universal Law of the Wall is used to specify the velocity profile from the wall to the fully turbulent region of the boundary layer. The grid cells adjacent to the wall should have their centres on or above the limit of the buffer region. Figure 2.4 shows the proper location of the cell centres. Prandtl postulated that the total shear stress in the near wall region is constant and that the size of the turbulent eddies is proportional to their distance from the wall.

The wall shear stress, τ_w, is defined such that

$$\tau_w = \rho k \sqrt{C_\mu} \tag{2.28}$$

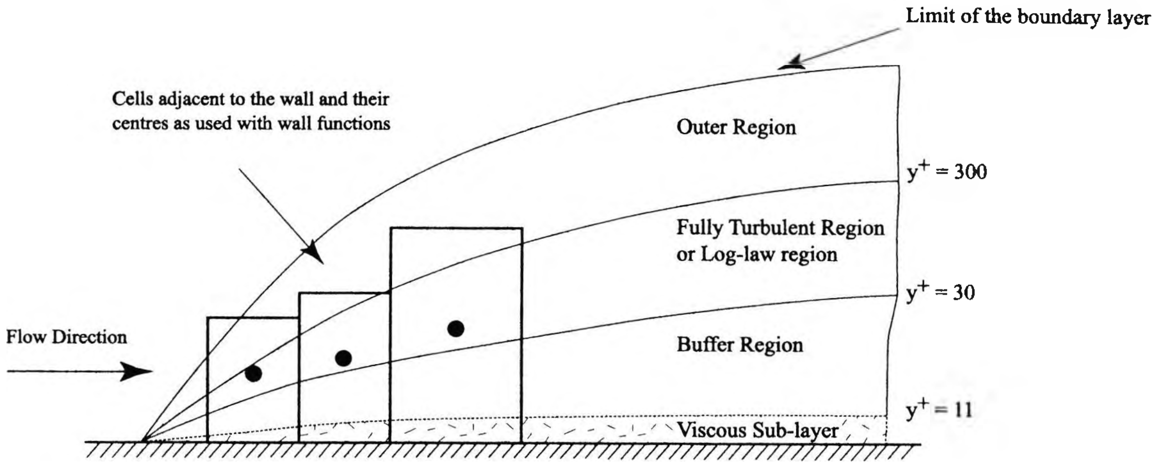

Figure 2.4: Near-wall region showing cells and boundary layer.

The non-dimensional velocity parallel to the wall in the x-direction is given as

$$\mathbf{u}^{+} = \begin{cases} y^{+}, & \text{for } y^{+} < y_0^{+} \\ \frac{1}{\kappa}\ln\left(Ey^{+}\right), & \text{for } y^{+} > y_0^{+} \end{cases} \tag{2.29}$$

In Equation 2.29, the term y^+ represents the non-dimensional distance from the wall. It can be expressed as

$$y^{+} = \frac{y u_\tau}{\nu} \tag{2.30}$$

where u_τ is the friction velocity given as

$$u_\tau = \sqrt{\frac{\tau_w}{\rho}} \tag{2.31}$$

Equation 2.29 shows that the scaled velocity varies linearly with distance between the wall and the limit of the viscous sub-layer, normally up to a $y^+ = 11$. Thereafter, it varies in a logarithmic fashion. The term, κ is von Kármán's constant. $\kappa \approx 0.4$. The wall roughness constant, E, may be set by the user. $E \approx 9$ for smooth walls.

The value of κ in Equation 2.28 is solved in the cells adjacent to the wall. The wall shear stress, τ_w, is obtained from this solution. The turbulence dissipation is obtained from the turbulent kinetic energy using the following equation

$$\epsilon = \frac{C_\mu^{3/4} k^{3/2}}{\kappa y} \tag{2.32}$$

The conditions set out by these empirical relationships do hold well over most of the near-wall regions, but problems can be experienced near regions of flow stagnation, separation, reattachment and regions with strong adverse flow field gradients in the flow direction.

Inlets

Inlet boundaries are Dirichlet boundaries where the values that define the condition at the boundary are set explicitly. The velocity is specified at an inlet in terms of the normal component or the u, v and w components. The resultant velocity component at the inlet must be non-zero so as to have a non-zero net mass flow through the domain. The velocity components are fixed relative to the global co-ordinate system. Turbulence parameters such as k and ϵ must also be set on the inlet boundary.

Pressure Boundaries

A Dirichlet boundary condition is imposed on the pressure by the user at pressure boundaries. For incompressible flows, the pressure can be set to a constant value.

Symmetry Planes

All parameters are mathematically symmetric across such planes. The component of velocity normal to the boundary and the component of the Reynolds shear stress and Reynolds flux involving the normal velocity component are zero.

Periodic Boundaries

The parameters at opposite sides of the fluid domain are set equal to each other.

2.3 Finite Volume Formulation

The finite volume method has its basis in the transformation of the exact form of the Navier-Stokes equations into a system on non-linear algebraic equations. It is a process by which arbitrary space, equations and time are discretised and the resulting equations are then solved in a steady state or transient manner. All of the work discussed in this thesis involves steady state solutions and this being the case, much time will not be spent discussing the mathematics of transient calculations.

The discretisation of space is provided by the mesh, that provides a finite number of regular control volumes at which the algebraic equations are solved. It also defines the extent of the fluid domain and allows for the imposition of the boundary conditions.

The equations are discretised by replacing the analytical form of the Navier-Stokes equations with algebraic expressions relating the values at the grid control points to each other.

The time discretisation is formed by choosing an interval of time and subdividing this interval into several not necessarily equal time steps. The system of equations is then solved over this time interval for each time steps.

2.3.1 Space Discretisation

In the finite volume formulation employed for this research, the given flow domain is discretised using a non-overlapping, fully structured, multi-block grid with body-fitted co-ordinates. A block is a topological entity comprising six faces arranged to form a regular parallelepiped. The nodes are arranged on the edge of each face according to a local co-ordinate system, (ξ, η, ζ), such that the adjacent nodes are formed according to the unit vector $\mathbf{i}, \mathbf{j}, \mathbf{k}$ in the ξ, η and ζ directions. A multi-block topology is structured in such a way that the block faces are coincident and the neighbouring cells can meet as part of entire faces.

The use of body-fitted co-ordinates permits the treatment of arbitrary two and three-dimensional geometries according to Rhie & Chow (1983). This method uses a curvilinear co-ordinate transformation to map the flow domain to a simple rectangular flow domain in computational space as depicted in Figure 2.5. The Cartesian co-ordinate system $x^i = (x, y, z)$, in the flow domain is replaced by a curvilinear co-ordinate system $\xi^i = (\xi, \eta, \zeta)$ so that the boundaries of the flow domain are surfaces such that $\xi^i = C$, where C is a constant. The governing equations in their conservation form are discretised in rectangular co-ordinate space and then transformed to the curvilinear co-ordinate system. The exact differential form of these equations and the continuous information they represent is replaced by discrete algebraic equations. The discrete form of these algebraic expressions relate the values of the transport equations at the cell centres. The equations are solved at the cell centres in rectangular computational space. The solution is then transformed to the Cartesian co-ordinate system for analysis as discussed at length by Anderson, J. D. Jr. (1995).

2.4 Equation Discretisation

The finite volume method uses a piecewise continuous, algebraic form of the Navier-Stokes equations that is solved over each control volume and therefore, the entire fluid domain. It is assumed that the parameters of interest vary linearly over the control volume. The piecewise variation of the general fluid parameter ϕ is evaluated from the integration of

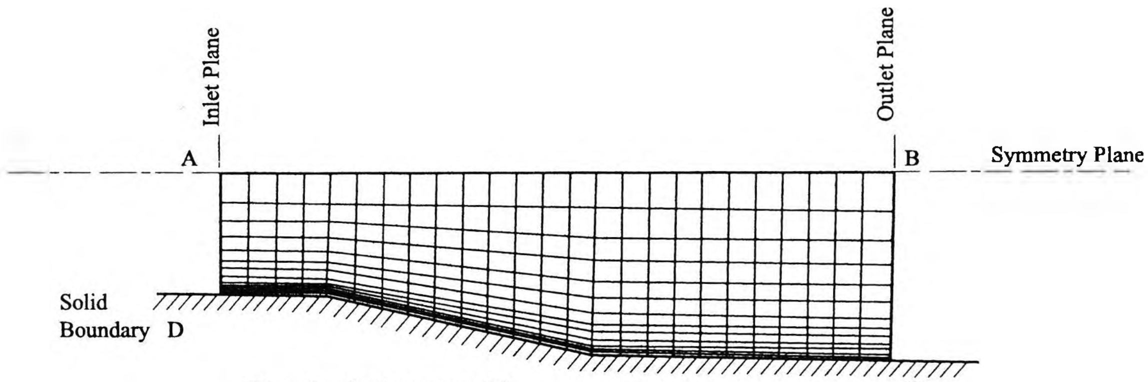

The physical space grid.

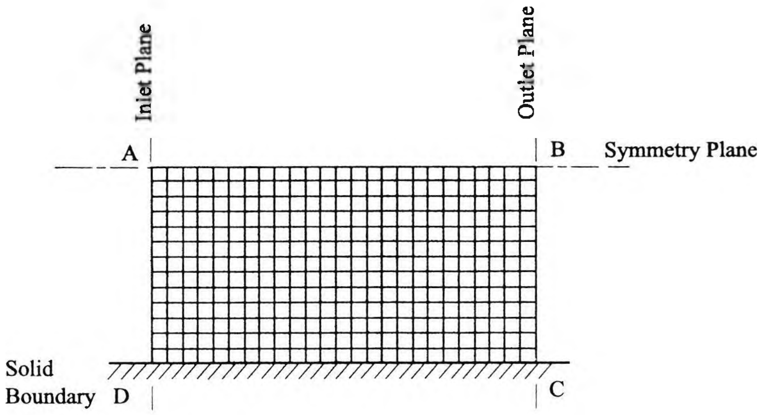

The computational space grid.

Figure 2.5: Physical and computational space. (CFX International (1998))

these equations. The parameter ϕ could represent the components u, v or w. A value of ϕ is calculated at the computational nodes located at the centre of each cell. The boundary conditions are imposed at the centre of the boundary faces. The discretisation equations provide values of ϕ at a group of computational nodes. These equations are consistent with the conservation of mass, momentum and energy. The conservation of these quantities is satisfied over any number of cells and as a result over the entire fluid domain. This will be clarified later in this chapter when the concept of the pressure velocity correction is discussed. This conservation is true in theory for any number of cells and not just for a large number of grid points. Thus, even for coarse grids, the solution produces exact integral balances.

The accuracy of the numerical solution is a function of the machine accuracy or round-off error and the discretisation error. For a given machine, there is nothing that can be done about the first error save the use of a double precision calculation as opposed to single precision. The accuracy of the numerical approximation is directly dependent on the structure and number of grid points. The finer the grid, the better the numerical solution. A finer grid results in the discretisation error which tends to zero as the number of grid points tends to infinity. If this occurs, the numerical discretisation is said to be consistent. However, practicality demands that there be a finite number of grid points because of the finite capacity of computers.

2.4.1 Two-Dimensional Finite Volume Discretisation

A simplified two-dimensional example as illustrated in Figure 2.6 will be used to introduce the discretisation theory as presented in Patankar (1980) and Demirdzic & Muzaferija (1997). A more general form of the momentum equations presented in Equations 2.16 to 2.18 is

$$\frac{\partial(\rho\phi)}{\partial t} + \nabla \cdot (\rho V \phi) - \nabla \cdot (\Gamma \nabla \phi) = S \tag{2.33}$$

where Γ is the relevant effective diffusivity of the generic parameter ϕ. S denotes the source term which comprises the grouping of all terms that are not convection or diffusion terms. Integrating Equation 2.33 over each control volume and therefore the entire fluid domain we get the following:

$$\int \frac{\partial(\rho\phi)}{\partial t} dV + \int \nabla \cdot (\rho\phi V) \cdot \mathbf{n} dA - \int \nabla \cdot (\Gamma \nabla \phi) \cdot \mathbf{n} dA = \int S\, ndV \tag{2.34}$$

For a two-dimensional case, Equation 2.34 becomes,

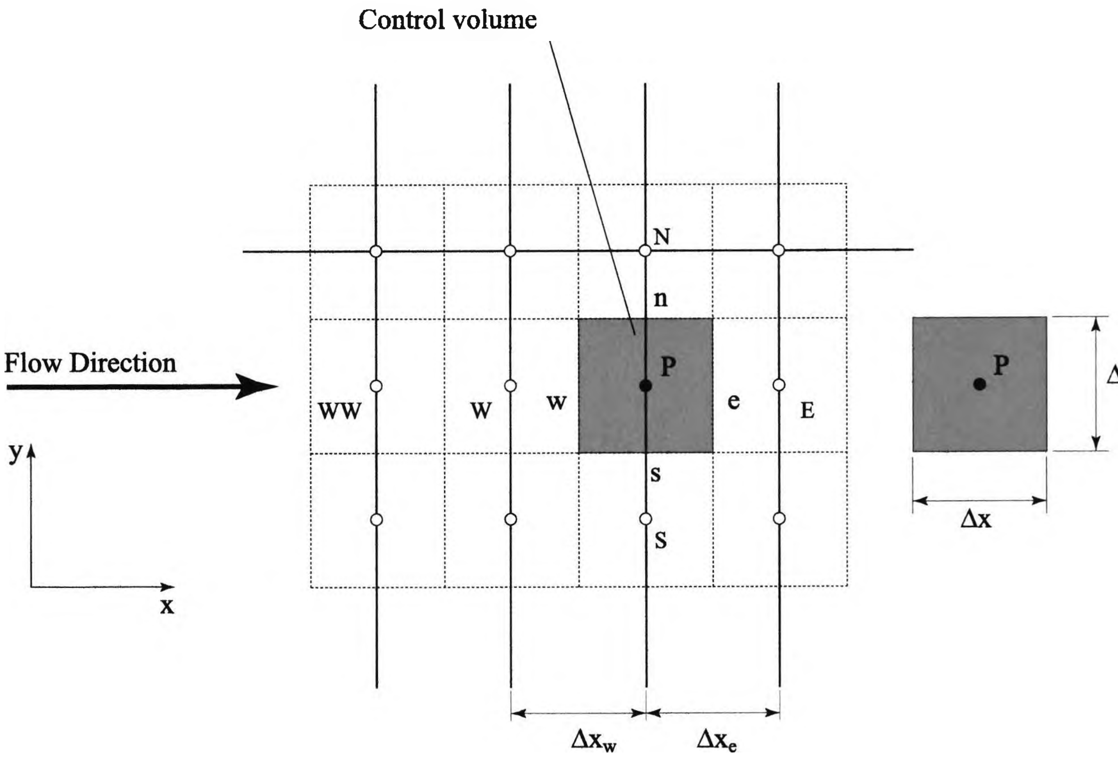

Figure 2.6: Two-dimensional control volume with compass notation.

$$\iint \frac{\partial(\rho\phi)}{\partial t}\,dxdy + \iint \nabla(\rho V\phi)\cdot\mathbf{n}\,dxdy - \iint \nabla(\Gamma\nabla\phi)\cdot\mathbf{n}\,dxdy = \iint S\,dxdy \tag{2.35}$$

Taking the terms independently we get the following:

$$\iint \frac{\partial(\rho\phi)}{\partial t}\,dxdy = 0 \tag{2.36}$$

because we are only considering steady state calculations. Next we integrate and expand the convection term:

$$\begin{aligned}
\iint \nabla(\rho V\phi)\cdot\mathbf{n}\,dxdy &= \iint \left[\frac{\partial(\rho u\phi)}{\partial x} + \frac{\partial(\rho v\phi)}{\partial y}\right] dxdy \\
&= \int [\rho u\phi]_w^e\,dy + \int [\rho v\phi]_s^n\,dx \\
&= (\rho u_e\phi_e - \rho u_w\phi_w)\,\Delta y + (\rho v_n\phi_n - \rho v_s\phi_s)\,\Delta x \\
&= \left(\rho u_e\frac{(\phi_E+\phi_P)}{2} - \rho u_w\frac{(\phi_W+\phi_P)}{2}\right)\Delta y \\
&\quad + \left(\rho v_n\frac{(\phi_N+\phi_P)}{2} - \rho v_s\frac{(\phi_S+\phi_P)}{2}\right)\Delta x
\end{aligned} \tag{2.37}$$

and finally, we integrate and expand the diffusion term:

$$\begin{aligned}\iint \nabla(\Gamma\nabla\phi)\cdot\mathbf{n}\,dxdy &= \iint\left[\frac{\partial}{\partial x}\left(\Gamma\frac{\partial\phi}{\partial x}\right)+\frac{\partial}{\partial y}\left(\Gamma\frac{\partial\phi}{\partial y}\right)\right]dxdy\\ &= \int\left[\Gamma\frac{\partial\phi}{\partial x}\right]_w^e dy+\int\left[\Gamma\frac{\partial\phi}{\partial y}\right]_s^n dx\\ &= \left[\Gamma\frac{\partial\phi}{\partial x}\right]_e dy-\left[\Gamma\frac{\partial\phi}{\partial x}\right]_w dy\\ &\quad+\left[\Gamma\frac{\partial\phi}{\partial y}\right]_n dx-\left[\Gamma\frac{\partial\phi}{\partial y}\right]_s dx\\ &= \left(\frac{\Gamma}{\Delta x_e}(\phi_E-\phi_P)-\frac{\Gamma}{\Delta x_w}(\phi_P-\phi_W)\right)\Delta y\\ &\quad+\left(\frac{\Gamma}{\Delta x_n}(\phi_N-\phi_P)-\frac{\Gamma}{\Delta x_s}(\phi_P-\phi_S)\right)\Delta x\end{aligned} \tag{2.38}$$

We can now substitute the terms from Equation 2.37 and Equation 2.38 into Equation 2.35, the two-dimensional momentum equation. But before doing this, the diffusion terms in Equation 2.38 can be simplified with the following expressions:

$$D_e=\frac{\Gamma}{\Delta x_e},\ D_w=\frac{\Gamma}{\Delta x_w},\ D_n=\frac{\Gamma}{\Delta x_n},\ D_s=\frac{\Gamma}{\Delta x_s}.$$

The result is the algebraic form of the two-dimensional momentum equation:

$$\begin{aligned}\phi_P\left(\frac{1}{2}u_e\Delta y+D_e\Delta y-\frac{1}{2}u_w\Delta y+D_w\Delta y+\frac{1}{2}v_n\Delta x+D_n\Delta x-\frac{1}{2}v_s\Delta x+D_s\Delta x\right)&\\ =\phi_E\left(-\frac{1}{2}u_e\Delta y+D_e\Delta y\right)+\phi_W\left(\frac{1}{2}u_w\Delta y+D_w\Delta y\right)&\\ +\phi_N\left(-\frac{1}{2}v_n\Delta x+D_n\Delta x\right)+\phi_S\left(\frac{1}{2}v_s\Delta x+D_s\Delta x\right)&\\ +S\Delta x\Delta y&\end{aligned} \tag{2.39}$$

We can simplify Equation 2.39 even further by defining four coefficients, a_E, a_W, a_N and a_S that are the sum of the convective and diffusive terms in each direction. so we have

$$a_E=\left(D_e-\frac{1}{2}u_e\right)\Delta y,\quad a_W=\left(D_w+\frac{1}{2}u_w\right)\Delta y,$$

$$a_N=\left(D_n-\frac{1}{2}v_n\right)\Delta x\quad\text{and}\quad a_S=\left(D_s+\frac{1}{2}v_s\right)\Delta x$$

Using the law of continuity, it can be shown that,

$$a_P=a_E+a_W+a_N+a_S$$

We get the final form of the discretised two-dimensional momentum equations as,

$$a_P\phi_P=a_E\phi_E+a_W\phi_W+a_N\phi_N+a_S\phi_S+b \tag{2.40}$$

where the coefficient, $b = S\Delta x \Delta y$, represents the source terms. These would be the sum of the body forces B, pressure forces, and viscous forces V_x and V_y. in the x and y directions. We could express these term as,

$$S_x = -\frac{\partial p}{\partial x} + B_x + V_x \tag{2.41}$$

$$S_y = -\frac{\partial p}{\partial y} + B_y + V_y\,, \tag{2.42}$$

$$\text{where} \quad B_x = \rho f_x \text{ and } \quad B_y = \rho f_y$$

We can refer to Equations 2.7 thru 2.18 for a reminder of the expressions for the viscous forces. It is a system of non-linear equations such as Equation 2.40 that are solved for any arbitrary geometry using blocked, iterative methods to improve the solution convergence.

2.4.2 Modelling of Convection Terms

The choice of a differencing scheme represents a choice between the speed, robustness and accuracy of the solution. Some of the schemes used in Navier-Stokes CFD codes in general and CFX-4.2 in particular will now be presented. On the lower order, robust side, there are simple, first order accurate, upwind schemes. On the higher order, less robust side, there are bounded, third order accurate schemes. The order of accuracy refers to the truncation error of the Taylor series approximation that is the basis for the finite difference discretisation of the equations. Referring to Figure 2.6, we can use a Taylor series expansion to arrive at an expression for the term $\phi_E - \phi_W$.

A Taylor series expansion of the quantities ϕ_E and ϕ_W according to the familiar finite difference methods set out in Smith (1985) could be expressed as follows:

$$\phi_E = \phi_P + \left(\frac{\partial \phi}{\partial x}\right)_P \Delta x + \left(\frac{\partial^2 \phi}{\partial x^2}\right)_P \frac{\Delta x^2}{2} + \left(\frac{\partial^3 \phi}{\partial x^3}\right)_P \frac{\Delta x^3}{6} + \ldots \tag{2.43}$$

$$\phi_W = \phi_P - \left(\frac{\partial \phi}{\partial x}\right)_P \Delta x + \left(\frac{\partial^2 \phi}{\partial x^2}\right)_P \frac{\Delta x^2}{2} - \left(\frac{\partial^3 \phi}{\partial x^3}\right)_P \frac{\Delta x^3}{6} + \ldots \tag{2.44}$$

If we subtract Equation 2.43 from Equation 2.44 we are left with

$$\phi_E - \phi_W = 2\left(\frac{\partial \phi}{\partial x}\right)_P \Delta x + 2\left(\frac{\partial^3 \phi}{\partial x^3}\right)_P \frac{\Delta x^3}{6} + \ldots \tag{2.45}$$

Rearranging the terms, we are left with

$$\left(\frac{\partial \phi}{\partial x}\right)_P = \frac{\phi_E - \phi_W}{2\Delta x} - \left(\frac{\partial^3 \phi}{\partial x^3}\right)_P \frac{\Delta x^2}{6} + \ldots \tag{2.46}$$

The last term on the right hand side is the truncation error of the approximation and it is this term that determines the accuracy. Equation 2.46 is a second order accurate approximation of the first derivative of ϕ with respect to x at the computational node P and can be written as

$$\left(\frac{\partial \phi}{\partial x}\right)_P = \frac{\phi_E - \phi_W}{2\Delta x} + O\left(\Delta x\right)^2 \tag{2.47}$$

where $\Delta x = \Delta x_e = \Delta x_w$. The last term in Equation 2.46 is rewritten as $O\left(\Delta x\right)^2$ in Equation 2.47 to reflect the order of accuracy.

2.4.3 Upwind Differencing

The upwind differencing scheme (UDS) is also known as the upstream-difference, or the donor-cell method. It was introduced by Courant, Issacson & Rees (1952), modified and represented by Gentry, Martin & Daly (1966) and more recently by Runchal & Wolfstein (1969). The upwind differencing scheme proposes that there is an alternative formulation for the convection terms other than that of simply taking an average between two computational points. For example, in other formulations, ϕ_e, the term at the eastern face of the control volume (see Figure 2.6), is taken to be the average of ϕ_P and ϕ_E. In the upwind scheme the convection term, ϕ_e, is assigned the value of ϕ from the computational node on the upwind side of the face. That is to say

$$\phi_e = \begin{cases} \phi_P, & \text{if } u_e > 0 \\ \phi_E, & \text{if } u_e < 0 \end{cases} \tag{2.48}$$

The value of ϕ_w can be determined in a similar way using the computational nodes, ϕ_W and ϕ_P. The rationale behind this scheme is that the computational nodes downstream are affected by those upstream subject to a flow field dominated by convection. The upwind scheme is first order accurate.

2.4.4 Central Differencing

The central difference scheme (CDS), calculates the parameters at any given cell face to be the arithmetic mean of the adjacent computational nodes. If we consider the eastern face then the central difference scheme would give

$$\phi_e = \frac{1}{2}\left(\phi_E + \phi_P\right) \tag{2.49}$$

The central difference scheme is second order accurate, but it can lead to an unstable calculation if the cell Reynolds number, $Re_{cell} > 2$, where

$$Re_{cell} = \frac{\rho u \Delta x}{\mu}$$

If $|Re_{cell}| > 2$, then the use of another scheme is essential.

2.4.5 Hybrid Differencing

The hybrid differencing scheme (HDS), is a modified differencing scheme first developed by Spalding (1972), where central differencing is used if $|Re_{cell}| < 2$.

If $|Re_{cell}| \geq 2$, then an upwind interpolation scheme is employed for the dominant convection terms and the diffusion terms are ignored. If $|Re_{cell}| < 2$, the use of this scheme is marginally better than upwind differencing because it is second order accurate. Central differencing is used across streams and in regions of low velocities.

2.4.6 Higher Order Upwind Differencing

The higher order upwind scheme (HUW), is a second order accurate scheme which is formed by extrapolating to the cell face from two upwind computational points.

On the western face of the control volume in Figure 2.6, ϕ_w, is given by

$$\phi_w = \frac{3}{2}\phi_W - \frac{1}{2}\phi_{WW} \tag{2.50}$$

The higher upwind difference scheme is more difficult to implement than other schemes such as simple upwind differencing and central differencing. This is due to the presence of the extra ϕ_{WW} term. To retain the structure of the solution matrix, the scheme can be expressed as,

$$\phi_w = \phi_W + \frac{1}{2}(\phi_W - \phi_{WW}) \tag{2.51}$$

This bracketed term in Equation 2.51 is included in the source terms of the matrix formulation using a type of deferred correction. ϕ at the eastern face is

$$\phi_e = \frac{3}{2}\phi_P - \frac{1}{2}\phi_W \tag{2.52}$$

The inclusion of these bracketed terms in Equation 2.51 and the equivalent terms for ϕ_e, carries certain complications with the retention of the solution matrix structure. These complications are addressed by including the bracketed terms in the source terms. This procedure is presented in CFX-International (1995).

2.4.7 Quadratic Upstream Interpolation of Convective Kinematics

The quadratic upstream interpolation of convective kinematics (QUICK), introduced by Leonard (1979), is third order accurate. It achieves this by interpolating between two computational points upstream and one downstream. At the western face of the control volume

$$\phi_w = \frac{3}{8}\phi_P + \frac{3}{4}\phi_W - \frac{1}{8}\phi_{WW} \tag{2.53}$$

and at the eastern face,

$$\phi_e = \frac{3}{8}\phi_E + \frac{3}{4}\phi_P - \frac{1}{8}\phi_W \tag{2.54}$$

This method can be unstable at high cell Reynolds numbers due to the addition of the downstream computational point. The possibility of instabilities has been discussed by Versteeg & Malalaskera (1995) and is addressed by the next and last scheme presented.

2.4.8 Curvature Compensated Convective Transport

The previously mentioned instability is a nuance of the higher order upwind schemes caused by non-physical overshoots in the solution. Turbulent energy, which should always be positive, can assume negative values in certain solutions where the QUICK scheme is employed. An example of this would be where too coarse a grid results in a shear layer not being adequately resolved. The CCCT scheme is a modified QUICK scheme which is bounded, thus eliminating these overshoots. CCCT interpolates between two upwind points and one downstream point as with the QUICK scheme but it differs in the following way for the western face,

$$\phi_w = \left(\frac{3}{8} - \alpha\right)\phi_P + \left(\frac{3}{4} - 2\alpha\right)\phi_W - \left(\frac{1}{8} - \alpha\right)\phi_{WW} \tag{2.55}$$

where α is related to the curvature of the variable ϕ as discussed in Alderton & Wilkes (1988). Numerically, CCCT is treated the same as the QUICK scheme.

2.5 Calculation of Pressure

Pressure cannot be calculated directly from the Navier-Stokes equations even though the pressure gradient appears on the right hand side of the Navier Stokes, Equations 2.16, 2.17 and 2.18. In solving these equations, the pressure terms that appear form a component of the source terms. The pressure does not feature explicitly in the continuity equation either, so the continuity equation cannot be considered as a pressure equation because it is a constraint on the momentum equations and the resulting velocity field to ensure the conservation of mass. This constraint can only be satisfied by correcting the pressure field. The problem lies with the fact that pressure has no governing transport equation and so it is not constrained by continuity.

Initially, it was not obvious how this correction was to be implemented. Various methods have been used to calculate pressure but these are of mostly historical value and will not be discussed here. Patankar (1980) provides detailed discussions of these methods. For steady state calculations, Patankar & Spalding (1972) developed the Semi-Implicit Method for Pressure Linked Equations (SIMPLE). The SIMPLE algorithm and variations of it such as SIMPLEC, Van Doormal & Raithby (1984), form the basis of the correction of pressure in most modern Navier-Stokes calculations.

2.5.1 SIMPLE

The SIMPLE method for the calculation of pressure defines the velocities and pressure as the sums of an initial guess, ϕ^* and a correction, $\phi^{'}$. In three dimensions, we express the velocities and pressures as follows:

$$u = u^* + u^{'} \tag{2.56}$$

$$v = v^* + v^{'} \tag{2.57}$$

$$w = w^* + w^{'} \tag{2.58}$$

$$p = p^* + p^{'} \tag{2.59}$$

The first step in this method is to make an initial guess of the pressure at each computational node. This initial guess for the pressure is denoted by p^*. In a 3D solution domain, we can then calculate u^*, v^* and w^* from p^*. It is unlikely that that u^*, v^* and w^* will satisfy the continuity equation and this necessitates the use of a correction to each component of the velocity. We refer to Figure 2.6, but considering a 1D, steady state flow by examining only the east and west points and faces. The appropriate discretised equation for this flow is,

$$a_P^u u_P^* = a_E^u u_E^* + a_W^u u_W^* + \frac{1}{\rho}\left(p_e^* - p_w^*\right) \tag{2.60}$$

The equation reflecting the application of the correction terms is,

$$a_P^u u_P^{'} = a_E^u u_E^{'} + a_W^u u_W^{'} + \frac{1}{\rho}\left(p_e^{'} - p_w^{'}\right) \tag{2.61}$$

In order to simplify the discretisation process, the corrected velocity components for the neighbouring nodes are now omitted from Equation 2.61. We now have,

$$a_P^u u_P^{'} = \frac{1}{\rho}\left(p_e^{'} - p_w^{'}\right) \tag{2.62}$$

or

$$u_P^{'} = \frac{1}{\rho a_P^u}\left(p_e^{'} - p_w^{'}\right) \tag{2.63}$$

Equation 2.63 is the velocity correction formula. To form an expression for the velocities at the east and west faces, we integrate the 1D continuity equation as expressed in Equation 2.64.

$$\frac{du}{dx} = 0\,. \tag{2.64}$$

Over the physical limits of the control volume in Figure 2.6, we have,

$$u_e - u_w = 0 \tag{2.65}$$

We now express u_e and u_w in terms of the initial guess and the correction terms.

$$u_e = u_e^* + u_e^{'} \tag{2.66}$$

and

$$u_w = u_w^* + u_w^{'} \tag{2.67}$$

Expressions equivalent to Equation 2.63, can be written for the velocity correction terms, $u_e^{'}$ and $u_w^{'}$ in Equations 2.66 and 2.67. The result is,

$$u_e^{'} = \frac{1}{\rho a_e^u}\left(p_E^{'} - p_P^{'}\right) \tag{2.68}$$

and

$$u_w^{'} = \frac{1}{\rho a_w^u}\left(p_P^{'} - p_W^{'}\right) \tag{2.69}$$

where the values for a_e^u and a_w^u are taken as the means of the adjacent computational points to give

$$\frac{1}{a_e^u} = \frac{1}{2}\left(\frac{1}{a_P^u} + \frac{1}{a_E^u}\right) \tag{2.70}$$

and

$$\frac{1}{a_w^u} = \frac{1}{2}\left(\frac{1}{a_P^u} + \frac{1}{a_W^u}\right) \tag{2.71}$$

We now rearrange the continuity equation to arrive at the following pressure correction equation that provide the corrected pressure.

$$a_p^p p_p^{'} = a_E^p p_E^{'} + a_W^p p_W^{'} + b^p \tag{2.72}$$

$$where, \quad a_E^p = \frac{1}{\rho a_E^u} \quad , a_W^p = \frac{1}{\rho a_P^u} \quad \text{and} \quad b^p = \left(u_E^* - u_W^*\right)\Delta y$$

where $\Delta y = 1$.

After calculating $p^{'}$, the corrected value for the velocity $u^{'}$ is obtained from Equation 2.63. The velocity, u, can then be calculated using Equation 2.56. If the continuity equation is not satisfied. u is assigned the value of u^* and p is assigned the value of p^*. Another iteration is then performed. In a 3D problem the same procedure would be performed with u^*, v^*, w^* and p^*.

The approximations introduced in the derivation of the pressure correction equation often cause the quantity $p^{'}$ to be overestimated. This leads to slow convergence or divergence of the solution. Under-relaxation is applied to u^*, v^*, w^* and p^* to address this problem. The discretised momentum equation becomes,

$$a_p\phi_p = (1-\alpha)\,\phi_p + \alpha\left(\Sigma a_n\phi_n + b\right) \quad \text{where,} \quad 0 < \alpha < 1. \tag{2.73}$$

and

$$p = p^* + \beta p^{'} \quad \text{where,} \quad 0 < \beta < 1. \tag{2.74}$$

SIMPLE Algorithm

A synopsis of the SIMPLE algorithm follows. A 1D formulation of the algorithm was presented but the reader is asked to assume that the form of the equations appropriate to 3D is being discussed.

1. Guess the initial pressure field p^*.

2. Solve the momentum equations, to obtain values for u^*, v^* and w^*.

3. Solve Equation 2.59 for $p^{'}$.

4. Calculate p from Equation 2.72.

5. Calculate u, v and w from u^*, v^* and w^* using equations of the form similar to Equation 2.63.

6. Solve the discretisation equation for relevant scalars quantities if they influence the flow field via fluid properties, source terms etc. If they do not influence the flow field, then it is best to wait until a converged solution has been achieved.

7. If the solution has not converged, then set $u^* = u$, $v^* = v$, $w^* = w$ and $p^* = p$ and return to step 2.

2.5.2 Coupling of Velocity and Pressure

Rhie & Chow (1983) developed a method to couple the velocity and pressure while foregoing the complexity and disadvantages of staggered grids as set out in Patankar (1980). This method uses a single grid and the discretised quantities for all the variables, u, v, w, p, etc. are stored at the cell centres. Immediately, a benefit is realised because the computer coding used to calculate the fluid variables is simplified. However, the main advantage of this method lies in the fact that it allows for the implementation of pressure algorithms, such as SIMPLEC, on non-staggered grids without the problems caused by chequerboarding in the pressure and velocity fields. It does this by estimating the facial velocities on each control volume so as to retain an approximate link between the velocities and pressure. Referring once again to Figure 2.6, the equations which for the basis of the algorithm are presented.

Assuming a constant Δx and Δy, on the west face,

$$u_w^* = \overline{u_w^*} + \frac{1}{a_w^p}\left[\overline{\left(\frac{\partial p^*}{\partial x}\right)_w} - \left(\frac{\partial p^*}{\partial x}\right)_w\right] \tag{2.75}$$

where

$$\overline{u_w^*} = \frac{1}{2}\left(u_W^* + u_P^*\right), \tag{2.76}$$

$$\frac{1}{a_w^p} = \frac{1}{2}\left(\frac{1}{a_W^p} + \frac{1}{a_P^p}\right), \tag{2.77}$$

$$\overline{\left(\frac{\partial p^*}{\partial x}\right)_w} = \frac{1}{2}\left[\left(\frac{\partial p^*}{\partial x}\right)_W + \left(\frac{\partial p^*}{\partial x}\right)_P\right] \tag{2.78}$$

and

$$\left(\frac{\partial p^*}{\partial x}\right)_w = \frac{p_P^* - p_W^*}{\Delta x} \tag{2.79}$$

On the east face,

$$u_e^* = \overline{u_e^*} + \frac{1}{a_e^p}\left[\overline{\left(\frac{\partial p^*}{\partial x}\right)_e} - \left(\frac{\partial p^*}{\partial x}\right)_e\right] \tag{2.80}$$

where

$$\overline{u_e^*} = \frac{1}{2}\left(u_P^* + u_E^*\right), \tag{2.81}$$

$$\frac{1}{\overline{a_e^p}} = \frac{1}{2}\left(\frac{1}{a_P^p} + \frac{1}{a_E^p}\right), \tag{2.82}$$

$$\overline{\left(\frac{\partial p^*}{\partial x}\right)_e} = \frac{1}{2}\left[\left(\frac{\partial p^*}{\partial x}\right)_P + \left(\frac{\partial p^*}{\partial x}\right)_E\right] \tag{2.83}$$

and

$$\left(\frac{\partial p^*}{\partial x}\right)_e = \frac{p_E^* - p_P^*}{\Delta x} \tag{2.84}$$

On the south face

$$v_s^* = \overline{v_s^*} + \frac{1}{a_s^p}\left[\overline{\left(\frac{\partial p^*}{\partial y}\right)_s} - \left(\frac{\partial p^*}{\partial y}\right)_s\right] \tag{2.85}$$

where

$$\overline{v_s^*} = \frac{1}{2}\left(v_S^* + v_P^*\right), \tag{2.86}$$

$$\frac{1}{\overline{a_s^p}} = \frac{1}{2}\left(\frac{1}{a_S^p} + \frac{1}{a_P^p}\right), \tag{2.87}$$

$$\overline{\left(\frac{\partial p^*}{\partial y}\right)_s} = \frac{1}{2}\left[\left(\frac{\partial p^*}{\partial y}\right)_S + \left(\frac{\partial p^*}{\partial y}\right)_P\right] \tag{2.88}$$

and

$$\left(\frac{\partial p^*}{\partial y}\right)_s = \frac{p_P^* - p_S^*}{\Delta y} \tag{2.89}$$

On the north face

$$v_n^* = \overline{v_n^*} + \frac{1}{a_n^p}\left[\overline{\left(\frac{\partial p^*}{\partial y}\right)_n} - \left(\frac{\partial p^*}{\partial y}\right)_n\right] \tag{2.90}$$

where

$$\overline{v_n^*} = \frac{1}{2}\left(v_P^* + v_N^*\right), \tag{2.91}$$

$$\frac{1}{a_n^p} = \frac{1}{2}\left(\frac{1}{a_P^p} + \frac{1}{a_N^p}\right), \tag{2.92}$$

$$\overline{\left(\frac{\partial p^*}{\partial y}\right)_n} = \frac{1}{2}\left[\left(\frac{\partial p^*}{\partial y}\right)_P + \left(\frac{\partial p^*}{\partial y}\right)_N\right] \tag{2.93}$$

and

$$\left(\frac{\partial p^*}{\partial y}\right)_n = \frac{p_N^* - p_P^*}{\Delta y} \tag{2.94}$$

The possibility of chequerboarding is eliminated because of the equations coupling the pressure gradient and the velocities (see Equations 2.75, 2.80, 2.85 and 2.90).

2.6 Solution Algorithms

The discretisation equations described in the previous sections produce a system of coupled, non-linear algebraic equations. An iterative solution procedure is generally used to solve the system of equations. The most popular methods are based on the Gauss-Siedel methods. The solution procedure involves linearisation of the equations to simplify the solution process. Direct solvers are not employed in such cases in part because of the excessive computational effort required to solve practical problems.

Most finite volume methods favour an iterative segregated procedure to solve the equations. In this approach, there are two iteration levels, an inner iteration and an outer iteration. The inner iteration is used to solve for the spatial coupling of each variable. Each variable is taken sequentially and all the others are regarded as constant. The number of iterations on each variable can normally be user specified as can the solver employed.

The outer iteration refers to the start of the next set of iterations on the transport variables and pressure. The non-linearity of the original equations is addressed by reforming the coefficients of the discrete equations using the most recently calculated values of the variables. The treatment of pressure, which was presented in previous sections, is the exception to this rule. This process continues until the maximum number of outer iterations is reached, until a converged solution is obtained or until the central processing unit (CPU) time is exceeded.

2.6.1 Linear Equation Solvers

For a two-dimensional, steady state, problem (see Figure 2.6), we have a set of coupled, non-linear equations of the form,

$$a_p\Phi_p - \sum_K a_k\Phi_K = b \quad (\mathrm{K = N, S, E, W}), \tag{2.95}$$

which are assembled in a system of linear algebraic equations of the form

$$A\Phi = \mathbf{b} \tag{2.96}$$

A is an N x N matrix. The vector Φ contains the values of the dependent variable Φ at N computational points and **b** is the source vector. The solution of the set of linearised algebraic equations can be addressed by different solvers. The choice of the solver can be decided by such factors as the complexity of the geometry, the block structure or the type of flow. Many of these solvers work by expressing the matrix A of Equation 2.96 as

$$A = B + E \tag{2.97}$$

An iterative procedure is then formed for the solution from the equation

$$(B + E)\,\phi = \mathbf{b} \tag{2.98}$$

This procedure is

$$B\phi^{k+1} = \mathbf{b} - E\phi^{k} \tag{2.99}$$

where k is the number of iterations. We now introduce a new expression, Equation 2.99 in the delta or error form and use Equation 2.97 to eliminate E from Equation 2.99. We now have

$$\begin{aligned} B\phi^{k+1} &= \mathbf{b} - (A - B)\,\phi^{k} \\ \text{or} \quad B\left(\phi^{k+1} - \phi^{k}\right) &= \mathbf{b} - A\phi^{k} \end{aligned} \tag{2.100}$$

where the correction vector is

$$\Delta\phi^{k} = \phi^{k+1} - \phi^{k} \tag{2.101}$$

and the residual vector is

$$\mathbf{r}^{k} = \mathbf{b} - A\phi^{k} \tag{2.102}$$

The matrix B is called the conditioning matrix and its purpose is to ensure that the numerical solution tends towards the exact one. E is called the error matrix. The calculation of ϕ^{k+1} or $\Delta\phi^{k}$ requires the inversion of the matrix B. Taking Equation 2.102 and expressing it in terms of $\Delta\phi^{k}$, we get

$$\Delta\phi = B^{-1}\mathbf{r}^{k} \tag{2.103}$$

and taking Equation 2.99 and expressing it in terms of $\phi^(k+1)$, we get

$$\phi^{(k+1)} = B^{-1}\left(\mathbf{b} - E\phi^{k}\right) \tag{2.104}$$

It is advantageous to have the inversion of B require as few operations as possible and that it creates as few non-zero elements as possible. It is also desirable if B is a good approximation of A, so that the minimum number of iterations are required to reach convergence of the solution. In the best case scenario, if B = A, then E = 0 and the solution would converge in one iteration. In this best case scenario, the method is direct.

Provided that the matrix is well conditioned the iterative solution process will be stable. As k tends to infinity, $\Delta\phi^k$ and $\mathbf{b}^k$ must tend to zero. Therefore, it is $\mathbf{r}^k$ that provides an indication of convergence.

The terms,

$$\left|\mathbf{r}^{k}\right| \quad \text{or} \quad \sum_{k=1}^{N} \mathbf{r}^{k},$$

are monitored and when their value decreases over a predetermined range, the solution is deemed converged and further calculations can be halted. Non-zero values of $\mathbf{r}^k$ are called residuals.

2.6.2 Underrelaxation

Underrelaxation is a numerical technique used to address the problem of solution instability which is mainly due to the non-linear nature of the discretised equations in the solution matrix. If used properly, it can decrease the number of iterations required to reach a converged solution. Underrelaxation works by scaling the coefficients of the flow variables by a factor, β , where $0 < \beta < 1$. The smaller the value for β, the more underrelaxation is employed.

Underrelaxation may also be regarded as a cell-specific pseudo-time step. A low value of β is analogous to a small time step and a large value of β is similar to large time step, tending to infinity. A low value of β can result in fewer iterations required to reach a converged solution because the approximation for subsequent iterations is better conditioned. Different underrelaxation factors can be applied to the flow variables.

With regards to the solution matrix, underrelaxation works by preconditioning the matrix. A low value of β will yield a strongly diagonal dominant matrix. This presents an easier problem for the linear solvers used in the calculations.

2.6.3 Deferred Correction

In turbulent flow calculations, a solution can fail to converge due to the cross derivative terms of k, ϵ and Reynolds stresses introduced by the use of non-orthogonal grids. A symptom of this problem is usually solution divergence caused by high residuals in a localised region. Further, it is common to find that there is a particular point in such a region where there is a very small value of ϵ and a large value of the turbulent viscosity, μ_t, that is not physical.

Deferred correction as explained in CFX-International (1995), underrelaxes the k and ϵ terms during the solution. The user chooses a start iteration before which the terms are omitted and an ending iteration, after which they are fully included. Between the start and end iteration, the terms are introduced linearly into the solution as extra source terms. In some problems, a solution is not possible even with deferred correction. In these cases, the ϵ terms are generally the source of the problem and they can be eliminated completely through the use of start and end iterations that are greater than the total number of iterations. In this case, the Navier-Stokes equations are not being fully discretised but this may not be crucial because the equation is dominated by terms of turbulent production, dissipation, convection and normal diffusion terms.

2.6.4 Algebraic Multi-grid Solver

The Algebraic Multigrid Method (AMG), as formulated by Lonsdale & Schueller (1993) solves the Navier-Stokes equations using a series of progressively coarser matrices. What this method actually does is make the matrix A in Equation 2.96 more coarse by dropping the coefficients that represent certain computational nodes. Thus, it can be said that the solution algorithm is not aware of the grid once the calculation has commenced. The advantage of this method is that these coarser grids have fewer grid points and so require less computer resources to reach a solution. Another advantage of the coarsening process is that it allows the boundary conditions to influence the internal nodes more quickly. The solution from the coarsest grid is then imposed on the finest grid and the iterative processes are continued until a predefined convergence is reached. The AMG solver has an advantage in that numerical errors can be dampened during the course of the solution. This method is recommended for turbulent flows where convergence has been difficult to achieve. It was the solver used for all of the sequential or single processor runs.

2.6.5 Preconditioned Conjugate Gradient Solver

The aim of preconditioning is to convert the original system of equations into one with a much lower condition number. The condition number of a matrix is a measure of a matrix's sensitivity to uncertainty and hence its suitability for the solution process. It would seem that the choice of a preconditioner can be more important than the performance differences between various iterative solvers. The conjugate gradient solver used in CFX-4.2 is the Incomplete Cholesky Conjugate Gradient method (ICCG) discussed by Demirdzic & Muzaferija (1997).

In order to be effective, faster convergence must offset the added computational costs of using the method. Other advantages of preconditioning are that the preconditioning matrix be sparse, easy to calculate and easy to invert. It is therefore a compromise between maintaining sparseness and getting the best approximate inverse of A. This solver was employed for all the three-dimensional parallel runs in the course of the numerical investigations.

2.7 CFX-4.2 Fluid Flow Solver

The full Reynolds averaged, Navier-Stokes equations were solved using the CFX-4.2 fluid flow solver written by the company CFX International. CFX-4.2 is a general purpose CFD code based on the finite volume method and as such, it is capable of solving problems which are incompressible or compressible and time dependent or steady state. It is capable of modelling flows, that involve combustion, heat transfer and flows with chemical species and reactions. It uses body-fitted co-ordinates and multi-block, structured grids. The code is also capable of using rectangular and cylindrical co-ordinates should the need arise. For turbulent flows, there is a choice of turbulence models that can be used for closure of the Reynolds averaged Navier-Stokes equations. Among these are the standard k-ϵ, the Low Reynolds number k-ϵ, k-ω, Algebraic Reynolds Stress and Differential Reynolds Stress models.

In CFX-4.2, all problems are three-dimensional. Two-dimensional problems are defined with one active control volume in the **k**-direction. The active control volumes are those on the interior of the flow domain. Exterior or *dummy* control volumes are automatically added to impose the boundary conditions. Therefore, the boundaries are the interfaces formed by the interior and exterior control volumes. The default boundary condition is a wall, and this necessitates that all other boundary types such as inlets, outlets, symmetry and pressure boundaries be set explicitly by the user. The initial conditions are used as a first guess in steady state problems and as the conditions at the first time step in time dependent problems.

The problem is submitted to the computer with a command file which specifies, the conditions on the non-wall boundaries, initial conditions, underrelaxation and other parameters. An example of a command file is provided in the Appendix as item A.6. Fortran subroutines can also be submitted as part of the problem.

2.8 Convergence

The methodology used to set up the numerical problems can have a significant impact on the results. The criteria used to influence convergence of the problems are presented in the discussion to follow. Representative solution histories for some of the two and three-dimensional cases are also presented. Some solutions shared similar convergence behaviour in terms of the absolute decrease in the residuals or the manner in which these residuals decreased. As a steady state solution is approached, the values on the right hand side of Equation 2.95 should approach zero. It is more likely that these values will not be precisely zero and it is these values for each variable that constitutes the residuals.

The author has only discussed the convergence histories for those solutions that differ significantly. The parameters presented in the course of discussing the convergence are momentum [kg m/s], turbulent kinetic energy rate, k [m^2/s^2], turbulence dissipation rate, ϵ [m^2/s^3] and mass flow rate, $\dot{m}$ [kg/s].

2.8.1 Convergence of Two-Dimensional Solutions

The AMG solution algorithm was used for all the two-dimensional calculations. The AMG algorithm was applied to all the transport equations with a mass source tolerance of 1.0 x 10^{-6} set as the convergence criterion. This same value was used in the calculations performed in work by Akanni & Henry (1995). Despite various approaches, it was soon realised that the problems discussed in this thesis would not achieve this level of convergence. The best level of convergence achieved for any two-dimensional solution was a mass residual of 7 x 10^{-5}. With this realisation, the mass source tolerance was left unchanged and used to force the calculations to continue so that the changes in the predicted pressure distributions about the wings with an increasing number of iterations could be examined.

Personal communications with Krus (1998) and Jones (1998) helped to determine a practical philosophy with regards to the mass source residual. The absolute reduction in the transport residuals is not the most important factor in determining whether a solution has reached convergence. It is more important that the transport residuals have dropped at least three orders of magnitude and continue to decrease or remain reasonably constant. This definition of convergence is taken from a code validation study performed by Fejtek (1997). The predicted aerodynamic forces were also monitored and used as an indication of solution convergence.

Several values of β were investigated to determine the effect of underrelaxation on the two-dimensional solutions. After careful consideration of the convergence behaviour, it was decided that a value of $\beta = 0.5$ was adequate to underrelax the equations for u, v, k and ϵ.

Figure 2.7 shows the convergence of a two-dimensional problem with the high downforce wing oriented at 3^o angle of incidence. This type of convergence is representative of all two-dimensional solutions between 3^o and 25^o angle of incidence. The convergence is characterised by a sudden increase in the turbulent kinetic energy and turbulent dissipation residuals at 2000^{th} iteration. There are also small oscillations to be seen in the ϵ residual in the latter part of the solution. The former characteristic is caused by the implementation of the deferred correction scheme as discussed in Section 2.6.3. The level attained by these two residuals is maintained until the 3000^{th} iteration after which a more normal behaviour of reduction in these residuals is seen.

The use of deferred correction does have an influence on the solution with the high downforce wing oriented at 27^o and 29^o angles of incidence but the effect is not as pronounced as that seen in the other cases. Figure 2.8 shows that there is no sudden increase in any of the residuals. However, there is a noticeable decrease in the residuals seen at the 3000^{th} iteration. Small oscillations in the ϵ residual are also seen in the latter part of the solution.

Figure 2.9 shows the convergence achieved with the use of complete deferred correction. In this case, the extra source terms arising from the special treatment of k and ϵ are omitted from the solution entirely. The effect of this omission is to reduce any oscillation of the residuals as seen in Figures 2.7 and 2.8. While the use of deferred correction had a profound effect on the transport residuals, there was no significant difference in the predicted forces at the final iteration.

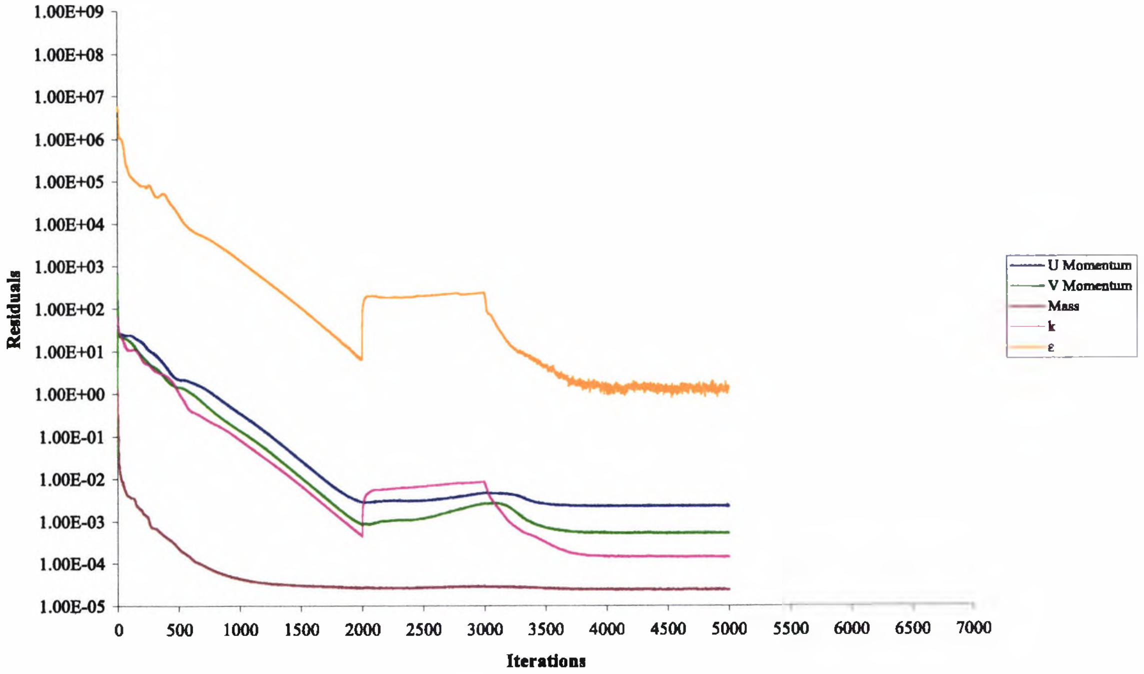

Figure 2.7: Convergence of two-dimensional solution, $\alpha = 3^o$.

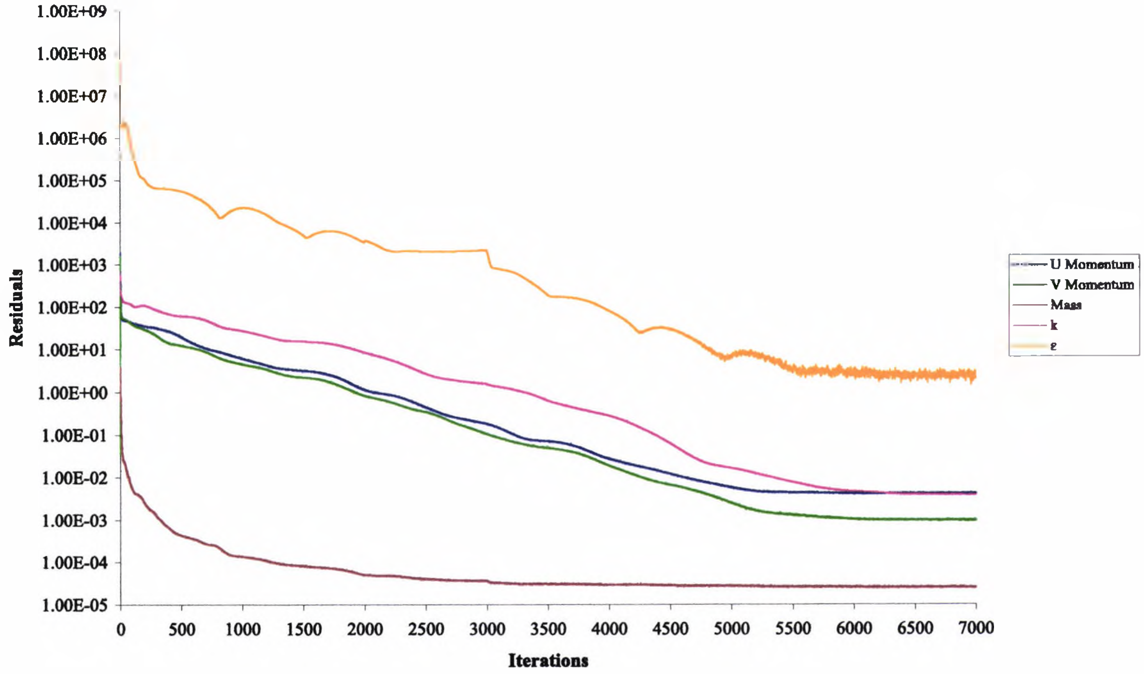

Figure 2.8: Convergence of two-dimensional solution, $\alpha = 29^o$.

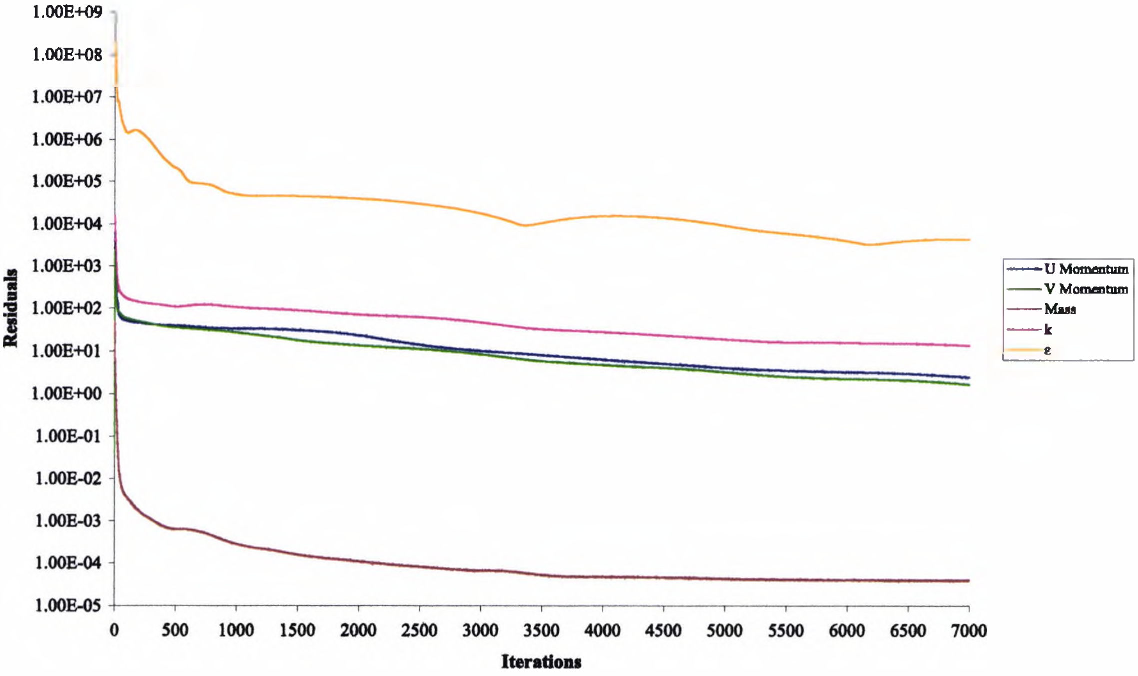

Figure 2.9: Complete deferred correction two-dimensional solution, $\alpha = 29^o$.

2.8.2 Convergence of Three-Dimensional Solutions

At the time these investigations were carried out, the preferred AMG solver was not available in parallel version of CFX 4.2. Therefore the ICCG solver was used with a mass source tolerance of 1.0 x 10^{-6} to solve all the transport equations for the three-dimensional problems. As a precaution against loss of data, the three-dimensional problems were run in steps of 500 iterations with restarts.

The same values of β used in the two-dimensional calculations were used to underrelax the equations for the three-dimensional models. A value of $\beta = 0.5$ was used to underrelax u, v, w, k and ϵ. Certain three-dimensional solutions experienced divergence and so the deferred correction scheme was used in all solutions to aid convergence. The solutions shown in Figures 2.10 and 2.11 are representative of most of the three-dimensional solutions performed in the investigations.

The solution for the 240 mm span, refined grid, clean wing solution is seen in Figure 2.10. This is typical of the other three-dimensional solutions including those for the 810 mm, full-span wing. Small oscillations in the ϵ residual are in evidence in the latter stages of the solution.

The solution presented in Figure 2.11 is different from any other three-dimensional solution used in the prediction of the performance of the high downforce wing. Beginning with the 500^{th} iteration and until the 2500^{th} iteration, there are sharp reductions in most of the residuals. Thereafter, the solution proceeds normally. There are also persistent but small oscillations in the ϵ residual for a significant portion of the solution.

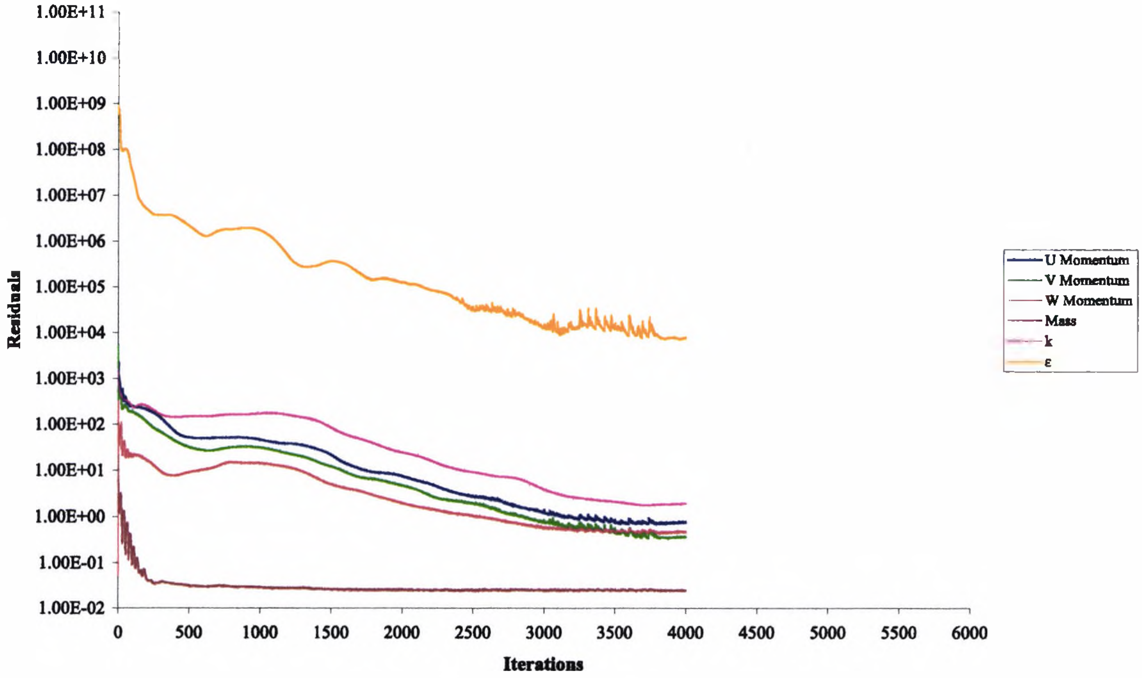

Figure 2.10: Convergence of 240 mm span, refined grid, clean wing solution, $\alpha = 29^o$.

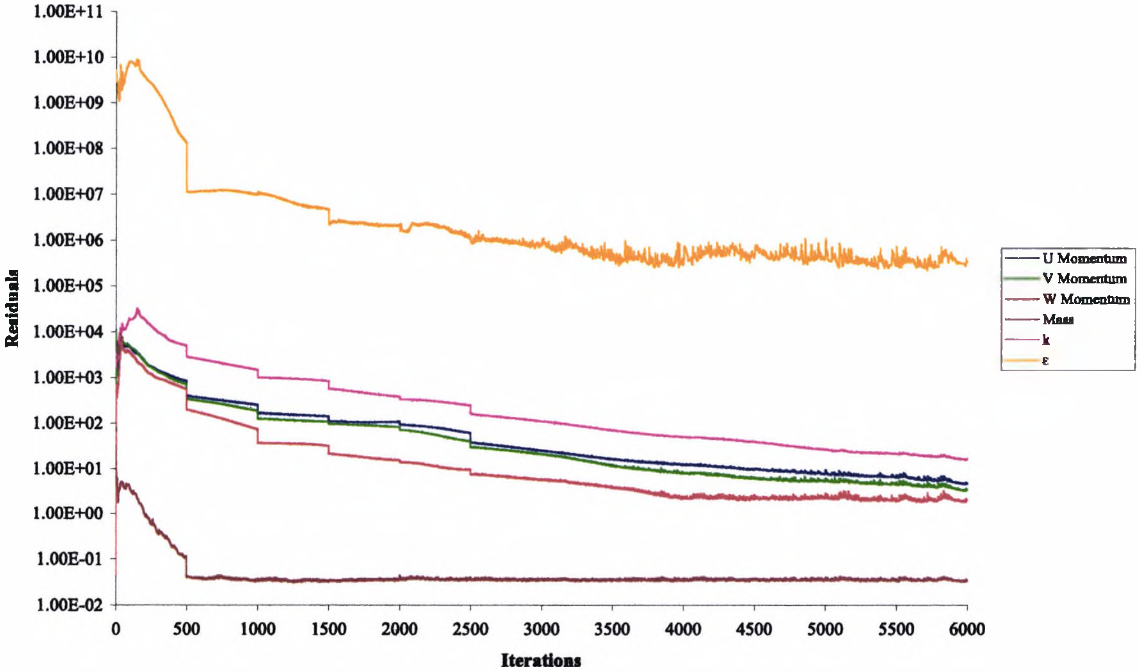

Figure 2.11: Convergence of air jet model, $P_{ajvg} = P_{atm}$, $\alpha = 29^o$.

Chapter 3

Numerical Models

3.1 Modelling Philosophy

Two and three-dimensional numerical models were used to predict the behaviour of the high downforce system at various angles of incidence. They are discussed in this chapter in terms of grids and boundary conditions, numerics, topology and convergence. The computer resources and time were limited and these two factors influenced the type of models used in this study.

3.2 Two-Dimensional Models

Grids were created for numerical models that were analogous to the experimental positions of the high downforce system between α of 3^o to 29^o in 2^o increments. Figure 3.1 illustrates the salient features of these models.

3.2.1 Two-Dimensional Boundary Conditions

The two-dimensional domains, shown in Figure 3.1, are 40 mm wide with the left and right symmetry planes at z = 20 mm and -20 mm. This was decided based on an air jet concept with 40 mm between jet centres. It was intended to re-use most of the two-dimensional topology to construct simple three-dimensional domains with periodic boundaries to study an infinite array of co-rotating air jets. As investigations developed, it was necessary to model the array explicitly. This is discussed further in Section 3.4. Figure 3.1 also shows the boundary conditions used in the two-dimensional cases. The fluid modelled was air at 313.16 K with a density of 1.12 kg/m^3 and a viscosity of 1.91 x 10^{-5} kg/ms. A velocity of 40 m/s was set at the inlet with u = 40 m/s and v = 0 m/s. The turbulent kinetic energy,

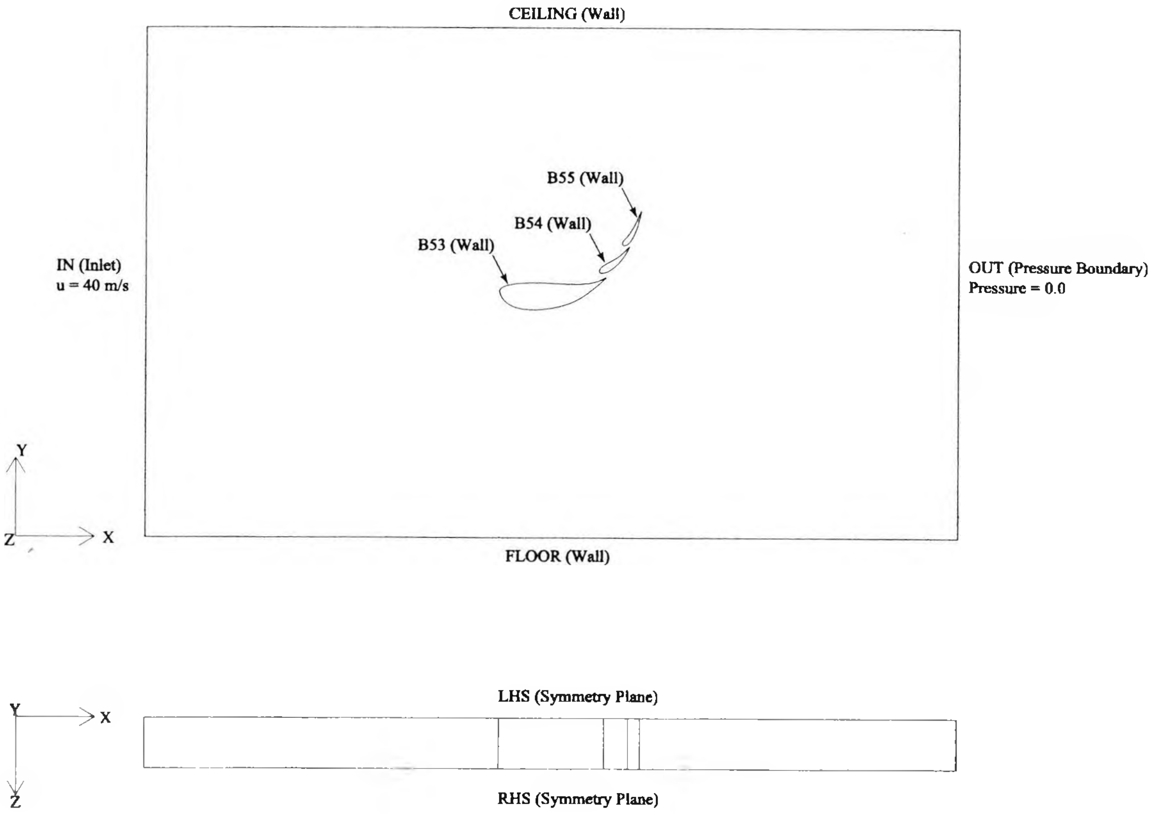

Figure 3.1: Representative two-dimensional domain with boundaries.

k and the turbulence dissipation, ϵ were also set at the inlet. The turbulent kinetic energy at the inlet, k_{inlet} is calculated by the equation,

$$k_{inlet} = 0.002u^2 \tag{3.1}$$

where u is the x-component of the velocity. The turbulence dissipation at the inlet, ϵ_{inlet} is given by,

$$\epsilon_{inlet} = \frac{k_{inlet}^{\frac{3}{2}}}{0.3C_h} \tag{3.2}$$

where k_{inlet} is provided by Equation 3.1 and C_h, the hydraulic diameter is given by

$$C_h = H \tag{3.3}$$

where H is the inlet height. The Reynolds number, Re, of the flow was calculated to be 5.72 x 10^5 where

$$Re = \frac{\rho V_\infty C}{\mu} \tag{3.4}$$

where $V_\infty = u_{inlet}$. C is taken to be the mainplane chord measured at 243.6 mm. The pressure was set to 0.00 Pa on the downstream boundary labelled 'OUT in Figure 3.1.

3.2.2 Two-Dimensional Differencing Schemes

A combination of differencing schemes was used to discretise the transport terms. The higher upwind scheme was used for the u and v-velocities while the hybrid difference scheme was applied to the equations for k and ϵ. The use of the QUICK and CCCT schemes were investigated, but they produced no change in the predicted pressures and further investigations were discontinued.

3.3 Two-Dimensional Topologies

A body-fitted grid was set up for all models used. Close-ups of the cell structure for the cases with $\alpha = 3^o$ and 29^o are shown in Figures 3.2 and 3.3. The block structure and the cell structure of the two-dimensional case with $\alpha = 3^o$ is shown in Figure 3.4. The quality metrics for this grid are shown in Figures 3.5 to 3.6. The CFX-Meshimport facility was not available at the time these grids were created and so they were not subjected to the reblocking procedure described in Section 2.1.4.

A total of 21,306 cells was used in this series of grids. The determinant, as shown in Figure 3.5 shows that the cells are all of good quality. A cell determinant of zero would be a cause for serious concern because any such cell would by definition have a negative volume making any solution with CFX-4.2 impossible. A review of Figure 3.5 shows that the minimum value for the determinant is 62.0403 and a mean value of 97.4715.

According to the ICEM-CFD definition of aspect ratio, it not appropriate to discuss the aspect ratio metrics of any of the two-dimensional grids. The maximum diagonals by far are those measured across the domain and when used in the aspect ratio calculations, they produce the artificially high values of the cell aspect ratios. A review of Figure 3.4 clearly shows that there is nothing untoward with regards to cell aspect ratios. The low aspect ratio cells are near the wings and the higher aspect ratio cells are in the far field areas.

In keeping with good gridding practice as described by Castro & Jones (1987), the author tried to minimise the skewness of the near-wall cells and all cells in general. A high degree of skewness is detrimental to a good solution because of the extra off-diagonal terms that are produced in forming the solution matrix for a particular problem. Techniques such as deferred correction are available in the CFX 4 solver suite to address this problem, but it was thought best to prevent the problem occurring as opposed to curing it. Figures 3.2 and 3.3 illustrate the attention paid to the near wing area. A combination of partial-C and partial-O grids was used in these areas to maximise cell orthogonality. The result of this effort for the model at 3^o is shown in Figure 3.6 with just over half of the cells possessing little or no skew. The maximum skewness is 0.367 and the mean is 0.019. The cell determinants are also of a high quality with most of the cells having determinants over 90. The grid quality described by Figures 3.5 and 3.6 is representative of all of the two-dimensional grids. The blocking structures of the various grids vary slightly with each α increment, but if the grids for larger angles of incidence are examined, the changes made to the blocking structure to improve orthogonality are more obvious. The entire block

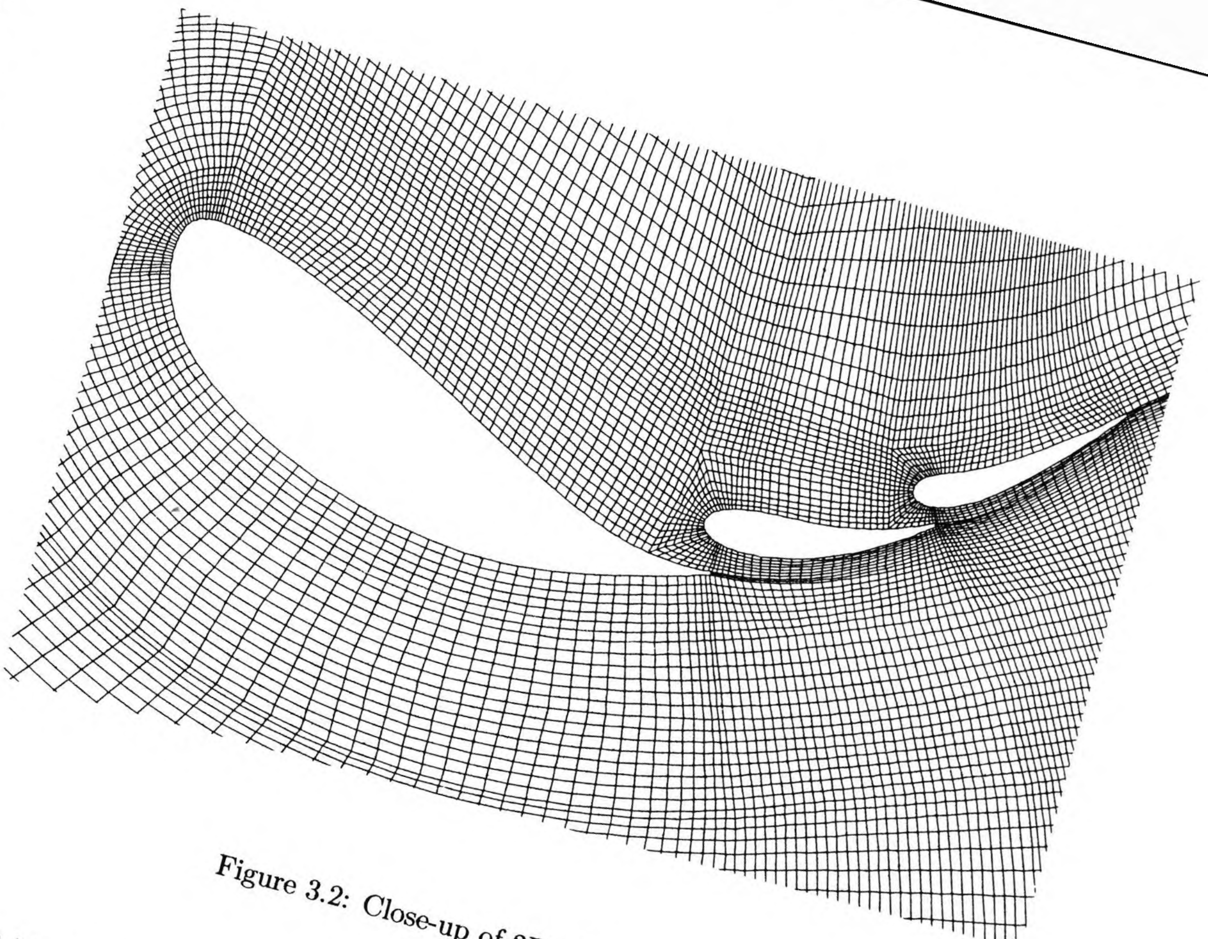

Figure 3.2: Close-up of 2D grid, $\alpha = 3^o$.

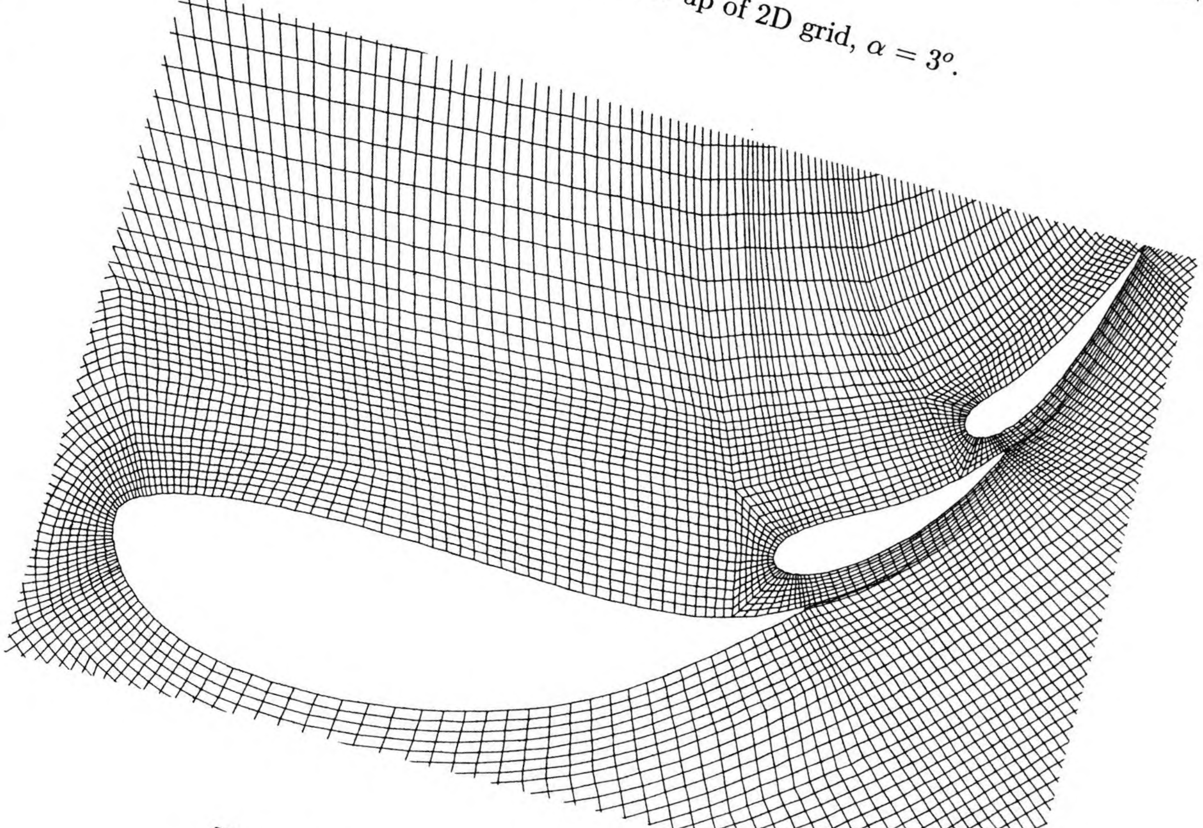

Figure 3.3: Close-up of 2D grid, $\alpha = 29^o$.

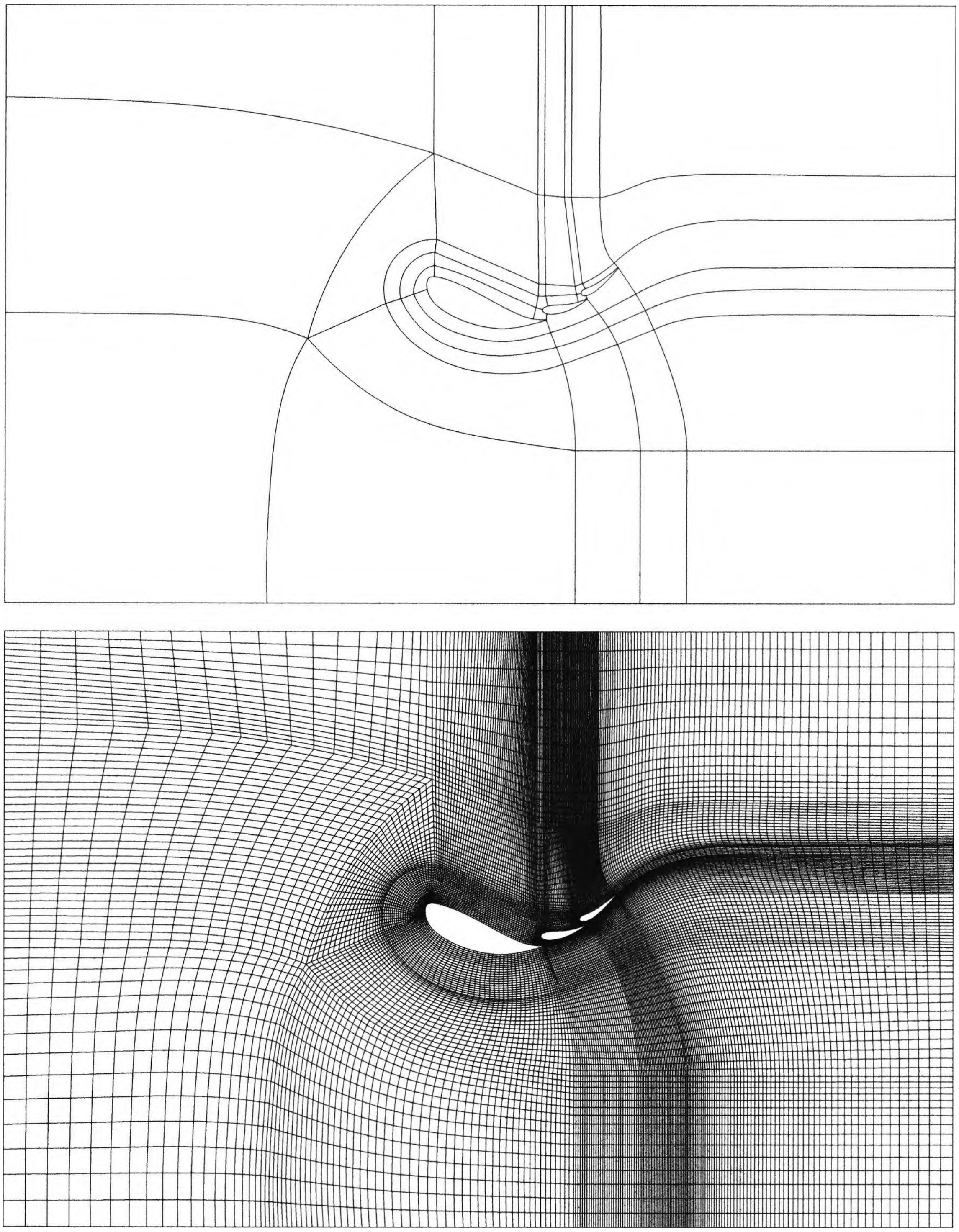

Figure 3.4: 2D block structure and grid, $\alpha = 3^o$.

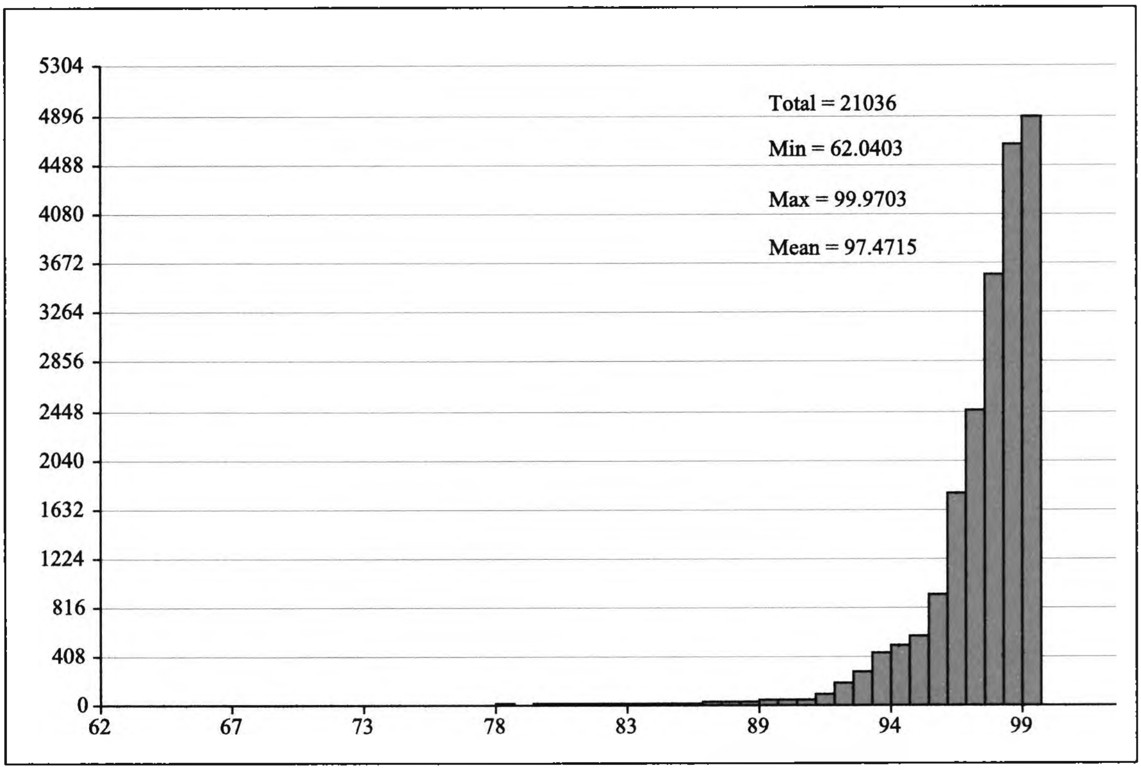

Figure 3.5: Determinant statistics of 2D grid, $\alpha = 3^o$.

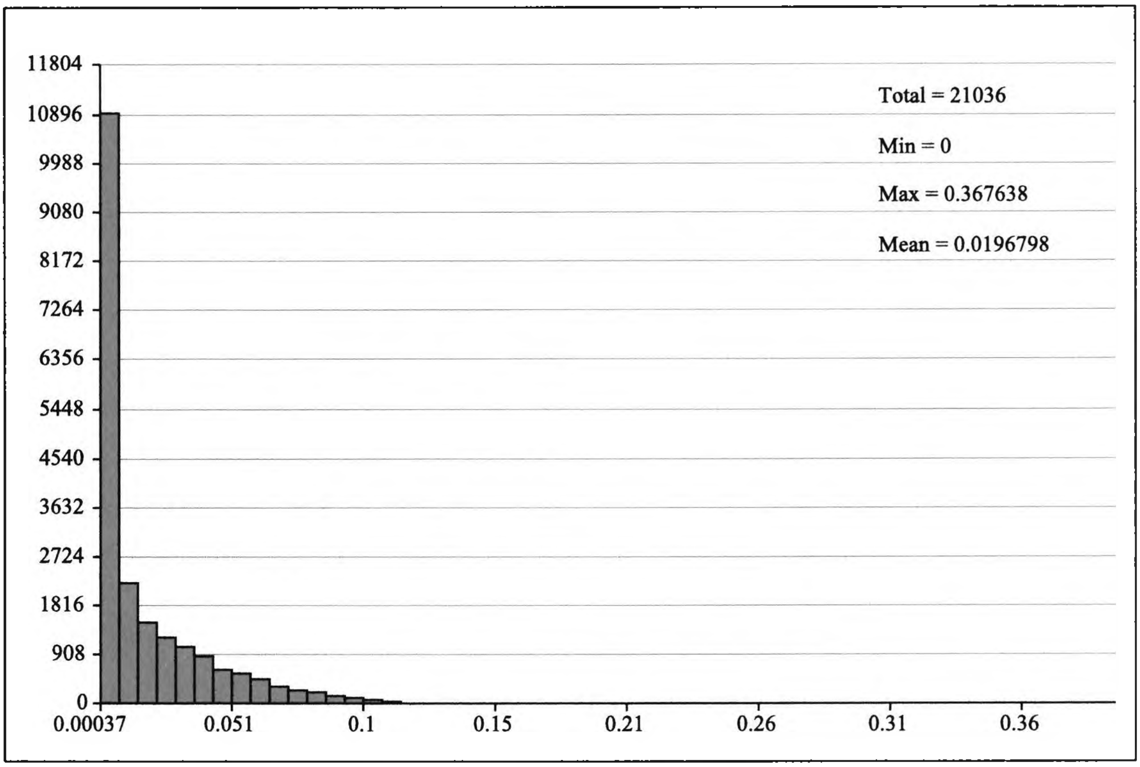

Figure 3.6: Skewness statistics of 2D grid, $\alpha = 3^o$.

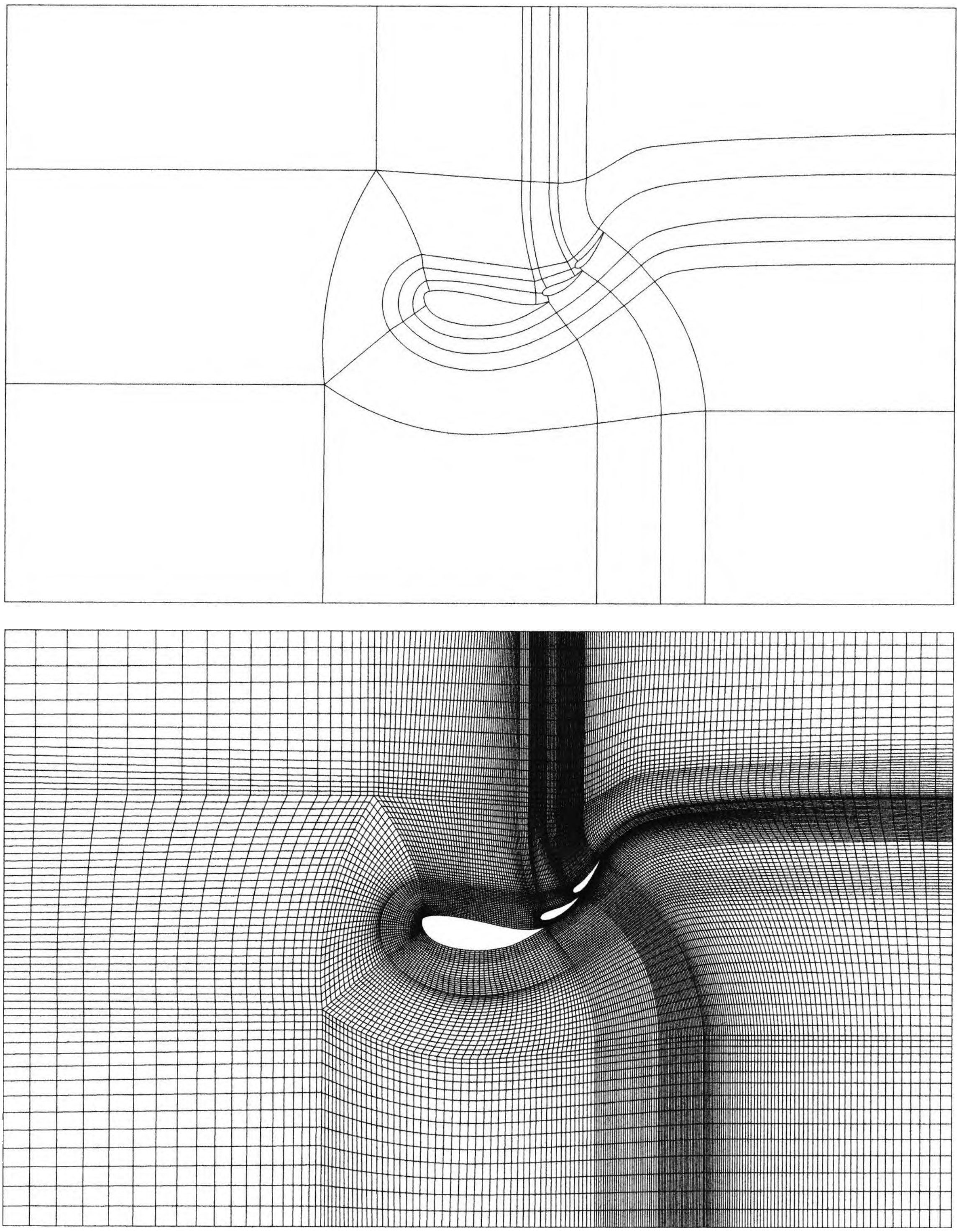

Figure 3.7: Block structure and grid of 2D model, $\alpha = 19^o$.

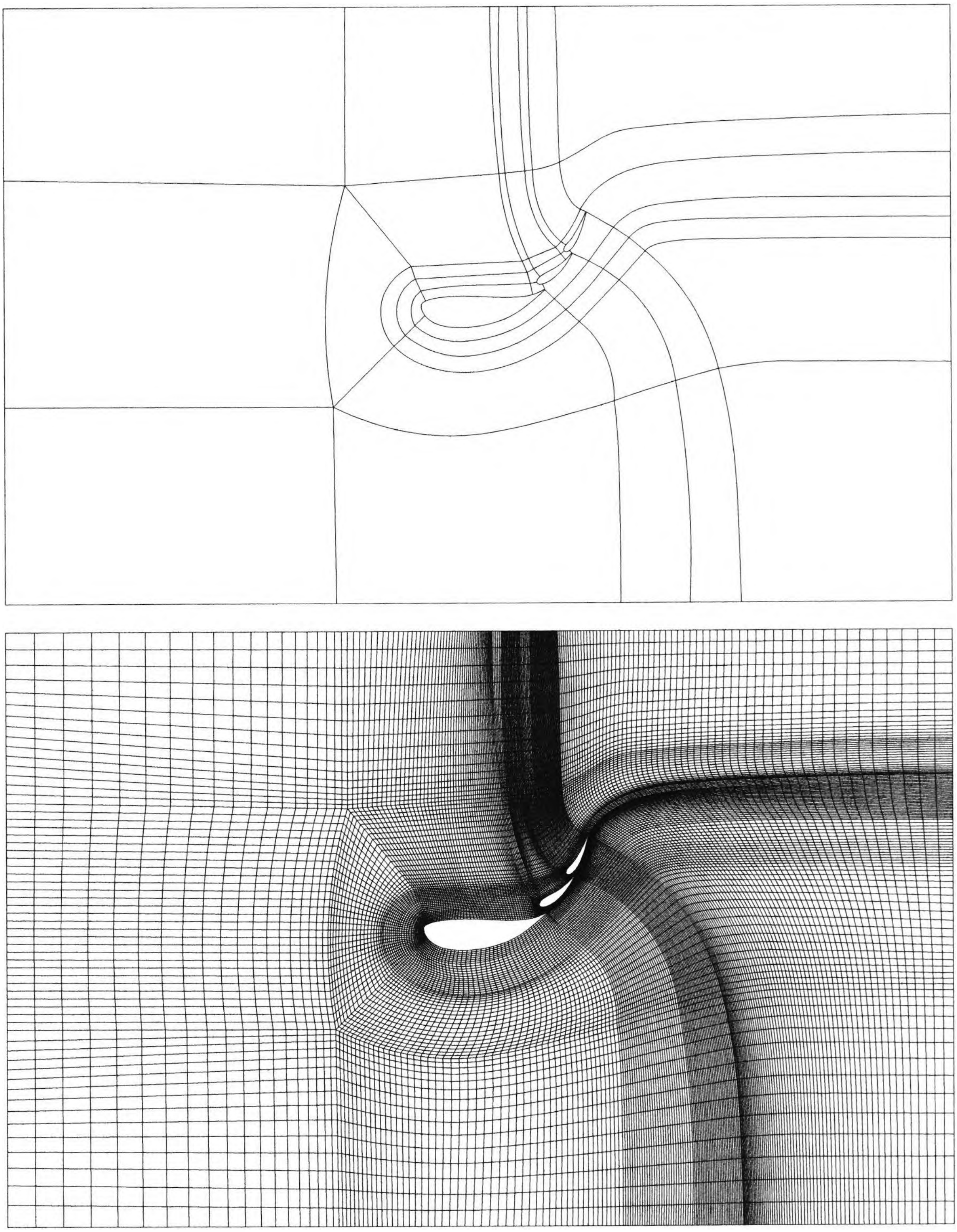

Figure 3.8: Block structure and grid of 2D model, $\alpha = 29^o$.

structure and grids for 19^o and 29^o are illustrated in Figures 3.7 and 3.8 respectively.

3.3.1 Two-Dimensional Grid Refinement

Variations of some coarse two-dimensional grids were modelled in an effort to study the effects of different grids. The angles of incidence chosen for the grid refinement were based on a personal communication from Sykes (1998), in which it was suggested to choose two angles of incidence for grid refinement cases, one at which the flow was known to be completely attached on the wings and one where there was flow separation. The author was primarily concerned with those angles where the high downforce system experienced flow separation because the air jets would only be used at these angles. However, at this early stage of the investigations, it was considered unwise to only attempt grid refinement at an angle which was know to produce a highly unsteady flow field in experiments.

Close-ups of these refined grids with the model at 3^o and 29^o are shown in Figure 3.9 and Figure 3.10 respectively. The entire original and the refined grids at3^o are presented in Figure 3.11. Due to the slot geometry there was no real scope for grid refinement normal to the wing surfaces without violating the requirement that $y^+ > 11$ or jeopardising the smoothness of the grid. The grid quality presented in Figure 3.12, shows that the desire to maximise cell orthogonality was realised with this particular effort at grid refinement. The doubling of the cells around the wings and the smoothing resulted in 65,346 cells compared to 21.036 for the coarse grid. Figure 3.13 shows a similar grid refinement for the two-dimensional model at $\alpha = 29^o$. The only difference being the block structures which were altered to maximise orthogonality and smoothness.

The difficulty in modelling this high downforce system with its high camber is compounded by the confines of the test section, the ceiling and floor of which are just over one wing assembly chord length from any wing surface. This is reflected in the comparison of grid skewness in Figures 3.12 and 3.14. The grid with $\alpha = 3^o$ has 8.4% more cells with little or no skewness than the grid for, $\alpha = 29^o$ The grid for the lower of the two angles of incidence also has slightly better determinant characteristics.

3.3.2 Two-Dimensional Models with Extended Far-Field Regions

In their experimental and numerical research on high downforce systems, Cao, Kusunose, Spalart, Ishimitsu, Rogers & McGhee (1994) showed that large blockages and far-field boundary conditions can have a profound effect on the results predicted by numerical methods. They demonstrated that such boundary conditions can introduce as much as a

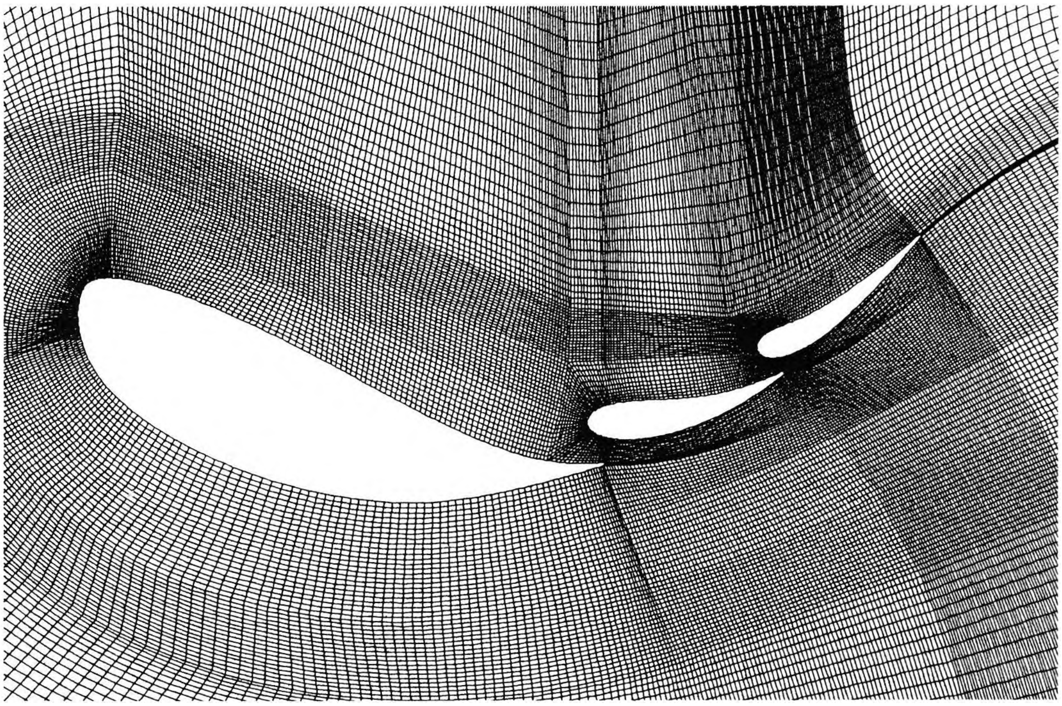

Figure 3.9: Close-up of refined 2D grid, α=3^o.

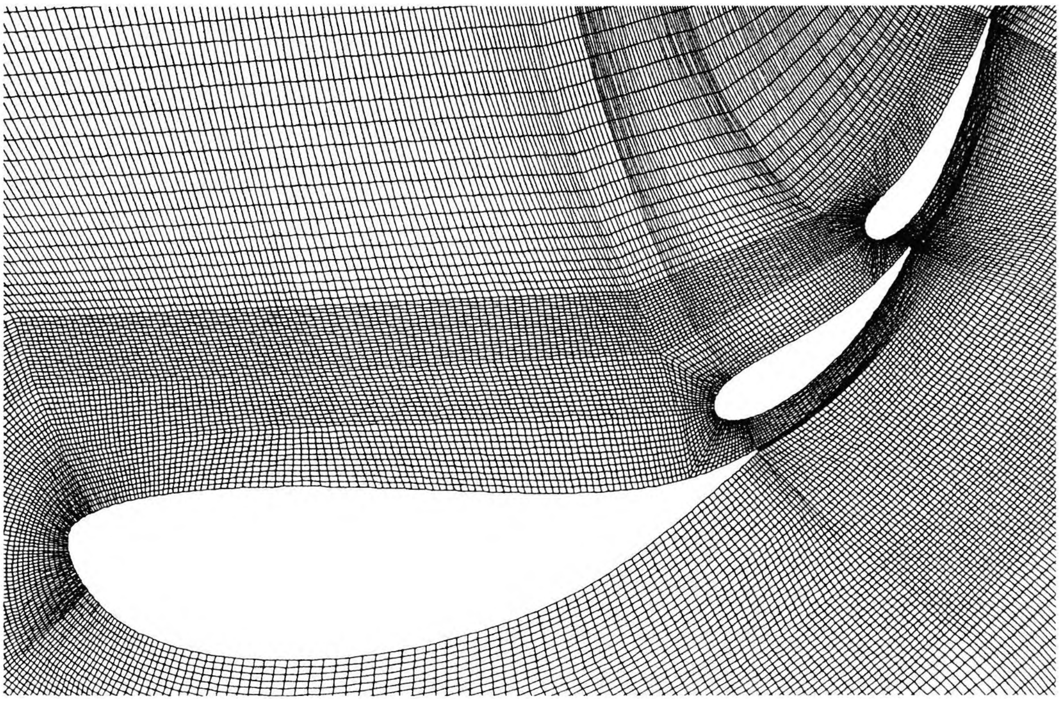

Figure 3.10: Close-up of refined 2D grid, α=29^o.

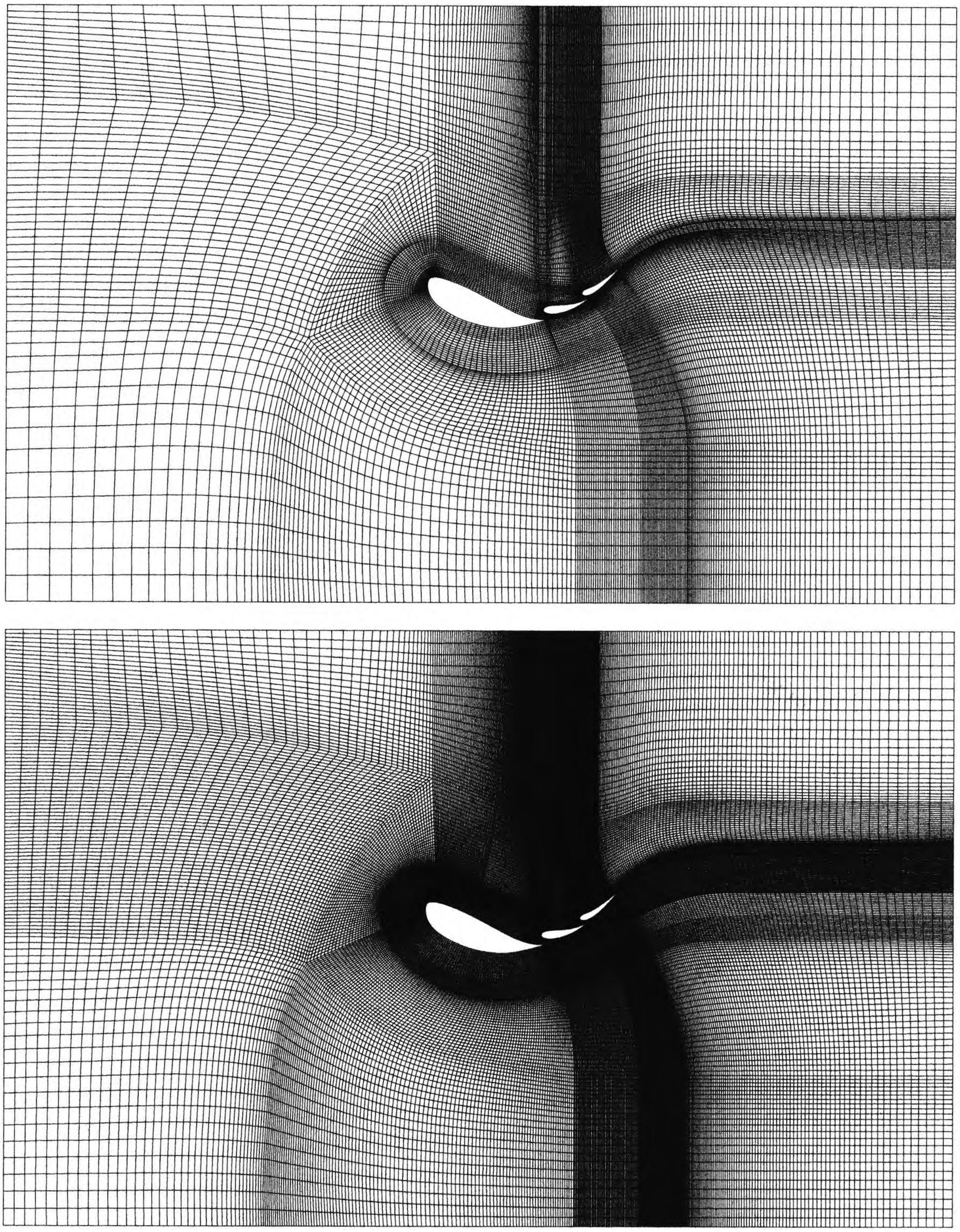

Figure 3.11: Coarse, (top) and refined 2D grid (bottom), $\alpha=3^o$.

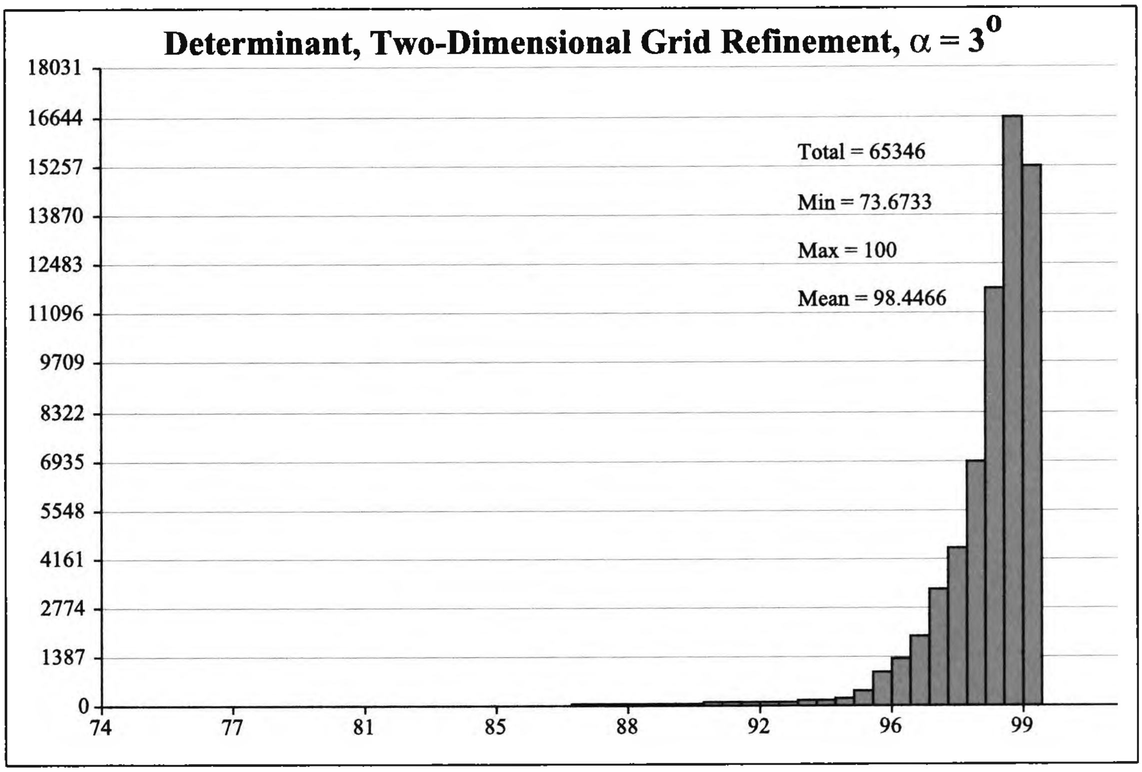

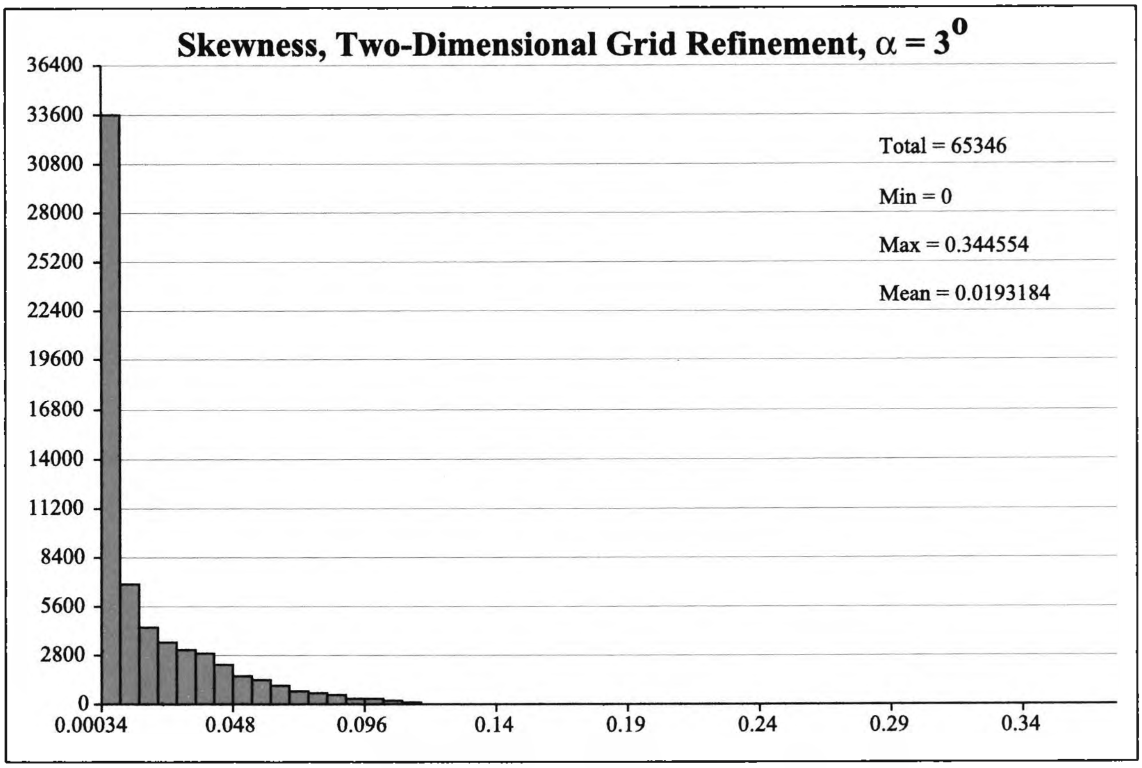

Figure 3.12: Quality metrics of refined 2D grid, α=3^o.

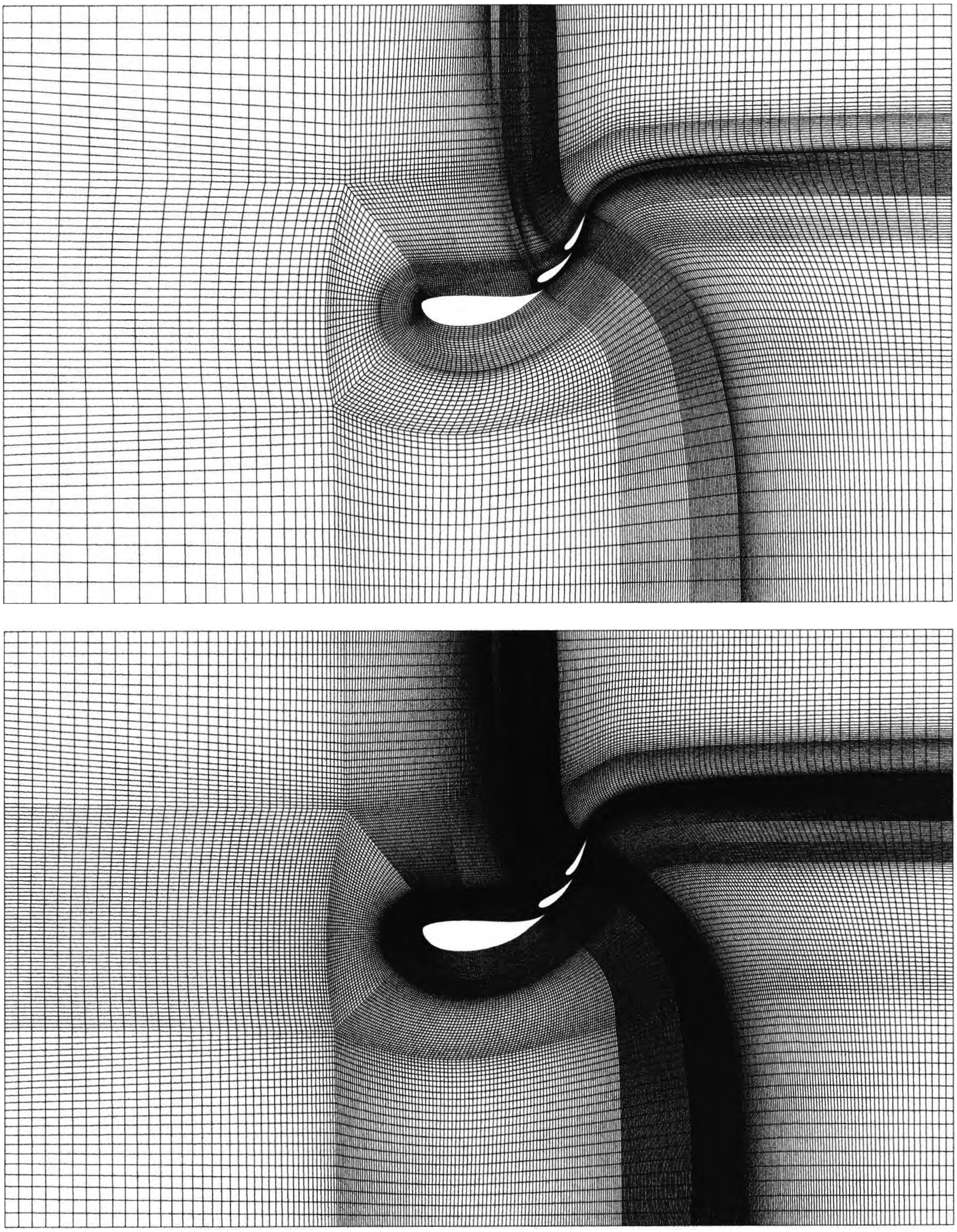

Figure 3.13: Coarse (top) and refined 2D grid (bottom), α=29^o.

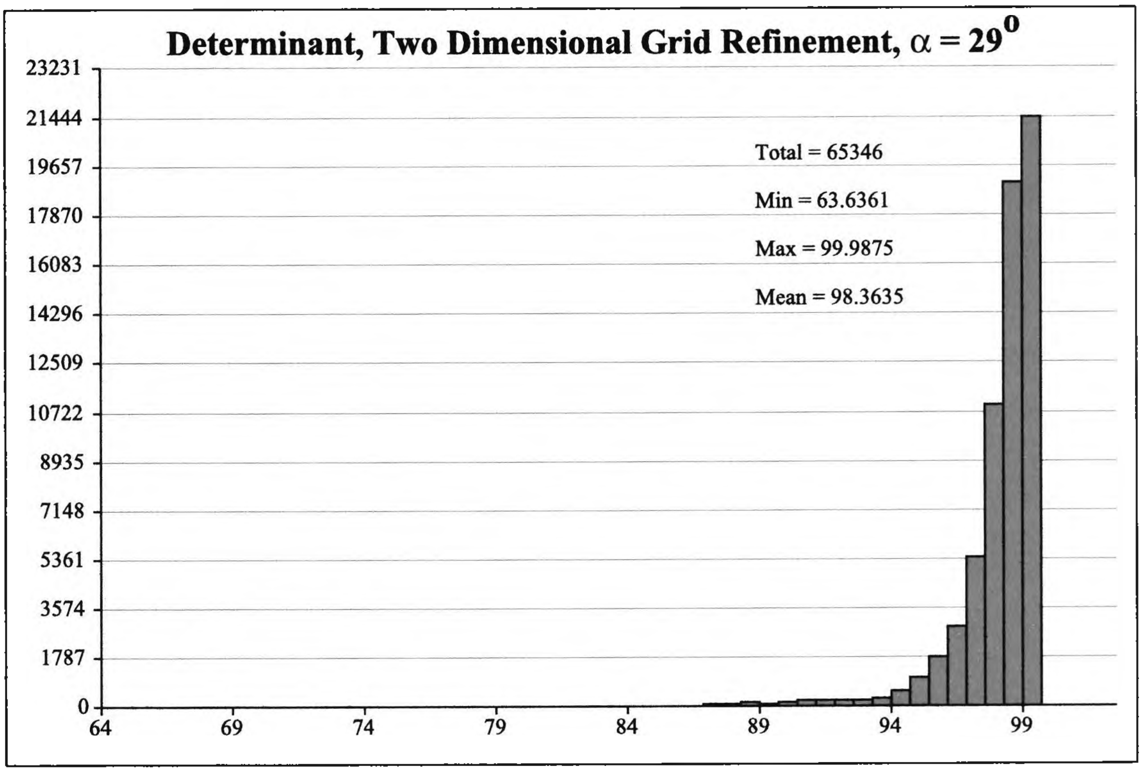

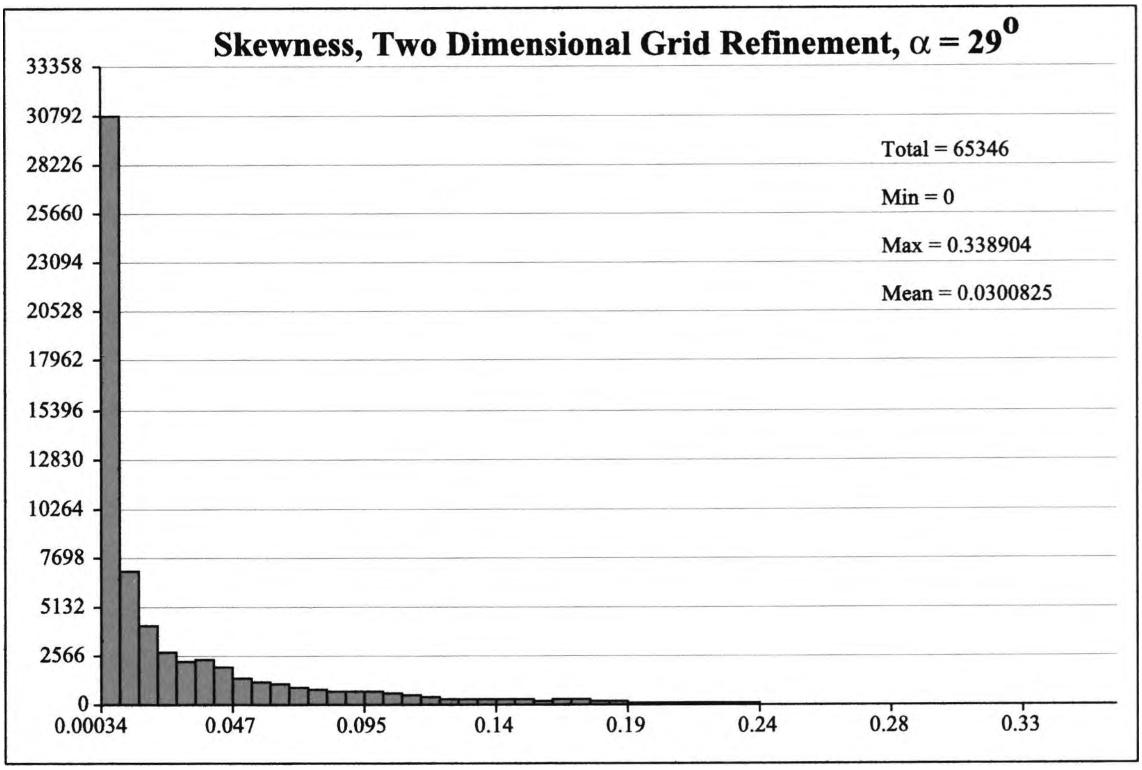

Figure 3.14: Quality metrics for refined 2D grid, α=29^o.

2% error in lift prediction and up to a 100% error in drag prediction. Cao et al. (1994) also showed that these errors can occur if the far field is located as close as twenty chord lengths away from a multi-element aerofoil inclined at a modest angle of incidence. It was determined that the effect of increasing the far field to 40 or even 60 chord lengths away from the aerofoils progressively decreased the error predominantly on the calculated lift but also on the drag.

Grid refinements incorporating two increases in the far field distance of 10 and 20 assembly chord lengths were used to examine their effect on the predicted pressure distribution. The calculations to predict the effect of these increases of the far field distance were conducted at $\alpha = 3^o$ and 29^o. While the results from some solutions were fraught with problems and therefore not promising, the results from the combination of grid refinement and extended entry lengths did provide some small improvements over the standard entry length models.

3.4 Three-Dimensional Models

The experiment in the wind tunnel could be characterised as one with flow separation on the lifting surfaces at high angles of incidence exacerbated by separation at the wing-tunnel wall interfaces. The use of air jet models that incorporated symmetric or periodic boundaries would have been inappropriate because such boundaries would result in the overprediction of the downforce. The elimination of the walls through the use of symmetric or periodic boundaries would eliminate the possibility of predicting separated flow at the wing-wall junctions.

It was not possible to construct a numerical model of the 810 mm span wing with all 19 air jets because of the prohibitive problem size and a lack of suitable, guaranteed computational resources. Two full span, clean wing cases and smaller 240 mm span models with and without air jets were used in the three-dimensional studies.

The author attempted to use models which captured the effects of the flow separation on the wings and at the wing-wall intersections on the performance of the high downforce system. All models were oriented at $\alpha = 29^o$ incidence as this was the angle known to produce the most extensive flow separation.

3.4.1 Three-Dimensional Boundary Conditions

With a few exceptions, this series of models are much the same as those set out in Section 3.2.1. The values of u = 35 m/s, v and w = 0 were used to set the freestream velocity. This reduction in V_∞ reflects the change made in the experiments to alleviate the stresses imposed on the tunnel caused by the aerodynamic buffeting between $\alpha = 21^o$ and 29^o.

The value of k_{inlet} for all the three-dimensional calculations was based on this new V_∞. The hydraulic diameter, C_h, was computed using

$$C_h = \frac{4A}{P} \tag{3.5}$$

where A is the frontal area of the inlet and P is the inlet perimeter. k_{inlet} is defined using Equation 3.1. The quantity ϵ_{inlet} was calculated using Equation 3.2. The Reynolds number was calculated to be 5.0 x 10^5 based on the mainplane chord with $V_\infty = 35$ m/s. The problems were modelled as steady state, fully turbulent, incompressible flows.

An array of five air jets was used in all the models incorporating air jets. The upstream face at the top of each air jet duct, was specified as a pressure boundary. The pressures on these boundaries were set to be the ambient atmospheric pressure to reflect the fact that the jets were using ram air. Values of 1.11 x 10^5 Pa and 1.16 x 10^5 Pa were used in some calculations to examine the effect of different air jet blowing pressures on the performance of the high downforce model.

The top, bottom, left and right boundaries were modelled as walls and the predicted boundary layers on these boundaries were calculated according to the initial conditions set out by V_∞, k_{inlet}, ϵ_{inlet} with subsequent conditions calculated by wall functions.

As a matter of convenience, the pressure was set to atmospheric pressure, on the downstream boundary labelled 'OUT' as illustrated in Figure 3.1. This reflected the fact that the downstream side of the wind tunnel test section is vented to the atmosphere.

3.4.2 Three-Dimensional Differencing Schemes

The Higher Upwind scheme was used to discretise the convection terms in the equations for the u, v and w velocities. The Hybrid Differencing scheme was applied to the equivalent terms for the k and ϵ equations.

3.5 Three-Dimensional Topologies

The CFX-Meshimport facility was used to create all of the three-dimensional grids as it is a recommended feature of any CFX 4.2 parallel run. This reblocking procedure is described in Section 2.1.4. The ICEM-CFD blocking philosophy and most of the cell distribution in the flow direction was taken from the two-dimensional models.

Careful attention was paid to the cell aspect ratios. The goal was to have cells with high aspect ratios in the far field and those with aspect ratios on the order of one, near to the wings. Figure 3.15 shows the typical location of the high aspect ratio cells. It is common gridding practice to ensure that such cells are located in the far field regions because such cells would not result in an accurate, converged solution if they were located in regions of high flow gradients.

3.5.1 810 mm span Clean Wing Models

The models of the full span, clean wings, high downforce system at $\alpha = 29^o$ were created to gain further insight into the three-dimensional nature of the air flow over the wing. Figure 3.16 shows the block structure used in this model. They are similar to the earlier two-dimensional models with additional blocking to grid the fillets in the wind tunnel test section. The gridding in Figure 3.16 is omitted for clarity but a partial surface gridding on the wings is presented in Figure 3.17. A gid refinement study was also carried out on

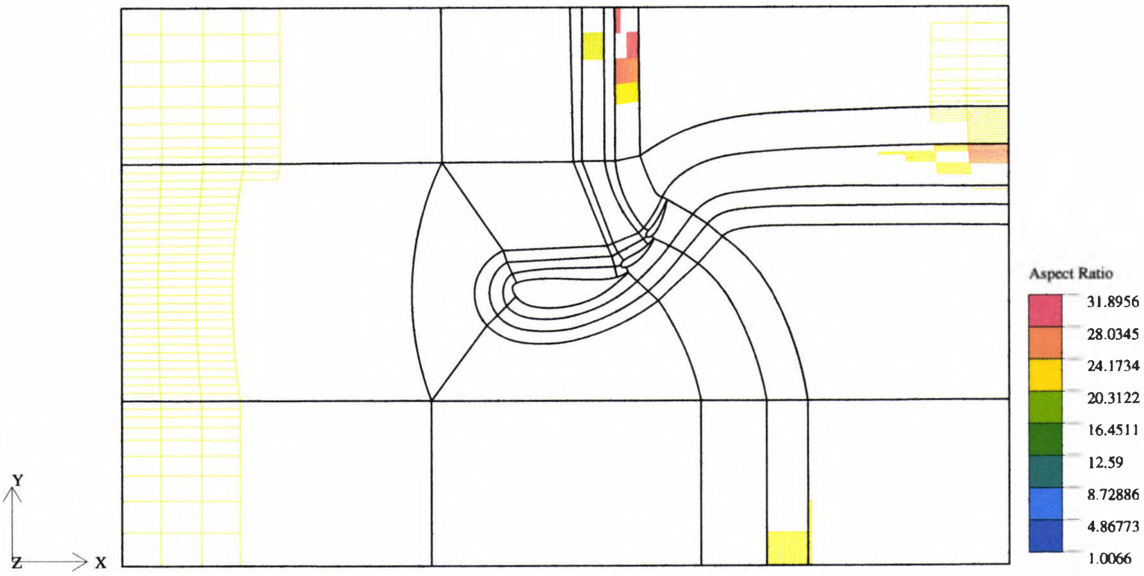

Figure 3.15: Location of high aspect ratio cells.

this model. This was achieved by doubling of the number of spanwise cells from the coarse grid. There was not much scope for grid refinements normal to the wing surfaces without violating the requirement that $y^+ > 11$ or jeopardising the smoothness of the grid.

3.5.2 240 mm Clean Wing Models

Several 240 mm span clean wing at 29^o incidence were used in this study. The first of these models was based on a coarse grid comprising 945,180 cells. Grid refinement studies were conducted on these geometries. Once again, this was achieved by doubling of the number of spanwise cells from the coarse grid. The results derived from the refined grids were not conclusive and are not included in the discussion.

3.5.3 Air Jet Models

All numerical models incorporating air jets used the same design and topology, namely a co-rotating array of five air jets. The air jet ducts were 2.5 mm x 10 mm at the intersections with the wing surface and spaced 20 mm between their centres. The air jets were pitch and skewed relative to local wing surface. The pitch angle, θ and skew angle, ϕ, were 30^o and 75^o respectively. The air jets centres were in a line along the 19% chord position with 40 mm between their centres. All chordwise positions are discussed in terms of the assembly chord.

This seemingly arbitrary chordwise position was determined by the construction of the wings used in the experiments. It was originally intended to place the air jet array

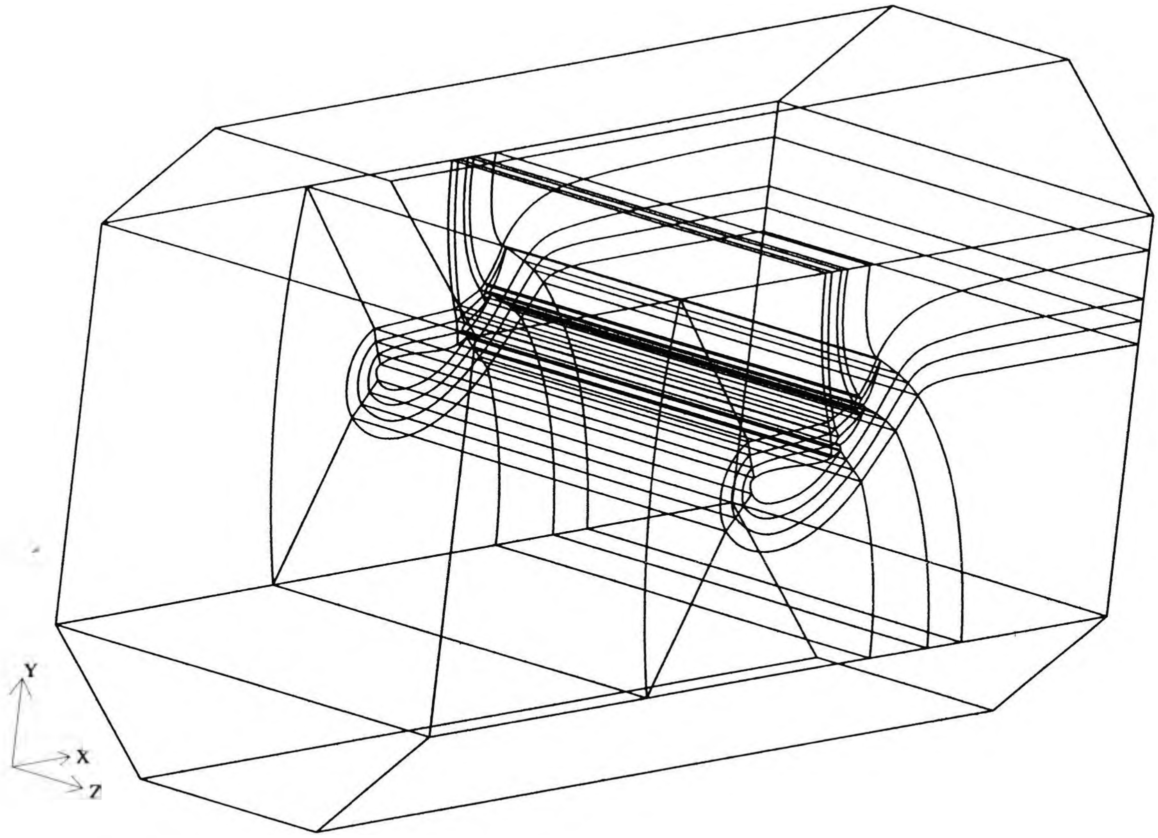

Figure 3.16: Block structure of full-span, clean model, $\alpha = 29^o$.

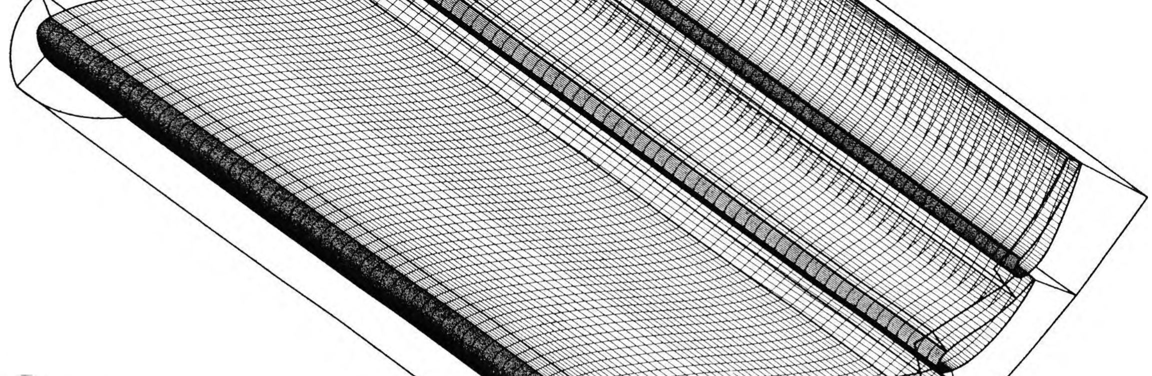

Figure 3.17: Surface grid and blocks near model.

between the 10% and 15% chord to make use of peak suction C_p but a carbon fibre spar was located in this region of the mainplane. The location of this spar dictated that the air jet centres be located further aft on the mainplane. Taking the wing structure and pressure distribution about the mainplane into account, the 19% chord location was the earliest viable position. Figure 3.18 shows the surface gridding typical of the air jet array and the surrounding area on the mainplane element. Figure 3.19, shows the block structure around a high downforce model with air jets. This topology is representative of these short span models.

Calculations were performed on several models based on the 240 mm high downforce wing incorporating AJVGs. These calculations were performed on the model with the wing at 29^o. The first type of model was meshed with 1,890,360 cells. The second model was a grid refinement study and meshed with 3,864,292 cells. The results derived from the refined grids of these air jet models were not conclusive and are not included in the discussion.

Some investigations were made to examine the effect of increases in the jet blowing pressure, P_{ajvg}. This would provide data on trends that might be expected, should the car exhaust or some other source be used to power the air jets array. Air jet blowing pressures of 10% and 15% above atmospheric were modelled. In order to save time, the results file produced at the end of 6000 iterations for the ram air jet case at 29^o was used as a restart for both these calculations.

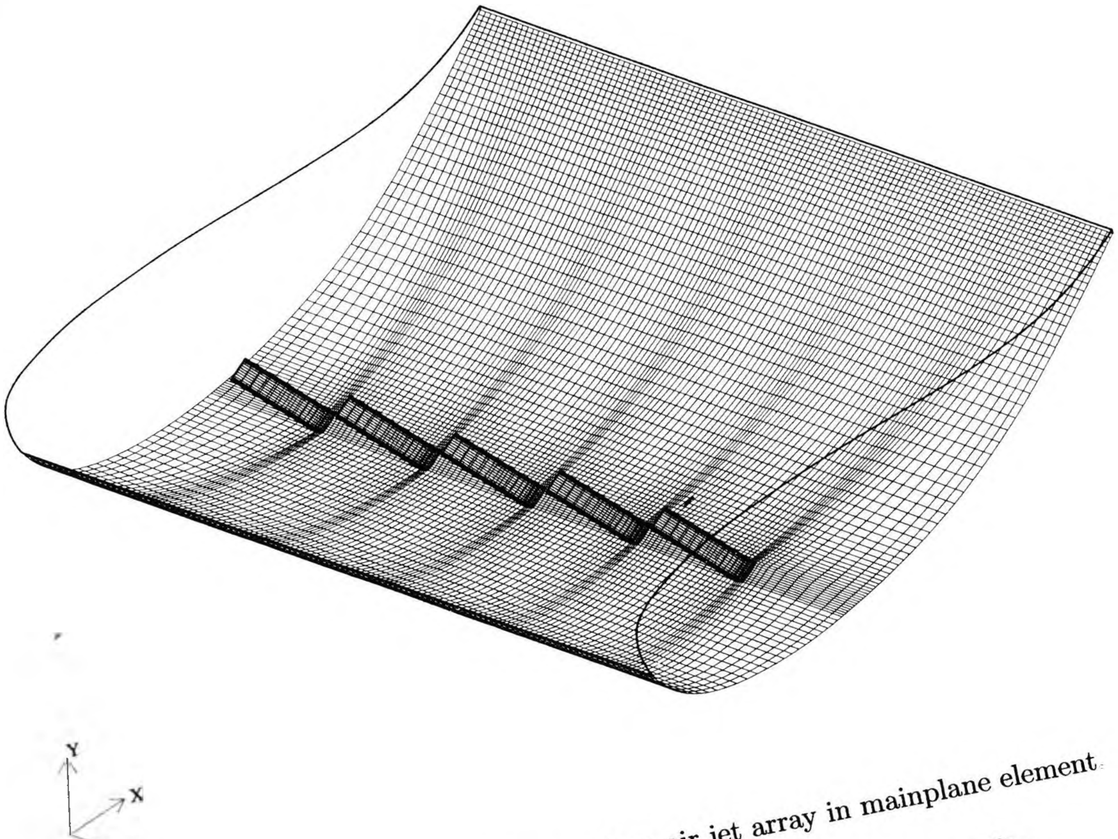

Figure 3.18: Typical grid around an air jet array in mainplane element.

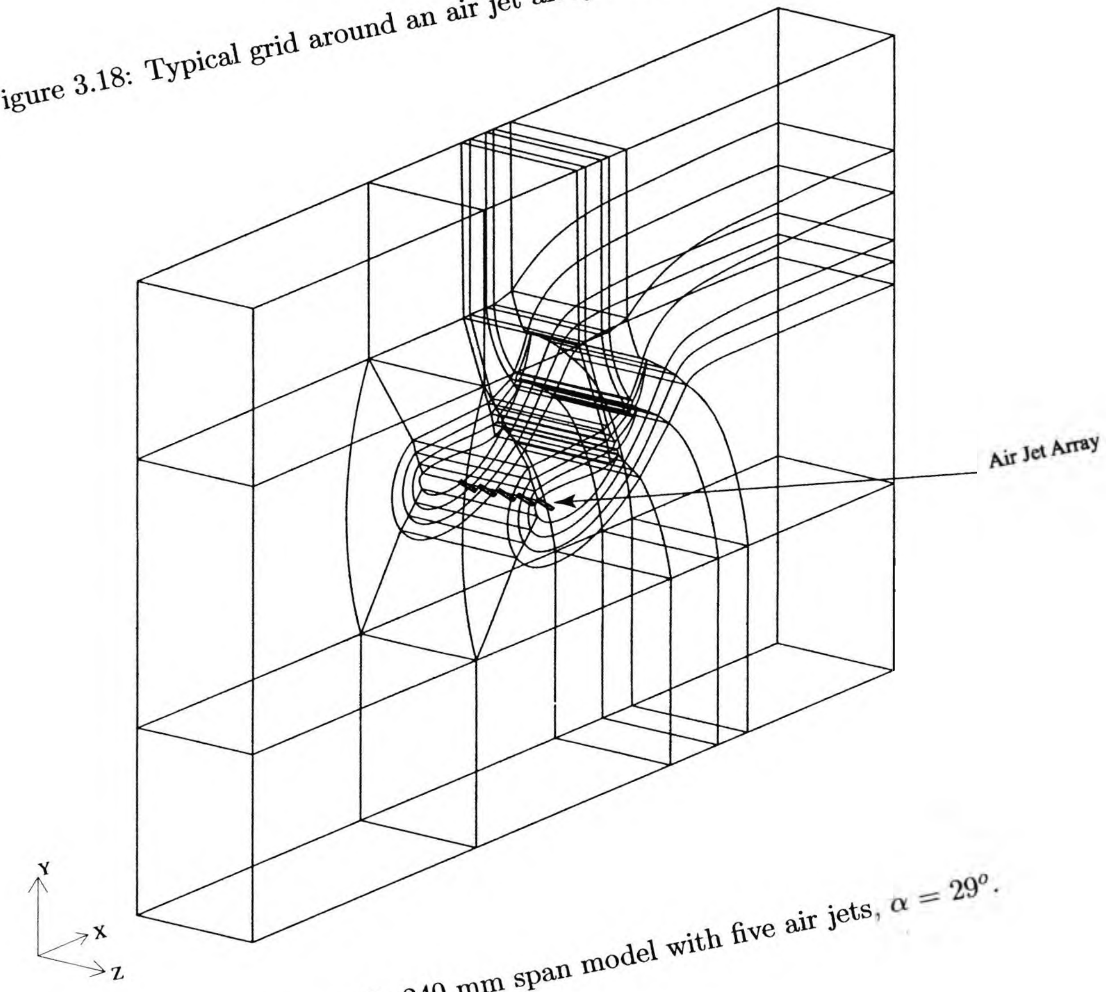

Figure 3.19: 240 mm span model with five air jets, $\alpha = 29^o$.

Chapter 4

Experimental Measurements

4.1 Experimental Overview

A series of experiments was performed in two separate sessions to investigate the performance of the high downforce system. All of these experiments were carried out in the City University Low Speed T2 Wind Tunnel. Details of the model, problems encountered and some technical specifications of the tunnel and instrumentation used are presented in this chapter.

4.2 Low-Speed Wind Tunnel

The City University T2 Low Speed Wind Tunnel is a closed circuit design with a working section measuring 1.78 metres long, 1.12 metres wide and 0.81 metres high. Corner fillets are used in the test section. It is capable of producing repeatable, constant test section velocities between 10 m/s and 45 m/s. This corresponds to a Reynolds number range of 0.7 to 3.1 million per metre. The turbulence level in the working section is quoted by City University staff to be less than 0.7%. The downstream end of the working section is vented to atmospheric pressure. The tunnel is equipped with a six component mechanical force balance mounted on top of the working section. This was not used in any of the experiments reported here. Figure 4.1 shows a schematic of this wind tunnel and the high downforce system is pictured in the working section of the tunnel looking in the downstream direction in Figure 4.2.

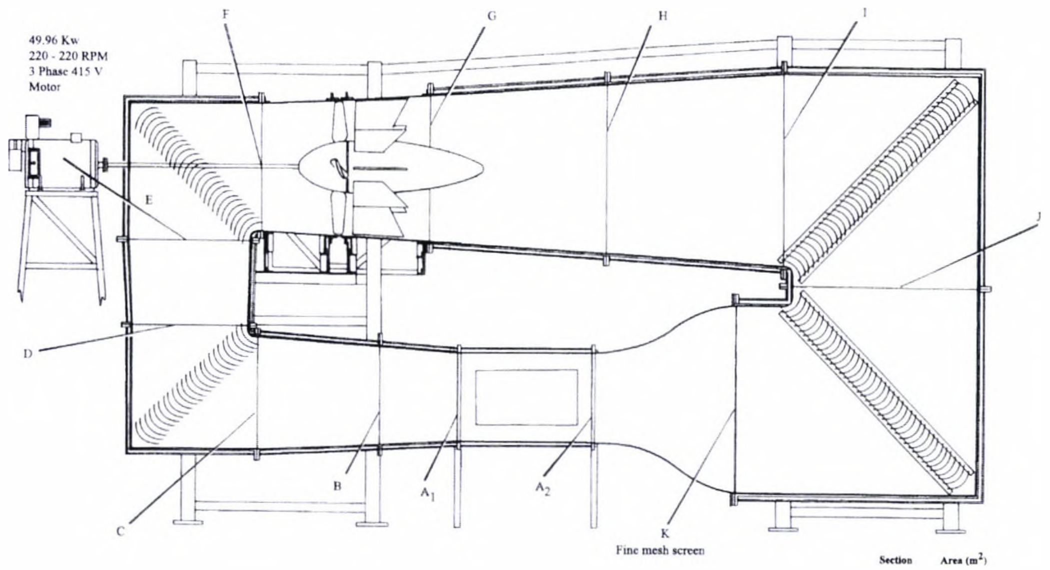

Section	Area (m^2)
A_1	0.908
A_2	0.908
B	1.039
C	1.351
D	1.351
E	1.582
F	1.582
G	2.056
H	2.685
I	3.437
J	3.437
K	3.437

Figure 4.1: City University T2 Low Speed Wind Tunnel. (MEAD schematic 1999)

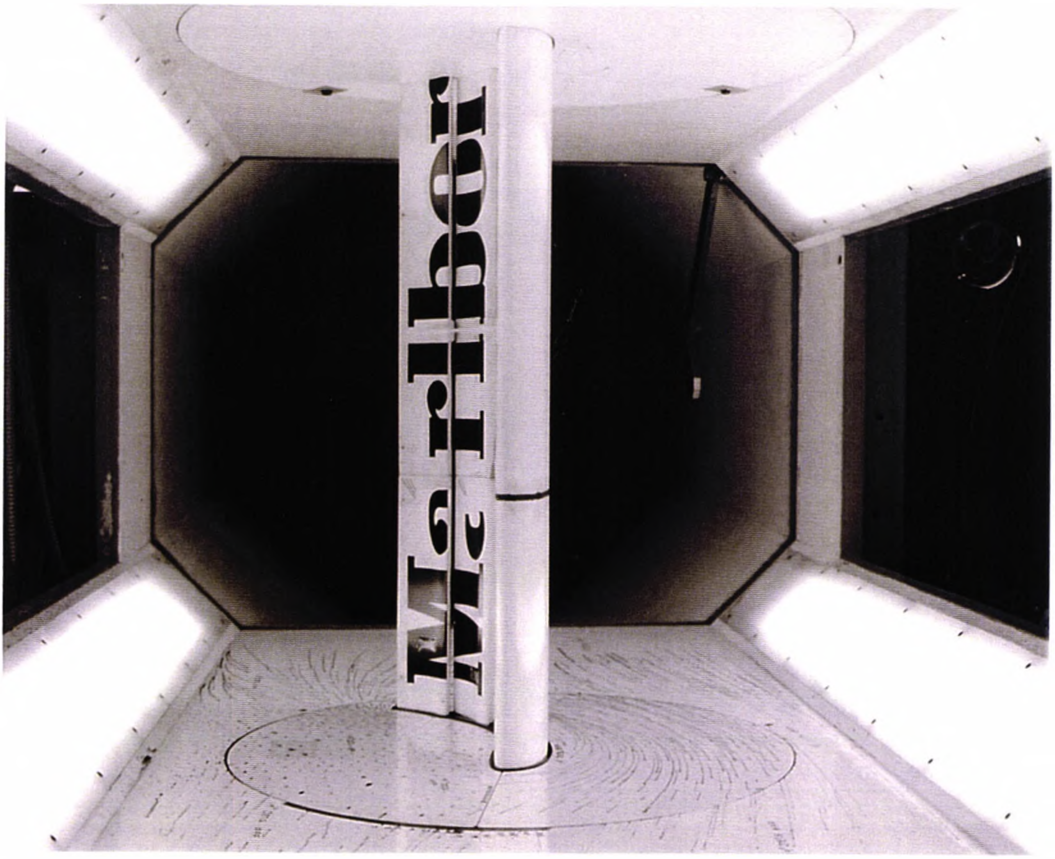

Figure 4.2: High downforce system mounted floor-to-ceiling in T2 working section.

4.3 High Downforce Wing

The full scale rear wing from the 1995 Ferrari Formula One car used in the experimental investigations was constructed with carbon fibre composites. This type of structure is very stiff and as such, large model deflections of the models were not a concern during the tests.

The wing comprised three elements, a 20% thick mainplane, an 18% thick vane and a 16% thick flap. These elements were fixed relative to each other for all experiments. All changes in the angle of incidence were facilitated by rotating the entire wing assembly. The dimensions of the model including chords, slot geometry and other data are given in Figure 1.17 on page 37.

The aerodynamic loads of the model were carried by three paths. One was a turntable, secured by three bolts, and fitted in the working section floor. The second load path was provided by a another turntable that was fitted around the wings and inside the tunnel ceiling with very tight clearances. The third load path was provided by a structure secured to the wind tunnel balance frame by a circular steel bar-mounting plate assembly which formed a journal bearing aligned with the centre of rotation of the turntable. There was enough freedom of movement to allow the model to be rotated and positioned with relative ease and good accuracy.

It is standard practice to employ some form of boundary layer control or endplates at the wing wall interfaces of a high downforce model. This is needed to ensure a nominal two dimensional flow over the wing through reduction of the thickness of the tunnel wall boundary layer. However, the use of such a system was not possible with this high downforce system due to the time available.

4.4 Air Jet Vortex Generator Design

In Section 3.5.3, it was explained that the AJVG centres were located 19% chord because of a wing spar that was situated between the 10% to 15% chord positions. The lateral spacing between the AJVGs was also of great importance because of the possible destructive interaction between adjacent vortices. Innes, Pearcey & Sykes (1995) found that a minimum lateral spacing of four times the jet length was required to prevent a destructive interaction between adjacent vortices. This was also in keeping with the findings of Johnston & Nishi (1989) and Freestone (1995). They independently investigated the lateral spacing of air jets and found that there was a minimum distance that should be maintained between the air jets to allow vortex structures that did not form and develop to the detriment of adjacent vortices. This detrimental effect occurs through the entrainment of low energy air from one vortex into an adjacent vortex system. A spacing of 40 mm was chosen after considering the findings from these investigators. Innes et al. (1995) also recommended a minimum distance of four times the air jet length from the tunnel walls because the interaction between the air jet effluxes and the wall boundary layers produced a separated corner flow. In keeping with this recommendation, the author placed the first and last air jets 40 mm from the nearest wall.

A co-rotating air jet array was chosen based on the findings of several researchers who compared counter-rotating and co-rotating VG arrays. Johnston & Nishi (1989), Henry & Pearcey (1994) and Innes et al. (1995) all found that co-rotating arrays were preferred to counter-rotating arrays because such vortex systems were not convected away from the test surface as rapidly as those created by counter-rotating arrays.

The air jets used in these investigations were rectangular measuring 2.5 mm x 10 mm. Some investigators have conducted research into the effectiveness of different types of air jet cross-sections. Shi-Ying & Fan (1987) performed experiments in which they investigated the use of air jets with crescent and circular cross-sections of the same area. They concluded that the crescent shaped jets showed were superior to circular jets because the former require lower mass flow rates to achieve the similar increases in C_f. Freestone (1995) conducted an inviscid study of vortex induced mixing. In this study, he concluded that air jets with rectangular cross-sections were most effective. A schematic of the air jet design used in this study is illustrated in Figure 4.3. The 2.5 mm x 10 mm rectangular duct for each air jet was machined from a solid, cylindrical, wooden plug 25 mm in diameter and 6 mm thick. Nineteen holes were machined in the mainplane suction surface. The wooden plugs were then oriented to a pitch angle, $\theta = 30^o$ and a skew angle, $\phi = 75^o$. Initially, the design called for $\phi = 45^o$ but investigations carried out by Peake et al. (1998) demonstrated that using AJVGs with $\phi = 75^o$ were more effective at reducing or eliminating flow separation on a test surface.

Figure 4.4 shows the wooden air jet plugs installed in the suction surface of the mainplane. The plugs were subsequently bonded into place using a high strength, cyanocryolate glue. With the exception of the area near the pressure orifices, the wings surfaces were painted white as a suitable background colour to perform oil and lampblack surface flow visualisation. Figure 4.5 shows the finished model standing on end and ready to be installed in the T2 wind tunnel. The internal mainplane structure was essentially hollow

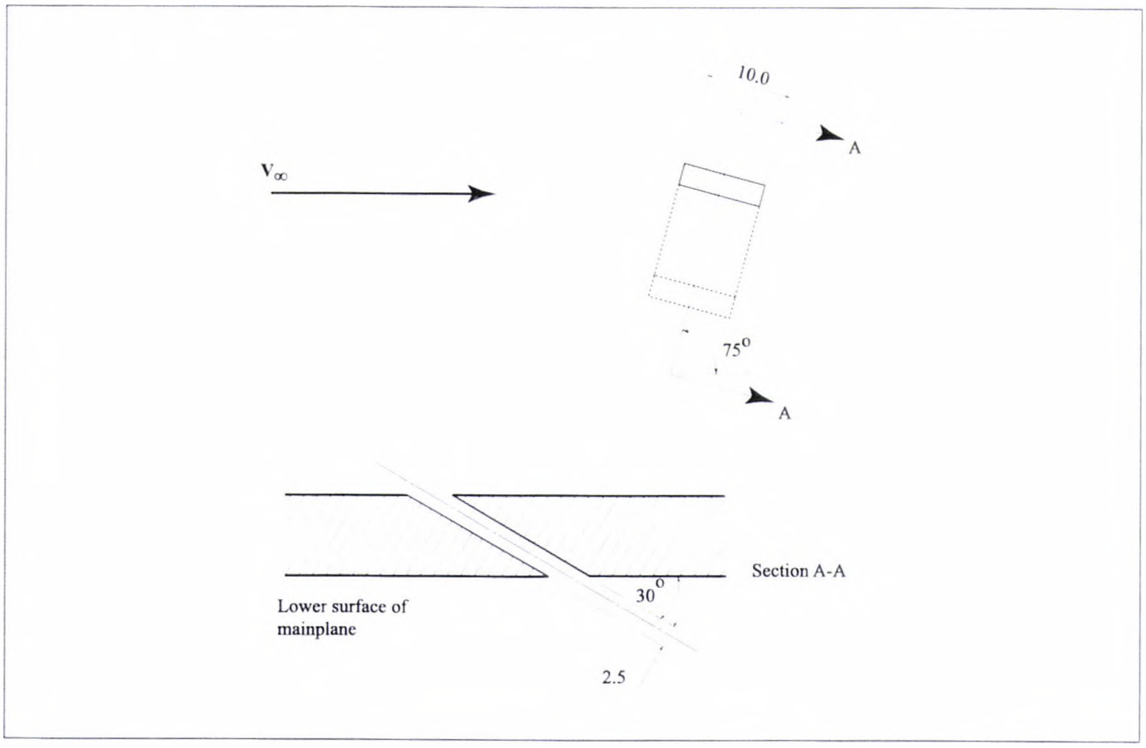

Figure 4.3: Air jet vortex generator design. (All dimensions in mm)

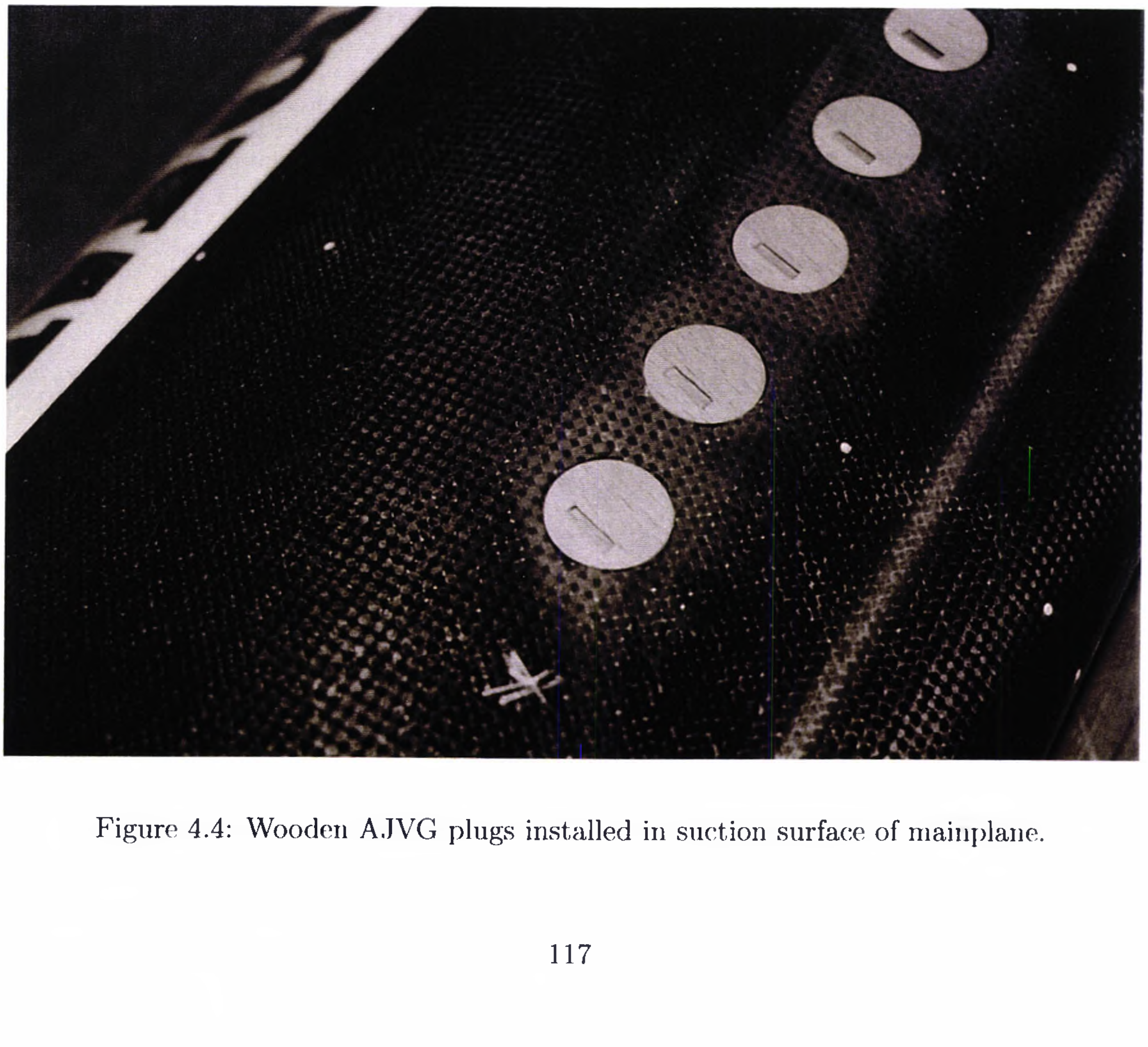

Figure 4.4: Wooden AJVG plugs installed in suction surface of mainplane.

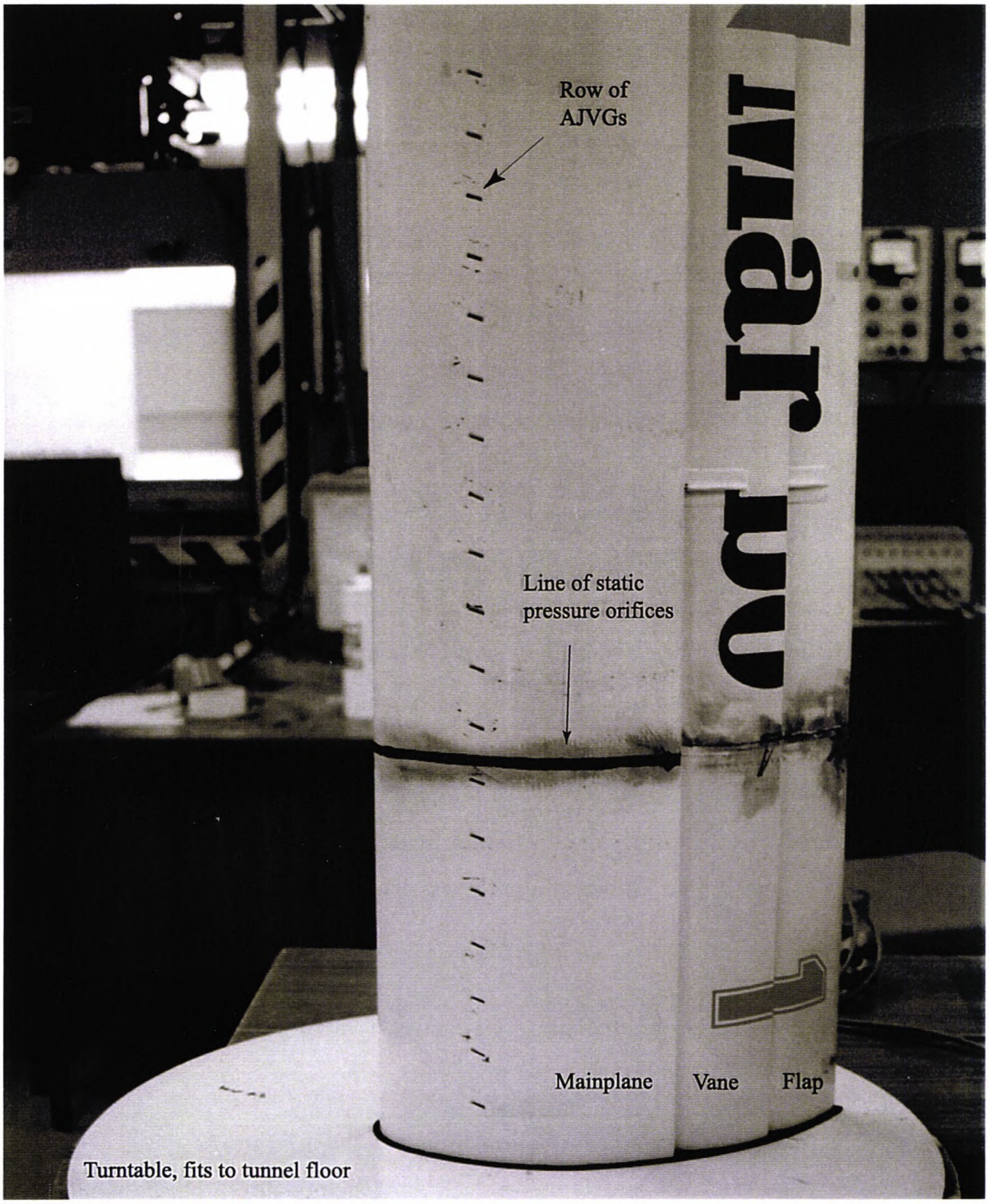

Figure 4.5: High downforce wing stood on end showing air jets.

and covered by two carbon fibre plates, one at each tip. These plates each had 2 holes, each 14 mm in diameter, that served as an air supply for the AJVGs. Figure 4.6 shows the location of the AJVG inlets. On those occasions when clean wing tests were required, these inlets were sealed with tight fitting rubber plugs and the jet exits were covered with a thin, matt, 3M Scotch Tape TM.

4.5 Measurement of Surface Static Pressure

Two systems were used to measure the static pressure about the high downforce model in the two separate series. In the first experimental session, a computer controlled data acquisition system developed by Innes (1995) was employed; while in the second, a system of alcohol manometers was employed. The use of the alcohol manometer system although slow to read, proved to be accurate and repeatable.

The wings were equipped with pressure orifices in a plane 103 mm from the wind tunnel test section centre line. It was not possible to locate these pressure orifices at mid-span because there was a carbon fibre spacer bonded to the wing components at this location. This spacer is a common part of any multi-element high downforce design in motor racing. It is used to maintain the intended slot geometry when the wings are subjected to an aerodynamic load. The 0.5 mm pressure orifices were made from stainless steel tube. The mainplane was equipped with 67 pressure orifices and the vane and flap were equipped with 43 each. They were arranged normal to the local surface, in a approximate cosine distribution around each element so as to have a higher tapping density in the areas of high flow field gradients. One pressure tapping was located in the trailing edge of each element.

4.5.1 Calculation of Surface Static Pressure Coefficients

A procedure was developed to eliminate the need for calibration of the pressure transducers used in the experiments. This procedure also eliminated the need to use the densities of the various alcohols in the manometers used to calculate the pressures. This is significant because the densities of the fluids were not known with any degree of certainty. An explanation of this procedure follows.

Using Bernoulli's equation, the standard equation for the pressure coefficient is

$$C_p = \frac{(P - P_{static})}{\frac{1}{2}\rho V_\infty^2} \tag{4.1}$$

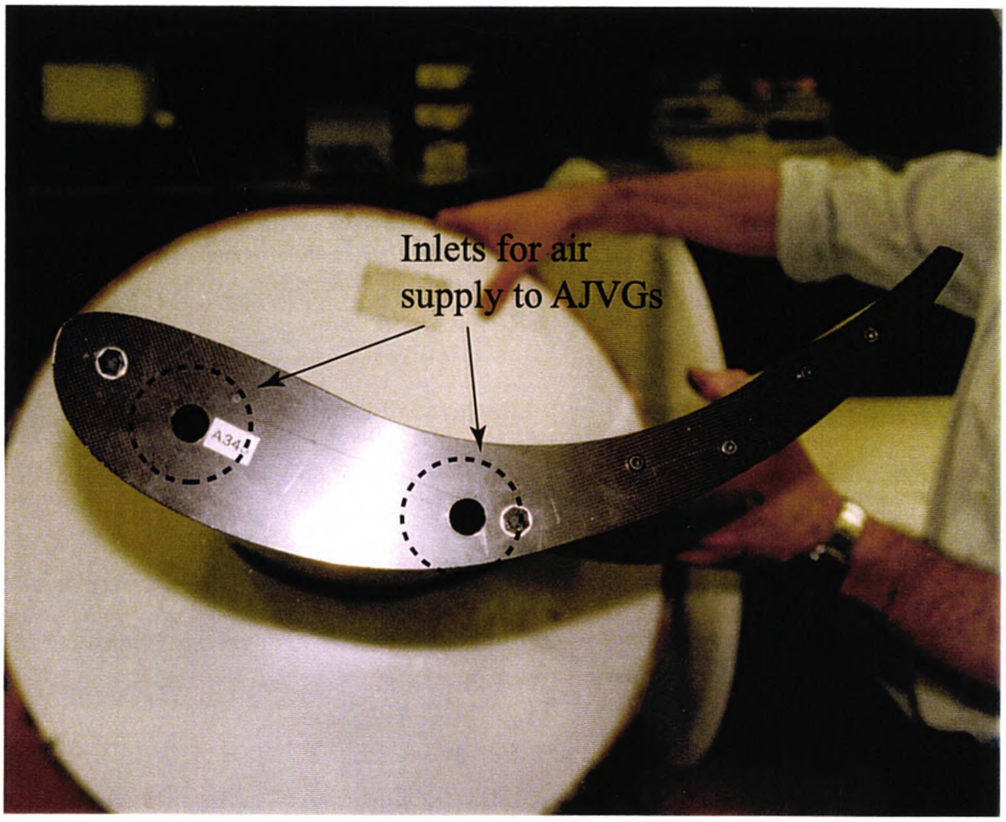

Figure 4.6: Two of four inlets for AJVG air supply.

This can be expanded using atmospheric pressure, P_{atm}, to give

$$C_p = \frac{(P - P_{atm}) - (P_{static} - P_{atm})}{\frac{1}{2}\rho V_\infty^2} \tag{4.2}$$

We now assume that

$$\frac{1}{2}\rho V_\infty^2 = K_1 (P_1 - P_2), \tag{4.3}$$

$$(P_1 - P_3) = K_2 (P_1 - P_2) \tag{4.4}$$

and

$$(P_2 - P_3) = K_3 (P_1 - P_2) \tag{4.5}$$

where $P_1 - P_2$ is the static pressure drop along the wind tunnel contraction and P_3 is the static pressure in the centre of the wind tunnel working section. These give,

$$C_p = \frac{(P - P_{atm}) - (P_2 - P_{atm})}{K_1 (P_1 - P_2)} + \frac{K_3}{K_1} \tag{4.6}$$

By operating the wind tunnel at various speeds, it is possible to obtain calibration constants for K_1, K_2 and K_3. Innes (1995) found the values of these constants to be as follows; $K_1 = 1.073$, $K_2 = 1.0368$ and $K_3 = 0.03675$. Equation 4.6 then becomes

$$C_p = \frac{(P - P_{atm}) - (P_2 - P_{atm})}{1.073\,(P_1 - P_2)} + 0.034 \tag{4.7}$$

The use of this system allows for C_p to be calculated from raw voltages alone provided that the output of the transducers is proportional to the input within the range of pressures measured. The pressure differences set out in Equations 4.3, 4.4 and 4.5 need to be measured at all times. Thus, certain pressure orifices were reserved to measure these quantities on both the scanivalve and hydrostatic systems. The pressures were measured with a variance of ± 0.25 %.

4.5.2 Electronic Data Acquisition System

Figure 4.7 shows the schematic of the data acquisition system as developed by Innes (1995). The system contained two separate electrical circuits, a scanivalve control circuit and the pressure measurement circuit. Both these circuits derived their power from the 240 Volt (V), 50 Hertz (Hz) alternating current electrical mains. The scanivalve control circuit consisted of a personal computer based on an Intel 486 microprocessor and an analogue to digital signal converter. The computer used a bespoke software package to control the system. Through the software, the user was able to enter information pertinent to a particular test as well as control parameters such as the number of pressure transducers used, the duration of pressure sampling and the range of pressure orifices sampled.

Pressure Measurement Circuit

The pressure measurement circuit used two Druck PDCR22 transducers with a range of 175 mbar and 37 mbar respectively. These transducers were characterised by excellent linearity, negligible hysteresis and low volume. The last quality is especially important in allowing accurate short duration scanning. These transducers were designed to be used with the scanivalve mechanism.

The transducer contains a silicon crystal diaphragm over which the pressure difference is applied. This diaphragm is integrated with a electronic strain gauge where the deflection of the diaphragm produces a change in the resistance and therefore, voltage in the circuit. The nature of the circuit is such that the difference in voltage is proportional and linear to the deflection of the diaphragm. The excitation voltage for the circuit was provided by a bridge conditioning unit. The signals generated by the direct current (DC) bridge transducers were in the microvolt range and this mandated the use of a signal amplifier before these analogue signals could be converted by the analogue to digital converter. A differential DC pre-amplifier was used to amplify all signals derived from both transducers.

Both transducers were used to monitor the pressure orifices in the wings and at the static and total pressure ports in the wind tunnel contraction and working section. These were connected at any given time to a total of 96 scanivalve ports by clear medical quality, vinyl tubing. Each tube was approximately 1 metre long. There were more pressure orifices than transducer ports and this meant that each run was done in two parts. The first part of each run was done with both transducers measuring the pressures on the mainplane and the second was used to measure those on the vane and flap.

Scanivalve Control Circuit

The scanivalve pressure measurement apparatus used in the first experimental session is an electro-mechanical device with 48 pressure ports arranged in two concentric rows of 24 ports each. The Druck PDCR22 transducer is fitted and sealed at the centre of the device. In its proper location, the transducer can sample each of the 48 ports in turn through the internal plumbing of the scanivalve. Access to each port is provided by a rotary solenoid drive which is controlled by a closed loop control system. Through this control system, the position of the drive and the port number is known at all times. It is through this facility that the scanning of certain ports can be eliminated thus saving time. The reader can refer to Figure 4.7 for details of how this system was implemented for these experiments.

4.5.3 Alcohol Manometer System

It was not possible to use the electrical data acquisition system for the second session of experiments. Five alcohol manometers were connected directly to the wings and the wind tunnel ports P_1, P_2 and P_3. These manometers used alcohols with different specific gravities and the columns were measured using imperial and metric units. In addition, the alcohol reservoirs for all of these manometers had uncertain maintenance histories. The use of Equation 4.7 obviated the need to make detailed calculations and unit conversions for each manometer. The method used to calculate the C_p was analogous to that employed with the electronic system. In this case, only the difference between the initial and final column heights was required to determine the C_p of any given port. The use of a completely different system provided the means to assess the repeatability of the measurements made in the first experimental session.

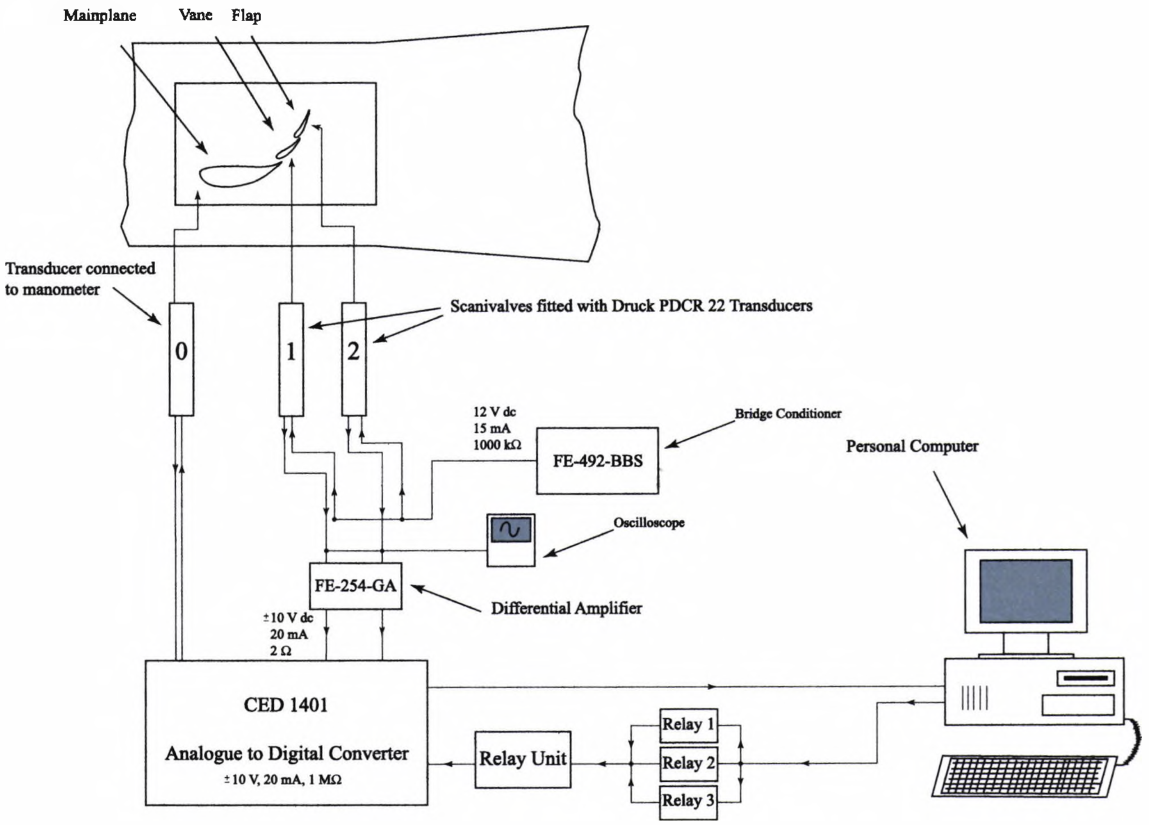

Figure 4.7: Schematic of electronic data acquisition system.

4.6 Variance and Error Assessment

Some procedures were used during the experiments in order to minimise the errors in and the variance of any data taken. In the preparation of the experiments there was a need to establish whether the wing geometry (aerofoils and slot gaps and overhangs), was the same as those originally defined by Ferrari. It was also necessary to ensure that the model angle could be accurately and repeatedly set in the tunnel. During the experiments, the test equipment, the ambient conditions and the wind tunnel parameters such as speed and temperature were constantly monitored as were all pressures in the test section and on the wings. At times, this practise allowed for the identification and replacement of faulty equipment, but for the most part, it was only used to monitor that the experimental set-up was functioning properly.

4.6.1 Close Range Photogrammetry

Ferrari provided the wings which had already been used in several grands prix. These wings were then subjected to modifications known in the composites industry as a *cut an shut*; a process where a finished composite component is modified in a way that requires cutting the structure followed by a modification and bonding process. Such a procedure was necessary to install the pressure orifices in the wings.

A *cut an shut* can often result in the relief of residual stresses in the structure which in turn can result in surface deformations. When this occurs the component can differ significantly from its *as designed* shape. When used on the racetrack, the wings are subjected to high frequency, small amplitude 20 g vibration in addition to the aerodynamic forces. All of these factors can affect the shape of the wings.

In order to verify the *as designed* shape of the wing assembly and the location of the pressure orifices, the wings and pressure orifices were examined using Close Range Photogrammetry. This technique uses highly accurate cameras to determine the shape and position of arbitrary objects in three dimensional space. Several photographic techniques can be used. The reader is referred to Atkinson (1996) for a detailed discussion of the principles governing Close Range Photogrammetry.

The photogrammetry work on the Ferrari high downforce model was carried out by Stuart Robson, then of the Civil Engineering Department of City University. A highly accurate, Kodak Megaplus 1.6i, self calibrating, charge coupled device (CCD), was used to take photographs of several hundred retro-reflective targets placed on the model. These retro-reflective targets, each 0.5 mm in diameter, were placed over each pressure tapping and at strategic locations along the chord and span of each wing element. These data were then used in conjunction with the CAD files provided by Ferrari to verify that the wings being tested were indeed the profiles that Ferrari intended. Figure 4.8 shows one of the analysis steps that the photogrammetry software employs. In this photograph, each target has been assigned a unique number. The location of the static pressure orifices and the aerofoil co-ordinates of each wing were measured and determined to within 42 μm, 43 μm, 54 μm for the x, y and z-co-ordinates respectively. The wings were all simple aerofoil sections of the same span with no aerodynamic *wash in* or *wash out*[1]. This made for an easy comparison with the Ferrari CAD surface data. Deviations between 0.01 mm and 0.2 mm were found for the modified wing structures when compared with this CAD data. The maximum deviations occurred on the vane and flap elements. The co-ordinates of the pressure orifices with the model at $\alpha = 29^o$ are provided in Section A.7 in the Appendix.

---

[1] A change in aerofoil or the angle-of-attack of the aerofoil at various spanwise stations

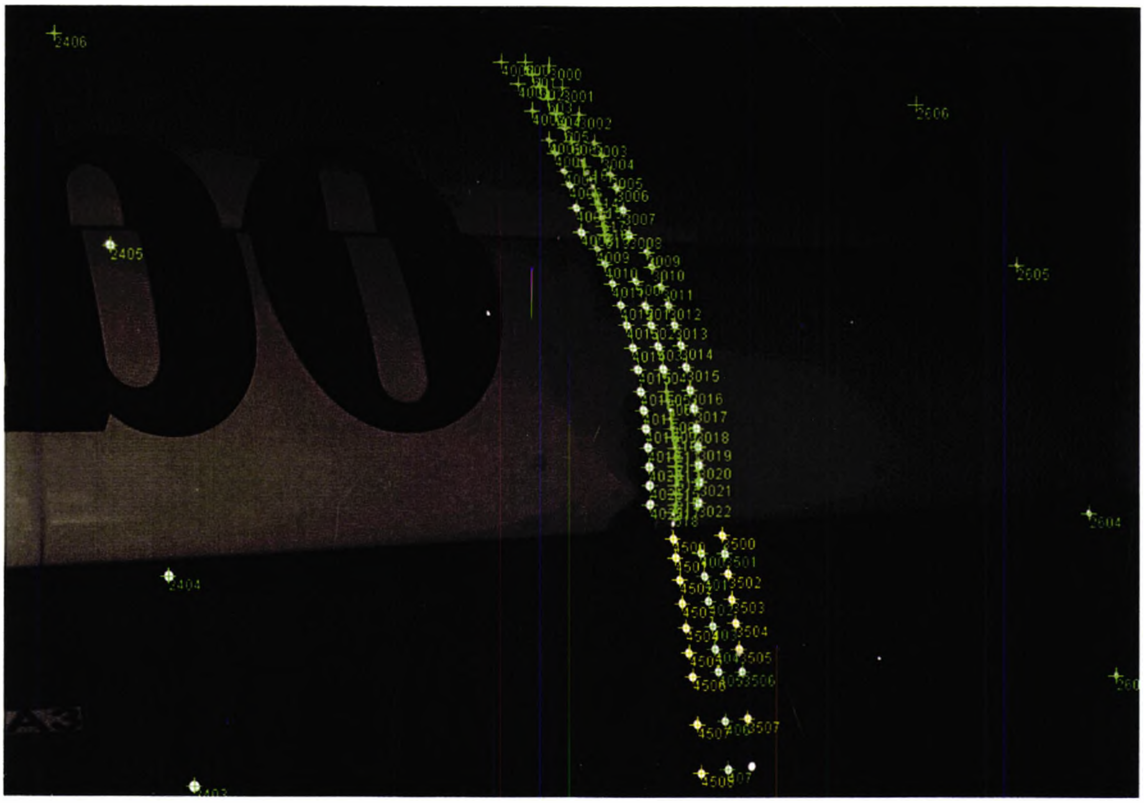

Figure 4.8: Tagged retro-reflective targets on suction surfaces of wings.

4.6.2 Position of High Downforce Wing in Wind Tunnel

Reference lines taken from the CAD files were drawn on the tunnel floor using a digital inclinometer. The references used were the lines formed by the test section fillets and the wind tunnel centre line. A line tangent with the leading edge of the mainplane and the upper trailing edge of the flap were also employed to set up angular references for the model. The last of these lines is labelled in Figure 1.17 as the "Practical Reference Line". Traditionally, this is the line that is used to measure the angle of incidence of a wing in motor racing because it is easily accessible. However, it was not practical to use this system in the experiments. A line offset by 29^o, parallel to the tunnel walls was used to align the model for all experiments. These references were used to align the model with an inclinometer that was integrated into the working section floor. This reference line and the inclinometer shown in Figure 4.9 were used to set the angle of incidence of the model. Repeated runs where the angle was measured with the digital inclinometer, showed that the model could be positioned to within $\pm 0.25^o$ of the angle indicated on the tunnel inclinometer.

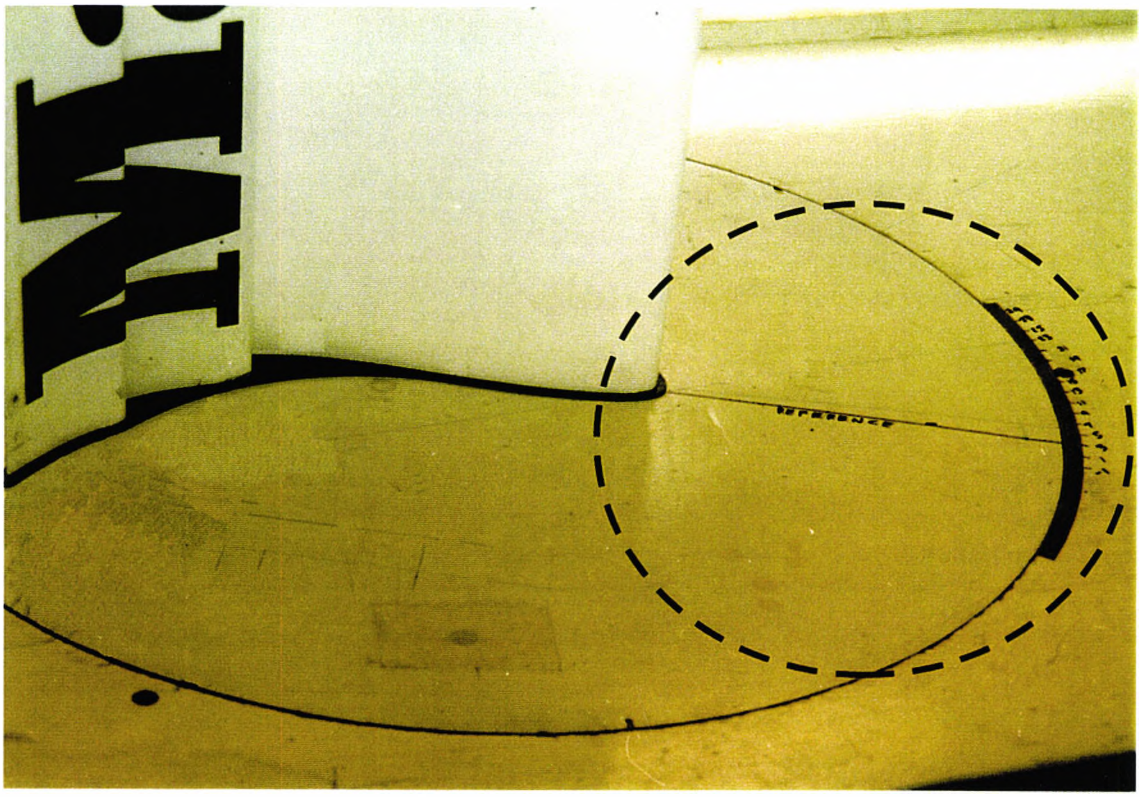

Figure 4.9: Demarcations and positioning lines.

4.6.3 Variances Associated with Electronic Pressure Measurement

This system was established in such a way that it was self calibrating. Innes (1995) found that the pressures measured varied by ±0.25%. This variance was most likely due to small differences in the flow field. The author also measured a similar variance in his investigations. The transducer voltages were displayed using an oscilloscope. This providing the capability to monitor the constants K_1, K_2 and K_3 returned by the system and through repeated runs. Once the author became familiar with the system, these procedures were used to identify any faulty equipment and spurious data.

Initially the author was concerned with the length of the vinyl tubes between the pressure ports and the scanivalve. The lengths of these tubes were approximately 1 metre. In their research into the air flow structure past circular cylinders, Luo & Gan (1992) used a scanivalve system similar to the one used by the author with 0.95 m long poly-vinyl chloride (PVC) tubing of 1.5 mm internal diameter. They found that the damping effect of the air in long tubing acts as a low pass filter and that the amplification factor of such tubes is dependent on the frequency of the signal being measured. The effect of such long tubing would be to dampen any fluctuation in pressure produced by unsteady behaviour about the high downforce system.

Unsteady aerodynamic behaviour was found at the highest angles-of-attack but the author was not able to address this through any type of signal processing. Steps taken to minimise any unsteadiness were a gradual increase in the air speed to the desired 35 m/s or 40 m/s and allowing the tunnel velocity to settle for at least two minutes before any measurements were taken.

The greatest problems were encountered at angles-of-attack greater than 19^o and at a test section speed of 40 m/s. Any runs at these angles produced increases in the circulating air temperature of up to 20^o C from an initial temperature that was in the range of 17^o C to 21^o C. Such runs resulted in erroneous C_p calculated by the data acquisition software. A sampling time of 0.5 seconds per port greatly reduced this increase in temperature from 5^o C to 10^o C because a shorter sample time reduced the total time per run thus reducing the heating of the air inside the tunnel circuit. The heating was higher when the wing was tested at the higher angles of incidence.

4.6.4 Errors Associated with Alcohol Manometer System

The minimisation of error with this system lay mainly with ensuring that the wind tunnel had settled down to a steady state condition and further that the manometers had also settled down. This system was even less equipped to handle any unsteady measurements than the electronic system because any measurements would have been further dampened by the alcohol columns. However, it was clearly visible whether or not the heights of the columns were constant. When there were regular oscillations of several millimetres amplitude, these levels were marked with a thin tipped felt pen and the median of these values was taken. The author was careful to ensure that the manometers were mounted vertically and to read and mark the bottoms of the menisci of all alcohol columns. All data were entered and verified with the help of a second party.

Several pens with felt tips of 0.2 mm were used to mark the manometers. The size of the tip itself is also a source of error. In this case, the magnitude of the error is the diameter of the tip. The author believes that such errors were negligible given the changes in height of the alcohol columns.

Despite the fact that this system is not very capable of measuring any unsteady behaviour about the wings themselves, the author did note the height fluctuations of the alcohol columns covering the suction sides of the mainplane and vane at the higher angles of attack. These fluctuations had amplitudes in the range of 5 mm to 30 mm and a time period of approximately 1 minute. With such a long time period, it is unlikely that their origin is the high downforce system. It is more likely that this behaviour originates from the air flow interacting with the larger dimensions of the wind tunnel. When this problem was encountered, the wind tunnel was stopped and then restarted and the data was taken after ensuring that there were no height fluctuations.

Chapter 5

Discussion of Results

5.1 Numerical Results

The numerical and experimental results are presented in this chapter through a discussion of the global flow features and detailed flow features of the predicted and experimental flow fields. The global flow features comprise two and three-dimensional flow visualisation. The detailed flow features are the pressure distributions and integrated force data.

The two-dimensional results represent an effort to better understand the characteristics of the high downforce system. These calculations were performed at angles of incidence ranging from 3^o to 29^o but with emphasis on $\alpha c_{l\,max}$ which from experimental results was thought to occur at approximately 19^o. Also discussed is the variation and position of the peak suction C_p on each element with respect to the angle of incidence and the trailing edge C_p on each element with respect to the angle of incidence.

The three-dimensional calculations performed included a validation case that models the high downforce system in the wind tunnel test section and oriented at 29^o incidence. All the models incorporating air jets are also three-dimensional with the representative high downforce wing oriented at 29^o incidence.

The numerical data are presented from the two-dimensional and three-dimensional solutions. The flow fields predicted by these calculations are discussed in terms of the pressure distributions, integrated forces, velocity vector plots, variable contours and streamline plots. The difficulties experienced by the author with these numerical models are also discussed at this time.

Comparisons are made between the numerical and experimental results and issues of certification, verification, validation and credibility of the numerical predictions discussed. Some of the problems encountered during the experimental investigations are included in this discussion. The numerical mdoels used are now listed:

1. **Two-Dimensional Models** - These comprise coarse and refined grid models bounded by symmetry planes on the left and right side to give a wing of infinite span. They were used to predict the general behaviour of the high downforce wing between 3^o and 29^o incidence.

2. **810 mm Span Clean Wings** - A span of 810 mm represents the full span of the wing within confines of the wind tunnel test section. These models were oriented at 29^o incidence. Coarse and refined grids were used as part of the grid independence exercise. Given that these were the only models for which a direct experimental counterpart existed, the predicted C_p were compared with those measured in the experiments.

3. **240 mm Span Clean Wing** - This 240 mm span mdoel was created to provide a clean wing comparison for the air jet models. It was oriented at 29^o incidence.

4. **240 mm Span Wings Incorporating Air Jets** - Due to the limited availability of computational resources for post-processing, the author could not use a numerical model with the full AJVG array of nineteen air jets. A smaller, more manageable model of five air jets was used to capture the salient features of the flow field. Using the AJVG spacing of 40 mm, the span for these wall bounded models was 240 mm. These models were oriented at 29^o incidence. Three different blowing pressures were used with this type of model, These are presented in the forthcoming discussion. The results from these air jet models were compared directly to the results from the 240 mm span clean wing model.

5.2 Two-Dimensional Predictions

5.2.1 Two-Dimensional Flow Visualisation

The flow about the high downforce model is discussed using velocity vector and streamline visualisation. The streamlines are shown over the entire computational domain and velocity vectors are used for the near-mainplane trailing edge region. The velocity legends are shown in metres/second. These visualisation techniques are presented for 3^o, 19^o and 29^o. These angles represent α_{min}, the approximate $\alpha c_{l\,max}$ and α_{max} respectively.

Figure 5.1 shows a streamline plot about the high downforce model at 3^o angle of incidence. There is a smooth flow about the model with no flow separation. There are no disturbances to be seen in the far-field area about the model. The mainplane stagnation point is located on the forward part of its leading edge. These streamlines also show that the predicted wake size is quite small because there is very little streamline divergence near the trailing edges of the elements.

The velocity vector plot presented in Figure 5.2 also shows attached flow on the mainplane in the very sensitive trailing edge area on the lower surface. The flow is also well behaved in the slots and on the vane and flap elements. The velocity vectors are consistent with a very small predicted wake.

At 19^o incidence, the flow remains smooth and attached to all the elements in the model but the flow field about the model had changed significantly from that seen at 3^o. The entire flow field is visualised with streamlines in Figure 5.3. At 19^o incidence, the model generates higher circulation and this causes a much higher turning of the flow near the mainplane leading edge. As a result, the mainplane stagnation point rests on the upper leading edge. In the region just behind the vane and flap elements, there is a notable divergence of the streamlines. The colour of these streamlines also show that this is an area of very low velocity. This divergence and the flow velocities in region show a larger predicted wake. Analysis of the angles between 3^o and 19^o show that the size of the wake increases with angle of incidence.

The velocity vectors shown in Figure 5.4 show a smooth flow about the mainplane trailing edge region. There is also a smooth flow predicted in the slot regions and about the entirety of the vane and the flap elements. The velocity vectors do not indicate the wake shown in Figure 5.3 because the region where the flow decelerates to produce this wake is to the rear of the area depicted in Figure 5.4.

The flow field for the entire computational domain with the model at 29^o incidence is shown in Figure 5.5. There is a more turning of the flow than at any other angle and there is significant divergence of the streamlines in the region immediately behind the model.

The velocity vectors at 29^o incidence, presented in Figure 5.6, show a smooth flow about the lower mainplane near trailing edge. In the region close to the trailing edge itself, there is a visible deceleration as the flow approaches the trailing edge but no flow separation. The flow about the slots and the vane and flap elements is smooth and attached. The flow from all three elements decelerates in the region immediately downstream to a very low velocity. This is the predicted wake region that is clearly shown with streamlines in Figure 5.5.

The near model velocity vectors about the model at 29^o, illustrated in Figure 5.6, show that there is no separated flow predicted anywhere about the high downforce model. The failure to predict flow separation may be due to certain limitations in the use of wall functions to model the near wall flows. This philosophy is not capable of capturing all of the flow developments that are physically possible because the flow field below $y^+ = 30$ is approximated by Equation 2.29 and not solved explicitly.

All the velocity profiles in the predicted boundary layers between the wall and the first interior point (just above the buffer region), are forced to have the same shape which is determined by iteration using Equation 2.29. This limitation in the near-wall region and the excessive numerical dissipation of the k-ϵ turbulence model as implemented in CFX-4.2 are most likely responsible for the failure in predicting flow separation on the mainplane. Despite the failure to predict flow separation in these investigations, it will be shown that the two-dimensional models do provide a reasonable prediction about the force trends of the high downforce system.

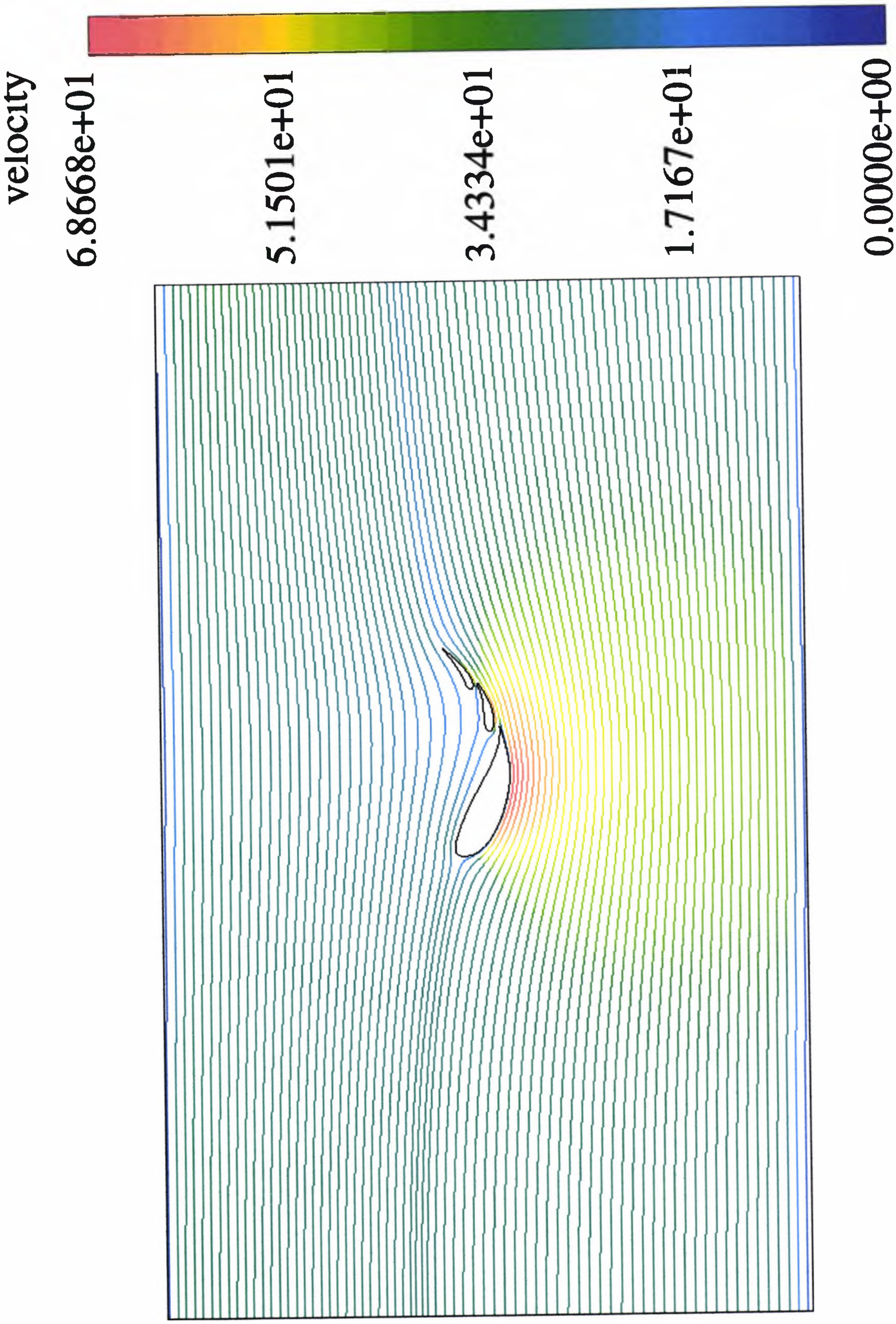

Figure 5.1: Streamlines about aerofoils at $\alpha = 3^o$.

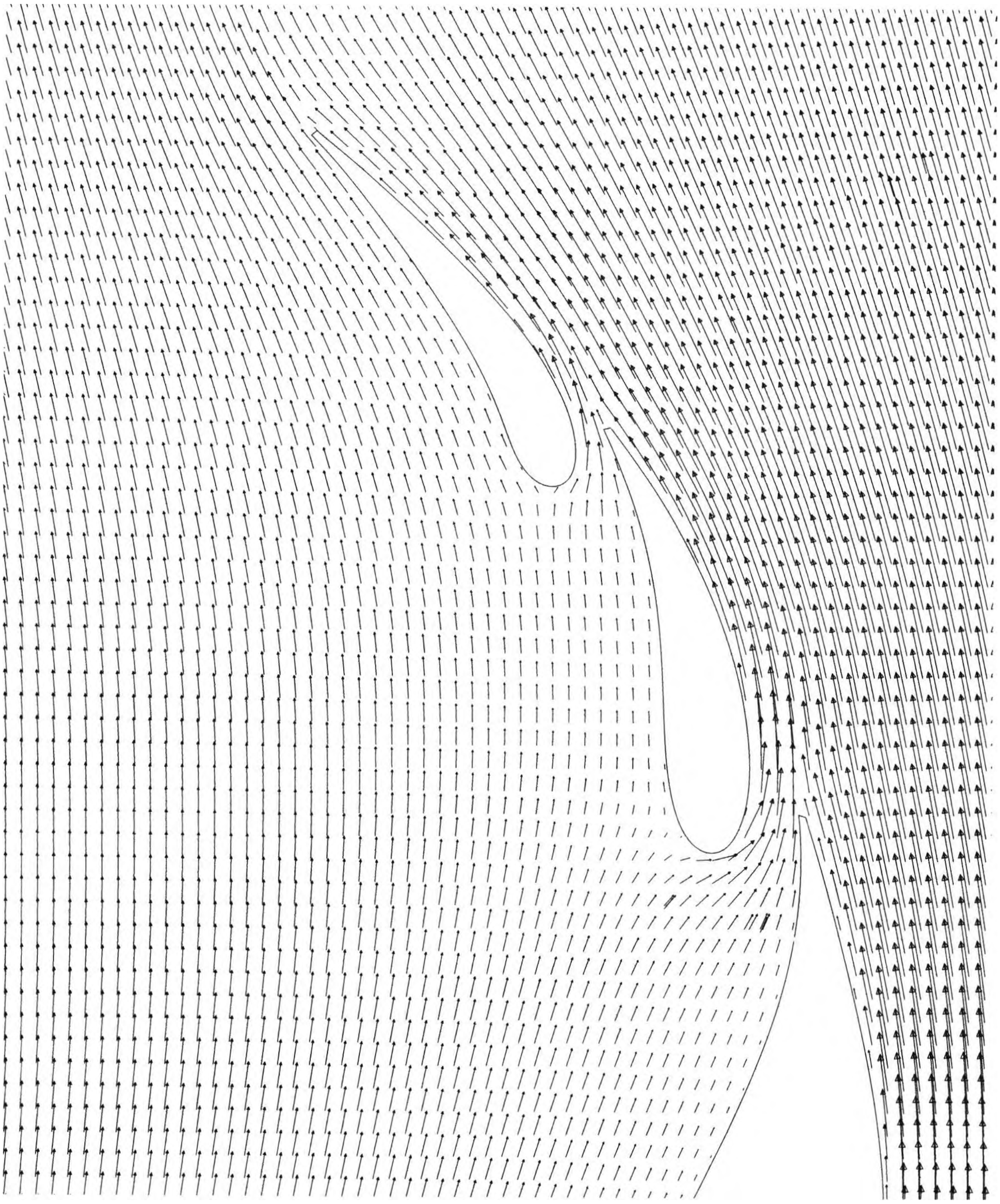

Figure 5.2: Velocity vectors about aerofoils at $\alpha = 3^o$.

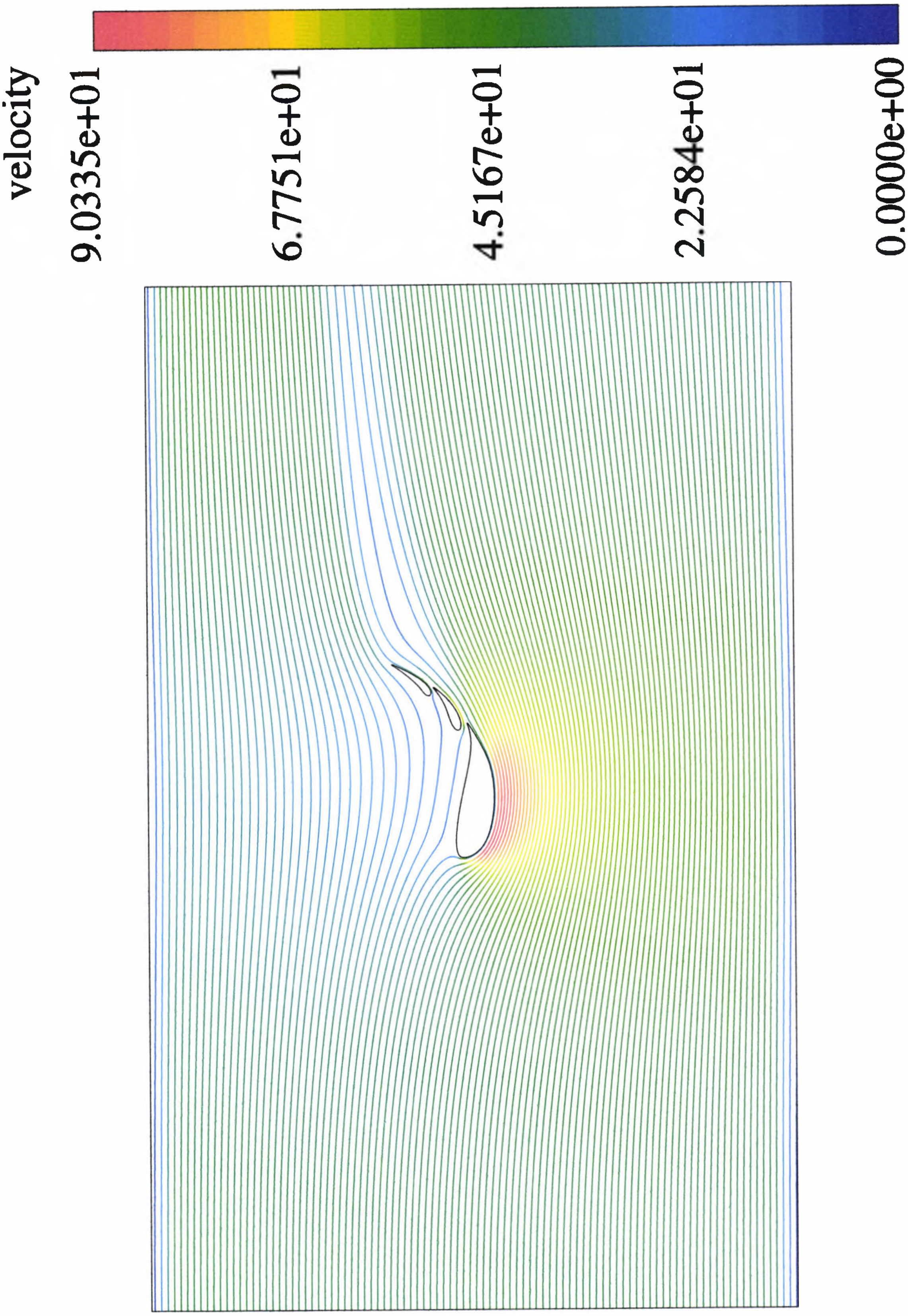

Figure 5.3: Streamlines about aerofoils at $\alpha = 19^o$.

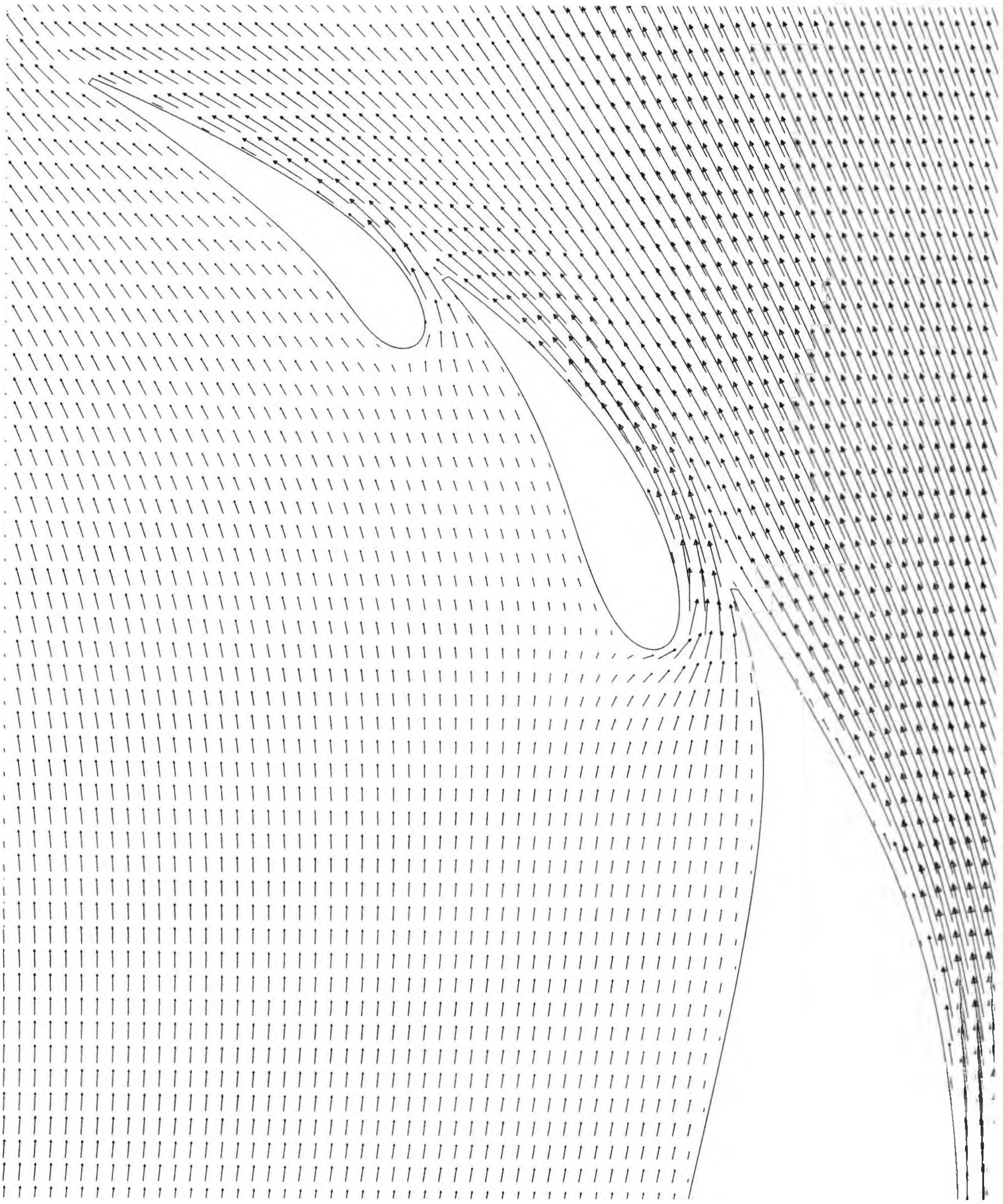

Figure 5.4: Velocity vectors about aerofoils at $\alpha = 19^o$.

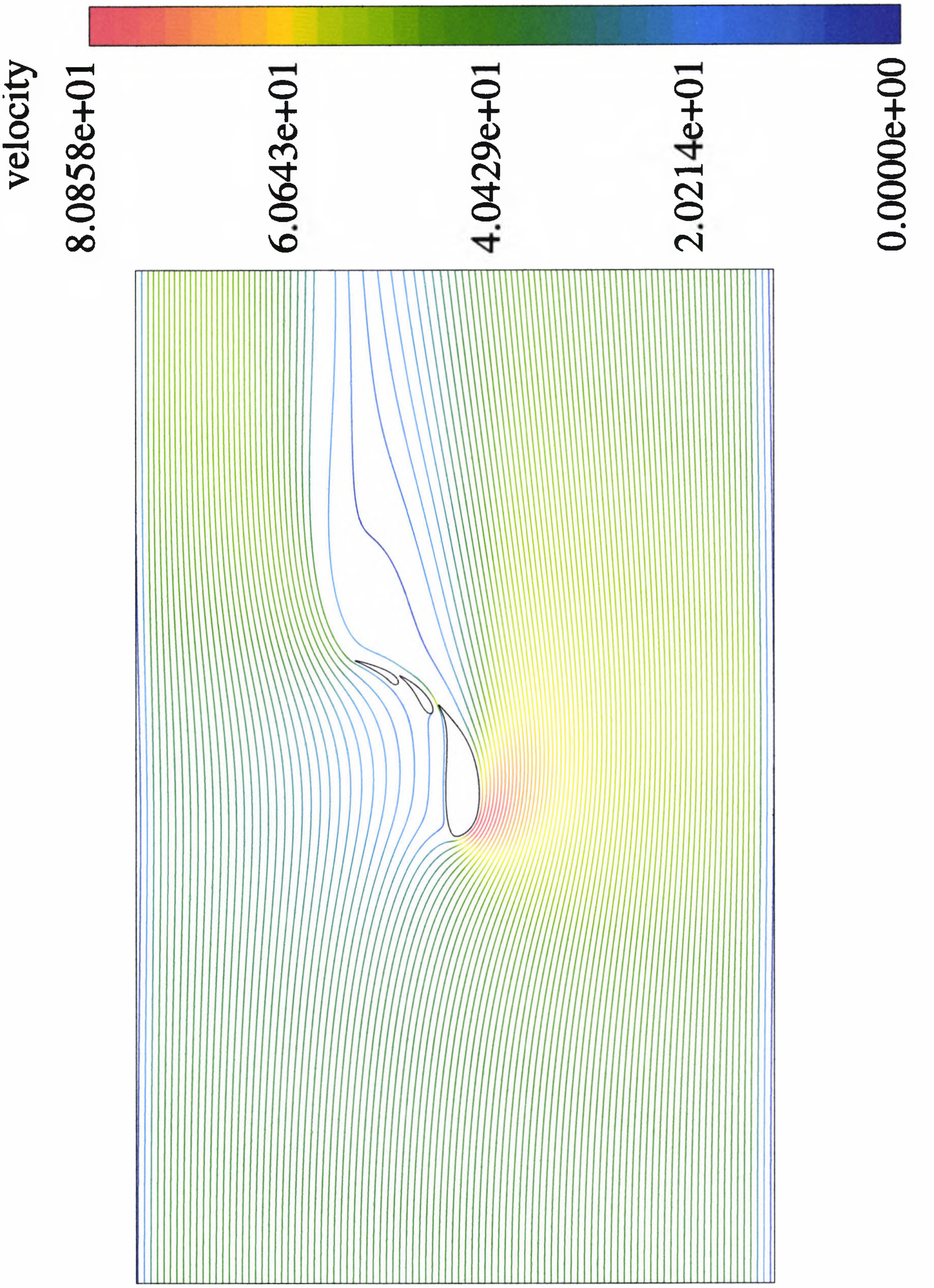

Figure 5.5: Streamlines about aerofoils at $\alpha = 29^o$.

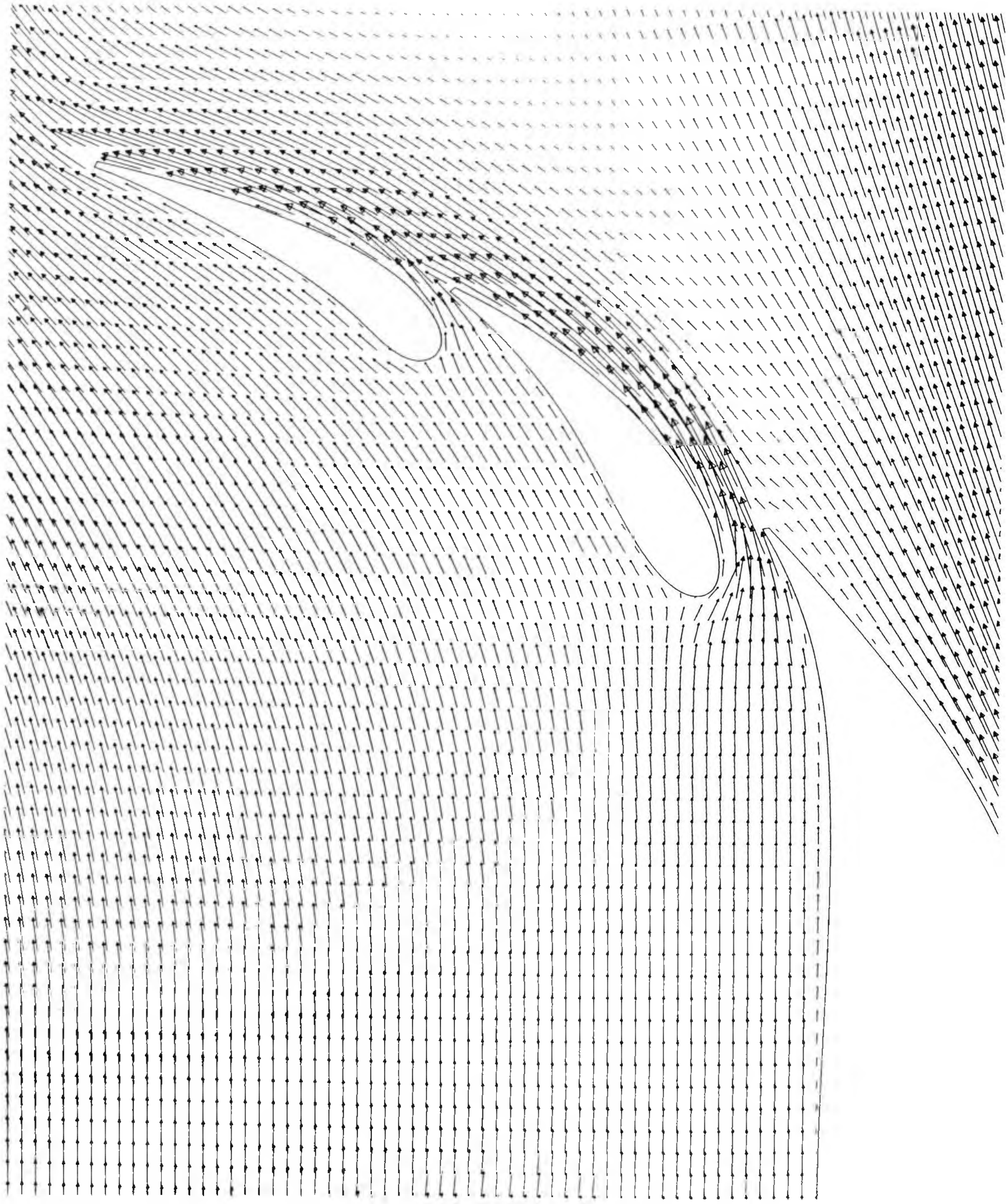

Figure 5.6: Velocity vectors about aerofoils at $\alpha = 29^o$.

5.2.2 Predicted Two-Dimensional Pressure Distributions

Some predicted pressure distributions are presented in Figures 5.7 to 5.19 for 3^o and 29^o angles of incidence at intervals of 2^o. These two-dimensional calculations were undertaken to predict the performance of the high downforce model. They were also carried out to establish if CFX 4.2 could predict realistic pressure distributions across a the angle of incidence range. The definition of C_p is given by Bernoulli's equation as expressed in Equation 4.1 where P is the pressure on the inlet boundary upstream of the high downforce system.

Two additional entry lengths combined with limited near-wing grid refinements were investigated. Both entry lengths were longer than that which represented the confines of the wind tunnel test section. These were 10 and 20 assembly chords upstream from the standard inlet. The near-wing grid refinement involved a general doubling of the number of cells around the aerofoils. It was not possible to achieve grid refinement through an increase in the number of cells normal to the aerofoil surfaces because this would have produced $Y^+ < 11$ for the near wall cells.

Figure 5.7 shows the predicted C_p about the elements of the numerical high downforce model at 3^o. The predicted pressures about the high downforce wing are generally in good agreement for both the coarse grids and the refined grids with extended inlet lengths. The latter models were used to establish the effect of the proximity of the inlet on the solution. Figure 5.7 shows that these changes made a negligible difference to the prediction of the pressure distribution about the high downforce system at 3^o angle of incidence.

The pressure distribution at 3^o angle of incidence is characterised by significant acceleration of the air flow around the leading edge of the mainplane. This can be seen as a peak formed by the sudden reduction in the C_p after stagnation. This is caused by the acceleration of the air flow around the mainplane leading edge and on to its high pressure, upper surface. This occurs because the mainplane is in an atypically high *nose-up* attitude at this angle of incidence and the stagnation line is located on the lower portion of the mainplane leading edge. The magnitude of this peak decreases with increasing incidence up to the maximum of 29^o.

It is in the range of 15^o to 29^o that the components of such a high downforce system are most likely to be employed. It is also within this range that the system exhibits more typical C_p distributions. Figures 5.12 to 5.19 shows the C_p distributions for 15^o to 29^o. It is seen that the high pressure peak around the mainplane leading edge diminishes with increasing incidence. Simultaneously, there is a decrease in the mainplane peak suction

C_p with increasing incidence as well as a forward migration of the location of the peak suction C_p.

The mainplane is the dominant element in the system due to its large surface area and the behaviour of its pressure distribution. This is seen in Figures 5.20 through Figure 5.21. Over the angle of incidence range, a peak suction ΔC_p of approximately -3.69 is predicted. By comparison, the vane and the flap elements are less sensitive to changes in α with the flap being the least sensitive. Between 3^o and 29^o, the vane exhibits a predicted peak suction ΔC_p of approximately 0.816 and the flap has a predicted peak suction ΔC_p of approximately 0.226.

The decrease in the peak suction C_p on the mainplane with increasing α is accompanied by a forward migration of its location. The location of the peak suction is particularly important with AJVGs because they rely very strongly on favourable pressure gradients for their mass flow.

Between 3^o and 19^o, there is a progressive decrease in the lower mainplane surface pressures and in peak suction. This increase is accompanied by a reduction in the pressure gradient on the lower mainplane surface between 45% chord and the mainplane trailing edge at 60% chord. This suggests the onset of trailing edge separation on the mainplane but the velocity vectors about the wing as depicted in Figure 5.6 shows no evidence of this separation. Further increases in the angle of incidence cause further reductions in the pressure gradient which are localised between 45% and 60% chord. The extent of this adverse pressure gradient remains reasonably constant with increasing incidence.

Significant changes in the predicted peak suction C_p on the mainplane can be seen for the solution on the refined grids at 29^o degree angle of incidence case as presented in Figure 5.19. The refined grid solutions with the domain inlets 10 chords and 20 chords upstream show good agreement. This suggests that at this angle the coarse grid is not a grid independent solution. All solutions on the vane and the flap elements demonstrate good agreement.

5.2.3 Predicted 2D Trailing-Edge C_p versus Angle of Incidence

The predicted trailing edge C_p on the flap was used as an indication of flow separation on the high downforce system in the two-dimensional calculations. The trailing edge C_p on the mainplane and vane were examined to quantify the predicted *dumping* velocity of the boundary layers from these elements. The predicted trailing edge C_p are presented in Figure 5.21.

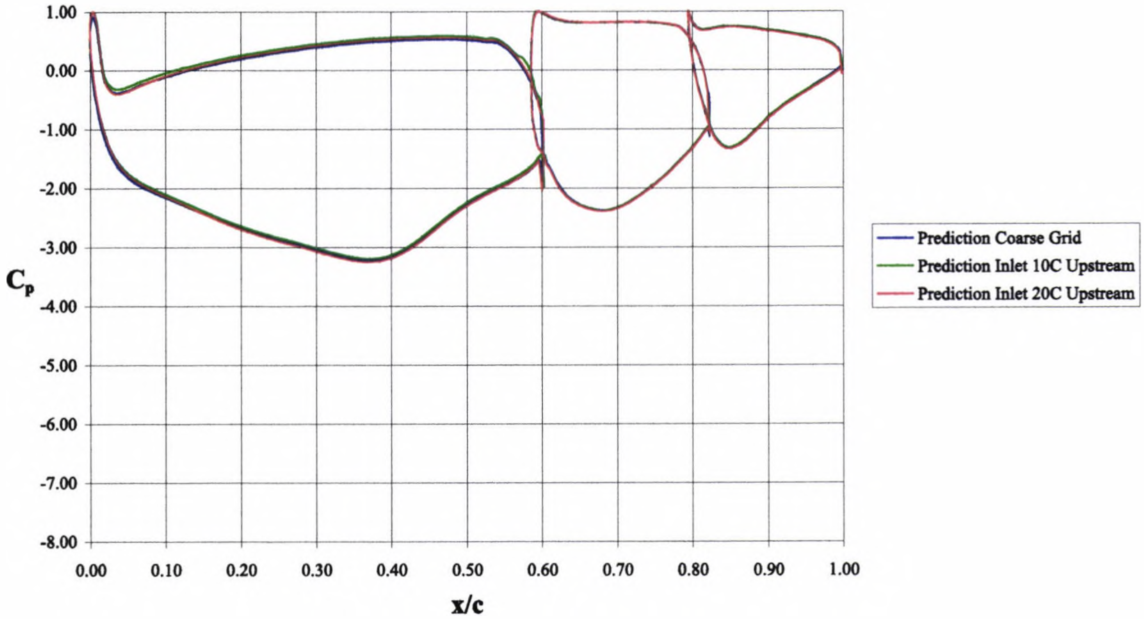

Figure 5.7: Predicted C_p about two-dimensional high downforce system, $\alpha = 3^o$.

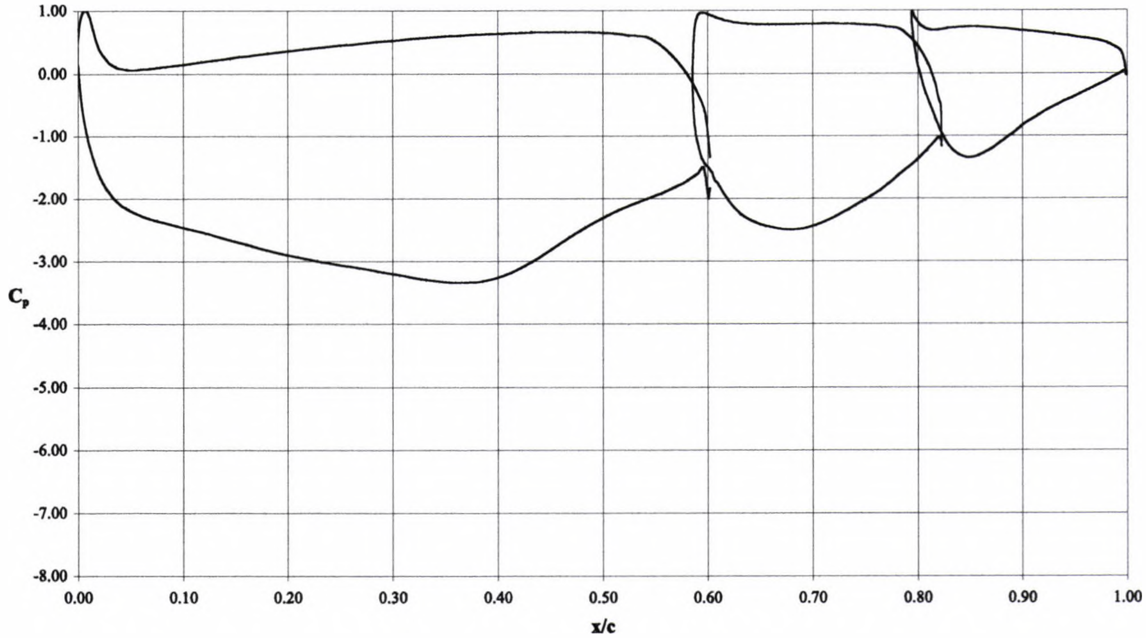

Figure 5.8: Predicted C_p about two-dimensional high downforce system, $\alpha = 5^o$.

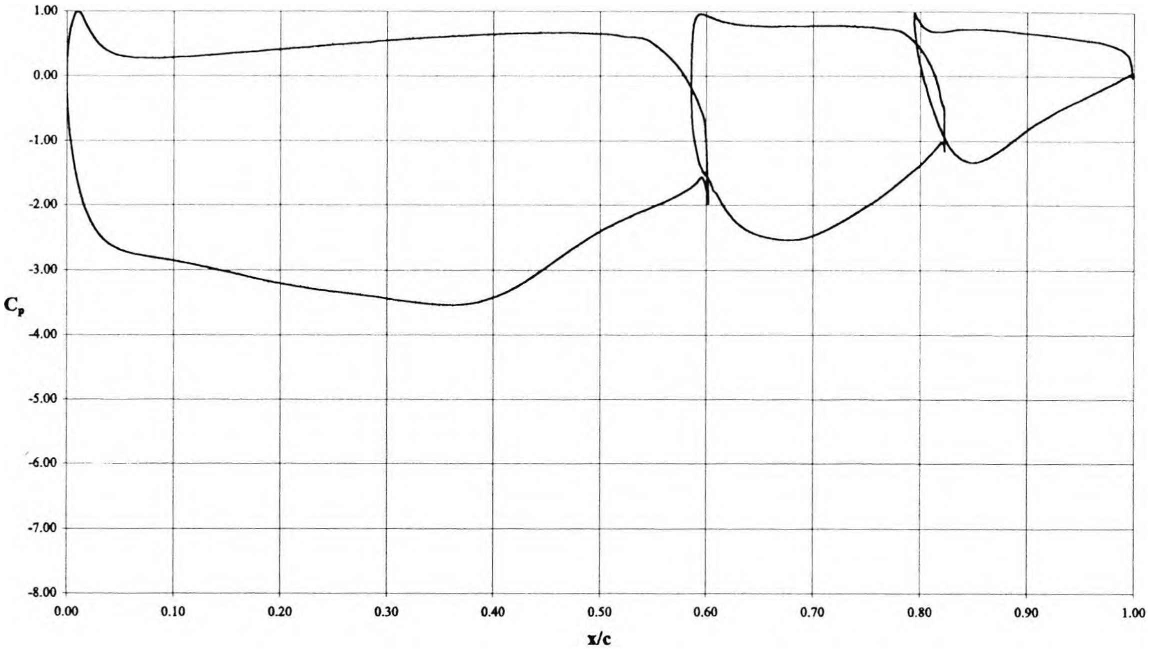

Figure 5.9: Predicted C_p about two-dimensional high downforce system, $\alpha = 7^o$.

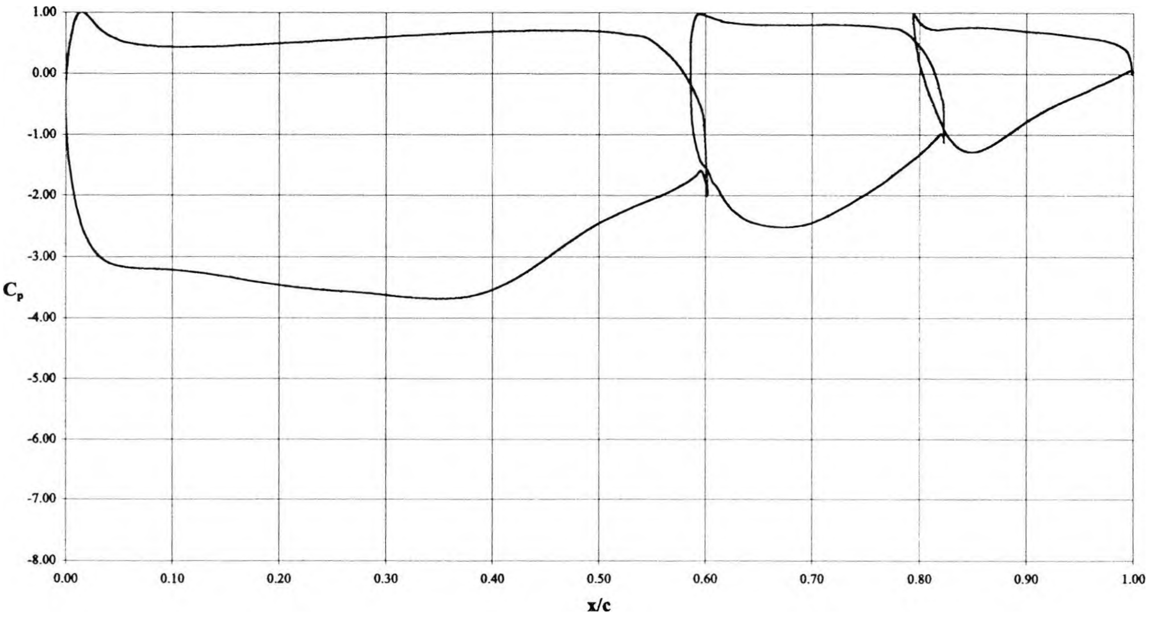

Figure 5.10: Predicted C_p about two-dimensional high downforce system, $\alpha = 9^o$.

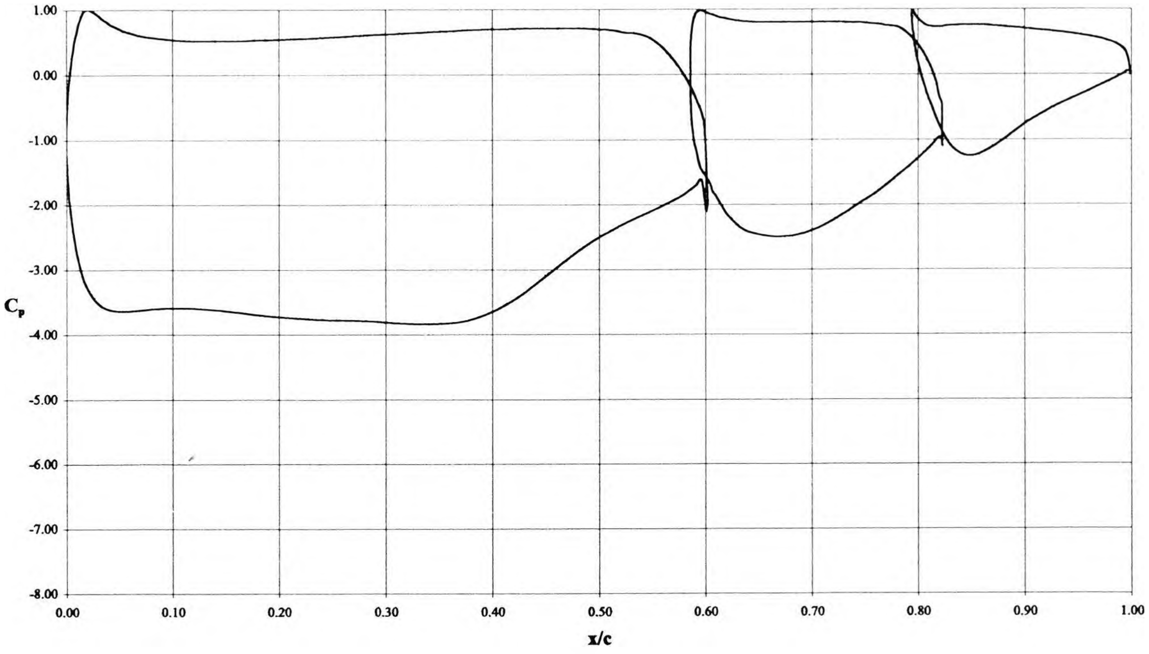

Figure 5.11: Predicted C_p about two-dimensional high downforce system, $\alpha = 11^o$.

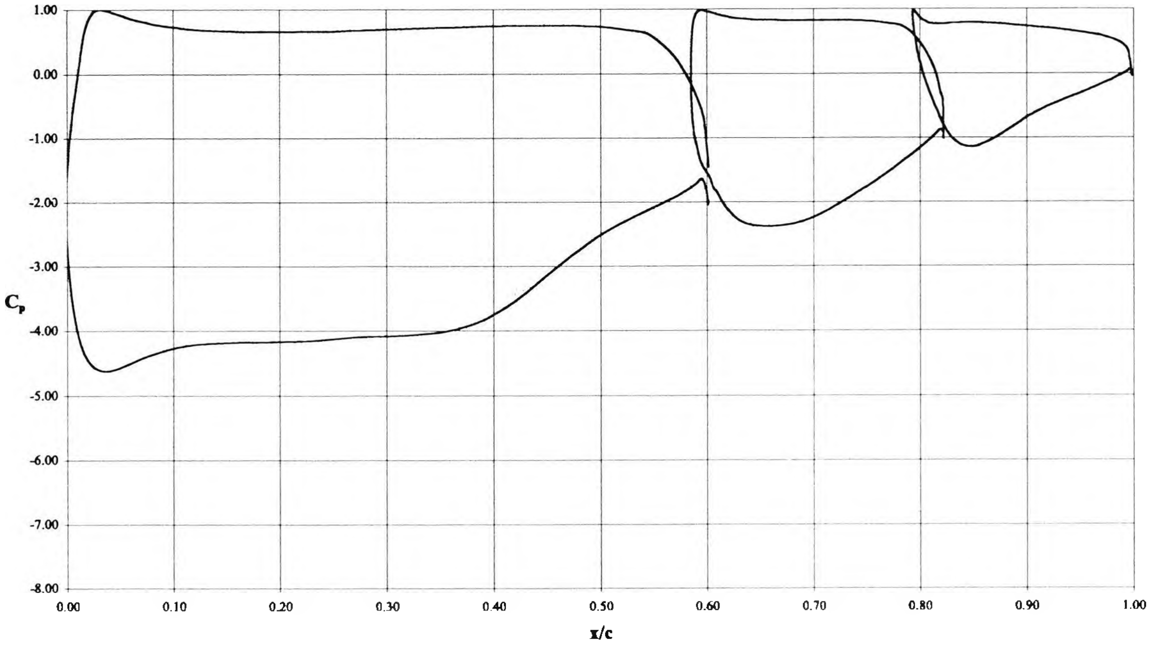

Figure 5.12: Predicted C_p about two-dimensional high downforce system, $\alpha = 15^o$.

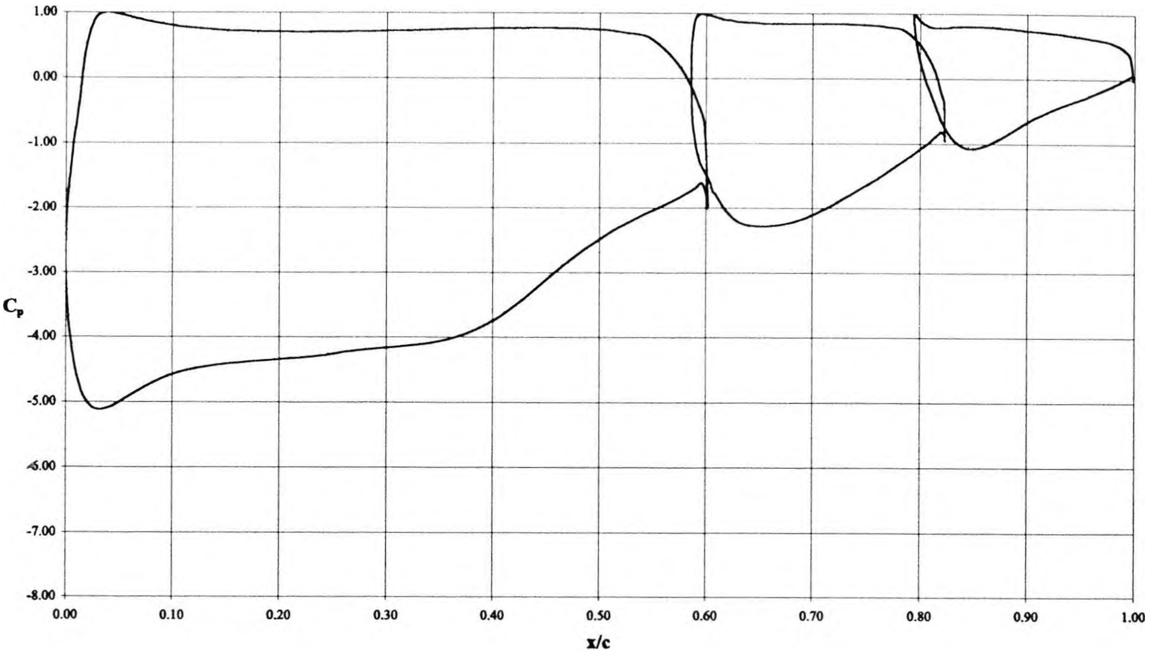

Figure 5.13: Predicted C_p about two-dimensional high downforce system, $\alpha = 17^o$.

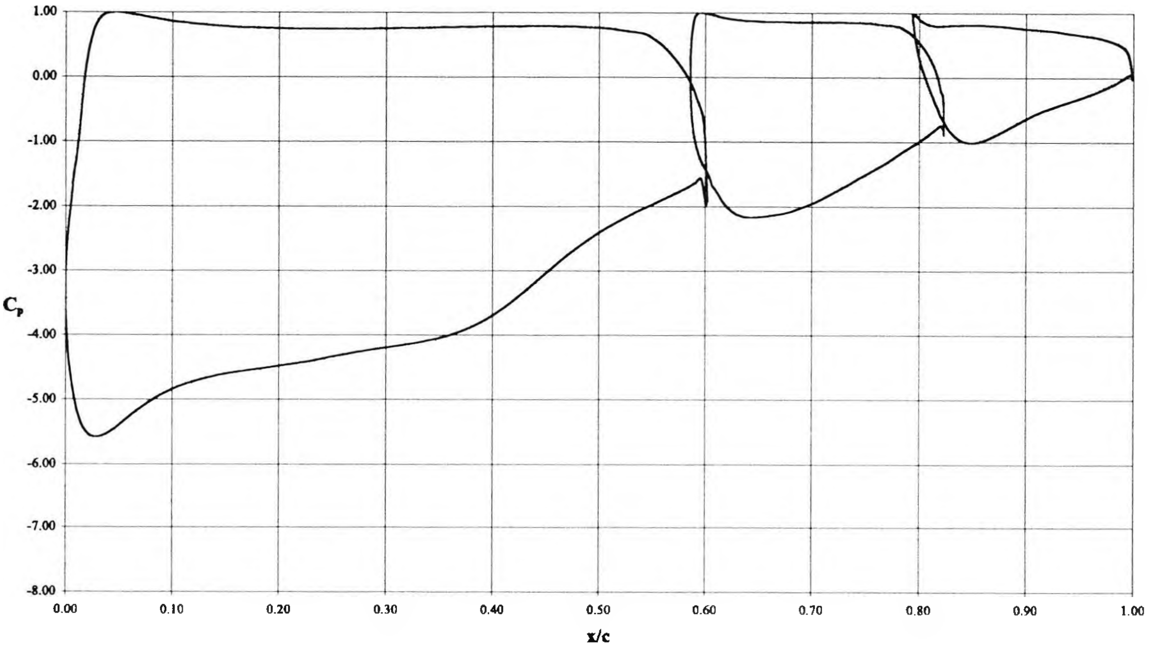

Figure 5.14: Predicted C_p about two-dimensional high downforce system, $\alpha = 19^o$.

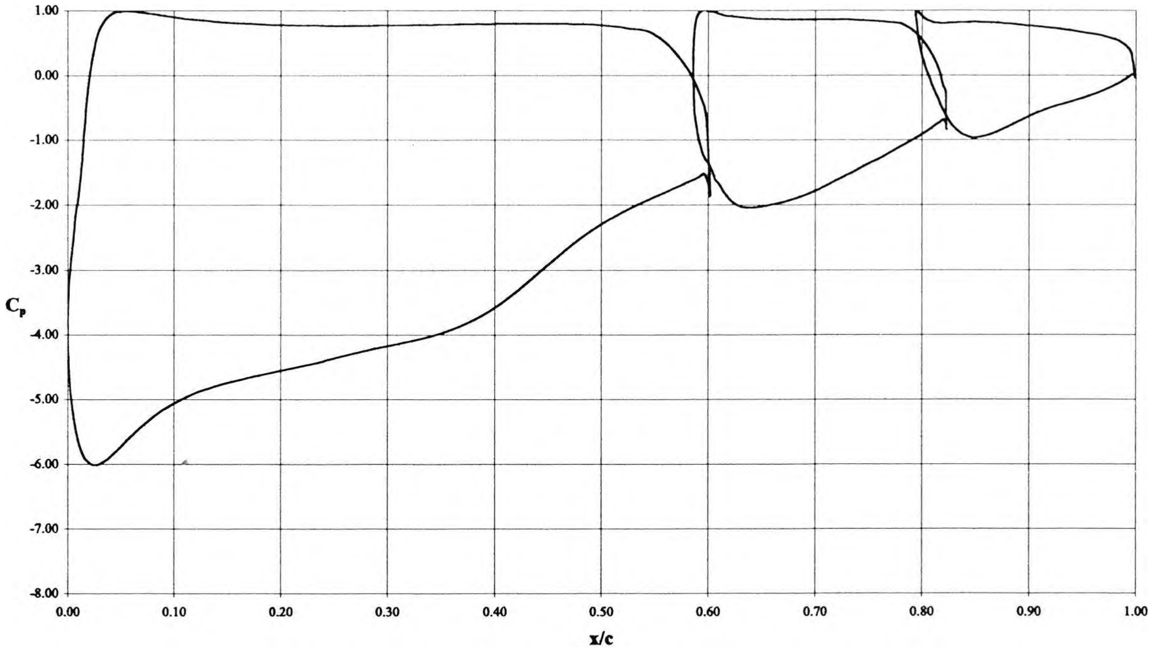

Figure 5.15: Predicted C_p about two-dimensional high downforce system, $\alpha = 21^o$.

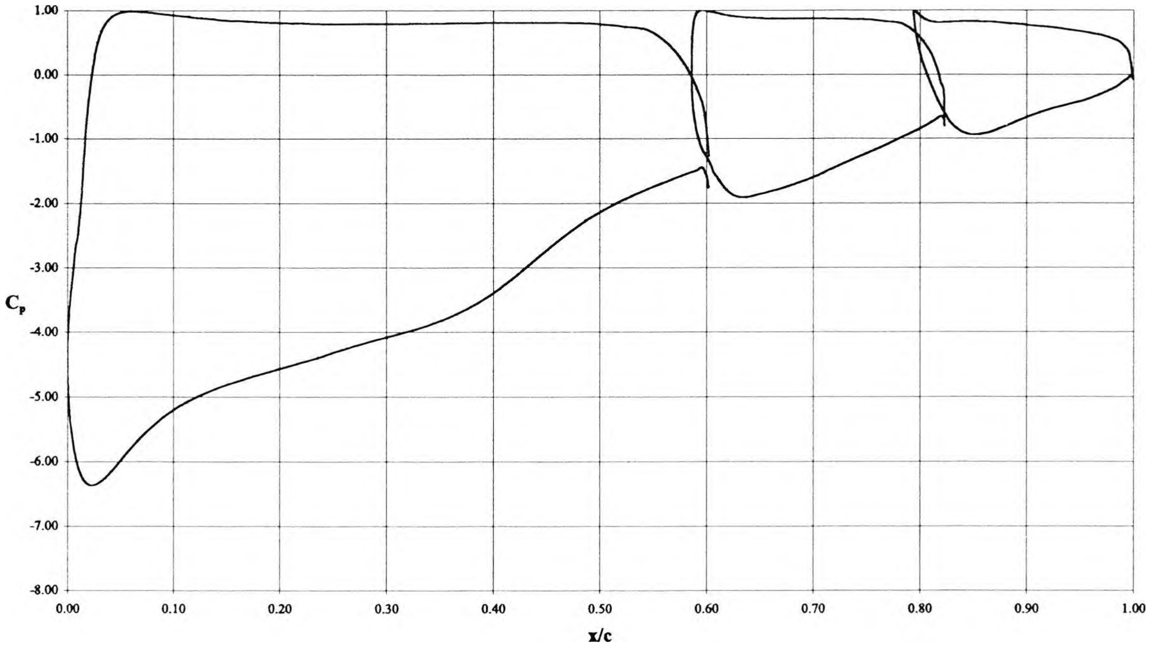

Figure 5.16: Predicted C_p about two-dimensional high downforce system, $\alpha = 23^o$.

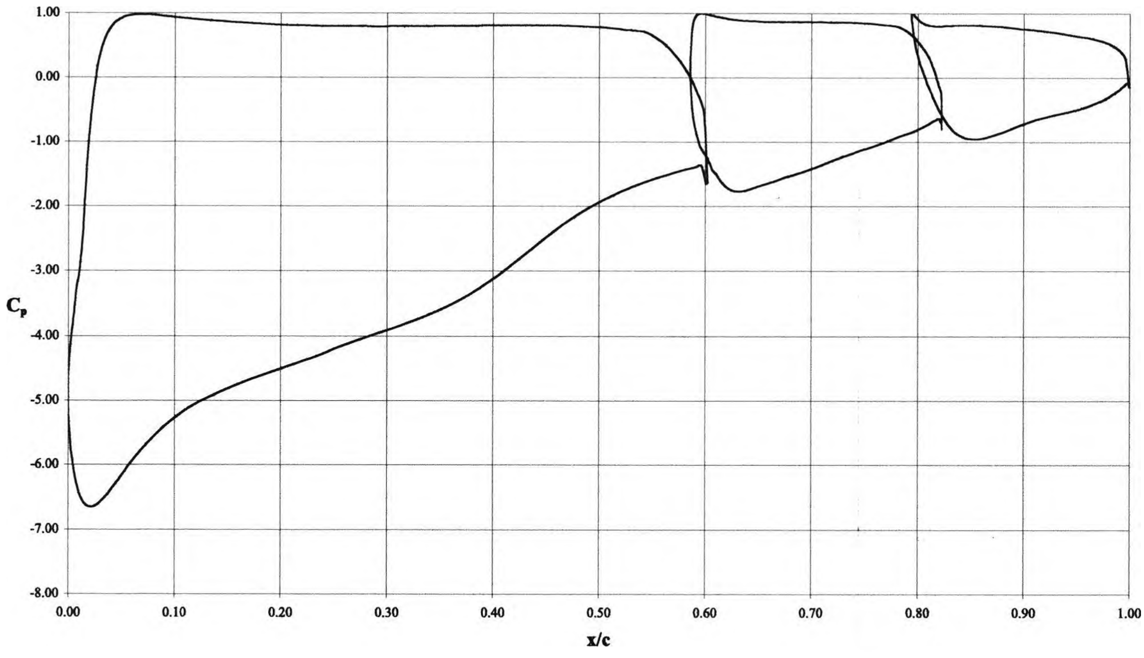

Figure 5.17: Predicted C_p about two-dimensional high downforce system, $\alpha = 25^o$.

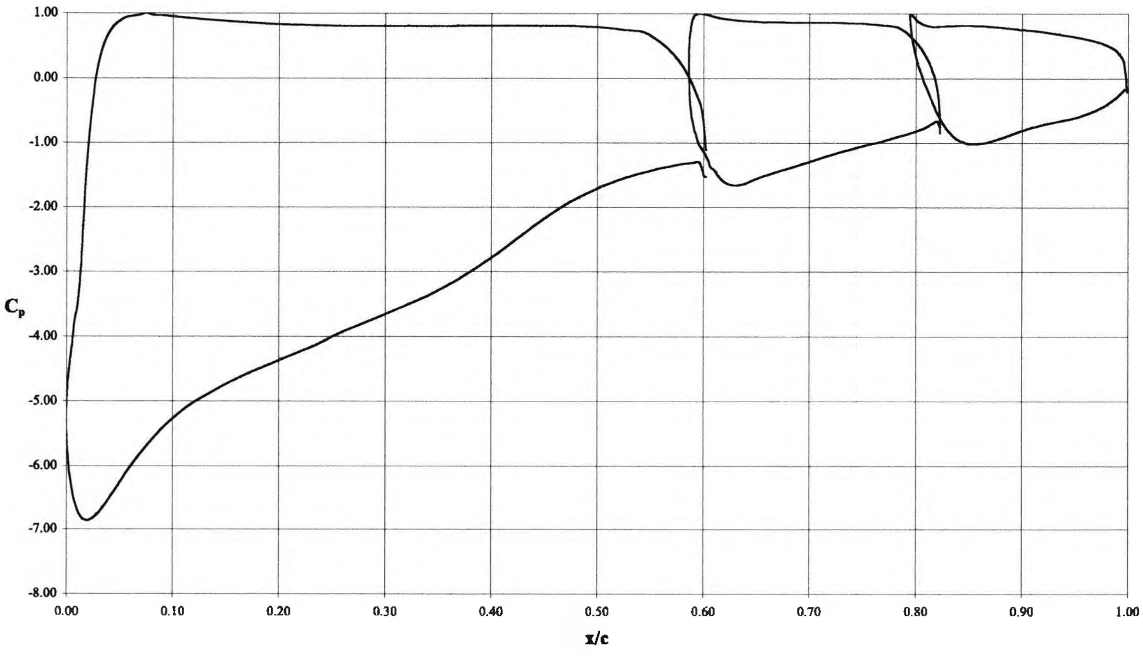

Figure 5.18: Predicted C_p about two-dimensional high downforce system, $\alpha = 27^o$.

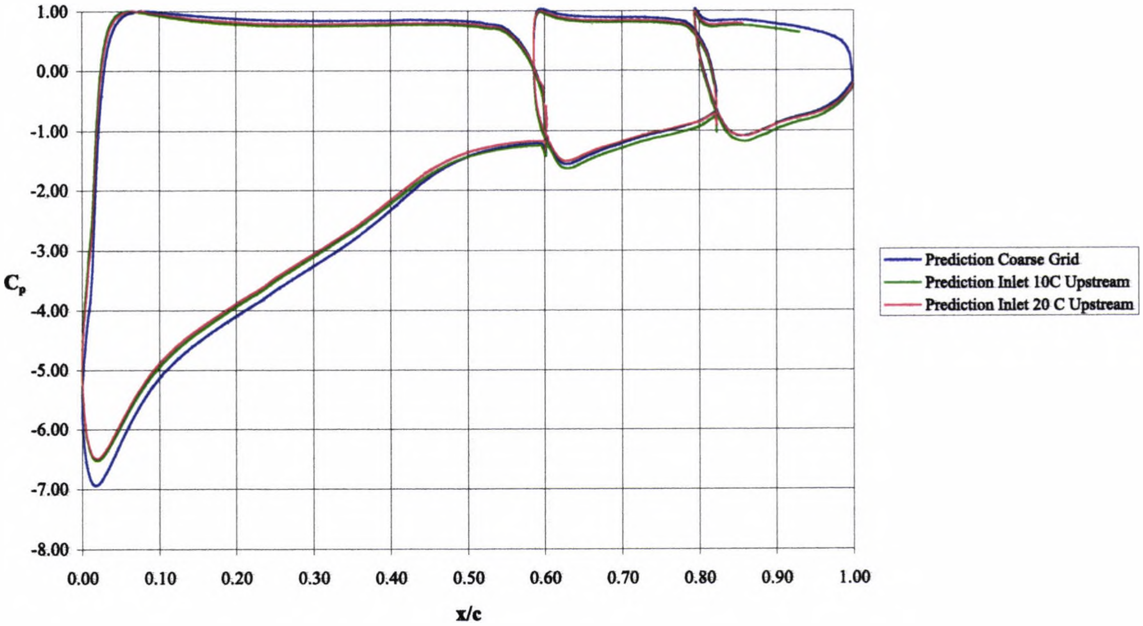

Figure 5.19: Predicted C_p about two-dimensional high downforce system, $\alpha = 29^o$.

The predicted trailing edge C_p on the mainplane are all negative showing clearly that the *dumping* velocity at the mainplane trailing edge is higher than freestream. The predictions also show that there is a decrease in the mainplane trailing edge C_p with increasing angle of incidence between 3^o and 13^o. Thereafter, a steady increase in the trailing edge C_p ensues until 29^o, signifying a progressive decrease in the velocity of the air flow in this region.

The C_p predicted at the vane trailing edge are all negative, but they are higher than those of the mainplane. This also demonstrates a qualitatively correct performance of the vane trailing edge C_p, namely that it also has a *dumping* velocity higher than freestream but not as high as that of the mainplane. Thus, the stage wise pressure recovery between the mainplane and the vane is captured in the prediction. The vane trailing edge pressures are predicted to increase gradually until 23^o whereupon there is a decreasing trend until 29^o.

The predicted behaviour of the flap trailing edge C_p is arguably the most important feature of this discussion. Between 5^o and 19^o, the flap trailing edge C_p are predicted to be positive, indicating that there is no flow separation on any of the elements in the model. The C_p become negative at 21^o where a C_p of -0.001 is predicted. The next significant C_p prediction that indicates flow separation on the model is -0.039 at 23^o. The flap trailing edge pressure becomes more negative with increasing angle of incidence up to α_{max} of 29^o.

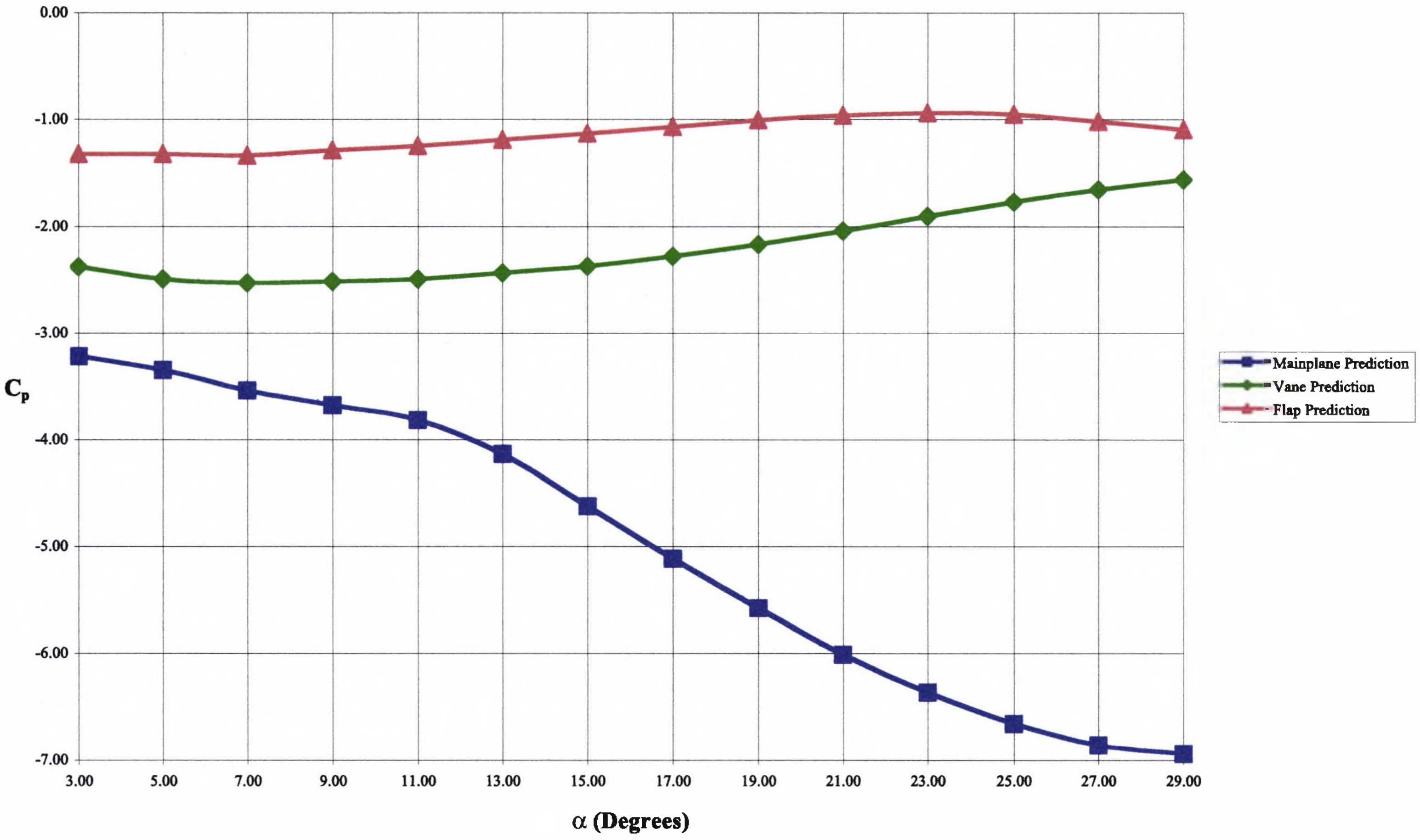

Figure 5.20: Predicted peak suction C_p versus α for each element.

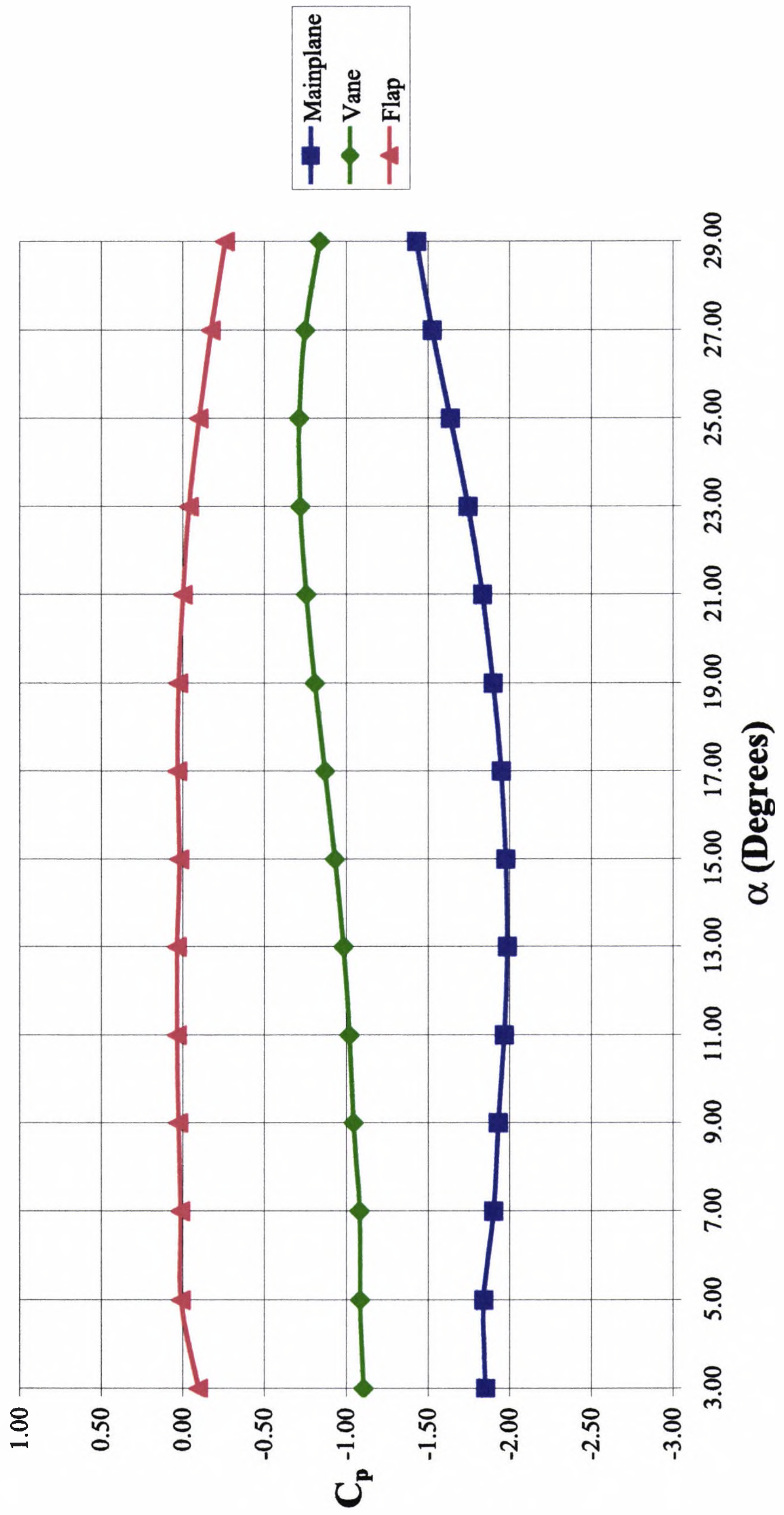

Figure 5.21: Predicted trailing edge C_p versus α for each element.

5.2.4 Predicted Normal Force versus Angle of Incidence

The normal forces are derived from a numerical integration of the predicted pressure distributions about the aerofoils in the two-dimensional model. The results are presented in Figure 5.22.

At 3^o, the predicted mainplane C_n is -2.55. The predicted C_n then increases in a relatively linear manner to reach a $C_{n\,max}$ of -4.85 at 23^o. Any further increases in the angle of incidence bring about a reduction in the mainplane C_n. The C_n predicted on this element at 29^o incidence is -4.496. Thus the Navier-Stokes solution predicts a gradual reduction in the mainplane C_n above 23^o incidence.

At 3^o, a C_n of -2.629 is predicted on the vane. Increases in the angle of incidence bring about small increases in the C_n so that the vane sees a $C_{n\,max}$ of -2.706 at 9^o. Thereafter, a progressive unloading of this element ensues until 29^o finally reaching a C_n of -1.963. The C_n on the vane shows that its role in the high downforce model is to benefit the flow on the flap through the effect of the slot. An examination of the flap C_n gives a better understanding of the relationship between these two elements.

The predicted C_n on the flap is -1.295 at 3^o and it remains relatively constant until 17^o. The loading on this element then begins to increase steadily until α_{max} of 29^o where a C_n of -1.465 is predicted.

An examination of the predicted loads on the elements in Figure 5.22 and the predicted trailing edge C_p in Figure 5.21 show a distinct correlation between these two parameters. On the mainplane and vane, the C_n decreases as the trailing edge C_p begins to increase. On the flap, an increase in the C_n with angle of incidence is coincident with an decrease in trailing edge C_p or an increase in the boundary layer *dumping* velocity. Figure 5.22 shows that the predicted behaviour of the assembly is largely dictated by the mainplane forces as the changes in the two curves over the angle of incidence range are closely related.

5.2.5 Predicted Axial Force versus Angle of Incidence

The predicted axial forces are presented in Figure 5.23. The predicted mainplane C_x at the lower angles of incidence is consistent with a thrust on this element. At 3^o, the predicted C_x is -0.373. The predicted results show a small thrust on the mainplane between 3^o up to approximately the middle 13^o angle of incidence. The C_x is also predicted to increase continually from 3^o up to 29^o. At 29^o, the C_x is predicted to be 1.032.

The prediction of the vane C_x shows that the axial load on this element is very insensitive to the angle of incidence. There is small increase in the axial load on this element

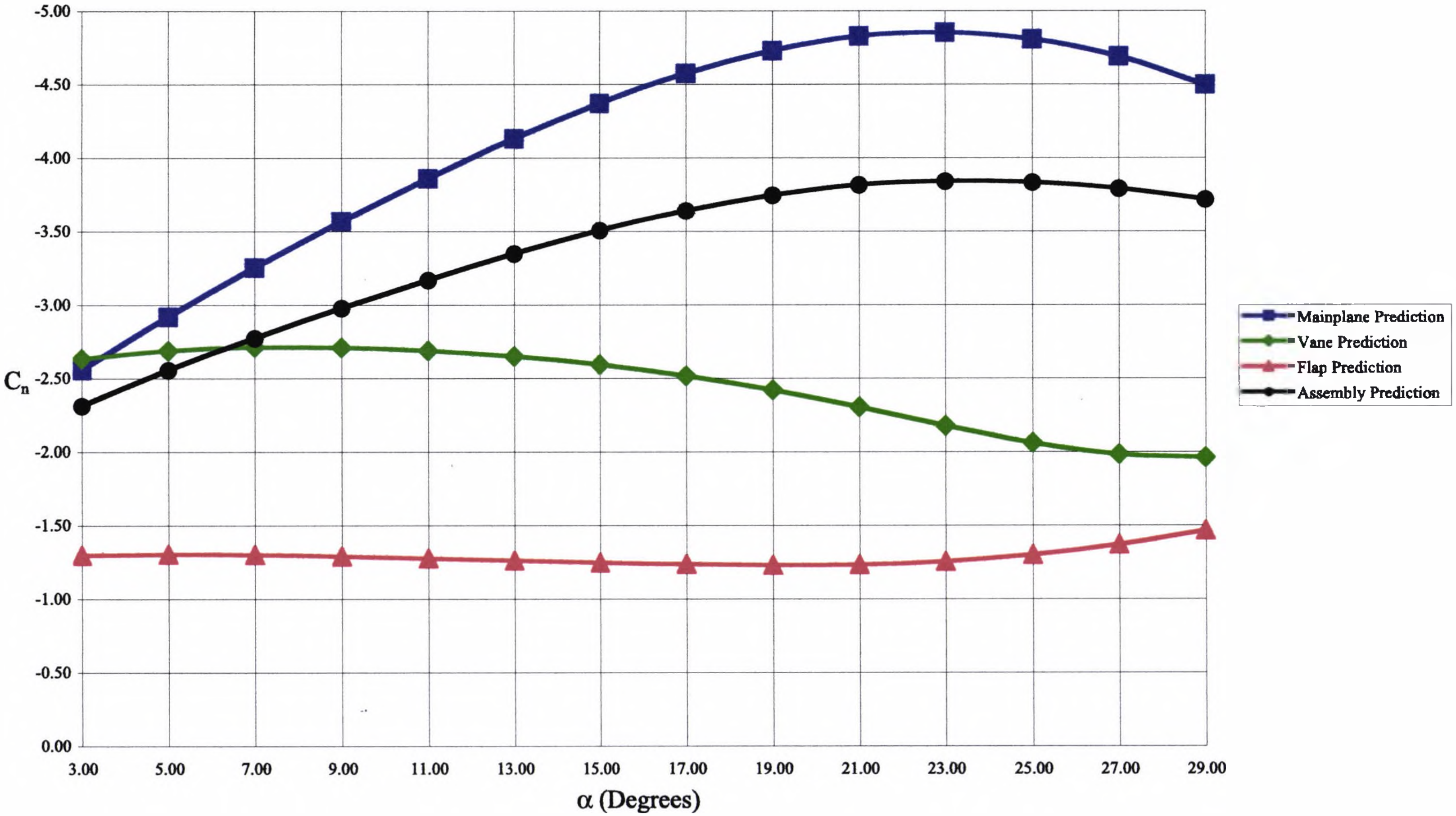

Figure 5.22: Predicted C_n versus α for two-dimensional high downforce system.

between 3^o and 29^o. At 29^o, the C_x is 0.028.

At 3^o, the flap is predicted to have a C_x of -0.005. The predicted flap C_x achieves a maximum of -0.013 at 17^o. At 29^o, the flap C_x prediction is -0.064. Therefore the predicted results show that the flap experiences a thrust over the entire angle of incidence envelope.

The predicted assembly C_x is very much determined by the mainplane C_x as can be seen in Figure 5.23. The assembly experiences an increasing but negative C_x between 3^o and 11^o. Thereafter all predicted C_x are positive and increasing until 29^o, the maximum angle of incidence.

5.2.6 Predicted Downforce versus Angle of Incidence for 2D System

The predicted c_l versus α curve as presented in Figure 5.24 exhibits typical lift curve slope characteristics. There is a linear slope at the lower angles of incidence, a $c_{l\,max}$ and thereafter a reduction in c_l with increasing incidence. According to the pressure distributions presented, no stall as such is predicted and so the predicted curve does not demonstrate a the sudden loss of downforce.

At 3^o, the predicted c_l is -2.50. The predicted c_l curve achieves $c_{l\,max}$ at 21^o with a value of -3.78. At the last and highest angle of incidence, 29^o, there is a predicted c_l of -3.50.

5.2.7 Predicted Drag versus Angle of Incidence for 2D System

The predicted drag of the high downforce models as presented in Figure 5.25 shows that the c_d increases with increasing α. The gradient of the c_d versus α curve is seen to increase between 19^o and 29^o. This can be explained by a review of the pressure distributions shown in 5.7 and 5.19. These figures show that between 19^o and 29^o, there is an increasing adverse pressure gradient on the lower surface of the mainplane.

5.2.8 Predicted Downforce to Drag Ratios for 2D System

The lift to drag ratio is a parameter that plays what is arguably the most important role in deciding the aerodynamic set-up of a Formula One car. The two notable exceptions are the set-ups for the Hungaroring and Monaco racing circuits. These are tracks where an extremely high downforce configuration is the goal even at the expense of aerodynamic efficiency.

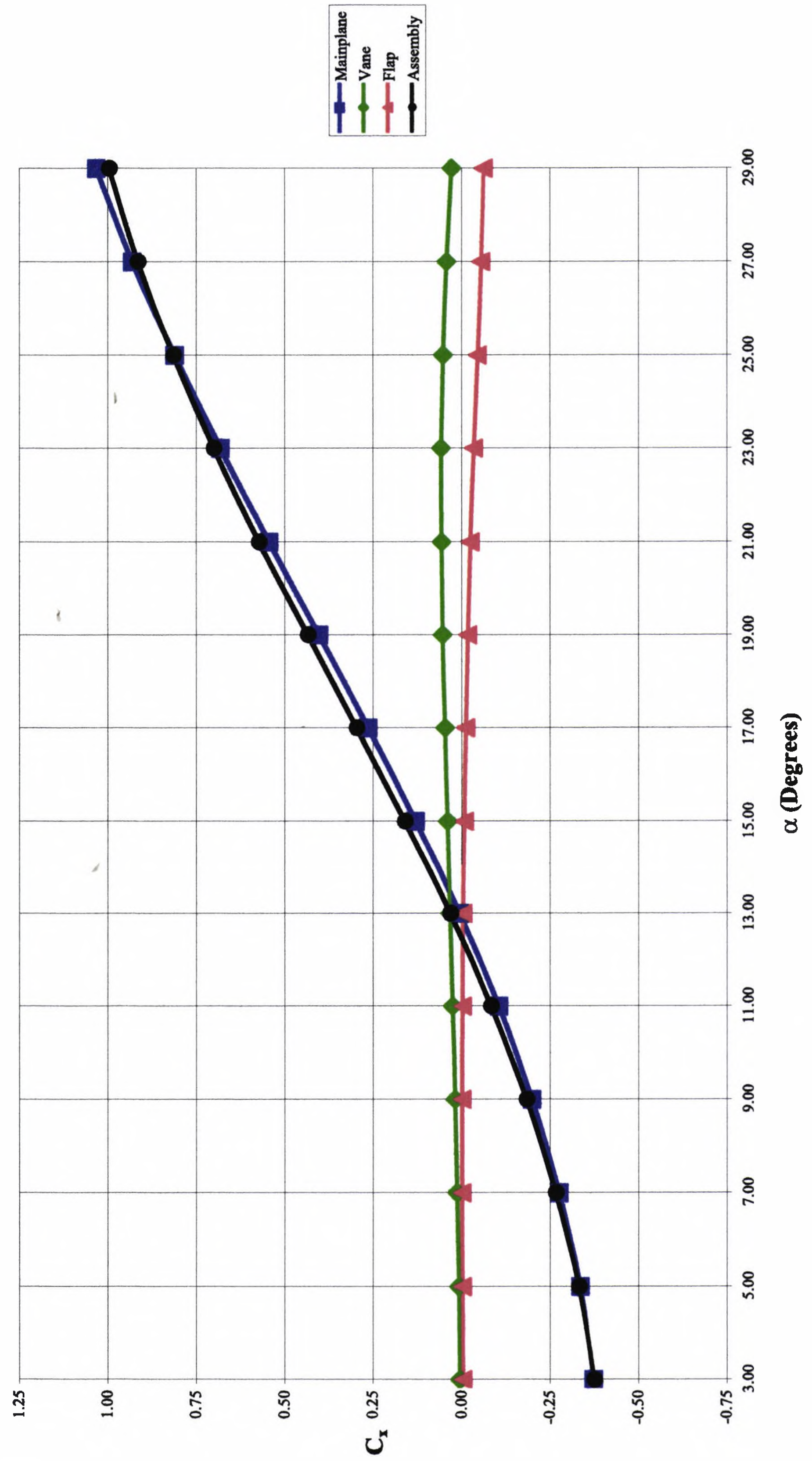

Figure 5.23: Predicted C_x versus α for two-dimensional high downforce system.

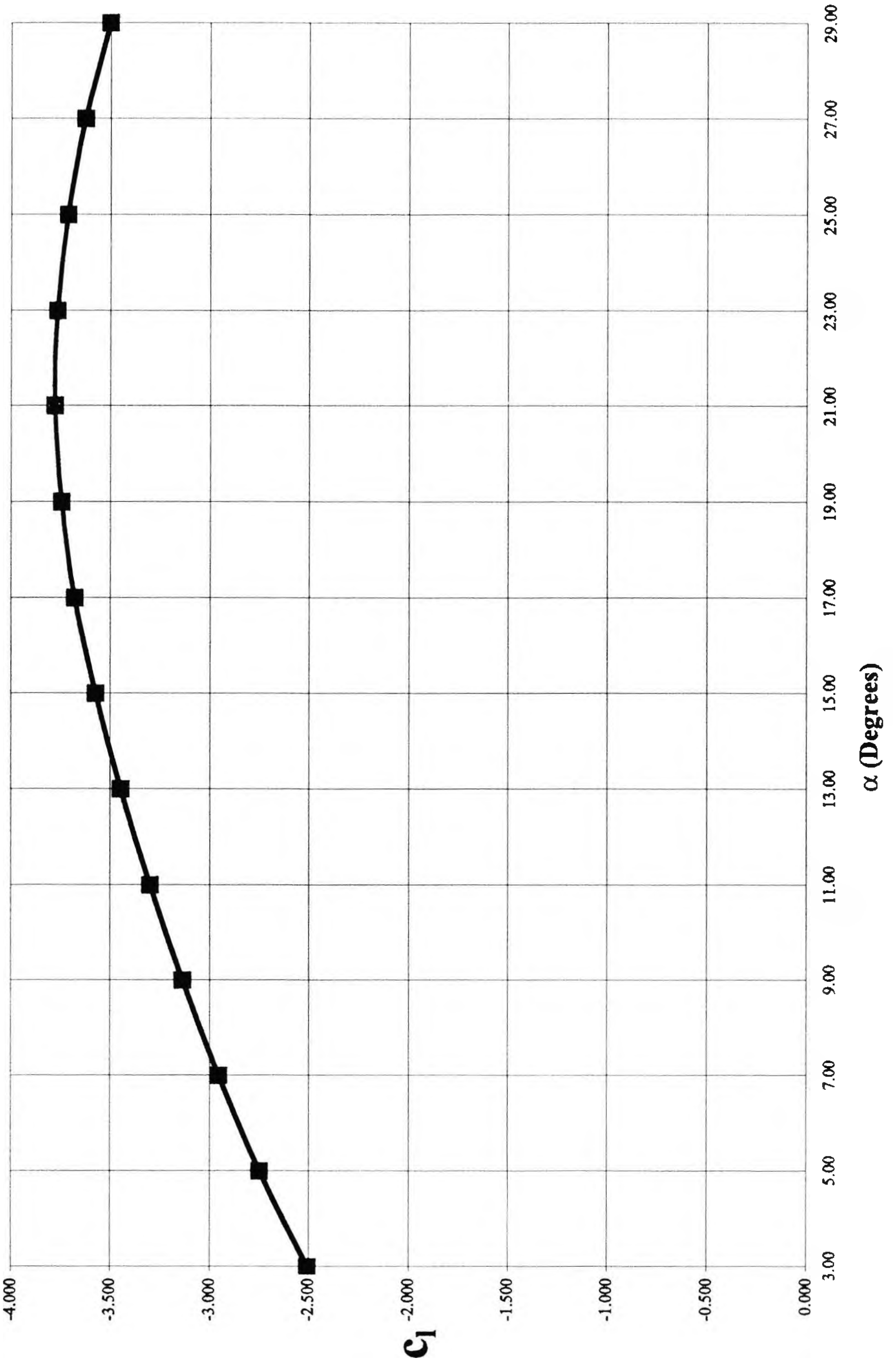

Figure 5.24: Predicted c_l versus α for two-dimensional high downforce system.

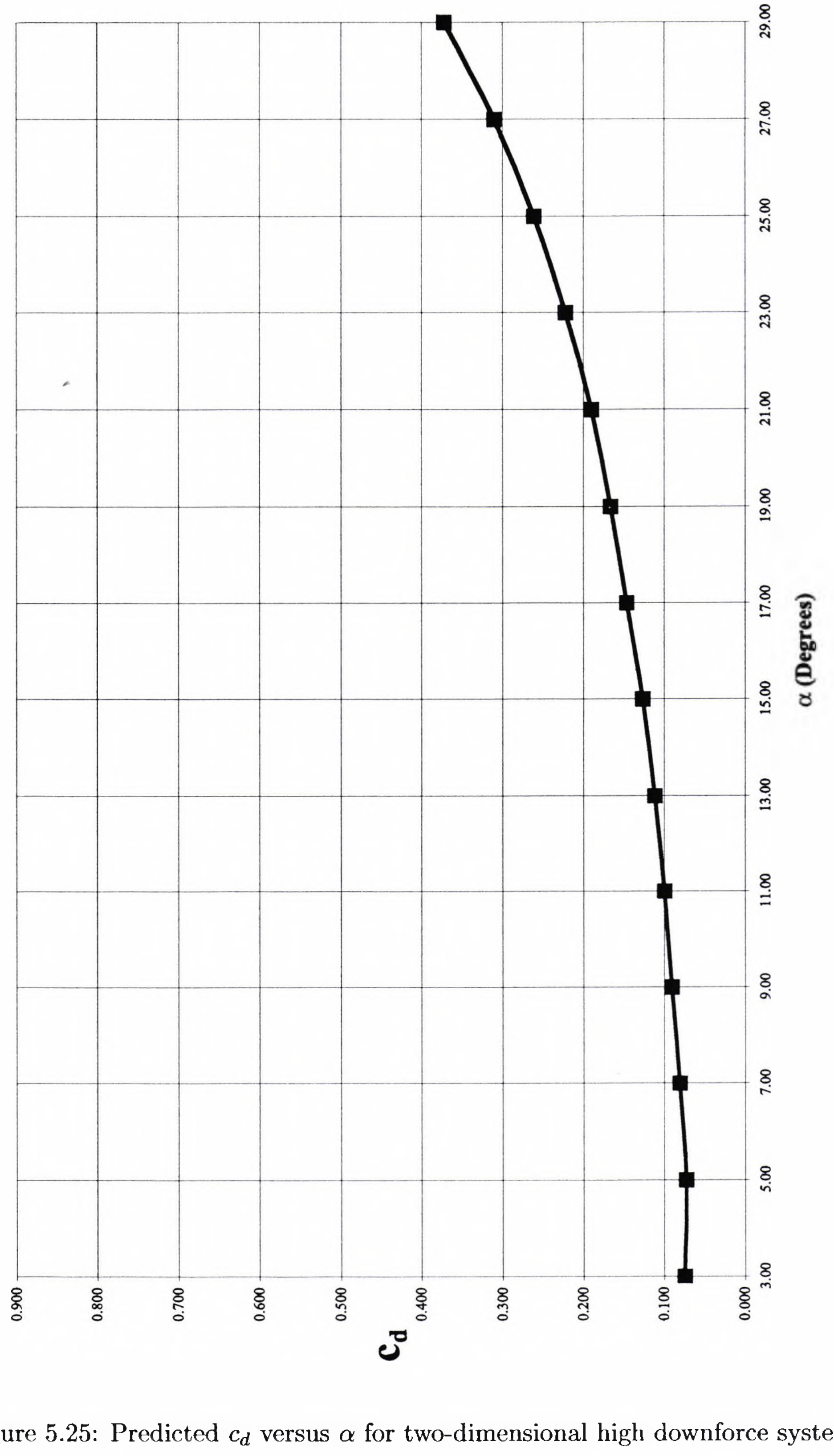

Figure 5.25: Predicted c_d versus α for two-dimensional high downforce system.

The highest aerodynamic efficiency is predicted at the lowest angles of incidence. The model is predicted to achieve an $\frac{l}{d}_{max}$ of 38.14 at 5^o. Figure 5.26 shows that the $\frac{l}{d}$ is predicted to decrease after 5^o incidence. The predicted $\frac{l}{d}$ decreases in what is effectively a linear manner up to 29^o.

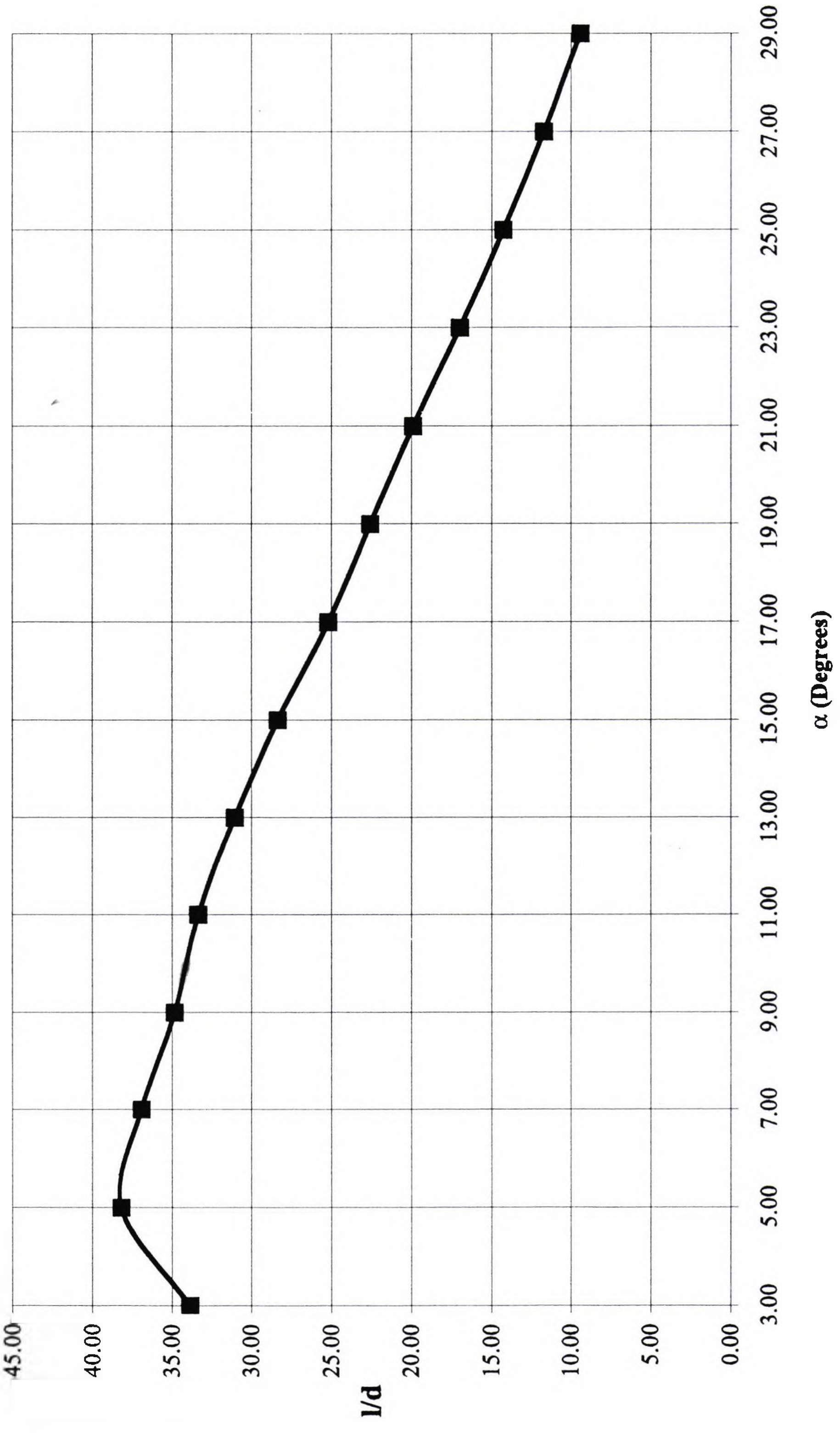

Figure 5.26: Predicted $\frac{l}{d}$ versus α for two-dimensional high downforce system.

5.3 Three-Dimensional Predictions

The first model discussed is the 810 mm span model that represents the experimental model positioned in the City University T2 Wind Tunnel test section at 29^o angle of incidence. Some smaller, 240 mm span, wall bounded, models with and without AJVGs are also discussed. These models are 240 mm span because it resulted in numerical models that were manageable given the computational resources available. These 240 mm span models were also oriented at 29^o angle of incidence.

Only the clean wing, 810 mm span, numerical model has an analogous experimental model. The other models have no experimental parallel and as such they are discussed solely in terms of the effects the various AJVG blowing pressures on the wing performance. The results are discussed globally using the shear stress contours and surface-limited velocity vectors. The surface-limited velocity vectors are presented to illustrate the nature of the flow field near the clean wings and the various models incorporating AJVGs. The investigations by Henry & Pearcey (1994) showed that the flow fields about even simple AJVG models on a flat plate can be very complex. In the cases where air jets are modelled, additional flow visualisation is provided in the form of transverse velocity vectors. These transverse plots are used to show the creation and development of the air jet vortices about the high downforce system.

Detailed data presented include the predicted spanwise distributions of wall shear stress coefficients at several chordwise positions. The pressure distributions are presented for all the AJVG models and compared to the pressure distribution about the 240 mm span clean wing in discussing the effect of the AJVGs on the details of the flow features. The chordwise pressure distributions about these models are presented at the 8%, 42% and 92% span and along the trailing edges of the three elements in all the models.

5.4 810 mm Span Clean Wing

5.4.1 Predicted Surface Flow Visualisation on 810 mm Span Clean Wing

Flow separation is only predicted on the mainplane of the high downforce wing in the region near the junction of the virtual wind tunnel walls and the model. Figure 5.27 shows the surface-limited velocity vectors 1.0×10^{-3} mm from the surfaces of the model of the clean high downforce system. Figure 5.28 shows the C_f contours on this same model. On the mainplane, there is a reasonably strong flow aligned with its surface except for the regions near the tunnel walls (not shown) where the vectors possess strong cross-span components and reversal relative to the freestream.

The relative size of the vectors in the area of the slots shows that the flows through the slots and over the vane and flap have higher kinetic energy than the flow over the mainplane in the areas of flow separation. Figures 5.27 and 5.28 show no flow separation in evidence on the vane and flap elements.

5.4.2 Predicted C_p Distributions about Clean 810 mm Span Wing

Figure 5.29 shows the predicted pressure distribution about the 810 mm span high downforce model. These predicted pressures were derived from calculations using the coarse and refined grids of 1,336,468 and 2,718,674 cells respectively. The pressures were examined at the wing surfaces in the plane located 103 mm from the model centreline or 302 mm from the lower wall. This location corresponds to the location of the plane of the static pressure orifices on the experimental model.

Figure 5.29 shows that there is good quantitative and qualitative agreement of the pressure distributions derived from the coarse and refined grid three-dimensional solutions about all the elements of the high downforce system. A comparison of the predicted C_p for the three-dimensional solution in Figure 5.29 with the two-dimensional shown in Figure 5.19 show significant differences in the predicted pressures. The predicted C_p for the three-dimensional cases are generally lower than those of the two-dimensional predictions. The exception to this trend is the predicted peak suction C_p on the mainplane.

These differences can be explained by the fact that the two-dimensional high downforce wing is an infinite span model with no possibility of the three-dimensional flow features that are detrimental to the creation of downforce. Figure 5.27 shows that flow separation is predicted at the extremities of the model on the mainplane element. These regions of flow separation have an influence on the inner regions of the model and the plane 103 mm from the centreline of the model lies close to one of the affected regions.

5.4.3 Predicted Lateral C_f about 810 mm Span Clean Wing

Predicted transverse shear stress distributions are examined at nine chordwise locations on the model. On the mainplane, these are 25, 27.5, 30, 35, 40, 50 and 60% chord, the last being just before the mainplane trailing edge. One chordwise position each is examined on the vane and the flap. These are the 70 and 90% respectively.

The x-component of velocity, u, is the dominant component of the resultant velocity. Thus for all the flows taken, when $u < 0$, the flow is reversed. The exception to this rule

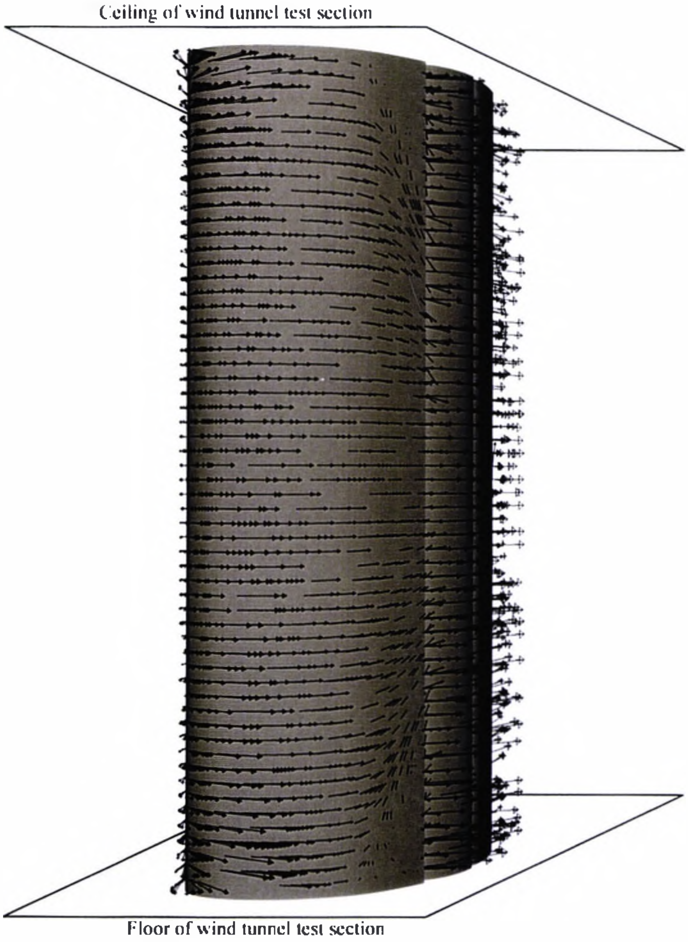

Figure 5.27: Limiting velocity vectors over 810 mm span clean model, $\alpha = 29^o$.

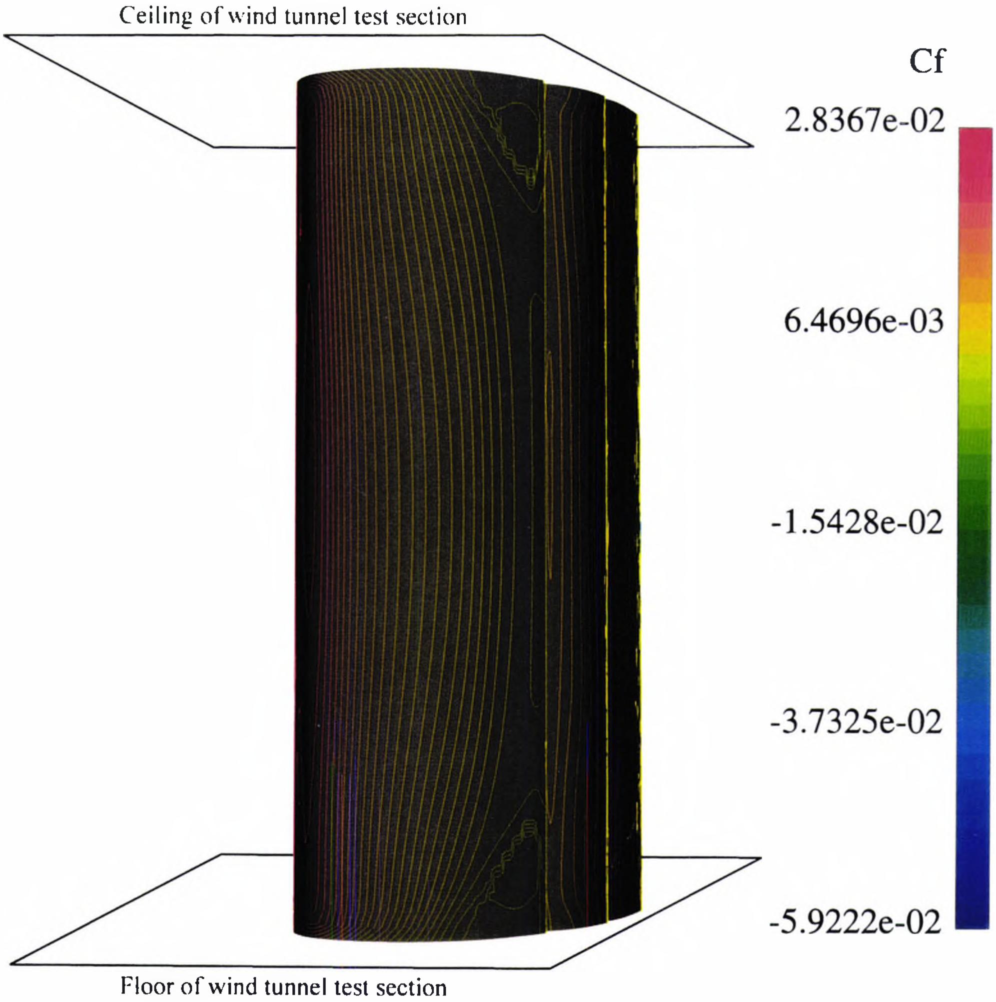

Figure 5.28: C_f contours over 810 mm span clean model, $\alpha = 29^o$.

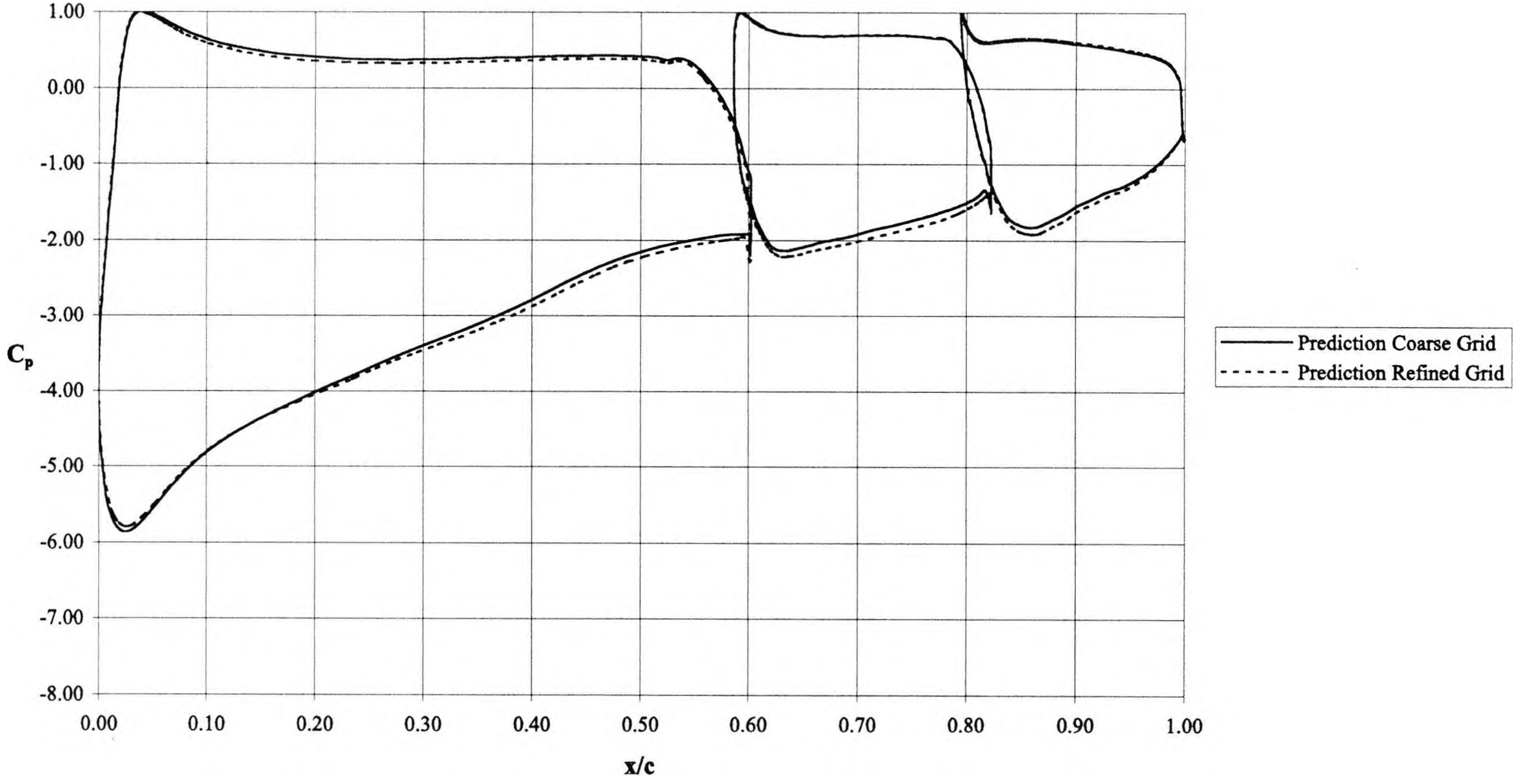

Figure 5.29: Predicted C_p about 810 mm span, clean wing, $\alpha = 29^o$.

is the flows near the leading edge of the elements. At some angles of incidence, these flows travel in the negative x-direction as they accelerate towards the lower surface of the mainplane. The author sought to include the direction of the flow field in the definition of the coefficient of shear stress, C_f seen in Equation 5.1.

$$C_f = \frac{\sqrt{(\tau_x^2 + \tau_y^2 + \tau_z^2)}}{\frac{1}{2}\rho V_\infty^2} \frac{-\tau_x}{|\tau_x|} \tag{5.1}$$

The term $\left(\frac{-\tau_x}{|\tau_x|}\right)$ in Equation 5.1 takes into account that CFX 4.2 reports the shear stresses that the wall imparts to the adjacent fluid cell and not those imparted to the wall by the fluid. The author uses the latter interpretation of the shear stress. This second term is also used to include the direction in the calculation of C_f. The predicted shear stress distributions on the mainplane are presented in Figure 5.30 through Figure 5.36. The distributions show that the shear stress on the mainplane decreases as the flow field progresses downstream. Flow separation is predicted to occur downstream of 35% chord and is present on the mainplane by 40% chord as is seen in Figure 5.34.

The areas of flow separation are limited to extremities of the mainplane span but a review of the shear stress at the 50% chord position shows that the size of the separated region increases significantly to cover approximately 20% of the mainplane span. The shear stress distributions also show a reduction below those of the values predicted upstream at the same spanwise locations.

Figure 5.36 shows that the flow is predicted to be attached again at the near trailing edge region of the mainplane. This is most likely due to the influence of the higher kinetic energy slot flow entraining the otherwise energy deficient flow field on the lower surface of the mainplane. However the predicted shear stresses on the outer 5% of the span are noticeably lower than the mid-span values. These lower values in this area are a vestige of the flow separation upstream.

The vane and flap shear stress distributions show no sign of separation with all the values being greater than zero. These distributions are shown in Figure 5.37 and Figure 5.38 for 70% and 90% chord respectively. The flow depicted in Figures 5.27 and 5.28 are consistent with the shear stress plots given in Figures 5.30 through Figure 5.38.

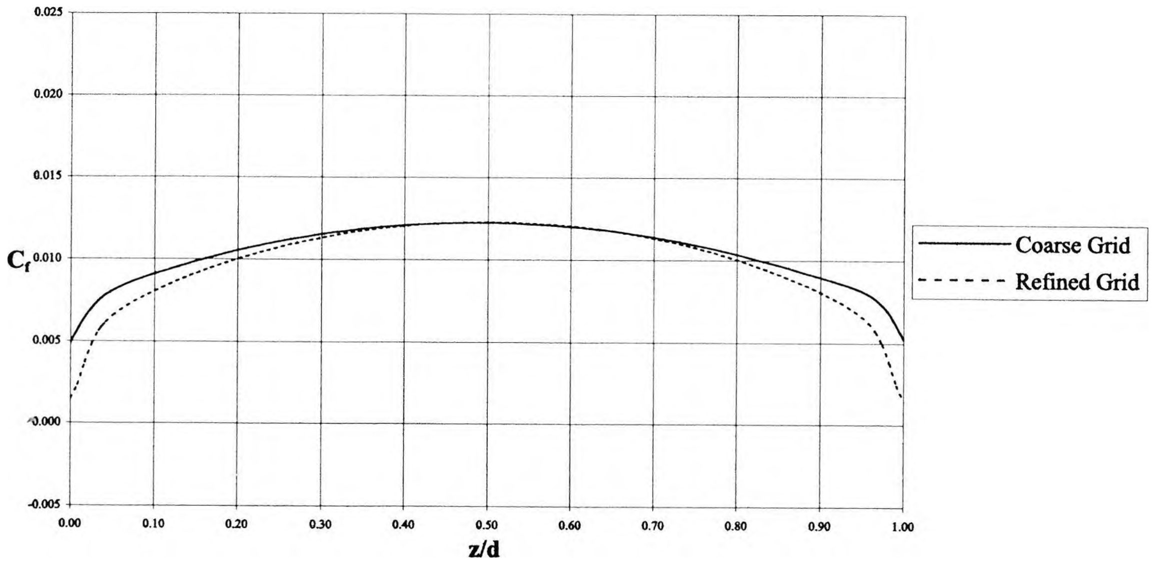

Figure 5.30: Predicted C_f at 25% chord on clean, 810 mm span models, $\alpha = 29^o$.

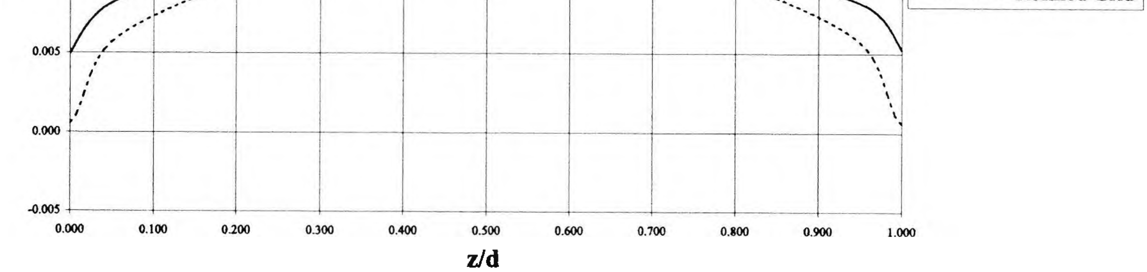

Figure 5.31: Predicted C_f at 27.5% chord on clean, 810 mm span models, $\alpha = 29^o$.

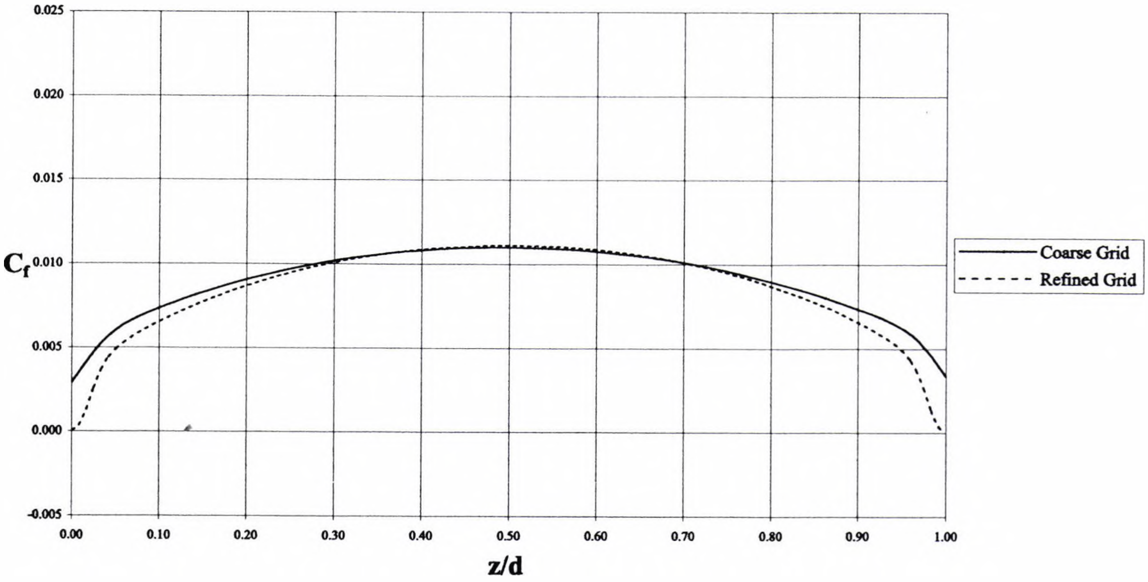

Figure 5.32: Predicted C_f at 30% chord on clean, 810 mm span models, $\alpha = 29^o$.

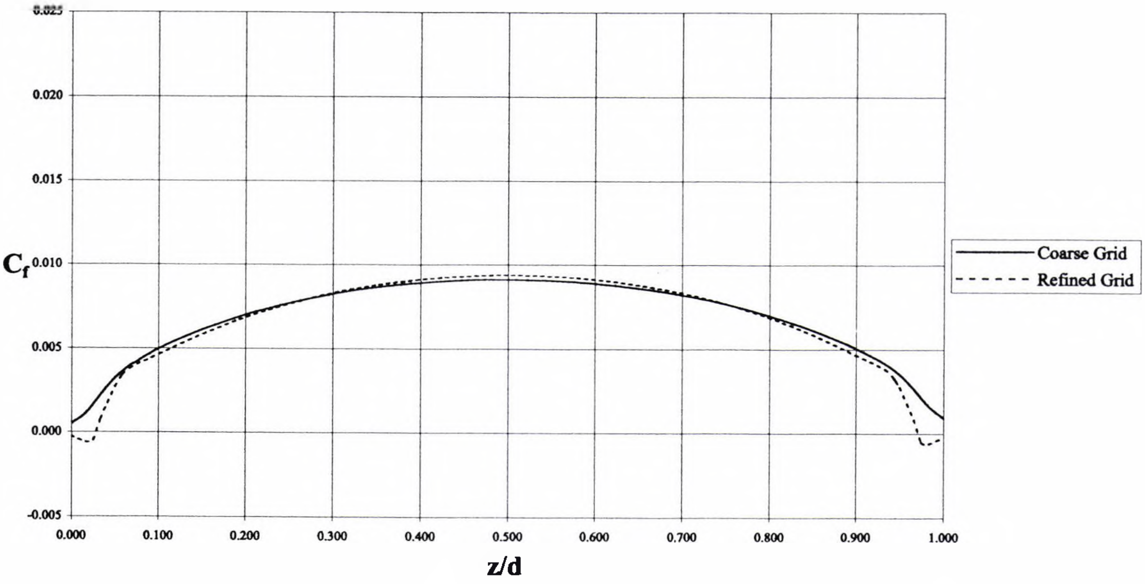

Figure 5.33: Predicted C_f at 35% chord on clean, 810 mm span models, $\alpha = 29^o$.

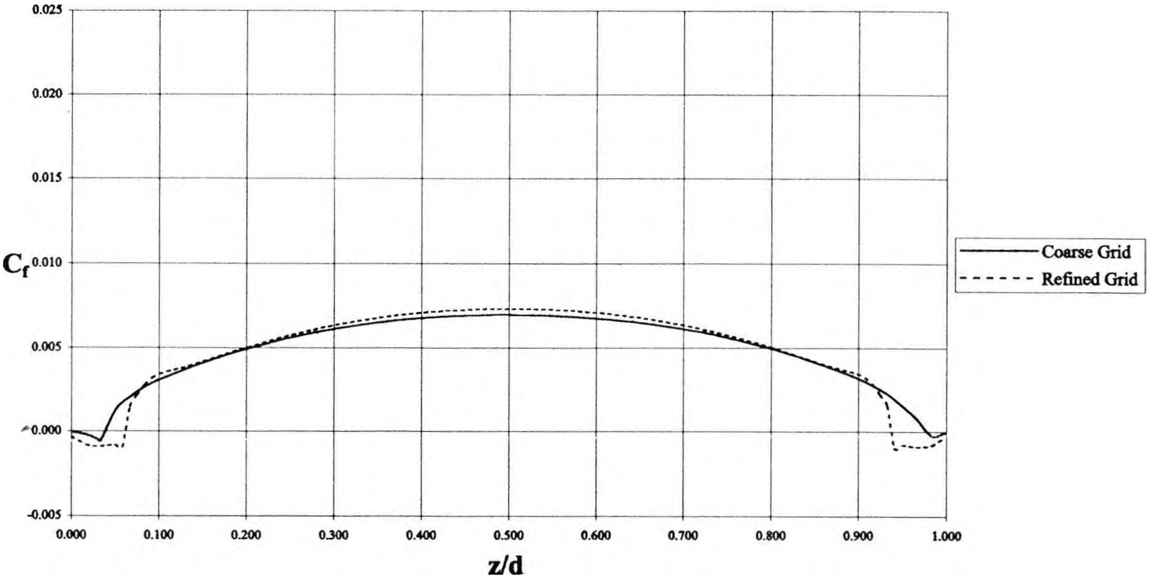

Figure 5.34: Predicted C_f at 40% chord on clean, 810 mm span models, $\alpha = 29^o$.

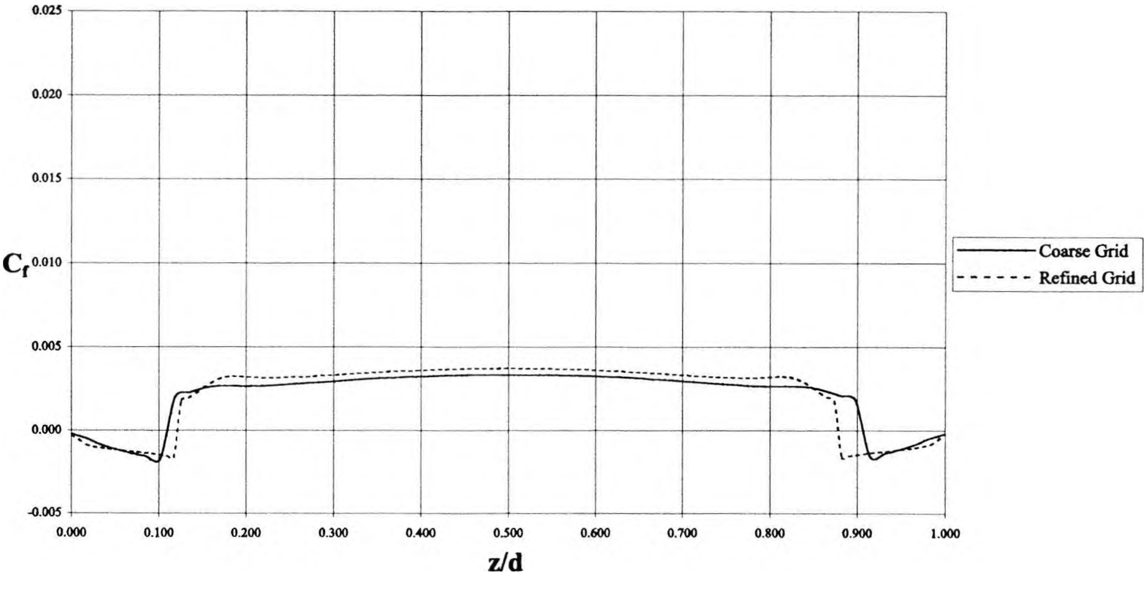

Figure 5.35: Predicted C_f at 50% chord on clean, 810 mm span models, $\alpha = 29^o$.

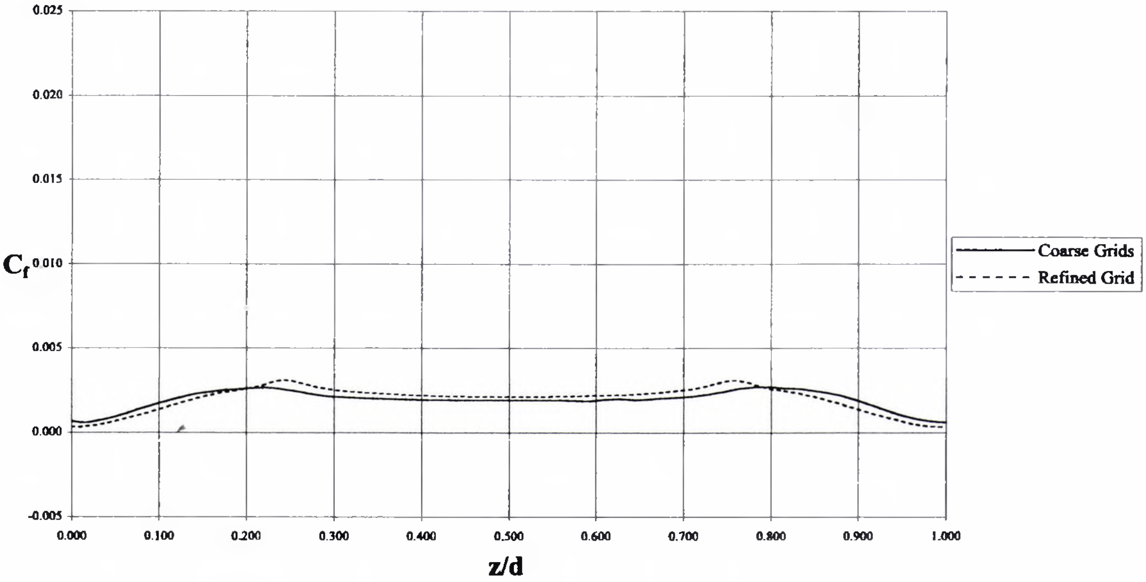

Figure 5.36: Predicted C_f at 60% chord on clean, 810 mm span models, $\alpha = 29^o$.

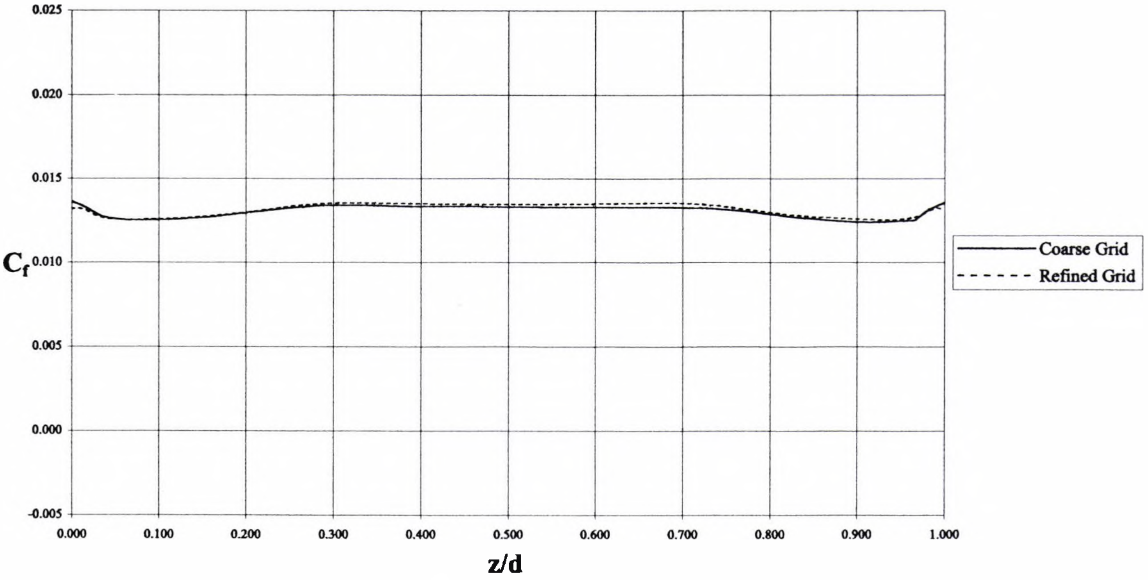

Figure 5.37: Predicted C_f at 70% chord on clean, 810 mm span models, $\alpha = 29^o$.

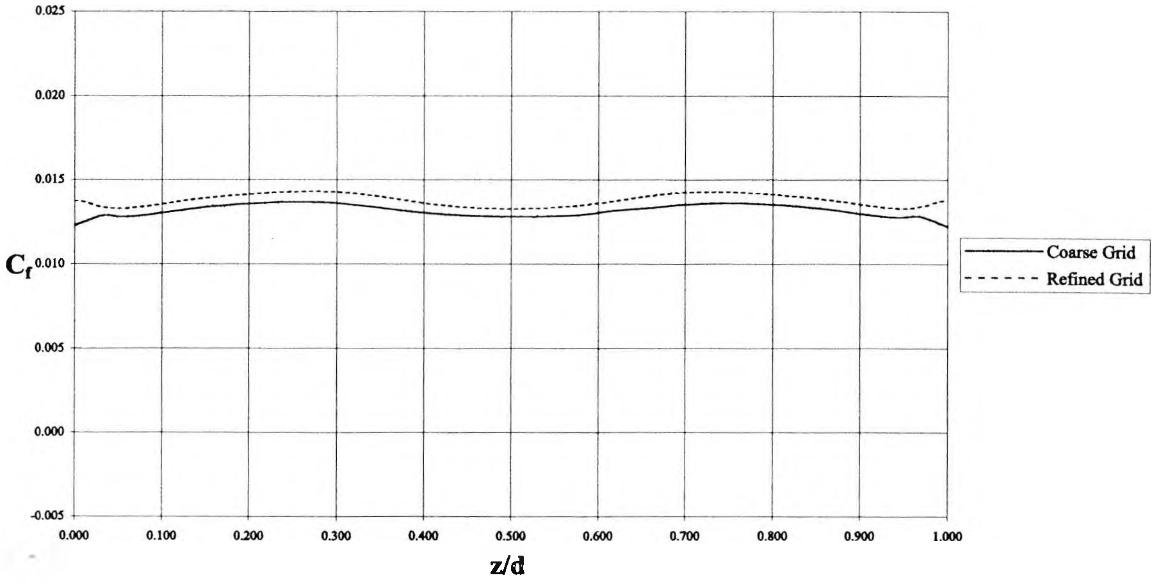

Figure 5.38: Predicted C_f at 90% chord on clean, 810 mm span models, $\alpha = 29^o$.

5.5 Air Jet Models

On a Formula One racing car, it is theoretically possible to use exhaust gas to force the AJVGs. Given this possibility, three higher pressures were applied to the pressure boundaries in the models to examine the effects of different blowing pressures. Thus the results for three forcing pressures, P_{ajvg}, appear in the figures used in this discussion. They are atmospheric pressure, P_{atm}, taken to be 1.01 x 10^5 Pa and 10% and 15% above P_{atm}. These are labelled '$P_{ajvg} = P_{atm}$', '$P_{ajvg} = 1.10P_{atm}$' and '$P_{ajvg} = 1.15P_{atm}$' respectively in the graphs presented.

5.5.1 Surface Limited Velocity Vectors about Air Jet Models

In addition to the C_f contours, the author presents some visualisation showing the surface limited velocity vectors. These are presented to provide a greater insight into the near-surface flow field on the 240 mm span clean models and on the AJVG models.

The 240 mm span clean wing visualisation is presented in Figure 5.39. The areas of flow separation are conspicuous by the paucity of velocity vectors. What few vectors are present are also of very low magnitude or are pointing in the negative x-direction. These characteristics indicate low momentum and flow reversal. That the areas of flow separation are only present near the walls reinforces the possibility that the separation originates with the corner flows. The vane and flap elements are seen to have completely attached flow.

The use of the AJVGs with $P_{ajvg} = P_{atm}$ is presented in Figure 5.40. The regions of flow separation are still present on the mainplane. However, there is a small decrease in the size of the separated region. This is mostly achieved in the chordwise sense. The vane and flap are seen to be without any separated flow.

As seen in Figure 5.41, an increase in the AJVG blowing pressure to give $P_{ajvg} = 1.10P_{atm}$, produces a clear improvement in the flow over the mainplane. The regions of flow separation are further decreased in size but there is a greater improvement on the right side of the mainplane than on the left. This is because the higher energy flow field created by the jets is convected toward the right side of the mainplane. It is possible that this convection is enhanced by the interaction with the wakes formed in the corners. The propensity of the flow to convect in this direction has its origins in the AJVG skew angle ϕ. Figure 5.41 shows that when $\phi = 75^o$, the air jets are oriented towards the right side of the model. The vane and flap are seen to experience attached flows.

An increase in P_{ajvg} to $1.15P_{atm}$ produces a flow field that sees the near elimination of the region of flow separation on the right side of the mainplane. However, this improvement is to the detriment of the flow field on the left side of the same element where there is a catastrophic breakdown of the flow field. Figure 5.42 shows that the separated region on the left side of the mainplane has increased in size and mainly in the spanwise direction. A review of Figures 5.41 and 5.42 suggests that the low momentum flow on the left side of the mainplane is entrained in the higher momentum flow on the right side. The degree of the entrainment is proportional to P_{ajvg}. It is possible that this is further evidence of a midification of the flow path due to interaction with the wakes formed by the corner flows. A possible solution to this problem would have been the installation of vane vortex generators on the virtual test section walls.

That the elimination of the flow separation one side of the wing is accompanied by a worsening on the other suggests that the AJVG design is not optimal. Akanni & Henry (1995) concluded that the use of co-rotating and counter-rotating AJVG arrays was application dependent. There is merit to investigate the use of counter-rotating AJVGs to ascertain whether both regions of flow separation can be eliminated. These results from these predicted flows agree with the findings of Pearcey (1961) when he concluded that the success of an AJVG array in inhibiting flow separation lay with adequate vortex strength and suitable positioning. This was deemed to be more important than the details of the boundary layer upstream.

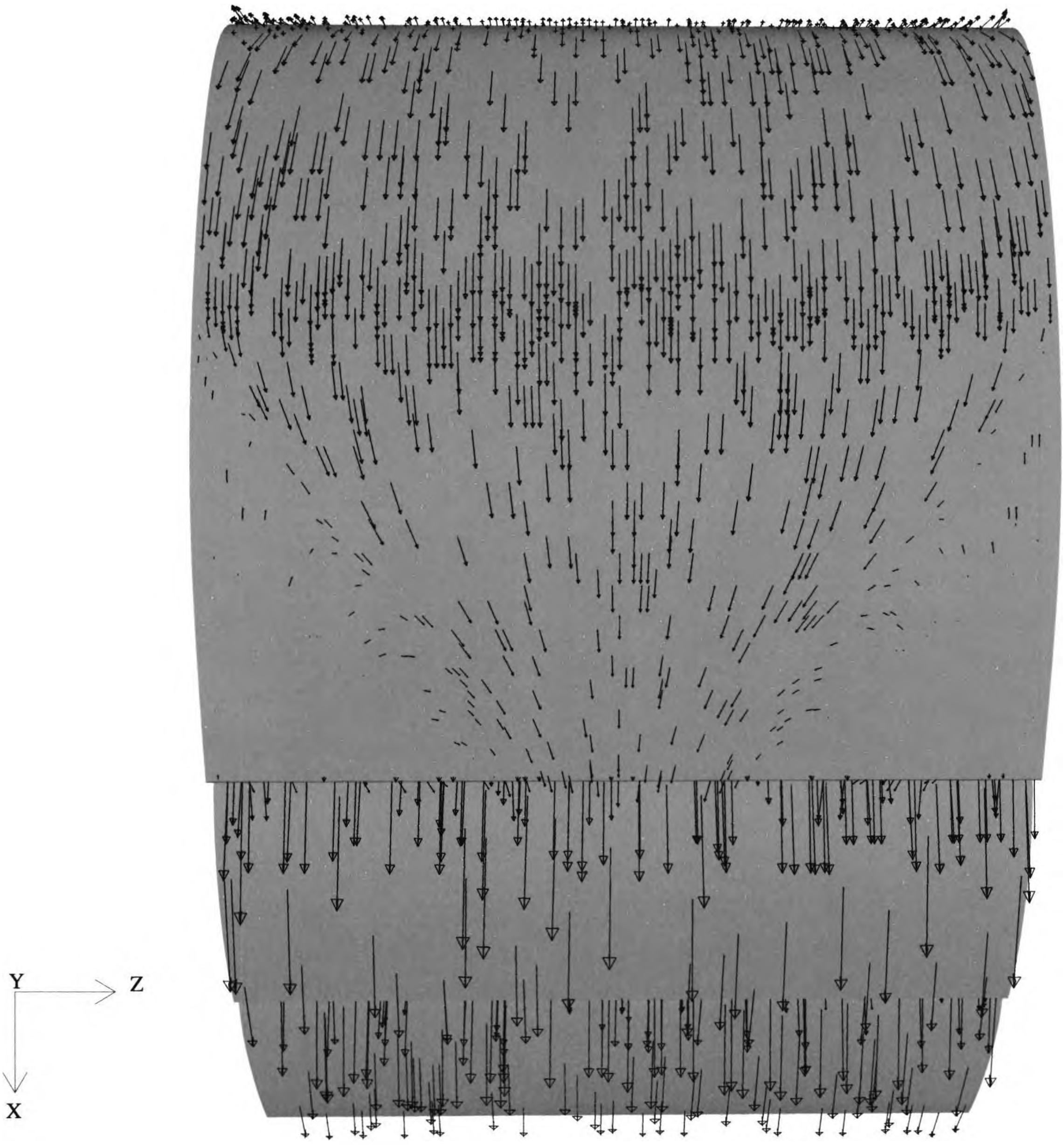

Figure 5.39: Limiting velocity vectors over clean, 240 mm span model, $\alpha = 29^o$.

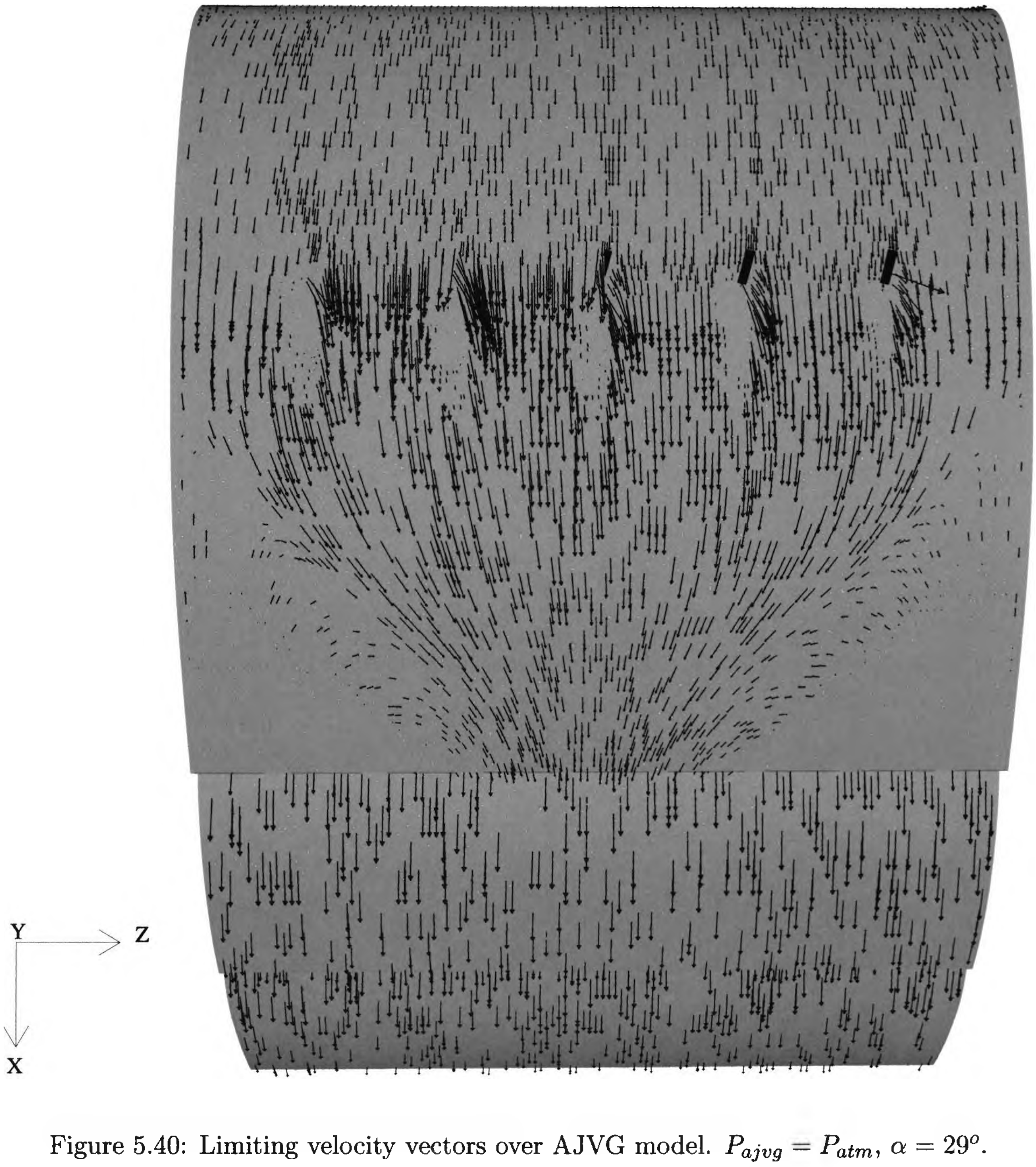

Figure 5.40: Limiting velocity vectors over AJVG model. $P_{ajvg} = P_{atm}$, $\alpha = 29^o$.

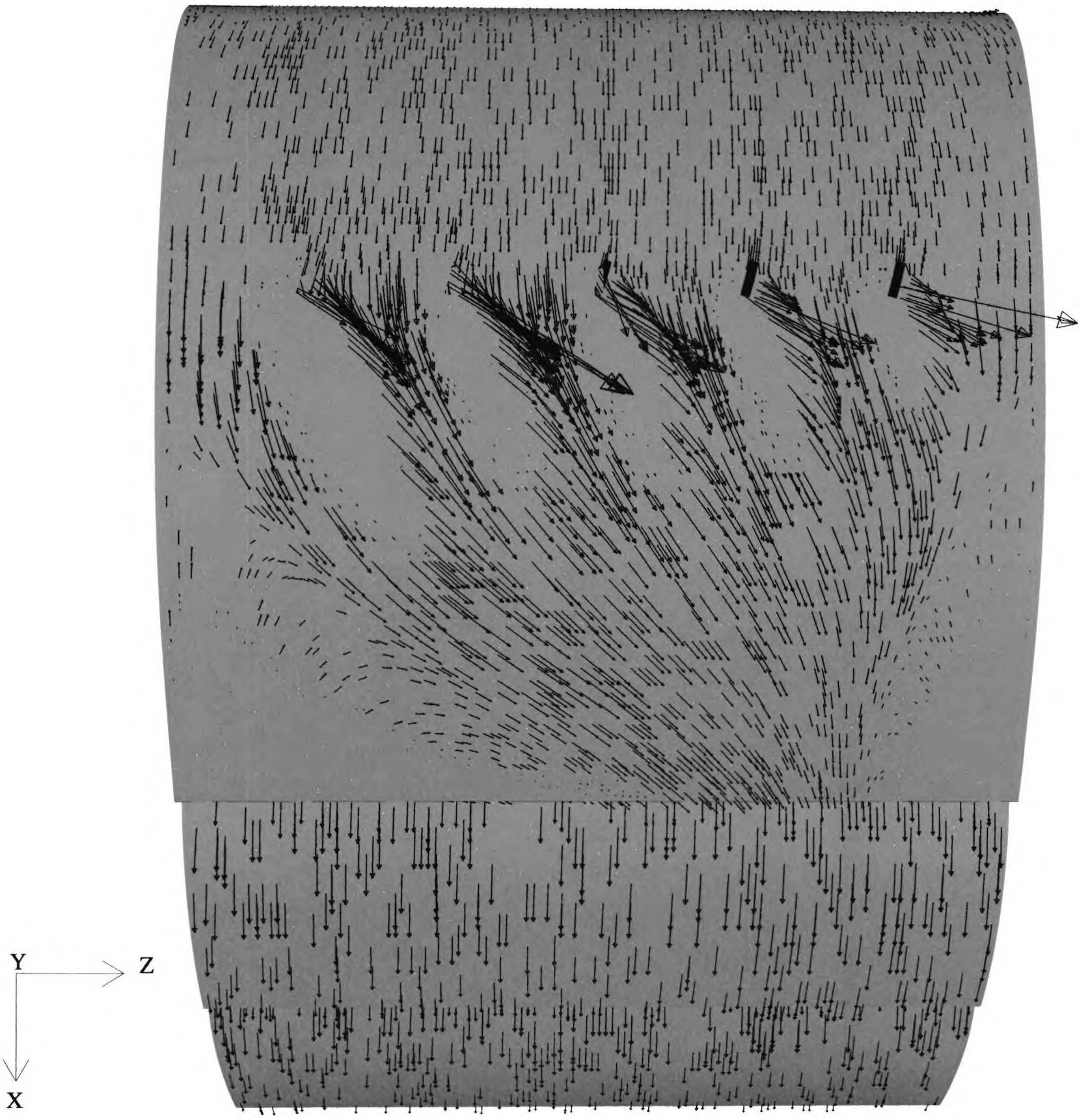

Figure 5.41: Limiting velocity vectors over AJVG model. $P_{ajvg} = 1.10 P_{atm}$, $\alpha = 29^o$.

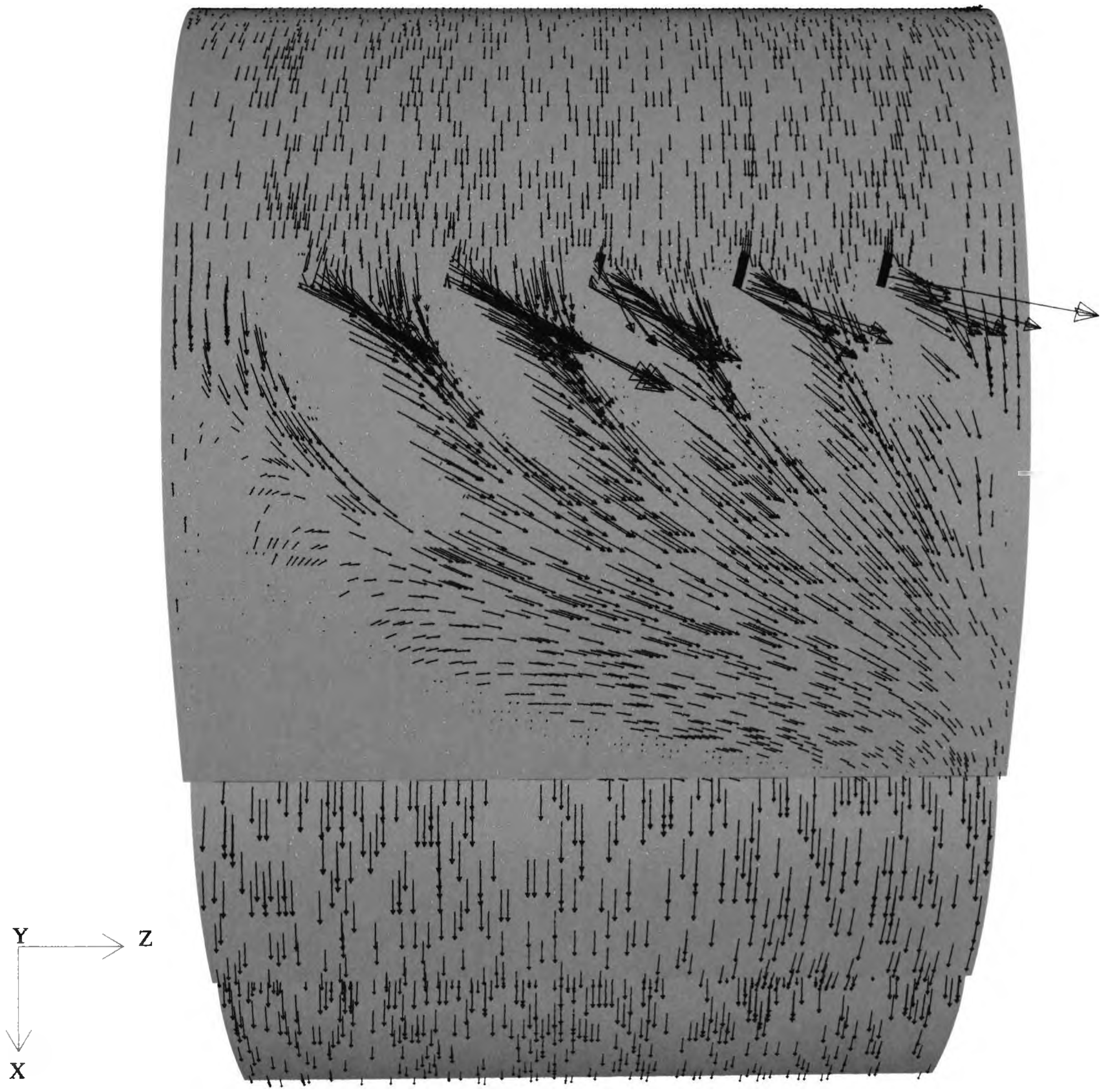

Figure 5.42: Limiting velocity vectors over AJVG model. $P_{ajvg} = 1.15P_{atm}$, $\alpha = 29^o$.

5.5.2 Transverse Velocity Fields about Air Jet Models

The development of the vortices was further investigated through the use of transverse velocity vectors about the AJVG models. Survey planes parallel to the plane x = 0 were used at 19% chord and all the locations previously presented in Section 5.5.4 are included as part of the discussion of transverse shear stress. The reader is reminded that the 19% chord position is along the centreline of the AJVGs. The vortices were tracked until their complete dissipation or until the 90% chord position.

The top of each plot coincides with the lower surface of the wing intersected by each survey plane. They are also presented as if the reader was looking downstream. They share the same orientation as the transverse shear stress distributions presented in Section 5.5.4.

The formation of the vortices about the wings is similar to the experimental findings of Innes et al. (1995) and the numerical predictions of Akanni & Henry (1995). These studies found that the AJVG efflux possesses a definite swirl and that the jet efflux travels through the vortex core thus making it a momentum rich region. This latter feature was highlighted by Peake et al. (1998) as one of the main differences between air jet vortices and those generated by vanes. The vortices generated by vanes possess momentum deficient cores. The vortex diameters are also seen to increase as they travel downstream. Figures 5.43 and 5.44 show the formation of the vortices over the surface of the mainplane. The inverted view and the use of velocity contours as opposed to vectors are used to aid clarity.

Figure 5.45 shows the development of the vortices when $P_{ajvg} = P_{atm}$. At 25% chord, the main vortices are weak and there are no detectable secondary vortices. It was previously shown by Akanni & Henry (1995) that a smaller secondary vortex is always produced regardless of the jet orientation. The strength of the secondary vortex was found to be inversely proportional to ϕ. With $P_{ajvg} = P_{atm}$, the vortices produced are predicted to be fully dissipated by 27.5% chord. Their coverage is not very extensive and therefore their ability to enhance the shear stress on the lower mainplane surface is limited.

That the vortices dissipate at such an early stage when $P_{ajvg} = P_{atm}$ is unlikely. It is possible that the predicted dissipation occurs prematurely due to the overly dissipative nature of the k-ϵ turbulence model. This shortcoming of the k-ϵ model has it origins in the eddy-viscosity concept and its limitation of using a single length scale to estimate the turbulent viscosity, μ_t. The resulting values of μ_t can be excessively high leading to higher levels of dissipation. Kim & Benson (1992) in their work on air jets proposed a novel multiple time scale turbulence model to better address this issue of over dissipation.

Despite this limitation, the author believes that the predicted dissipative trend of the various vortical flow fields is correct.

An increase in P_{ajvg} to $1.10P_{atm}$ produces vortices that, upon exiting the mainplane surface, are immediately stronger at 19% chord when compared to the same location with $P_{ajvg} = P_{atm}$. The development of these vortices is presented in Figures 5.46 through 5.48. With the increase in P_{ajvg}, the spanwise and downstream development of the vortices merits closer scrutiny.

Pauley & Eaton (1988) performed an experimental study using vane vortex generators to create longitudinal co-rotating and counter-rotating vortex pairs imbedded in turbulent boundary layers. Two types of counter-rotating vortex pairs were studied, where the flow between the adjacent vortex cores was directed towards and away from the wetted surface. The behaviour of these vortex pairs have certain similarities with the two vortices nearest the walls in the high downforce model with AJVGs. These vortex pairs were labelled "common flow down" and "common flow up", respectively. Given the inverted orientation of the AJVG high downforce model, the labels used by Pauley & Eaton (1988) are inappropriate. Instead, the author uses the terminology "common flow towards" and "common flow away" as direct analogies to "common flow down" and "common flow up".

The left and right walls bounding the AJVG models at $\frac{z}{d} = 0$ and $\frac{z}{d} = 1$ interact with the vortices to modify the rate at which they convect away from the lower surface of the mainplane. The resulting vortex behaviour is similar to that observed by Pauley & Eaton (1988). At 19% chord, shown in Figure 5.46, the first vortex has its core at approximately 14% span and given its proximity to the wall at $\frac{z}{d} = 0$, it is reasonable to say that it behaves as one vortex from a "common flow towards" pair. It remains close to the main surface until it is entrained in the adjacent vortex to the right. This entrainment is a recurring phenomenon until the final remaining vortex is dissipated further downstream.

By contrast, the rightmost vortex begins with its core at 85% span and is closest to the wall at $\frac{z}{d} = 1$. It behaves as one vortex from a "common flow away" pair. At 19% chord, all of the vortices form at approximately the same $\frac{y}{d}$ location under the mainplane surface. However, as early as 25% chord, it is clear that they are starting to convect away from the mainplane surface at different rates with the rightmost vortex predicted to have the highest rate of convection. The velocity vector plots, of which Figure 5.46 is a good example, show that as we go from $\frac{z}{d} = 0$ to $\frac{z}{d} = 1$, each vortex has an increasingly negative y-velocity component. It is this velocity component that is evidence of the rate of convection away from the mainplane surface.

It must also be taken into consideration that each vortex sees its image due to the proximity of the mainplane surface and that this enhances the spanwise convection of the vortices. This spanwise convection is evident in Figure 5.46. It is not clear whether the normal or spanwise convection is stronger.

The other vortices persist closer to the mainplane surface for longer periods and dissipate more quickly. Their momentum is lost in re-energising the mainplane boundary layer and this is seen as an enhancement in the local C_f. It is known that the primary mechanism by which vortices lose their circulation is through interaction with walls. Due to its high convection rate brought about by its interaction with the right wall, the vortex at the far right of the model has the least opportunity to interact with the mainplane surface and in so doing, it loses the least amount of energy and is able to persist downstream the longest until 35% chord. As Figure 5.48 shows, there are no discernible vortex structures from 40% chord.

The characteristics of the vortices produced with $P_{ajvg} = 1.15P_{atm}$ are illustrated in Figures 5.49 through 5.54. Once again, an increase in P_{ajvg} in predicted to increase the intensity of the vortices. It is seen that the all aspects of the convective behaviour of the vortices is also intensified at this higher blowing pressure. This is due to a combination of the higher energy possessed by these vortices and their interaction with the vortex images formed by the mainplane and the walls.

Arguably the most significant effect of increasing P_{ajvg} is that it creates vortices that are more resilient to dissipation. Figure 5.50 shows that in this model, at 35% chord, all but the rightmost of the vortices created have disappeared. That this vortex still exists, albeit weakly at 90% chord highlights the effect of increasing P_{ajvg}. The vortex convects quite a long distance away from the mainplane so despite persisting so far downstream, it is of no use in terms of promoting attached flow on the mainplane. As in the previous cases, the greatest utility is derived from those vortices that remain in intimate contact with the mainplane surface.

5.5.3 Visualisation of C_f Contours on Air Jet Models

The C_f contours on the clean wing are shown in Figure 5.55. The flow in the central span of the mainplane is attached as are the flows over the entirety of the vane and flap elements. The two regions of flow separation occur on the mainplane. They are triangular in shape and are seen as the areas covered by zero and negative C_f. The highest gradients are seen in the regions where the flow field begins to separate. The C_f contours on the

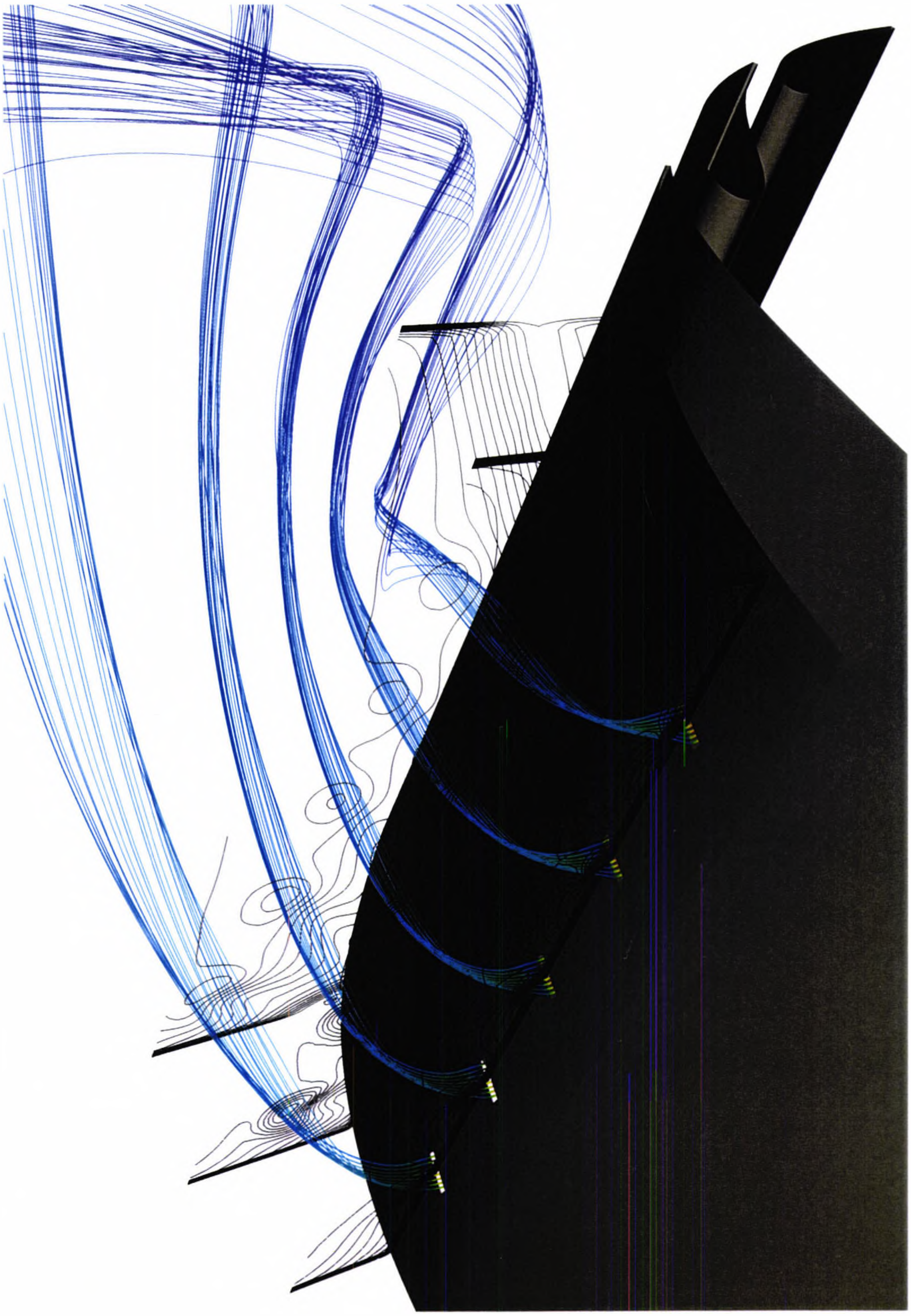

Figure 5.43: Looking Downstream: Vortices produced with $P_{ajvg} = 1.15P_{atm}$, $\alpha = 29^o$.

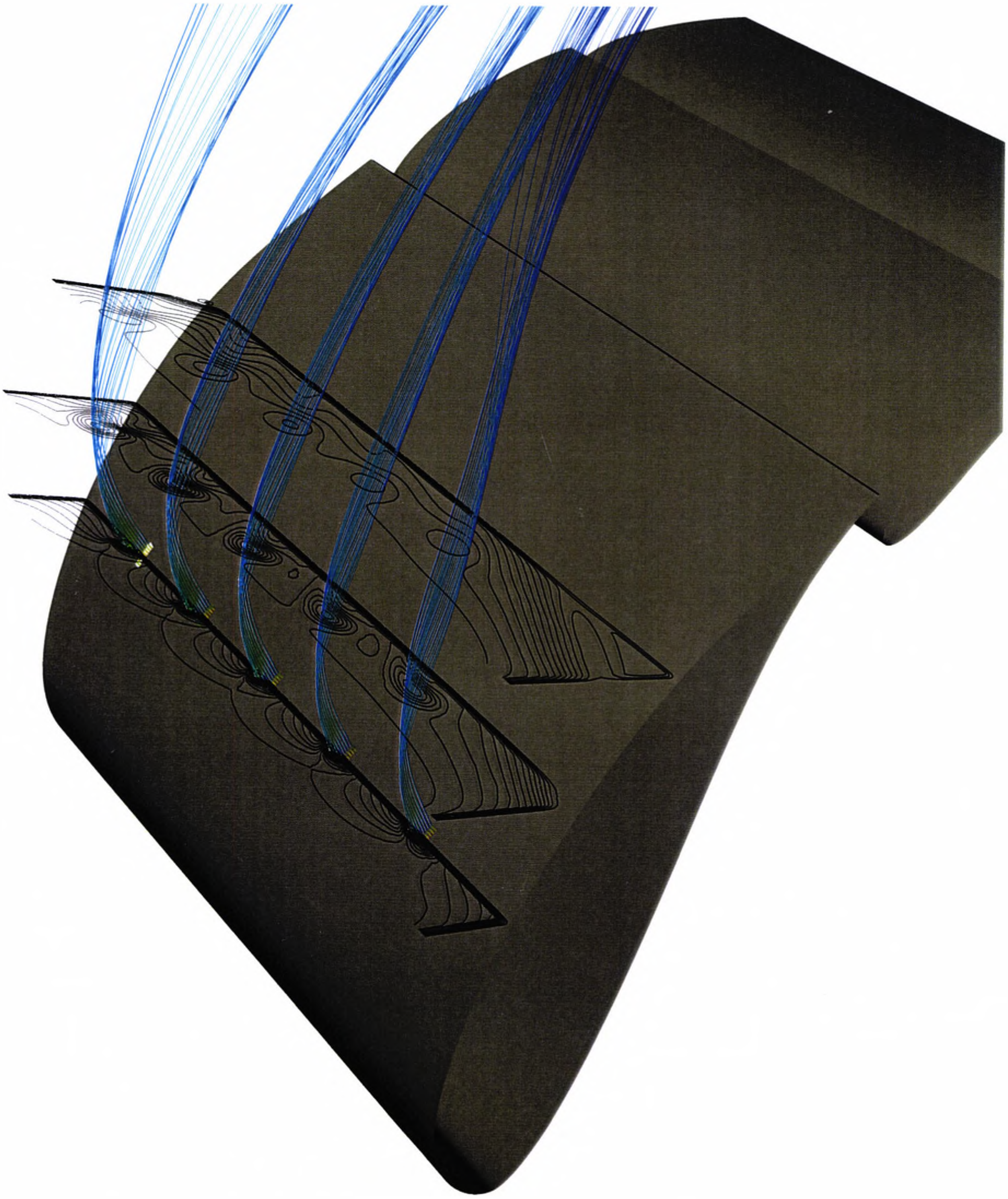

Figure 5.44: Cross-stream: Vortices produced with $P_{ajvg} = 1.15P_{atm}$, $\alpha = 29^o$.

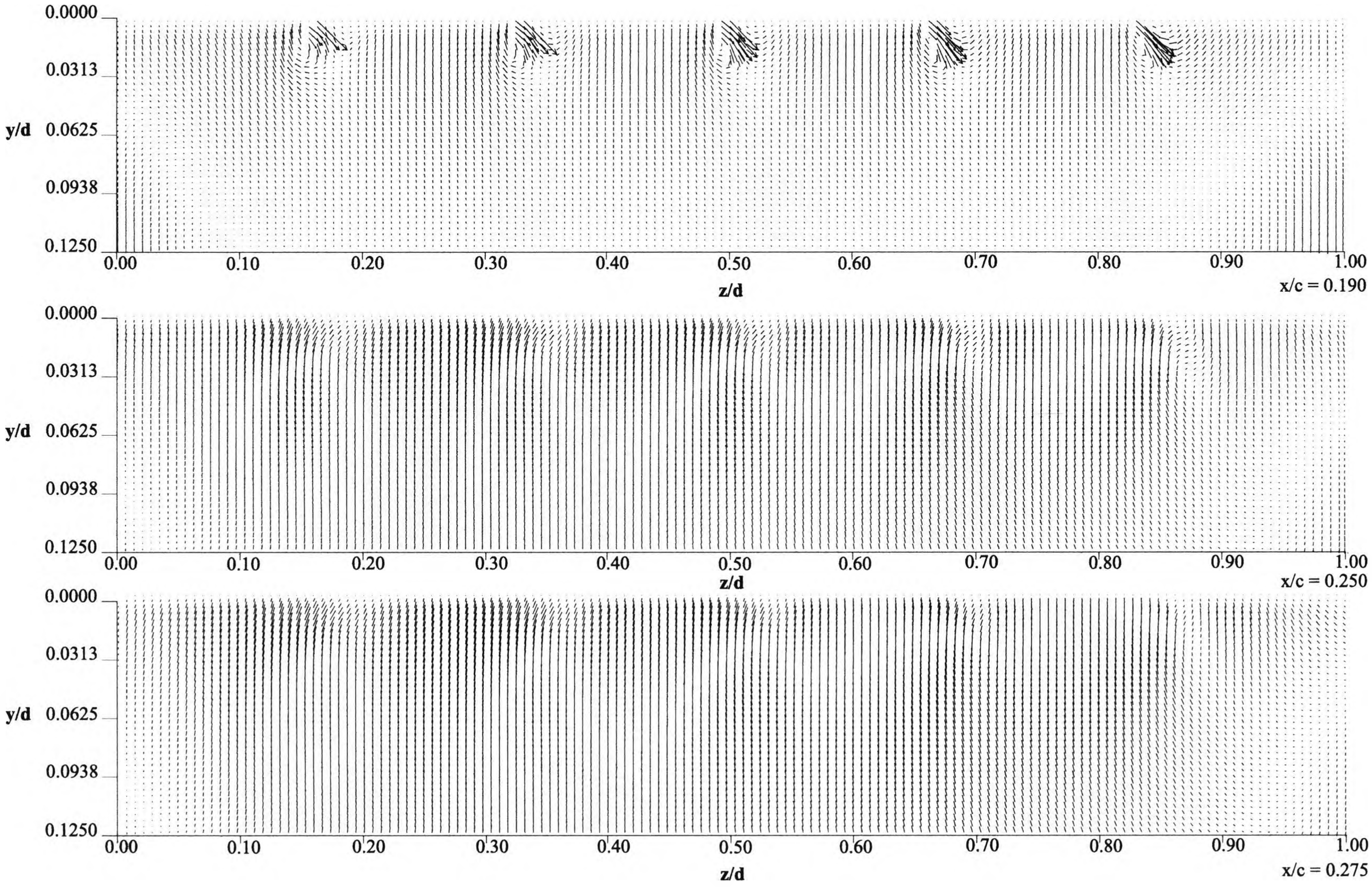

Figure 5.45: Velocity vectors at 19%, 25% and 27.5% chord, $P_{ajvg} = P_{atm}$, $\alpha = 29^o$.

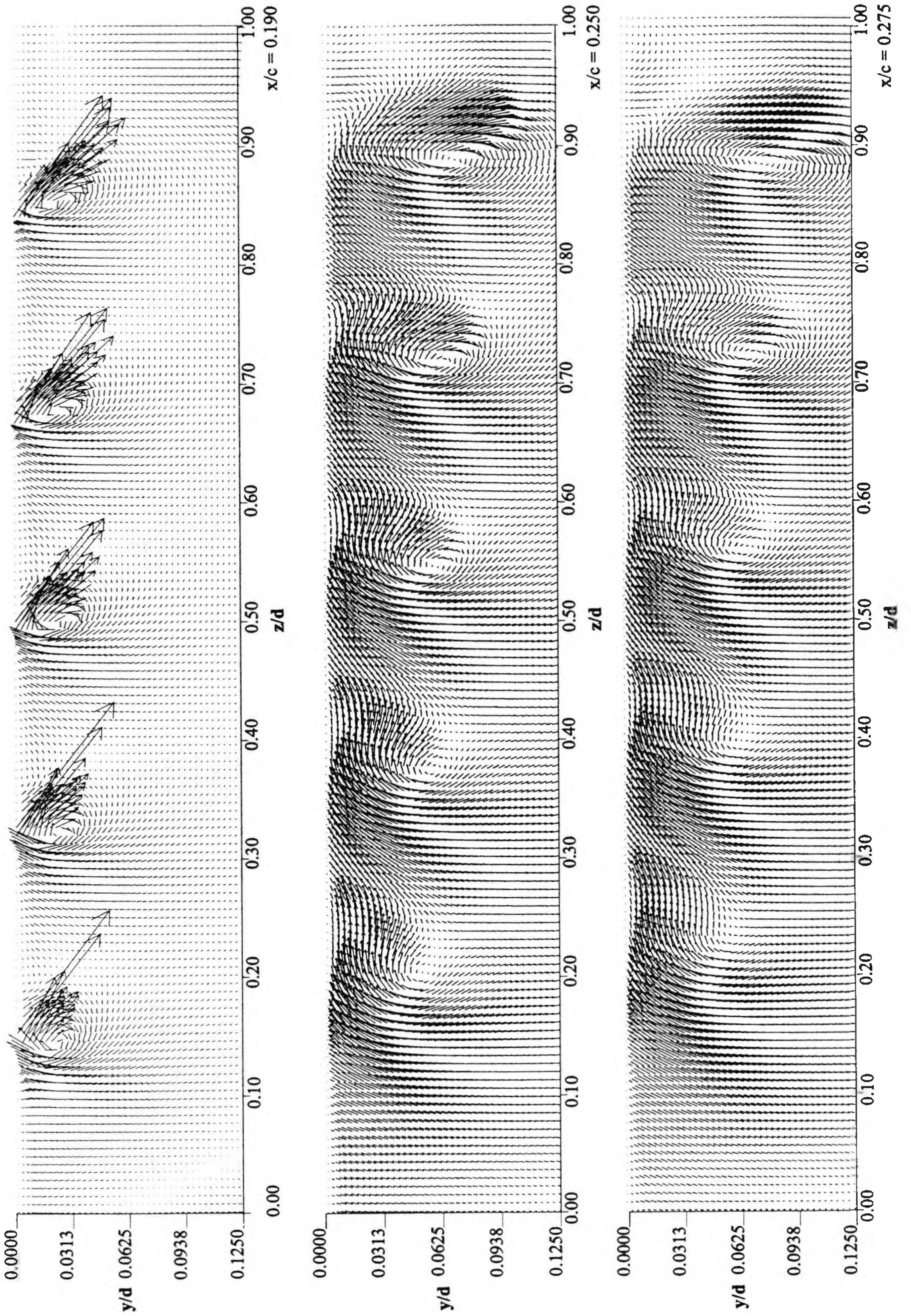

Figure 5.46: Vectors at 19%, 25% and 27.5% chord, $P_{ajvg} = 1.10P_{atm}$, $\alpha = 29^o$.

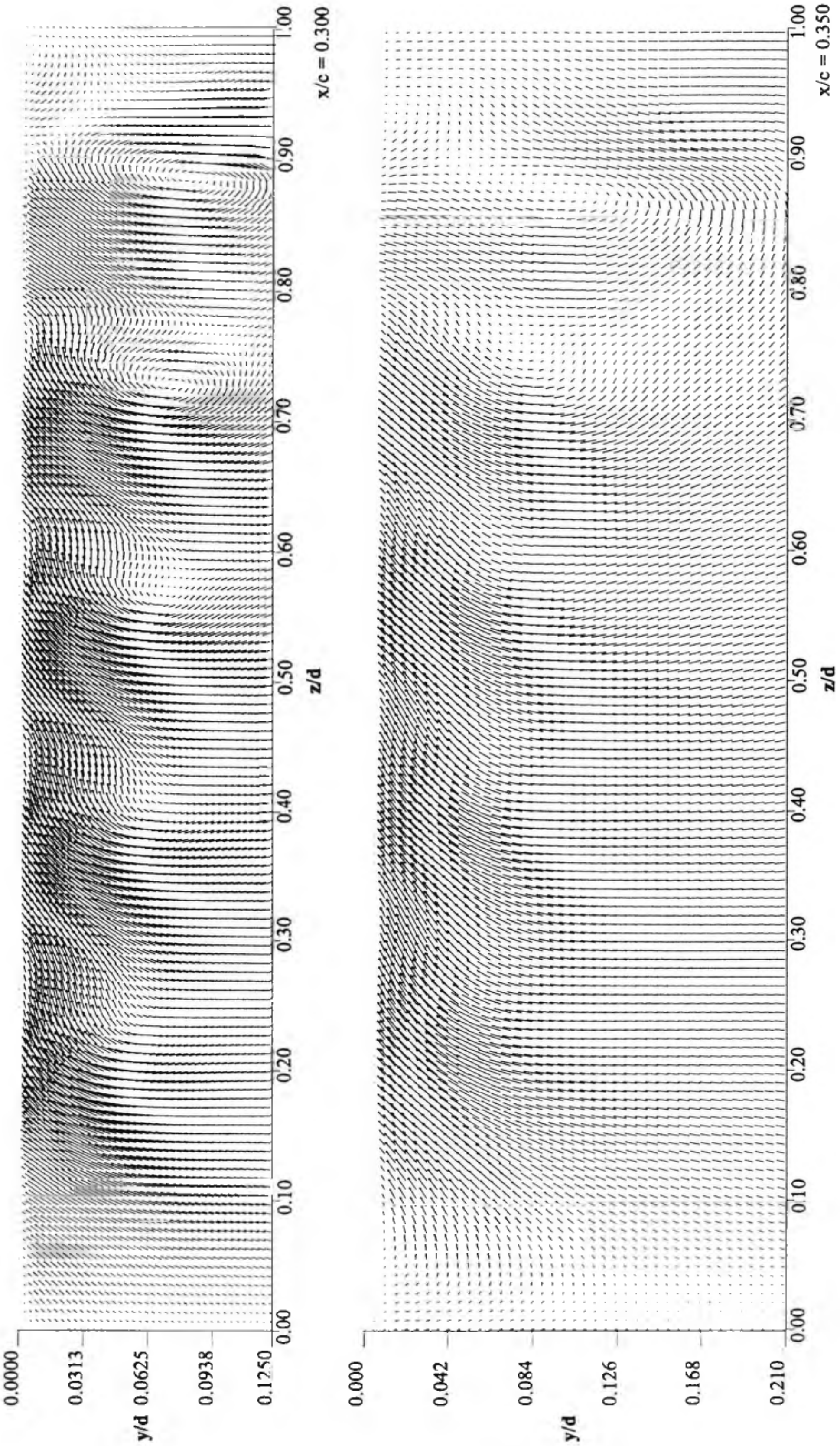

Figure 5.47: Velocity vectors at 30% and 35% chord, $P_{ajvg} = 1.10P_{atm}$, $\alpha = 29^o$.

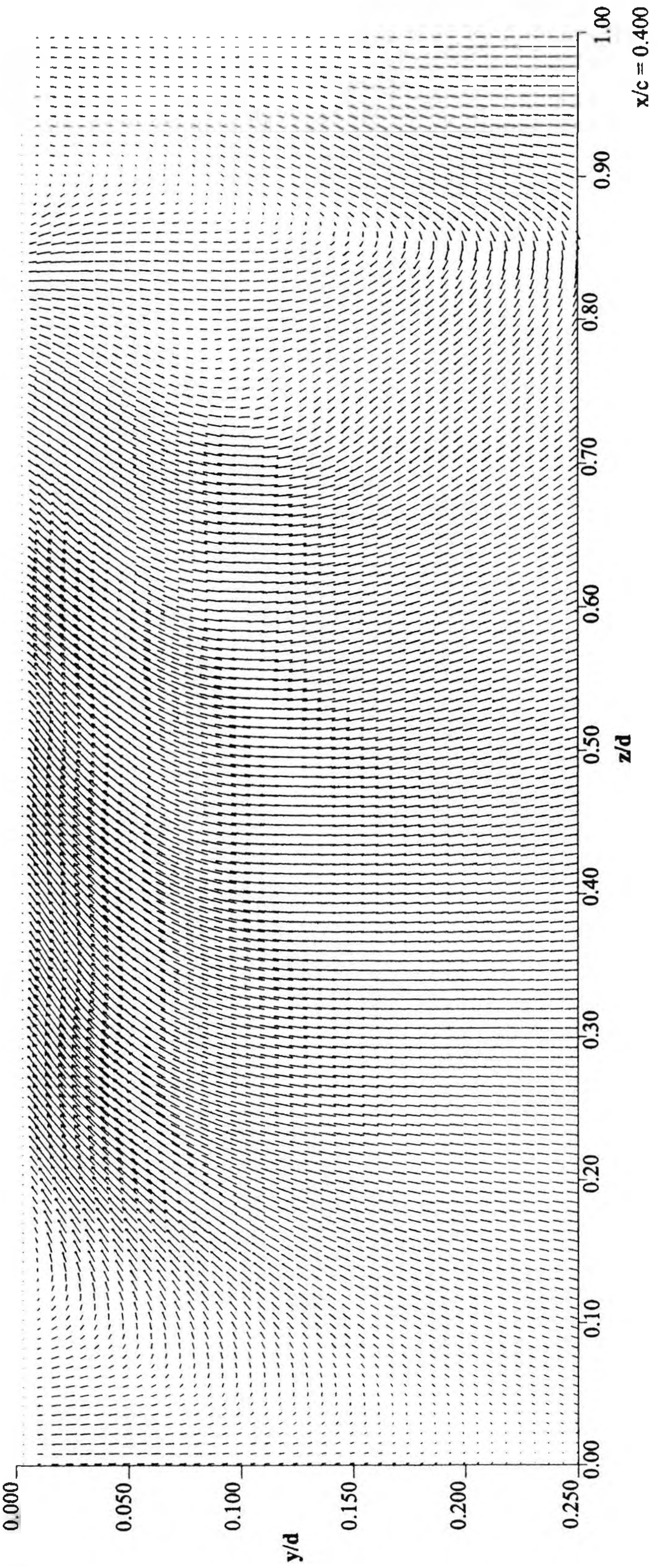

Figure 5.48: Velocity vectors at 40% chord, $P_{ajvg} = 1.10 P_{atm}$, $\alpha = 29^o$.

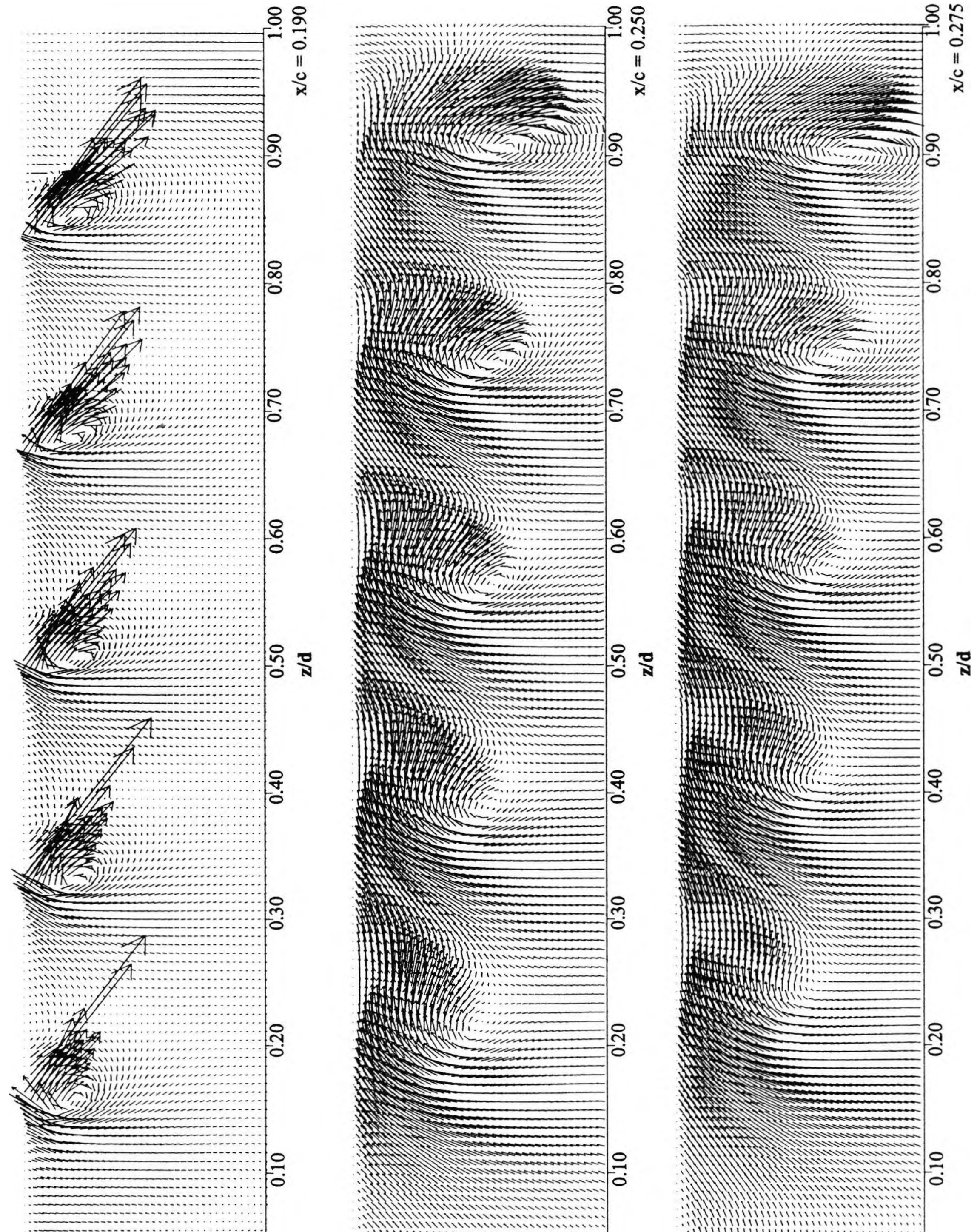

Figure 5.49: Vectors at 19%, 25% and 27.5% chord, $P_{ajvg} = 1.15P_{atm}$, $\alpha = 29^o$.

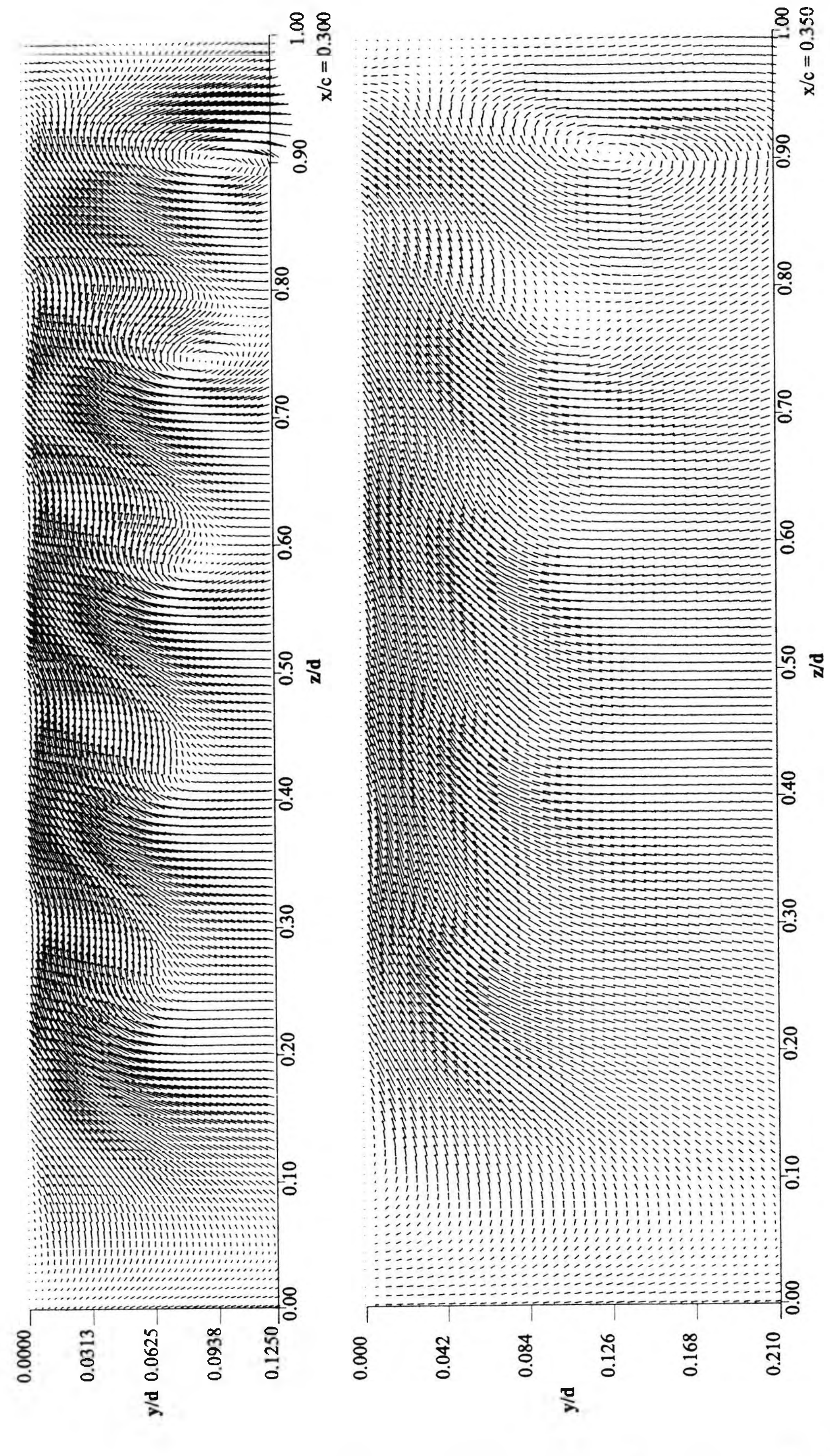

Figure 5.50: Velocity vectors, 30% and 35% chord, $P_{ajvg} = 1.15 P_{atm}$, $\alpha = 29^o$.

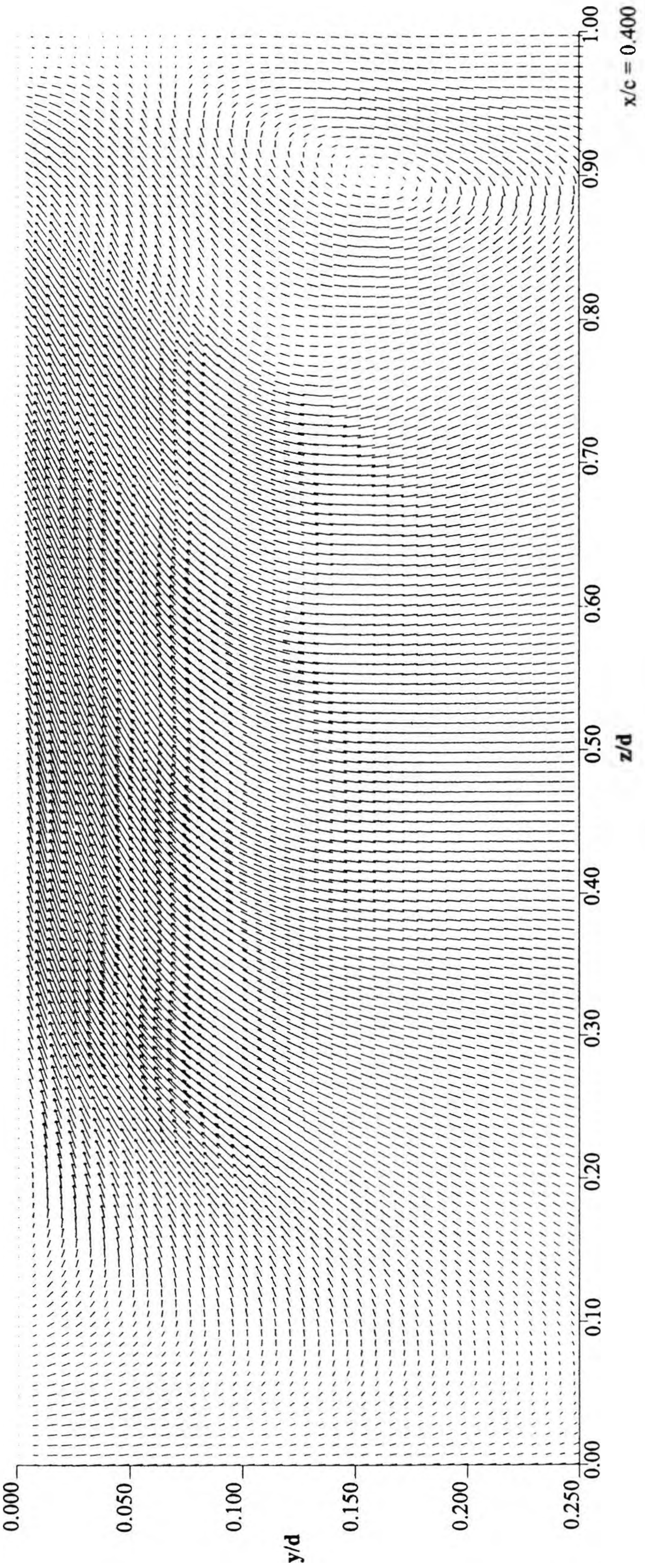

Figure 5.51: Velocity vectors 40% chord, $P_{ajvg} = 1.15P_{atm}$, $\alpha = 29^o$.

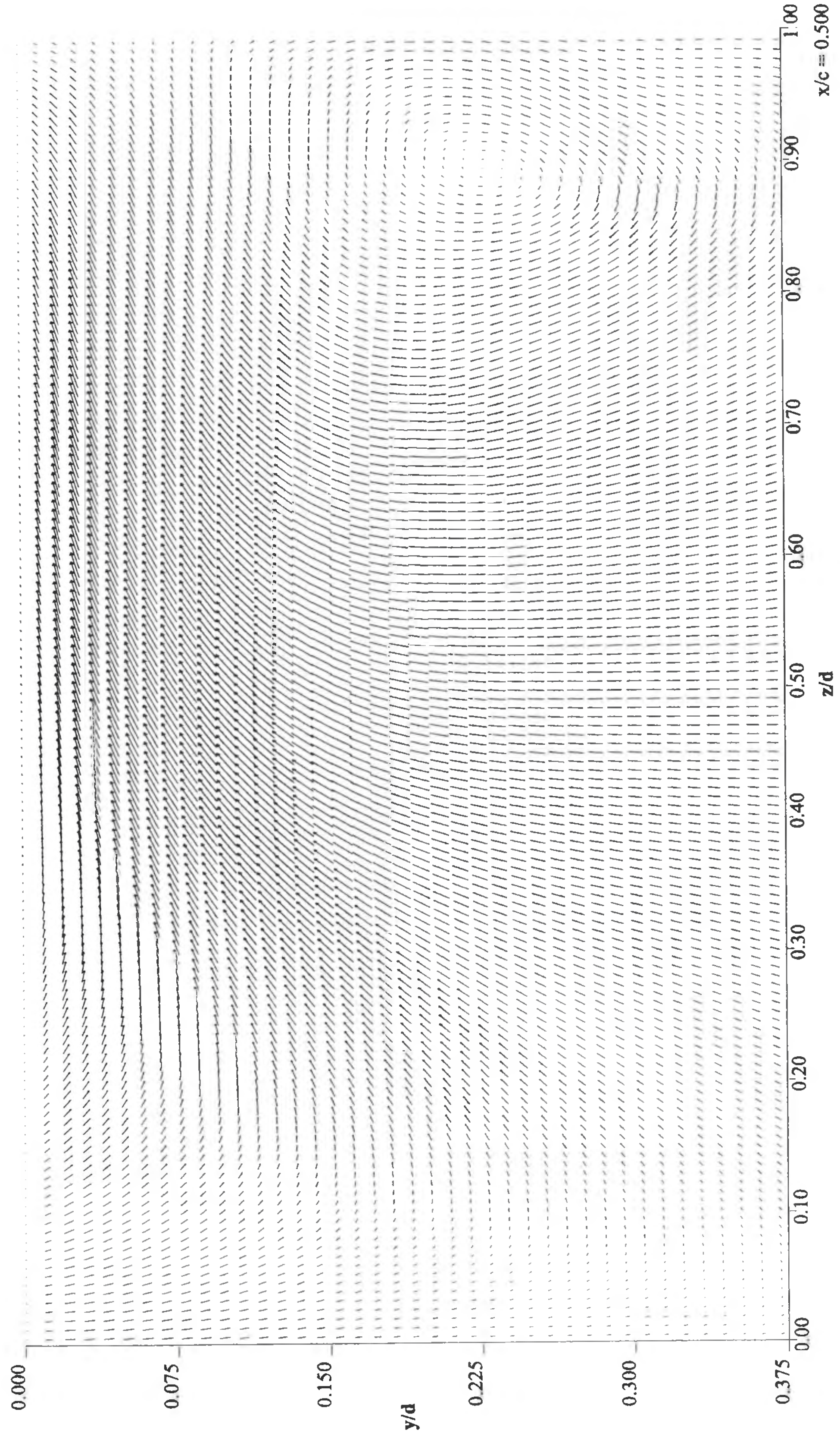

Figure 5.52: Velocity vectors 50% chord, $P_{ajvg} = 1.15P_{atm}$, $\alpha = 29^o$.

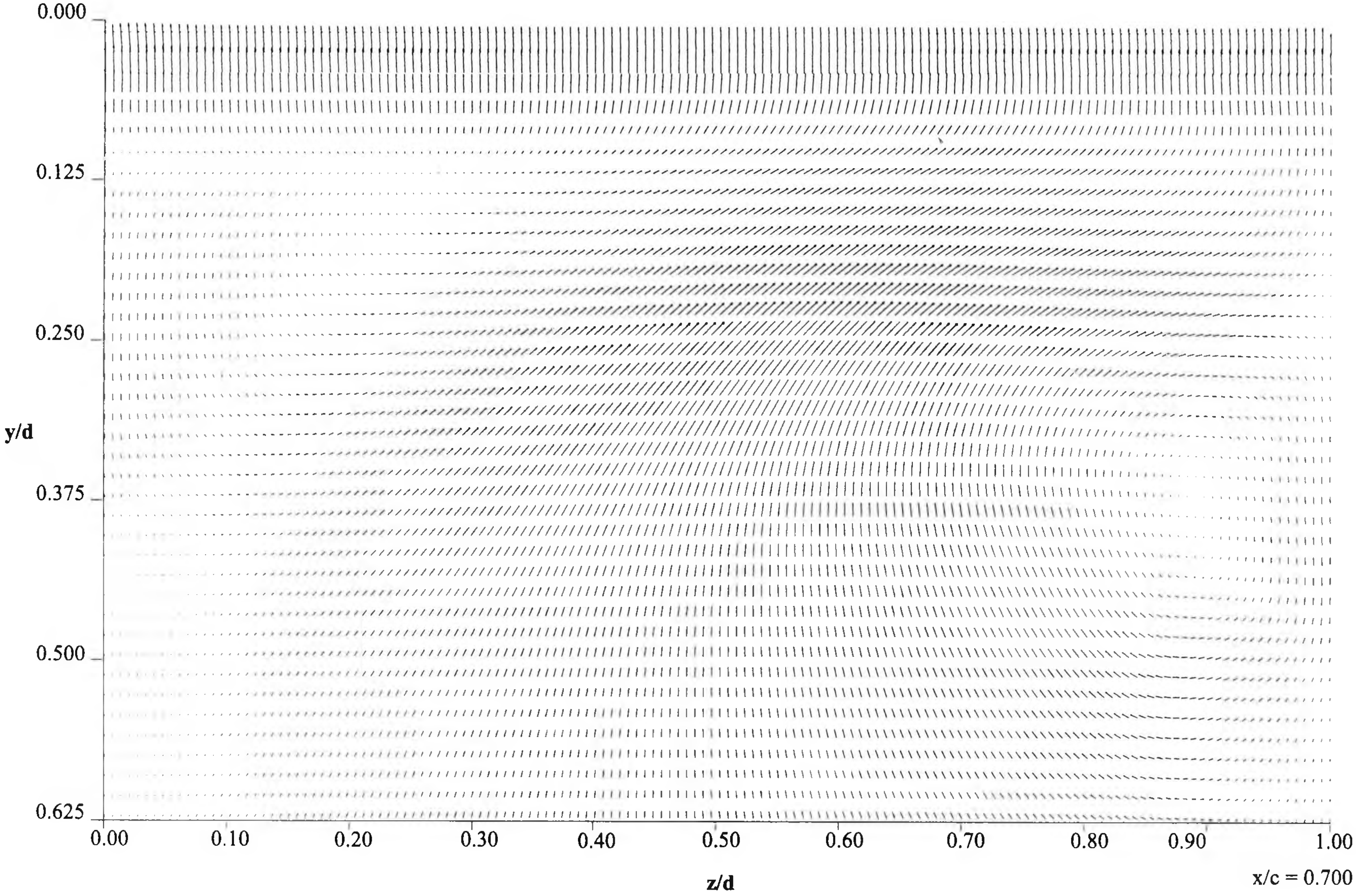

Figure 5.53: Velocity vectors, 70% chord, $P_{ajvg} = 1.15P_{atm}$, $\alpha = 29^o$.

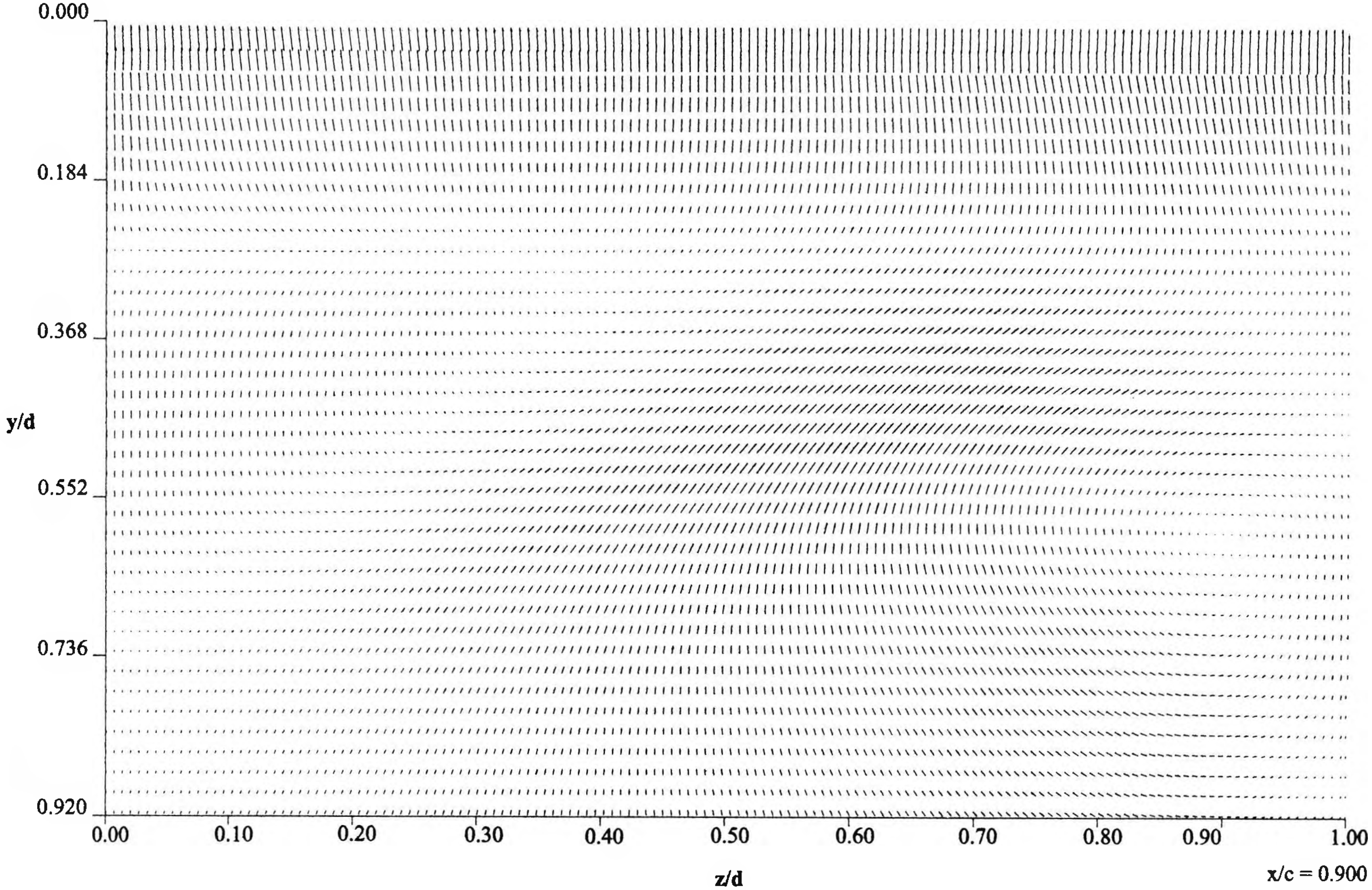

Figure 5.54: Velocity vectors, 90% chord, $P_{avg} = 1.15 P_{atm}$, $\alpha = 29^o$.

vane and flap elements show completely attached flow with symmetrical isolines.

Figure 5.56 shows that the addition of AJVGs to the model with $P_{ajvg} = P_{atm}$ does not have a significant impact on the size of the regions of separated flow. The size of the attached flow region on the central mainplane is also unaffected but the effect of the AJVGs is reflected in the C_f contours. The highest C_f values occur near the air jet exits and there are five regions of high C_f gradients downstream of each air jet. This enhancement in C_f is a direct result of the stronger vortices created by a higher P_{ajvg}.

Increasing P_{ajvg} from P_{atm} to $1.10P_{atm}$ increases the effectiveness of the AJVGs in terms of combating the flow separation predicted on the clean mainplane. Figure 5.57 shows that the size of the separated region on the left side of the mainplane is increased, while that on the right side is significantly reduced. Most of the reduction of the flow separation is achieved in the spanwise sense. The C_f contours exhibit much higher magnitudes and gradients in the immediate vicinity of the AJVGs. The contours also have a stronger spanwise component that results from the skew angle, ϕ, entrainment due to influence of the vortex images created by the mainplane and convection due to interaction with the wakes formed by spearated flows in the corners.

The contours on the vane and flap show that the flow is asymmetric but fully attached. This asymmetry is induced on the vane boundary layer by the wake shed from the mainplane. In the discussion of trailing edge C_p on each element, it will be seen that the *dumping* velocity at the mainplane trailing edge is higher towards the left side of the mainplane. It will also be seen that the vane has a similar but much weaker asymmetric effect on the flap C_f contours by virtue of the dumping velocities at its trailing edge.

Figure 5.57 and 5.58 show that the AJVGs are capable of enhancing the skin friction above the clean wing level. However, it is clear that the orientation of the jets needs to be carefully considered when corner flows are a possibility. The can be significant interaction between the air jet effluxes and the boundary layers on any walls bounding the wing. The dramatic effect of such interaction can be seen in Figure 5.59 with P_{atm} to $1.15P_{atm}$, where flow separation can be seen on the left side the mainplane and the left wall. This contrasts sharply with Figure 5.60 where the mainplane and right wall are predicted to experience a fully attached flow.

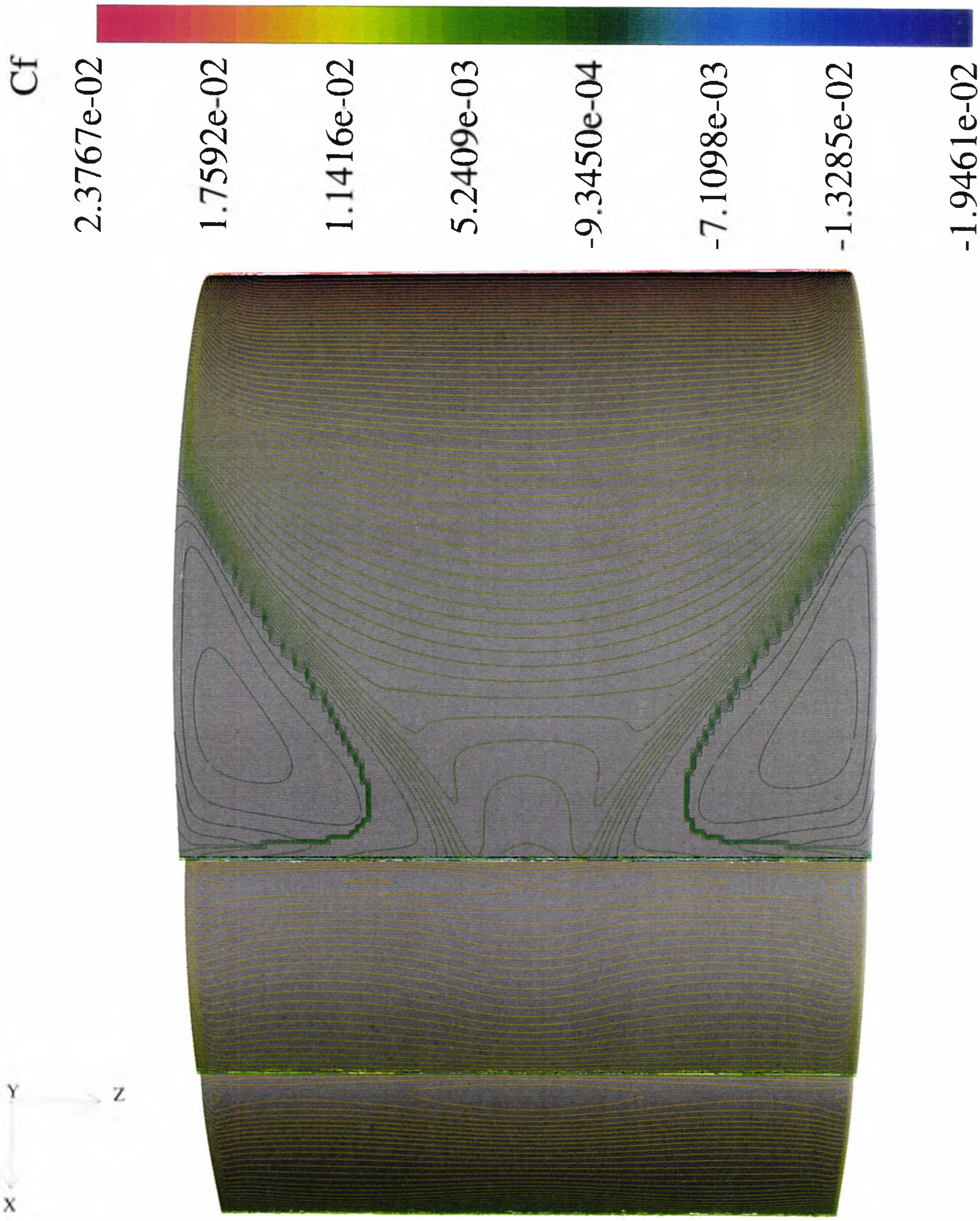

Figure 5.55: C_f contours on clean 240 mm span wing, $\alpha = 29^o$.

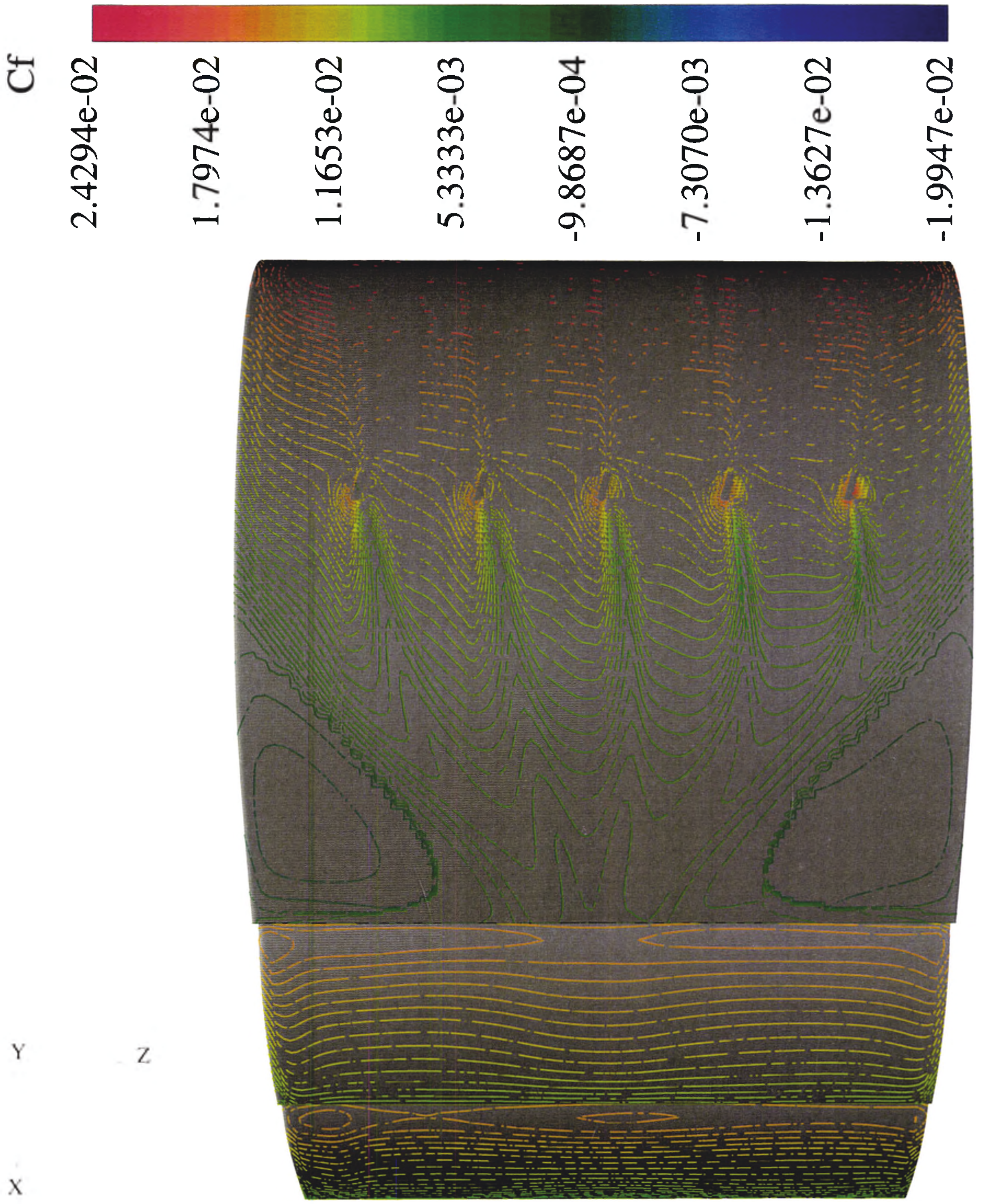

Figure 5.56: C_f contours on wing with AJVGs. $P_{ajvg} = P_{atm}$, $\alpha = 29^o$.

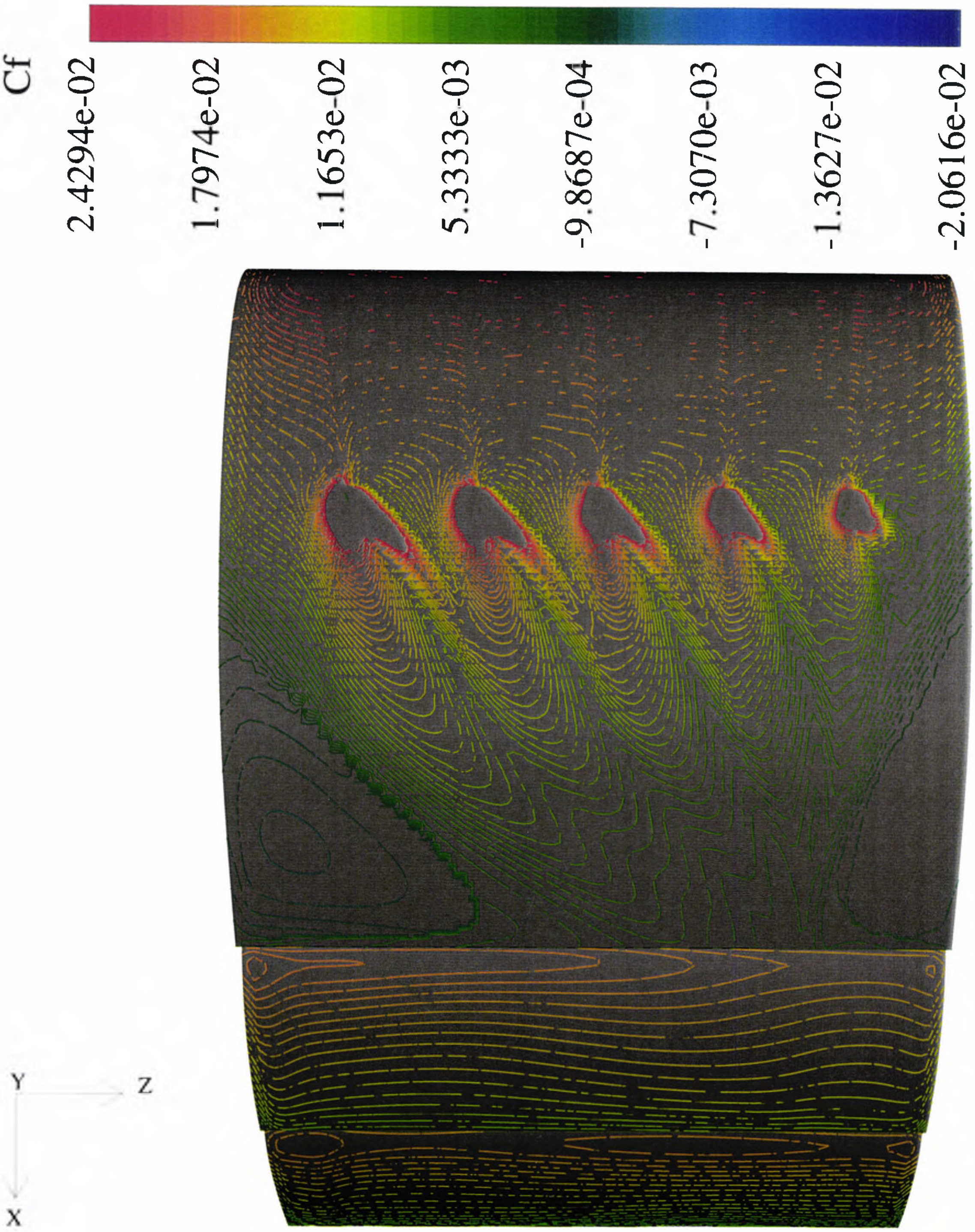

Figure 5.57: C_f contours on wing with AJVGs, $P_{ajvg} = 1.10P_{atm}$, $\alpha = 29^o$.

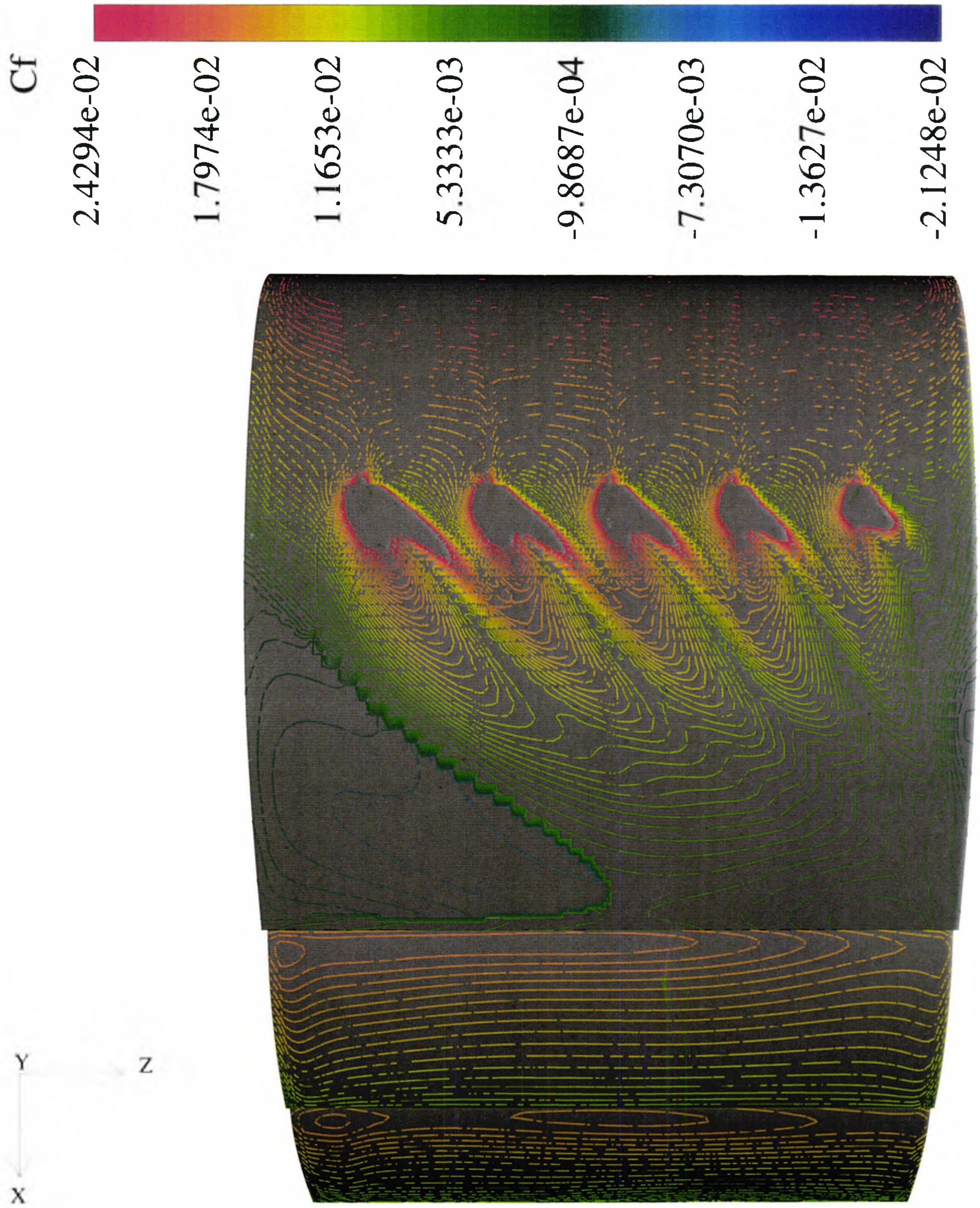

Figure 5.58: C_f contours on wing with AJVGs, $P_{ajvg} = 1.15P_{atm}$, $\alpha = 29^o$.

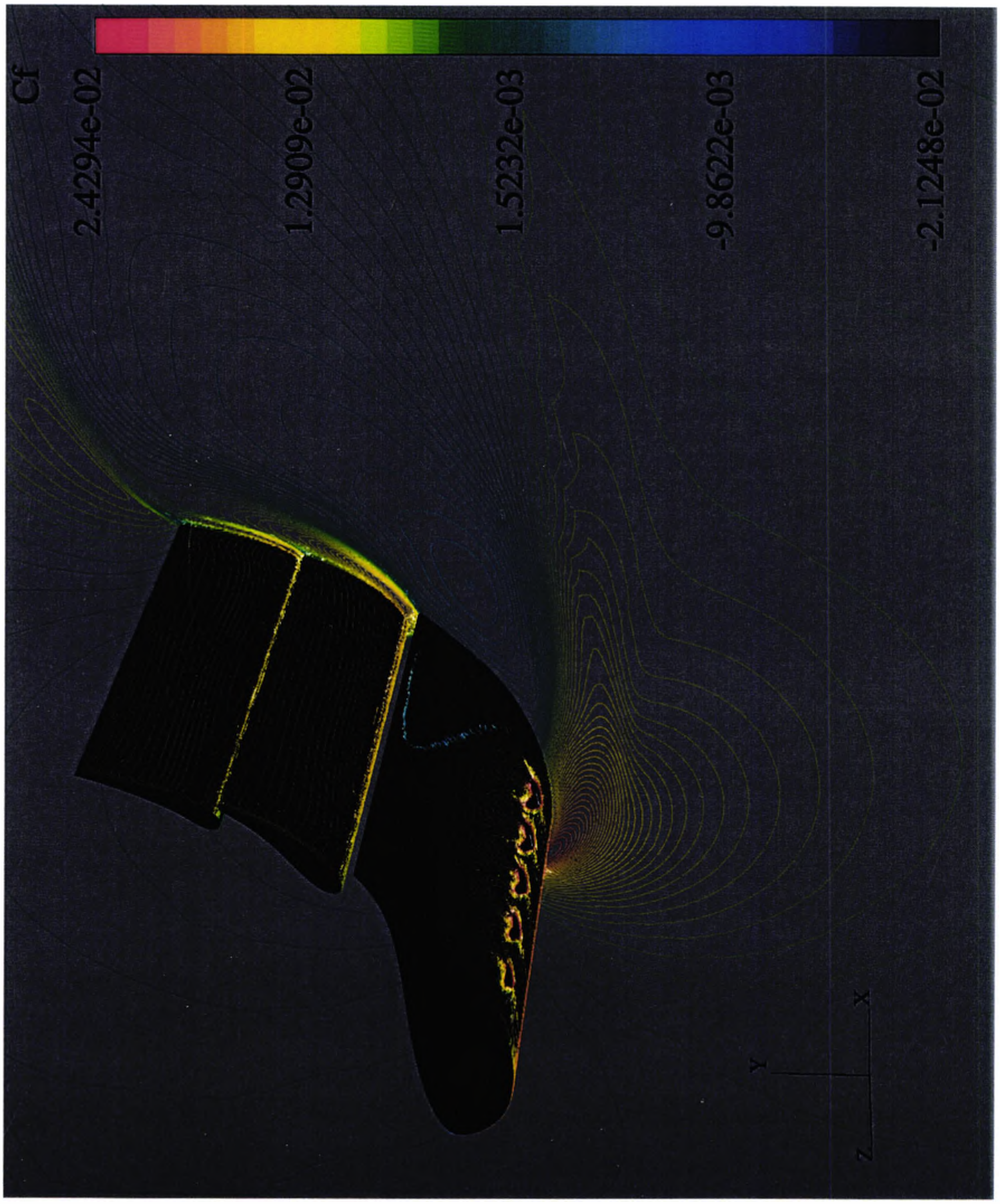

Figure 5.59: Flow separation on wing and left wall $P_{ajvg} = 1.15P_{atm}$, $\alpha = 29^o$.

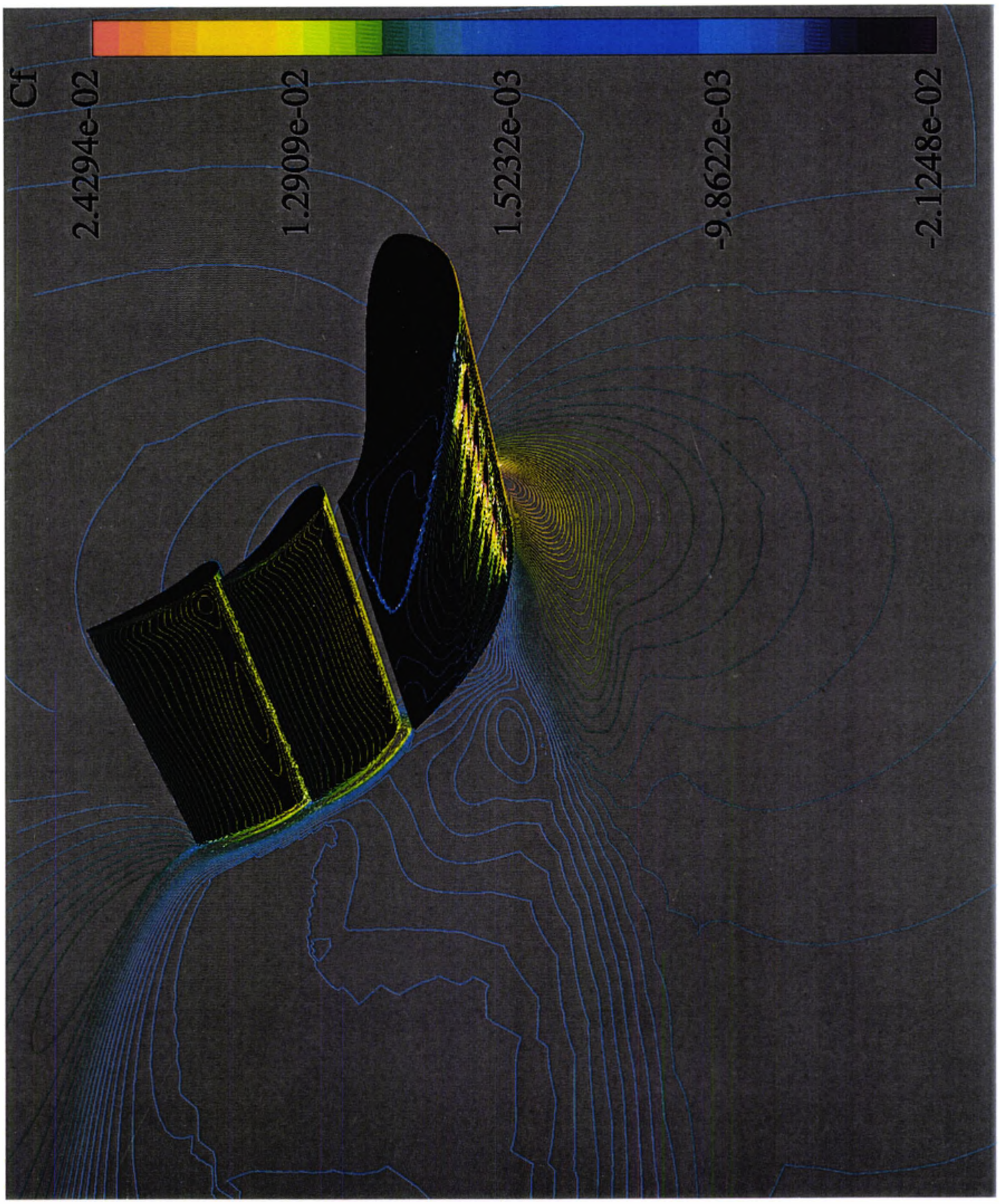

Figure 5.60: Attached flow on wing and right wall $P_{ajvg} = 1.15P_{atm}$, $\alpha = 29^o$.

5.5.4 Predicted Lateral C_f Distribution about Air Jet Models

In the models investigated, a performance enhancement occurs with the AJVGs when the ratio $C_{f\,ajvg}/C_{f\,Clean\,Wing} > 1$. The reader can develop an appreciation for the local values for this ratio by reviewing Figures 5.61 through 5.69 where the lateral shear stresses at various chordwise positions are presented. However a review of these lateral C_f plots does not always provide an unambiguous indication of whether or not the AJVGs have enhanced the total shear stress. The author attempts to address this issue in the following section.

A review of the lateral shear stresses presented in Figures 5.61 through 5.69 further illustrates the complexity of the flows predicted in these AJVG models. In general the figures show that a higher AJVG blowing pressure is beneficial for enhancing the shear stress. However, this trend is complicated by the presence of the sidewalls where the lowest values of the shear stresses are seen at each chord position for all the models. With few exceptions, the AJVGs do enhance the shear stresses in the near-wall regions as well.

Figure 5.61 shows that at 25% chord, $P_{ajvg} = P_{atm}$, is predicted to provide the lowest enhancement of shear stress over the clean wing values. There are two very small regions of separated flow at the extremities of the mainplane span. It can be seen that the enhancement of C_f is proportional to P_{ajvg}. Figure 5.61 also shows that the AJVG influenced C_f distributions are sinusoidal in shape across the span with the highest values of C_f occurring between 0% and 40% span. These trends of enhancement and the shape of the C_f distributions persist through the 27.5% chord position, as shown in Figure 5.62, until the 30% chord where some significant changes begin.

At the 30% chord position, reversed flow on the AJVG equipped wing is predicted for the first time. In the model where $P_{ajvg} = 1.15P_{atm}$, the region up to 5% span is seen to have $C_f < 0$. All other AJVG equipped wings are predicted to have attached flow at this location. However at 98% span, the AJVG equipped wings with $P_{ajvg} = P_{atm}$ and $1.10P_{atm}$ are seen to be marginally separated while there is no flow separation on the AJVG model with $P_{ajvg} = 1.15P_{atm}$.

Figure 5.64, shows that at 35% chord, with the exception of $P_{ajvg} = 1.10P_{atm}$, all other models, clean wing or AJVGs alike, experience separated flows. The lowest values in the lateral C_f distribution occur with the highest value of P_{ajvg} and the two best occur with $P_{ajvg} = P_{atm}$ and $1.10P_{atm}$. This sudden reduction in C_f brought about by the use of the AJVGs results from the flow in this corner interacting with the jet effluxes.

The lateral C_f presented for the AJVG models in Figures 5.62 through 5.67 show that the onset of flow separation on the mainplane begins on the left hand side of the model and progresses across the span as the flow proceeds along the mainplane surface. The breakdown of the flow on the mainplane is sudden and asymmetric and the C_f distribution at 50% chord with $P_{ajvg} = 1.15P_{atm}$, seen in Figure 5.66 is the best example of this. There are several factors responsible for this trend. They are as follows:

1. There is the wall induced flow separation that is present on both sides of the clean wing. The potential for this separation also exists on the AJVG equipped wings.
2. The direction of the AJVG effluxes points away from the left model wall and towards the right wall. These effluxes interact with the freestream flow to entrain the flow away from the left wall and towards the right wall.
3. The higher values of P_{ajvg} act to exacerbate the flow conditions as described in No. 2.

The effect of the AJVGs has dissipated significantly at the mainplane trailing edge as is seen from the C_f distribution in Figure 5.67. With the exception of two negligible tip regions for $P_{ajvg} = 1.10P_{atm}$, all the lateral C_f distributions demonstrate attached flow with very low values of C_f and reasonable symmetry. That the flow is predicted to be weakly attached at the mainplane trailing edge is most likely due to entrainment of the near trailing edge flow by the higher kinetic energy mainplane-vane slot flow.

The vane, being isolated from the mainplane by the slot flow, is not significantly affected by the use of the AJVGs. Increases in C_f are seen on this element at some spanwise locations towards the left side of the element. The most significant of these increases in this location occurs when $P_{ajvg} = 1.15P_{atm}$. However, on the right side of the element, C_f is seen to decrease below the level of that seen on the clean wing.

With the exception of some regions of slightly increased C_f on the flap, the AJVGs do not have any significant impact on the lateral C_f over this element. The most notable increase in C_f is produced when $P_{ajvg} = 1.10P_{atm}$.

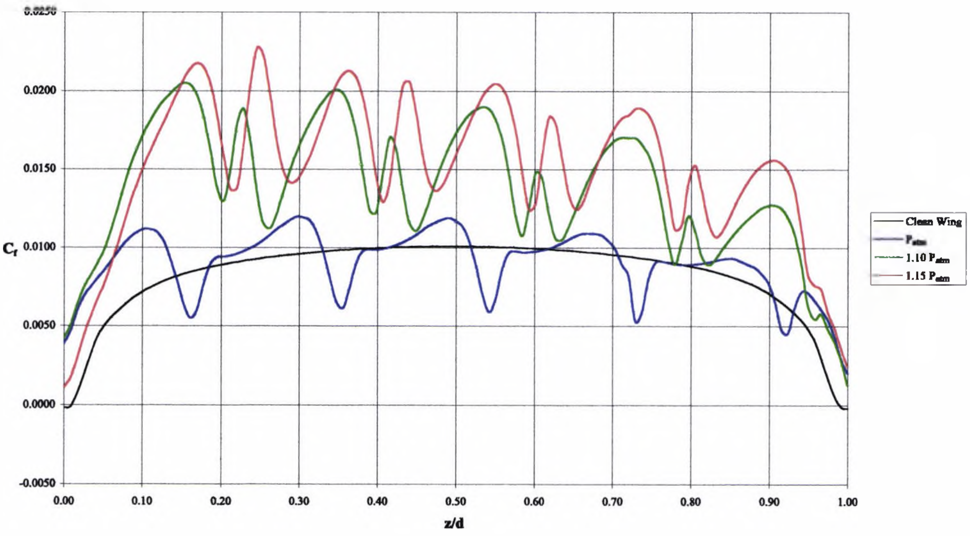

Figure 5.61: Lateral C_f distribution at 25% chord, $\alpha = 29^o$.

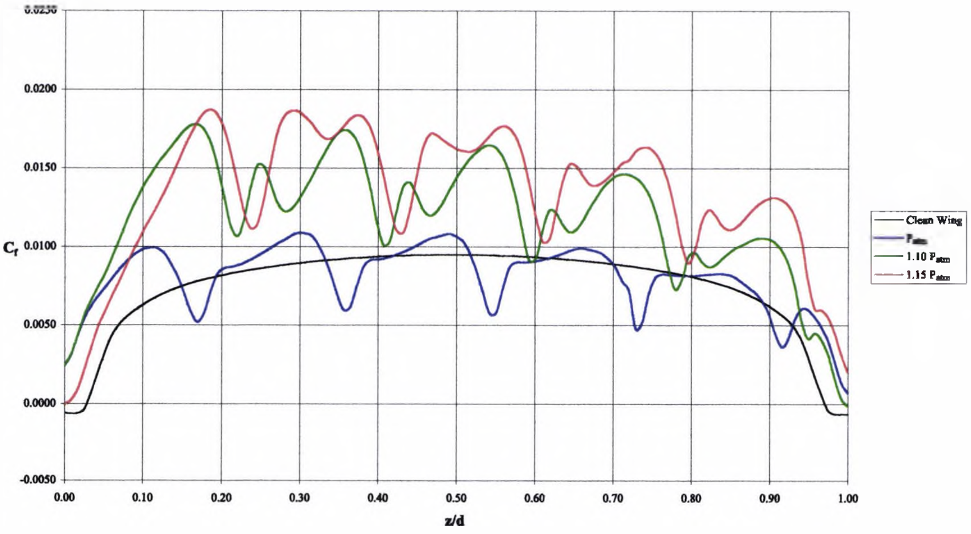

Figure 5.62: Lateral C_f distribution at 27.5% chord, $\alpha = 29^o$.

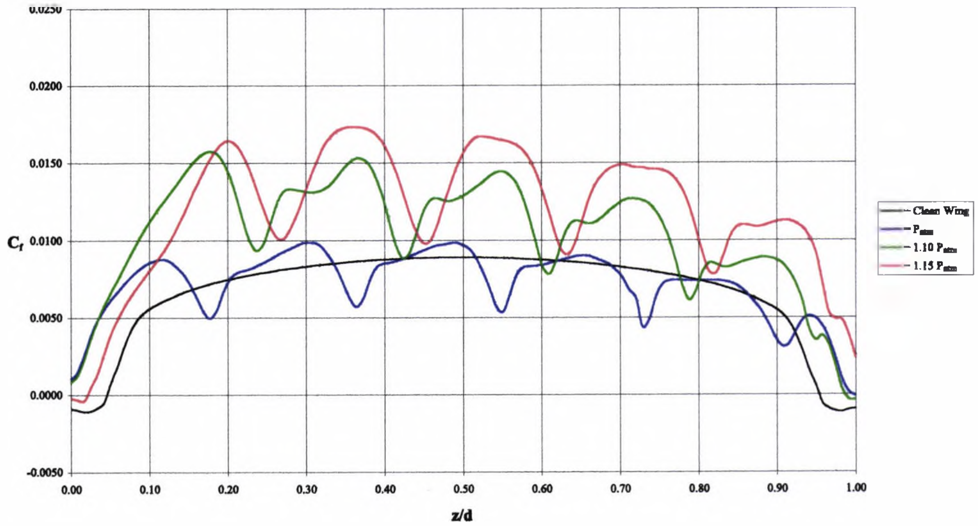

Figure 5.63: Lateral C_f distribution at 30% chord, $\alpha = 29^o$.

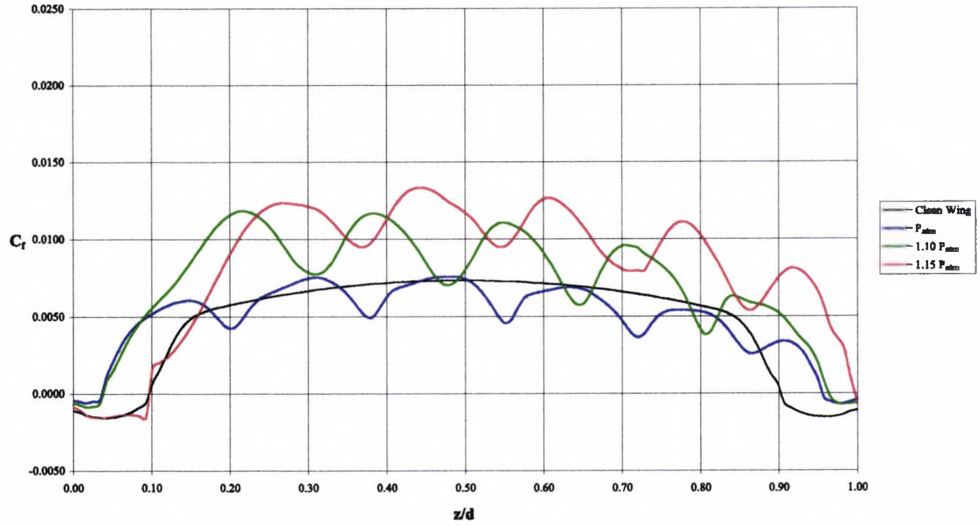

Figure 5.64: Lateral C_f distribution at 35% chord, $\alpha = 29^o$.

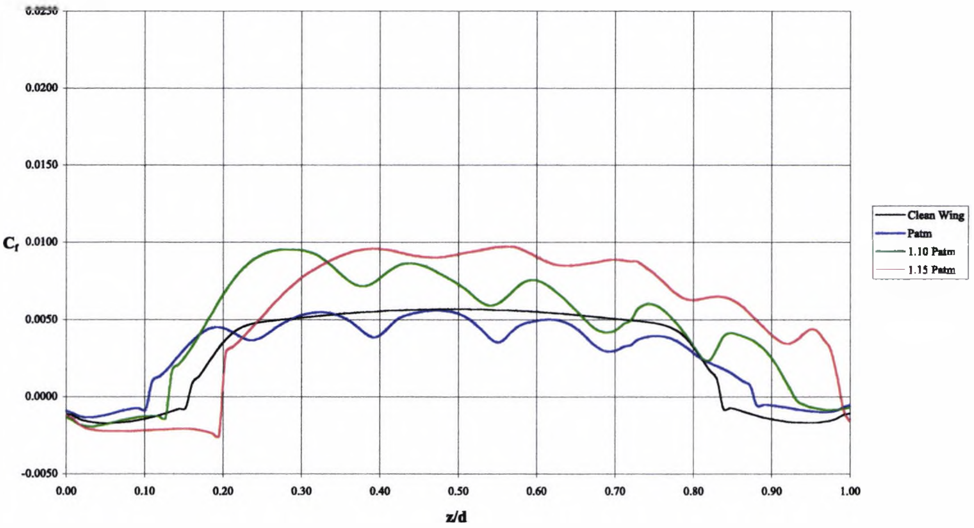

Figure 5.65: Lateral C_f distribution at 40% chord, $\alpha = 29^o$.

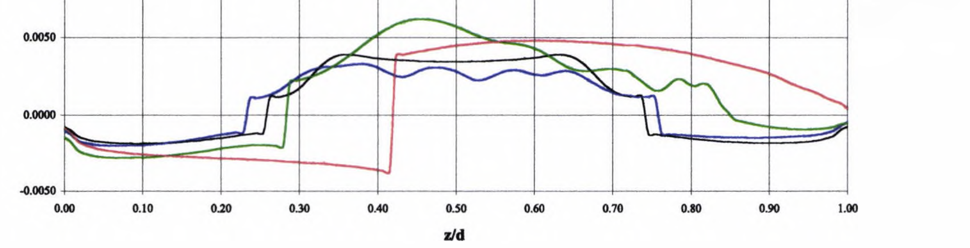

Figure 5.66: Lateral C_f distribution at 50% chord, $\alpha = 29^o$.

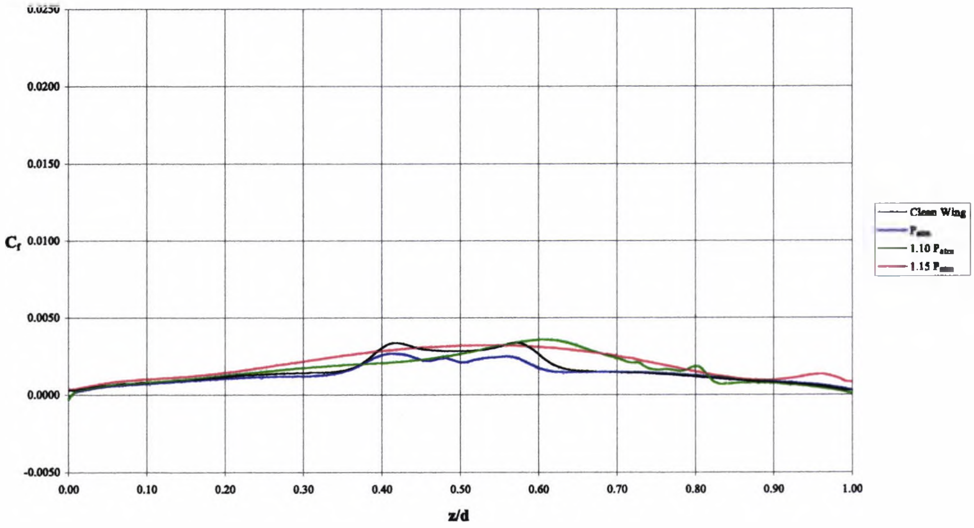

Figure 5.67: Lateral C_f distribution at 60% chord, $\alpha = 29^o$.

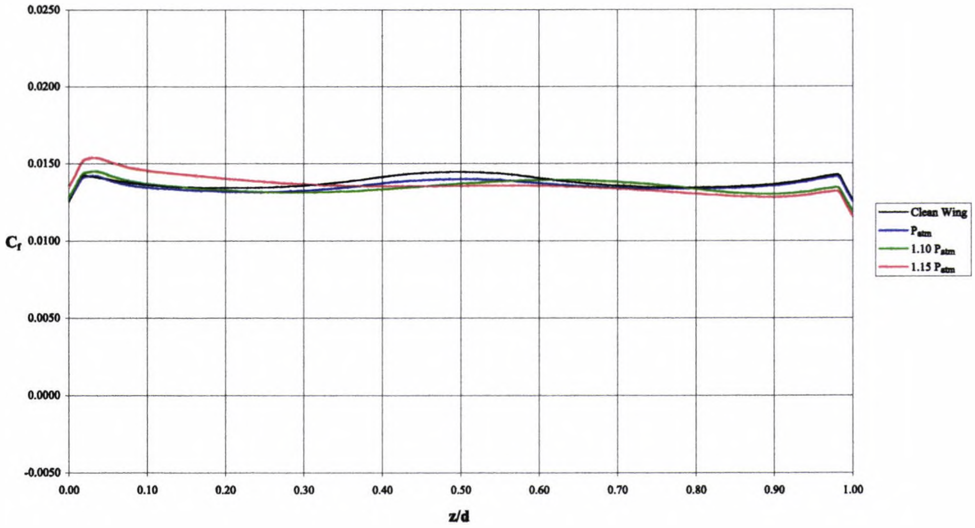

Figure 5.68: Lateral C_f distribution on the vane at 70% chord, $\alpha = 29^o$.

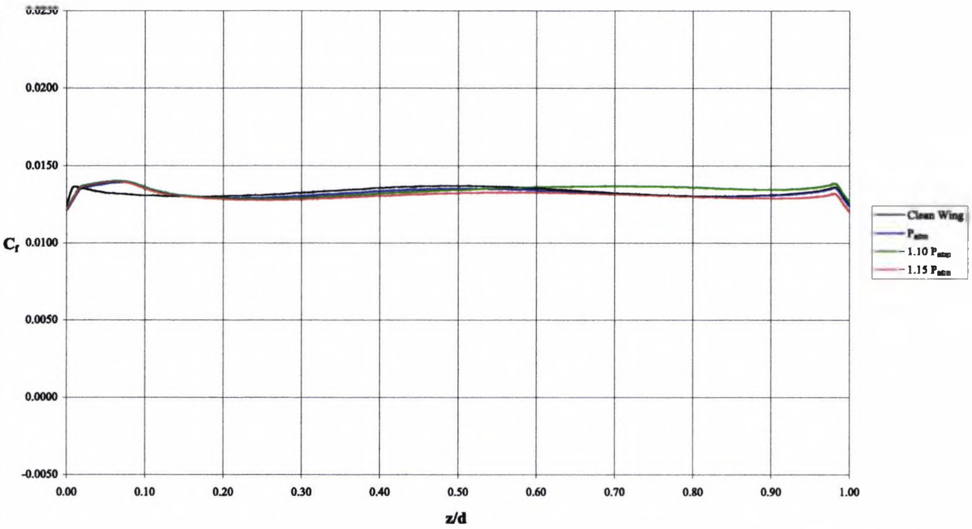

Figure 5.69: Lateral C_f distribution on the flap at 90% chord, $\alpha = 29^o$.

5.5.5 Effectiveness of Air Jets

The uncertainty about AJVG derived shear stress enhancements at the various locations about the model can be removed by integrating the difference in $C_{f\ ajvg}$ and $C_{f\ Clean\ Wing}$ across the span at each chord position. The author has performed such calculations using equation 5.2. The results from these calculations are presented in Figure 5.70 as a quantity called the air jet vortex generator enhancement factor, E_{ajvg}.

$$E_{ajvg} = \frac{d}{z}\int_{\frac{z}{d}=0}^{\frac{z}{d}=1} (C_{f\ ajvg} - C_{f\ Clean\ Wing}) \left(\frac{z}{d}\right) \tag{5.2}$$

Figure 5.70 shows that the AJVGs are most effective on the mainplane. At the mainplane chords, the AJVG model with the highest blowing pressure is the most effective with the lowest blowing pressure being the least effective. The AJVG model with $P_{ajvg} = P_{atm}$ is only providing a benefit in C_f over the clean wing up to 30% chord. At all other locations this model shows inferior C_f distributions at the chords examined.

There is one exception to this trend and it occurs at 50% chord in the AJVG model where $P_{ajvg} = 1.15P_{atm}$. There is a sudden decrease in E_{ajvg}. Despite this sudden decrease, E_{ajvg} remains positive at this location. This sudden decrease in E_{ajvg} can be explained by Figure 5.66 where a significant deterioration in the shear stress occurs at this location in this AJVG model.

The vane element in all the AJVG models is predicted to be better in the clean wing model as all values of E_{ajvg} at 70% chord are seen to be less than zero. The flap is seen to have a very small benefit from the two highest values of P_{ajvg} with E_{ajvg} being just above zero.

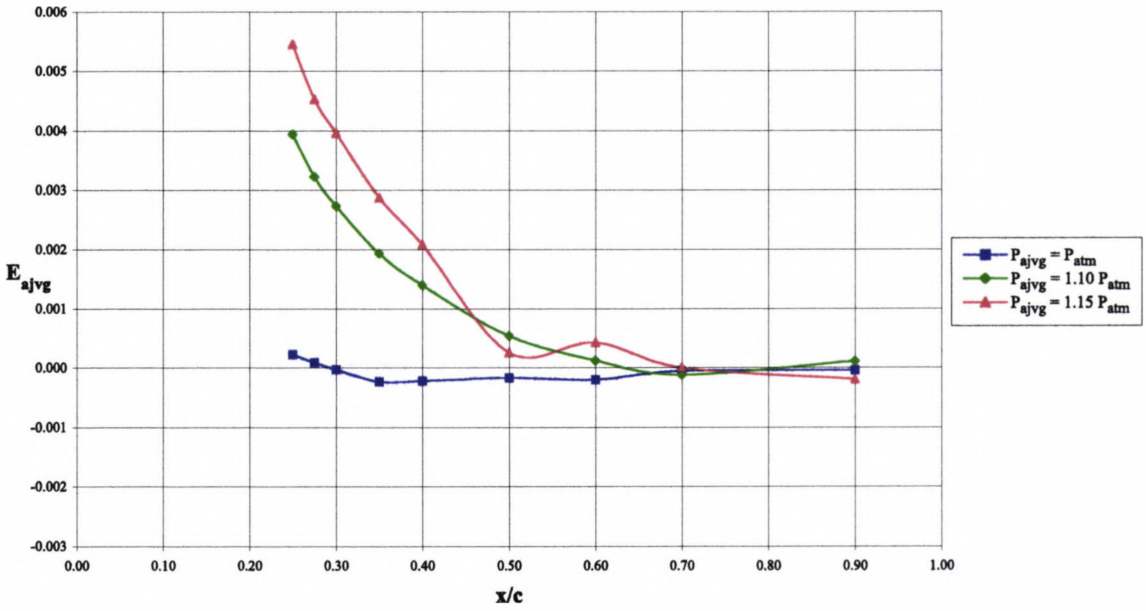

Figure 5.70: E_{ajvg} versus $\frac{x}{c}$ for all AJVG models.

5.5.6 Predicted C_p about Air Jet Models

The relative locations of the 8%, 42% and 92% span locations with respect to the location of the AJVGs are presented in Figure 5.71. The initial directions of the air jet efflux are also illustrated. The author has included this diagram in an effort to clarify that the AJVGs are blowing towards the plane at 8% span, that there is one air jet on either side of the plane at 42% span and that the AJVGs are blowing away from the plane at 92% span.

At 8% span, a comparison of the clean wing and AJVG model pressure distributions in Figure 5.72 shows that the effect of the AJVGs is seen mostly on the mainplane from the leading edge up the 30% chord position of the model. The clean wing C_p distribution suggests that the flow separates as early as 30% chord. The C_p on the lower surface are reduced by the use of the AJVGs but there is only a noteworthy decrease in the peak suction C_p when P_{ajvg} is at least 10% above P_{atm}. A comparison of the C_p of the AJVGs models with P_{ajvg} at 10% and 15% above P_{atm}, shows that the mainplane with AJVGs and $P_{ajvg} = 1.10P_{atm}$ is predicted to be more capable of decreasing the C_p over the lower mainplane surface at this location when compared to the case with $P_{ajvg} = 1.15P_{atm}$.

There is no flow separation in evidence on the vane but the use of the AJVGs is predicted to have an effect on the C_p distribution about this element. Figure 5.72 shows that $P_{ajvg} = P_{atm}$ increases the lower surface C_p on the vane. It is only when P_{ajvg} is 15% above P_{atm} that any significant reduction of the C_p on the lower surface of the vane is seen. At 8% span, when compared to the clean wing model, there is no significant change in the C_p distribution about the flap in any of the AJVG models. At 42% span the C_p distribution about the AJVGs model with $P_{ajvg} = P_{atm}$ is close to that of the clean wing. Figure 5.73 shows that the clean wing C_p about the vane and flap are more favourable than those produced by the AJVGs with $P_{ajvg} = P_{atm}$. Thus, the discussion about the pressure distribution at this location will focus on the mainplane and to a lesser extent, the vane.

At 42% span, it is only with $P_{ajvg} > P_{atm}$ that we see any improvement in the C_p. Figure 5.73 shows that the peak suction C_p on the mainplane decreases with an increase in P_{ajvg}. Also, with the exception of an increase in the lower surface mainplane C_p between 18% and 24% chord, all other C_p predicted on the mainplane of these two AJVG models are seen to decrease. On the mainplane, this local increase in C_p is caused by the interaction of the co-rotating vortices on either side of the plane at 42% span where the C_p are taken. After 24% chord all C_p on the lower mainplane surface remain well below those of the clean wing and the jet model with $P_{ajvg} = P_{atm}$.

Figure 5.73 also shows that the C_p about the vane are improved with increased blowing pressure but the effect is restricted to the vane's leading edge region and is much smaller than that seen on the mainplane. The peak suction C_p on this element are seen to decrease only when the $P_{ajvg} > P_{atm}$ and the lowest peak suction C_p in this plane is produced when $P_{ajvg} = 1.15P_{atm}$.

The C_p about the various models in the plane at 92% span are presented in Figure 5.74. The use of the AJVGs does not produce any clear enhancement of the C_p distribution about the mainplane at this location. The most promising AJVG results are predicted to occur when $P_{ajvg} = P_{atm}$ and the effect on the C_p distribution is best described as marginal. The worst result is seen when $P_{ajvg} = 1.15P_{atm}$.

The C_p distribution about the vane at 92% span is not improved upon by the use of the AJVGs because the lower surface pressures are seen to increase for the most part. The two highest AJVG blowing pressures produce very similar pressure distributions about this element but the most favourable pressure distribution produced by the use of the AJVGs is predicted to occur when $P_{ajvg} = P_{atm}$. The C_p distribution about the flap is predicted to be insensitive to the introduction of the AJVGs and any change in P_{ajvg}.

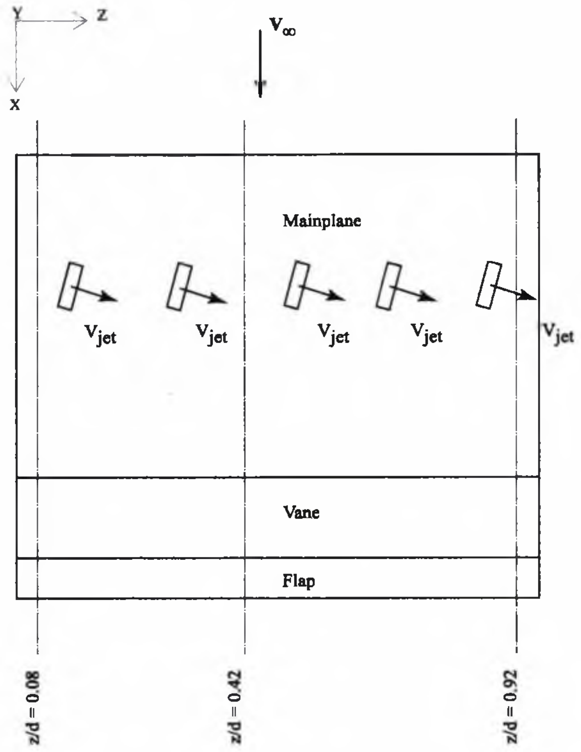

Figure 5.71: Relative location of cut planes and AJVGs.

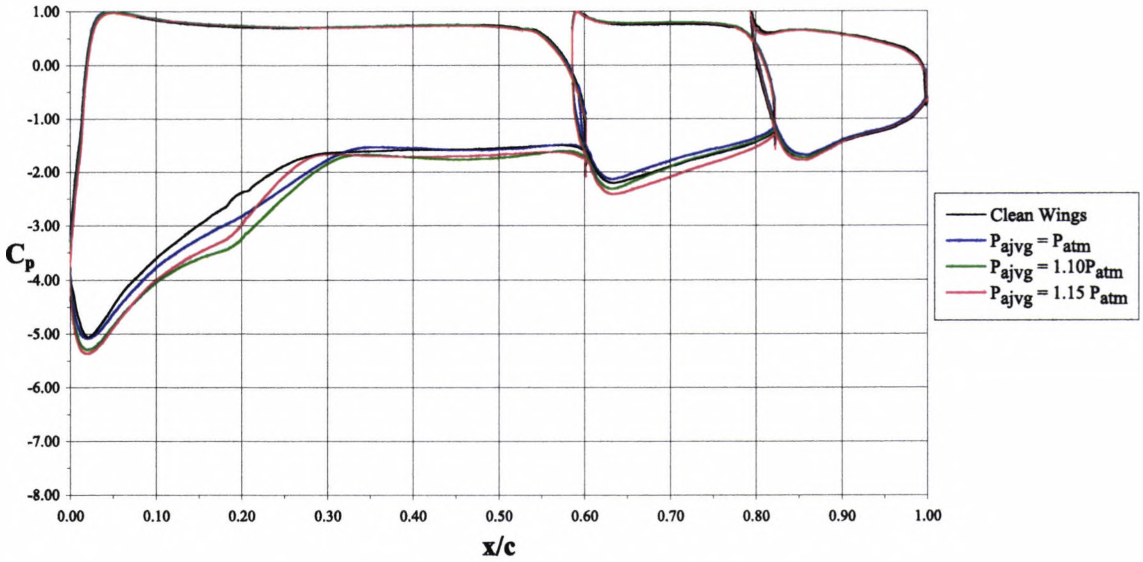

Figure 5.72: Predicted C_p about AJVG wing at 8% span, $\alpha = 29^o$.

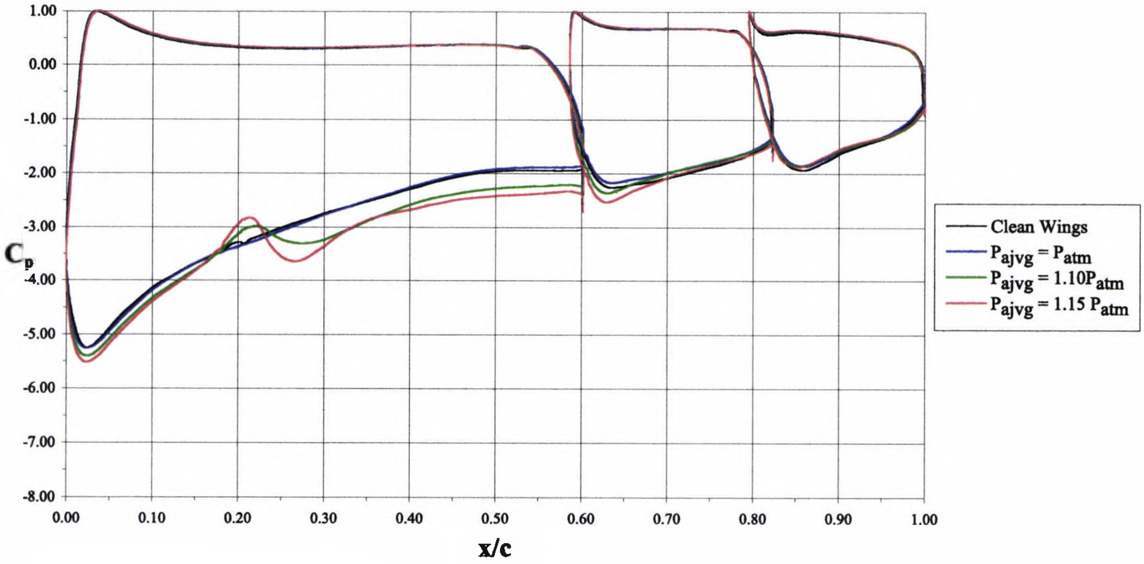

Figure 5.73: Predicted C_p about AJVG wing at 42% span, $\alpha = 29^o$.

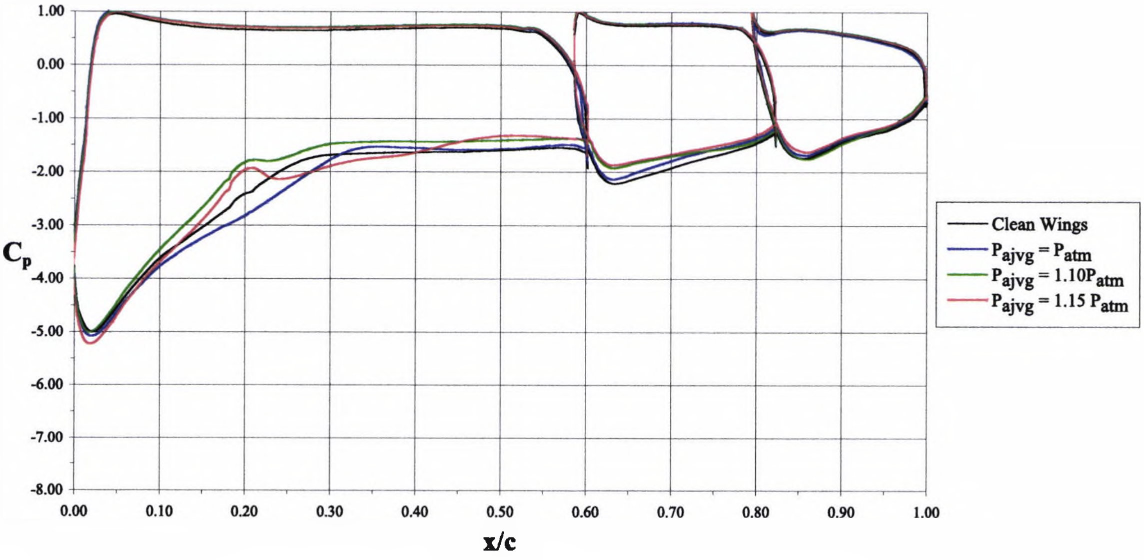

Figure 5.74: Predicted C_p about AJVG wing at 92% span, $\alpha = 29^o$.

5.5.7 Predicted Trailing Edge C_p with Air Jets

An examination of the element trailing edge C_p provides another indication about the complexity of the effect of the AJVGs on the performance of this high downforce model. The trailing edge C_p on the mainplane and vane elements provide an indication of the predicted dumping velocities on these elements. The predicted trailing edge C_p on the flap provides an indication of how well the Kutta condition is satisfied at the flap trailing edge for the wing when the AJVGs are used.

The mainplane trailing edge C_p from the various models are presented in Figure 5.75. A decrease in the trailing edge dumping velocity across the entire mainplane is predicted when $P_{ajvg} = P_{atm}$. This would increase the peak suction C_p on the vane. Indeed, Figures 5.72 through 5.74 show that all the clean wing peak suction C_p for the vane are lower than the AJVG models with $P_{ajvg} = P_{atm}$.

It is further seen in Figure 5.75 that increasing P_{ajvg} has the benefit of decreasing the mainplane trailing edge C_p. However, these lower trailing edge C_p do not extend across the entire mainplane span. With the exception of the AJVGs with $P_{ajvg} = P_{atm}$, the spanwise extent of the benefits seen are proportional to P_{ajvg}. Thus the most favourable result is predicted to occur when $P_{ajvg} = 1.15P_{atm}$. None of the AJVG equipped mainplanes achieve trailing edge C_p lower than that of the clean wing across the entire mainplane span.

The vane trailing edge C_p presented in Figure 5.76 show a trend similar to those on the mainplane. There is a minimum value of P_{ajvg} required to decrease the vane trailing edge C_p. It is seen that $P_{ajvg} = P_{atm}$ is actually detrimental to the dumping velocity on the vane because the trailing edge C_p for this value of P_{ajvg} at most spanwise locations are higher than those of the vane from the clean wing configuration. These higher trailing edge C_p are an indication of the lower trailing edge velocities in the flow field. The higher values of P_{ajvg} produce increasingly higher dumping velocities at the vane trailing edge but these higher dumping velocities do not persist across the entire span. The lower vane trailing edge C_p for the higher values of P_{ajvg} are not predicted to induce any significant changes in the peak suction C_p on the flap. The vane trailing edge C_p are all greater than those of the mainplane. This is an indication of the stagewise pressure recovery on the elements of high downforce systems as discussed by Smith (1975).

The flap trailing edge C_p from the various models are presented in Figure 5.77. These C_p indicate that all the models are predicted to have some degree of flow separation because none of the trailing edge C_p are greater than zero. However, all of the AJVG models do produce some increase in the C_p at various locations on the flap trailing edge. The models with $P_{ajvg} = P_{atm}$ produce the most consistent result with all the trailing edge C_p being greater than those of the clean wing flap.

Figure 5.77 also shows that there is a clear increase in the flap trailing edge C_p between 55% span and 100% span for the two highest AJVG blowing pressures. Of the two values of P_{ajvg}, the more favourable Kutta condition between these spanwise locations is predicted to occur when $P_{ajvg} = 1.10P_{atm}$. These flap trailing edge C_p are consistent with a reduction in the amount of flow separation but not with its elimination.

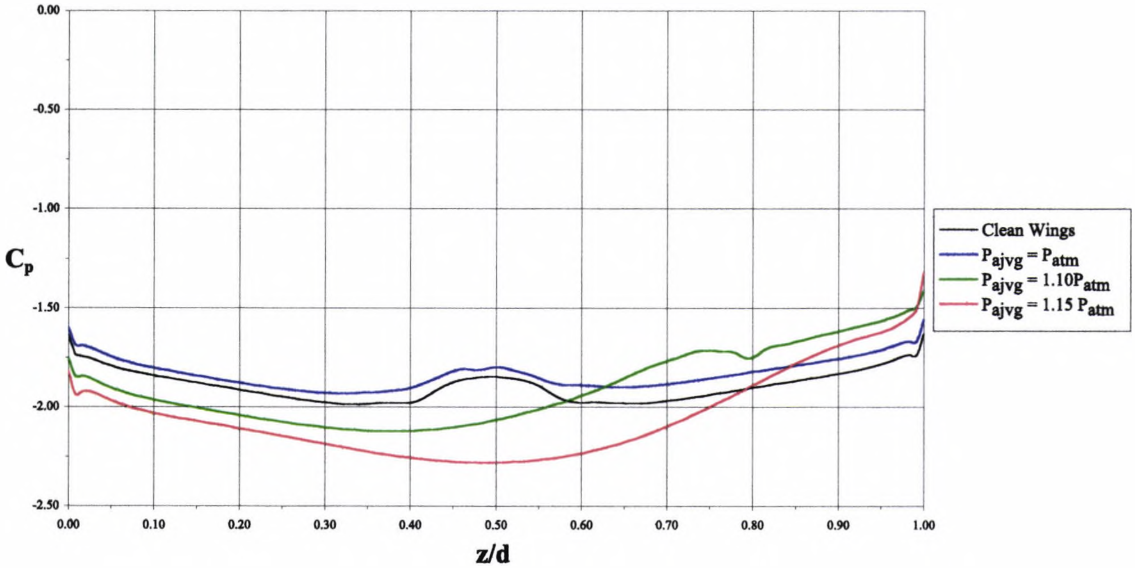

Figure 5.75: Comparison of predicted C_p along mainplane trailing edge, $\alpha = 29^o$.

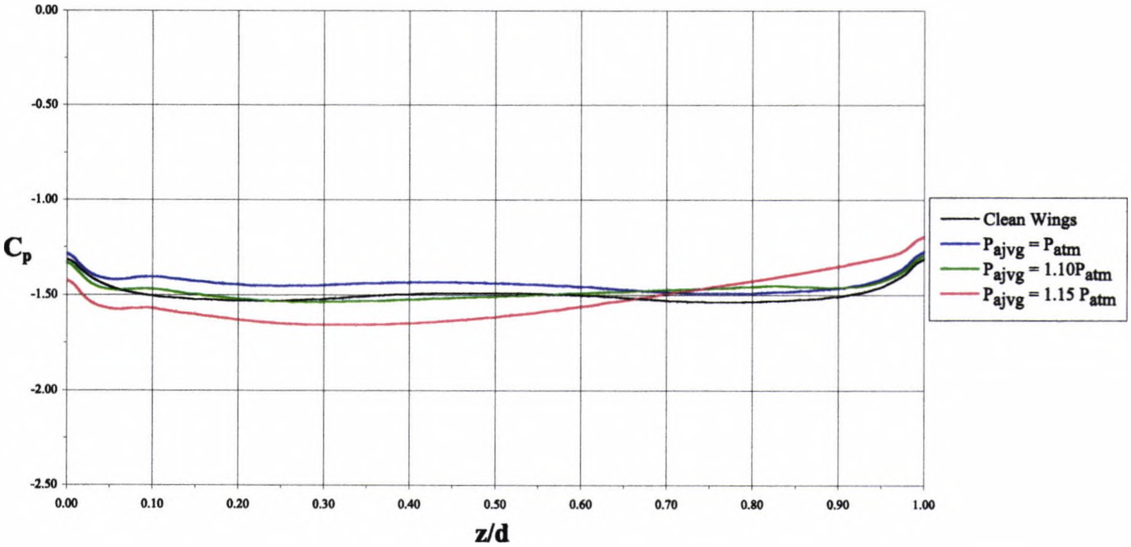

Figure 5.76: Comparison of predicted C_p along vane trailing edge, $\alpha = 29^o$.

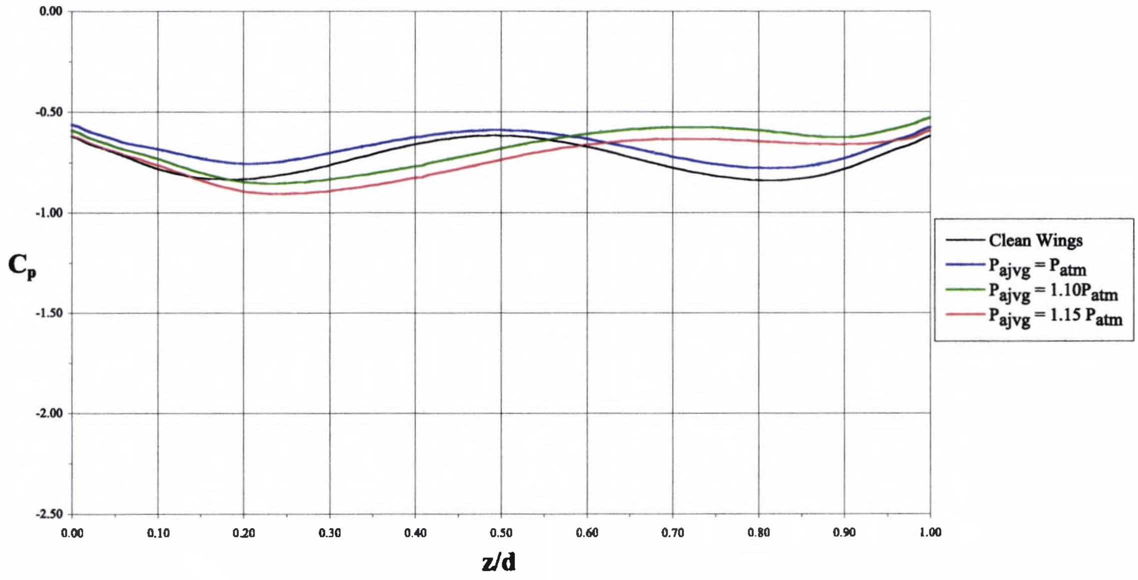

Figure 5.77: Comparison of predicted C_p along flap trailing edge, $\alpha = 29^o$.

5.5.8 Predicted Loads with Air Jets

The most important indication of the effect of the AJVGs lies with the changes in downforce predicted for each model. The predicted C_L, C_D and $\frac{L}{D}$ from the smaller clean wing models and the AJVG equipped models are listed in Tables 5.1, 5.2 and 5.3. The 240 mm span wing planform area of 0.075 m^2 was used as the reference area to non-dimensionalise the aerodynamic forces. The definition of the aerodynamic efficiency used in the discussion follows the Formula One aerodynamic convention, namely to ignore the negative sign of the lift. Thus $\frac{L}{D}$ is actually $|\frac{L}{D}|$.

The use of the AJVGs is predicted to increase the C_L generated by the high downforce system. It is also predicted that a blowing pressure of $P_{ajvg} = P_{atm}$ and all subsequent increases in P_{ajvg} produce additional increases in the C_L produced by the high downforce system. Table 5.1 shows that most of the increase in C_L predicted with the AJVG equipped models is derived from the increased loading on the mainplane. Comparisons made between the clean wing and AJVG models show that the changes of the vane and flap C_L remain relatively small.

The maximum increase in C_L with the use of AJVGs is predicted to occur with $P_{ajvg} = 1.15P_{atm}$. The use of this blowing pressure sees the high downforce system produce a C_L of -3.789 compared to a clean wing C_L of -3.312 for an increase of 14.4%. The use of the AJVGs at this blowing pressure is also predicted to increase the C_D from 0.923 for the clean wing to 0.954 for the AJVG equipped wing. This represents an increase in C_D of 3.35%.

Table 5.2 shows that the predicted C_D on each element from the clean and AJVG equipped wings. The use of the AJVGs is predicted to increase the mainplane C_D and each subsequent increase in P_{ajvg} also produces a corresponding increase in the mainplane C_D. Taking the range of C_D between the clean wing and AJVG case with $P_{ajvg} = 1.15P_{atm}$, there is a 158% increase in the predicted mainplane C_D from 0.017 to 0.044. The vane and the flap elements are predicted to have higher C_D than the mainplane but in terms of changes in drag, these elements are fairly insensitive to the use of AJVGs and any changes in P_{ajvg}.

The use of AJVGs is predicted to improve the aerodynamic efficiency of the high downforce system. With the exception of the AJVG equipped model with $P_{ajvg} = 1.10P_{atm}$, the predicted trend in $\frac{L}{D}$ shows that each subsequent increase in P_{ajvg} in predicted to produce additional increases in $\frac{L}{D}$. The case with $P_{ajvg} = 1.10P_{atm}$ is predicted to have an $\frac{L}{D}$ of 3.837 which is 1.3% lower than the case with $P_{ajvg} = P_{atm}$ and $\frac{L}{D} = 3.887$. The maximum aerodynamic efficiency of 3.972 is predicted to occur with $P_{ajvg} = 1.15P_{atm}$. For comparison, the clean wing case is predicted to have an $\frac{L}{D}$ of 3.588. These increases in $\frac{L}{D}$ are predicted with each increase in P_{ajvg} despite the predicted increases in drag.

Table 5.1: Predicted Element C_L for Clean and AJVG Equipped Wing.

Numerical Model	**Mainplane C_L**	**Vane C_L**	**Flap C_L**
Clean Wing 240 mm Span	−2.592	−0.500	−0.222
Air Jets, $P_{ajvg} = P_{atm}$	−2.866	−0.488	−0.218
Air Jets, $P_{ajvg} = 1.10P_{atm}$	−2.982	−0.508	−0.222
Air Jets, $P_{ajvg} = 1.15P_{atm}$	−3.062	−0.506	−0.221

Table 5.2: Predicted Element C_D for Clean and AJVG Equipped Wing.

Numerical Model	**Mainplane C_D**	**Vane C_D**	**Flap C_D**
Clean Wing 240 mm Span	0.017	0.448	0.458
Air Jets, $P_{ajvg} = P_{atm}$	0.025	0.435	0.459
Air Jets, $P_{ajvg} = 1.10P_{atm}$	0.034	0.455	0.478
Air Jets, $P_{ajvg} = 1.15P_{atm}$	0.044	0.453	0.457

Table 5.3: Predicted Assembly Loads for Clean and AJVG Equipped Wing .

Numerical Model	C_L	C_D	$\frac{L}{D}$
Clean Wing 240 mm Span	−3.312	0.923	3.588
Air Jets, $P_{ajvg} = P_{atm}$	−3.573	0.919	3.887
Air Jets, $P_{ajvg} = 1.10P_{atm}$	−3.711	0.967	3.837
Air Jets, $P_{ajvg} = 1.15P_{atm}$	−3.789	0.954	3.972

5.6 Experimental Results

The experiments were carried out focused on the performance of the high downforce system at 19^o angle of incidence. From other experiments performed, it was determined that 19^o represented the approximate $\alpha C_{L\,max}$, the angle at which maximum lift occurred. The author used this angle as a validation case for the numerical results and also to establish the performance of wing incorporating the AJVGs.

Flow visualisation results are presented to show the global effect of the active and quiescent AJVGs on the surface flow fields over the high downforce system. A mixture of black pigment and mineral oil was applied to the model as uniform sized droplets with a calligrapher's pen. Each droplet was approximately 2 mm to 3 mm wide after spreading. Each application of this mixture took approximately 20 minutes. After applying the solution, the wind tunnel was brought up to a speed of 35 m/s and this speed was maintained for approximately 4 minutes to ensure that the oil traces had dried sufficiently so that they would not flow under gravity while being photographed.

However some problems did arise in the flow visualisation exercise for which the author did not find a reasonable solution. The surface flow visualisation at high angles on incidence was affected by the fact that transient effects were encountered at tunnel start up. The air jet flows established themselves on the mainplane surface and inthe upper corner before that of the local freestream. This gave the false impression that the high downforce model was experiencing more severe flow separation than the clean wing.

Black wool tufts approximately 1.5 mm in diameter were applied in the corners of the model and along the span of the various elements with transparent tape. Eventually they were only used as a diagnostic tool in the upper corner of the model because they proved to difficult to photograph while the wind tunnel was being operated.

Detailed effects of the active and quiescent AJVGs are presented in the form of the measured pressure distributions about the elements of the high downforce system. As with the predicted pressure distributions, the measured pressure distributions are discussed in terms of the peak suction C_p on each element and on the mainplane in particular. The effect of the use of the AJVGs on the element trailing edge C_p is also discussed.

The sectional c_l, c_d and $\frac{l}{d}$, derived from the integrated pressure distributions are also presented to provide an estimate of the effect of the AJVGs on the aerodynamic forces on the wing.

5.6.1 Flow Visualisation on Clean Wing at 19^o Incidence

Figure 5.78 shows the oil drop based surface flow visualisation on the surface of the high downforce system with quiescent AJVGs. The general sense of the flow pattern is in the freestream flow direction along the mainplane surface. Figure 5.78 shows that some of the oil traces possess a small spanwise component. This could be interpreted as evidence of an adverse pressure gradient acting on the flow field over the mainplane in these regions.

Other regions along the mainplane show flow patterns that have a strong fore-aft sense along the mainplane surface but the oil patterns end before reaching the mainplane trailing edge despite having enough oil to complete the path. This is evidence of trailing edge flow separation as it suggests that there is not enough momentum in the flow field to carry the oil trace to the mainplane trailing edge.

The vane exhibits fully attached flow along the entire span and this is visualised by the oil traces that have definite flow patterns going from the region of the mainplane-vane slot directly to the vane trailing edge. There is a small disturbance in this general flow pattern in the immediate area of the slot gap spacer but this does not lead to flow separation as the oil traces are seen to flow to the vane trailing edge.

In Figure 5.78, the flap is seen to be operating with largely attached flow but with some areas of very low momentum on the upper half of its span. The momentum in this area is not enough to sustain such the oil traces up to the flap trailing edge against the force of gravity. They are seen to almost reach the flap trailing edge and then turn through 90^o to flow down the flap approximately parallel to its trailing edge. The lower regions of the flap are seen to have oil traces that have little to nothing in the way of a spanwise component. The flow visualisation in Figure 5.78 shows that the slot gap spacer does cause some disturbance to the flow field on the flap and this should be considered as a contributing factor to the flow features seen on the upper regions of the flap because the flow field immediately downstream is significantly disturbed.

Figure 5.79 shows the several tufts on the upper wall of the wind tunnel test section in the wind-on conditions. In the upper photo of this figure, oil traces can be seen on the elements of the high downforce system with the AJVGs quiescent. The lower photograph in Figure 5.79 shows the oil traces on the lower span of the high downforce system and the floor of the wind tunnel test section. The tufts shown in the upper photograph were used mainly for diagnostic purposes during testing. The flow visualisation on the tunnel floor shows much more information. In the lower photograph, the oil traces show the low momentum wake region as an area of little or no downstream development of the oil traces. The wake region is immediately downstream of the vane and flap elements. The presence and proximity of the wake to the flap element is further evidence that the flap trailing edge is a region of low momentum which explains the tendency of a significant number of oil traces to flow down its span under the influence of gravity.

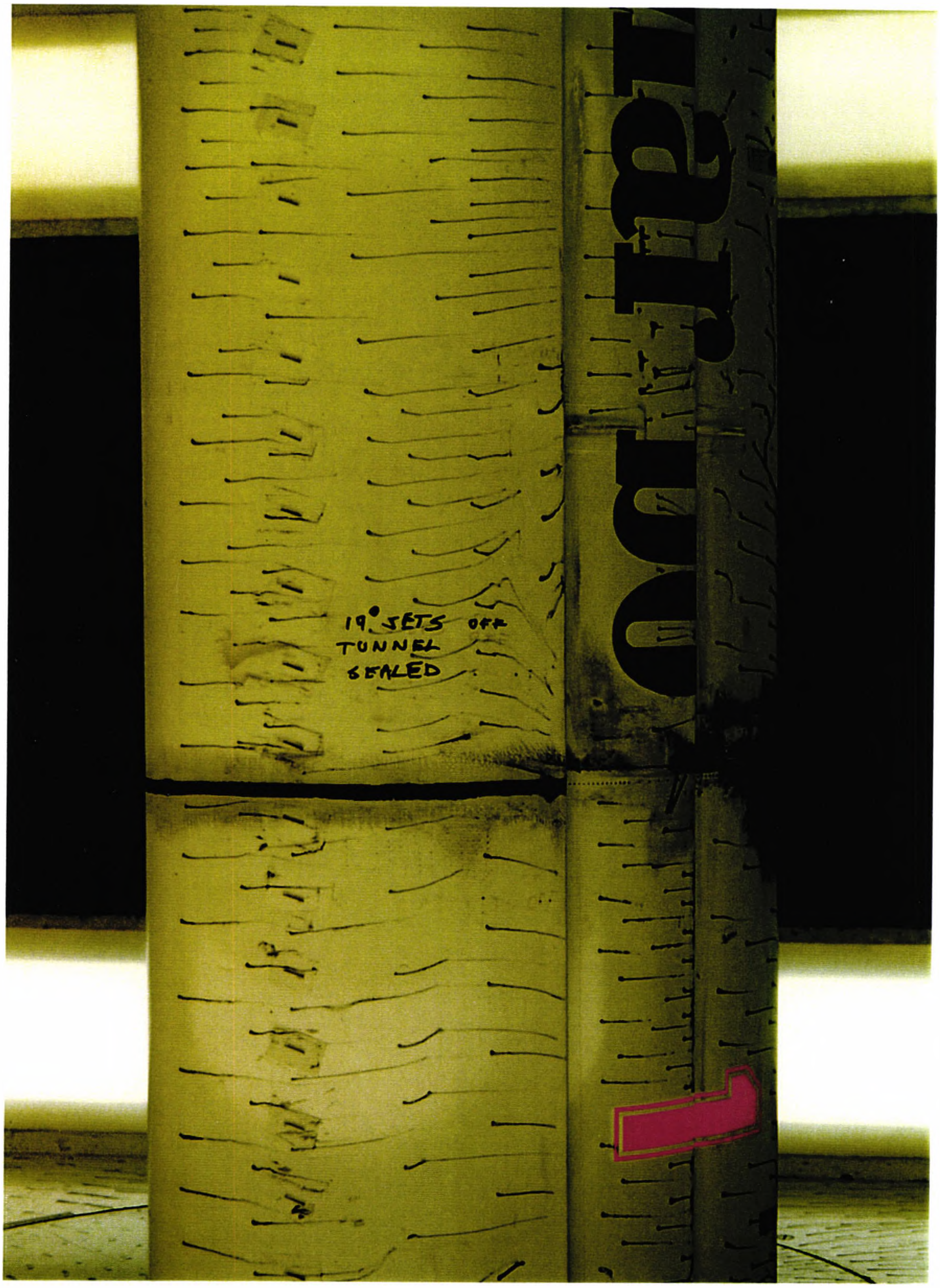

Figure 5.78: Surface flow visualisation on clean high downforce wing, $\alpha = 19^o$.

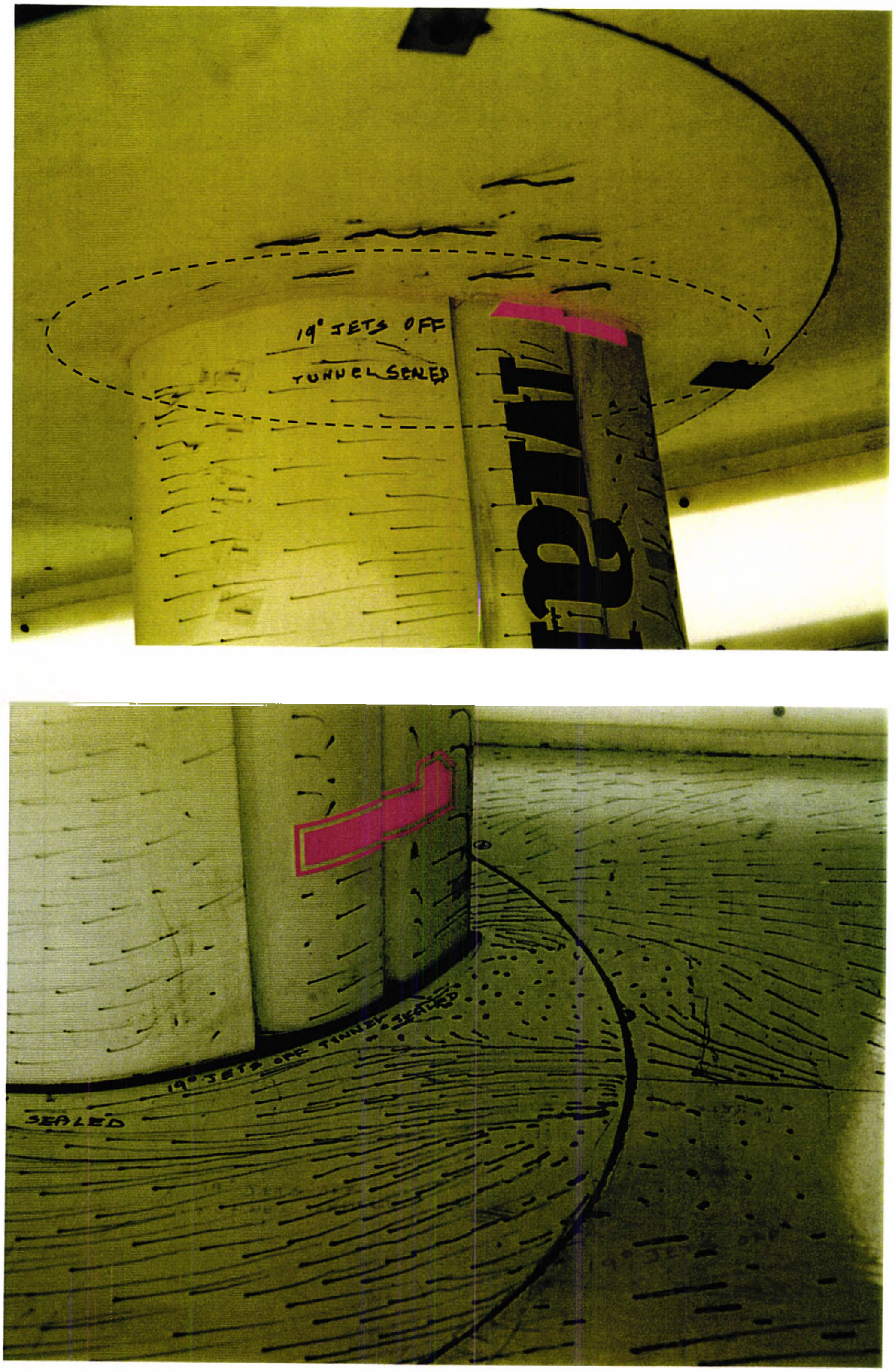

Figure 5.79: Flows on ceiling (top) and floor (bottom) with clean wing, $\alpha = 19^o$.

5.6.2 Flow Visualisation on Wing with Air Jets at 19^o Incidence

Figure 5.80 shows the oil based flow visualisation on the low pressure surfaces of the high downforce wing with the AJVGs active and oriented at 19^o incidence. The flow pattern on the wing is noteworthy due to the flow field on the upper span of the mainplane. A closer view of the upper section of the wing presented in Figure 5.81 shows that the oil traces on this part of the mainplane possess a strong downward spanwise component. This flow pattern was caused by the air jet flow establishing itself over the mainplane surface and being modified by the presence of the upper tunnel wall before the effect of freestream flow was established over the mainplane. This flow pattern is misleading because it suggests that this region of the wing was operating with flow separation.

Figures 5.80 and 5.81 show some evidence of fully attached flow on the mainplane when the AJVGs are in use. It can be seen that those oil traces with enough fluidity do reach the mainplane trailing edge. A comparison of Figure 5.80 with Figure 5.78 shows that the flow field in the former is improved in terms of the extent of attached flow.

The flow visualisation over the vane as seen in Figure 5.80 is somewhat inconsistent but there is enough evidence to show that this element was operating with fully attached flow. The evidence of fully attached flow on the vane comes from the oil traces on the upper span of this element. Some oil drops are seen to be underdeveloped on the lower span. This was due to the evaporation on the oil droplets before they could flow along the vane surface.

Flow visualisation on the flap also proved to be problematic due to the evaporation of some oil droplets before they could be influenced by the surface flow field. However, it can be seen in Figure 5.80 that the flap is operating with fully attached flow because the majority of the oil traces do attain the trailing edge. In some instances, there was excess oil after the oil trace has reached the flap trailing edge. When this occured, low momentum and gravity acted in concert to cause the excess oil to flow downwards and along the flap trailing edge.

5.6.3 Pressure Distribution about Clean Wing at 19^o Incidence

A listing of the peak suction and trailing edge C_p on each element is provided in Table 5.4 and Table 5.5 respectively. The clean wing pressure distribution and the effect of the use of air jets on this pressure distribution are presented in Figure 5.82. The predicted pressure distribution about the two-dimensional high downforce wing is also presented in this figure as part of the validation exercise. The results presented in Figure 5.82 were

Figure 5.80: High downforce wing with AJVGs at 19^o incidence.

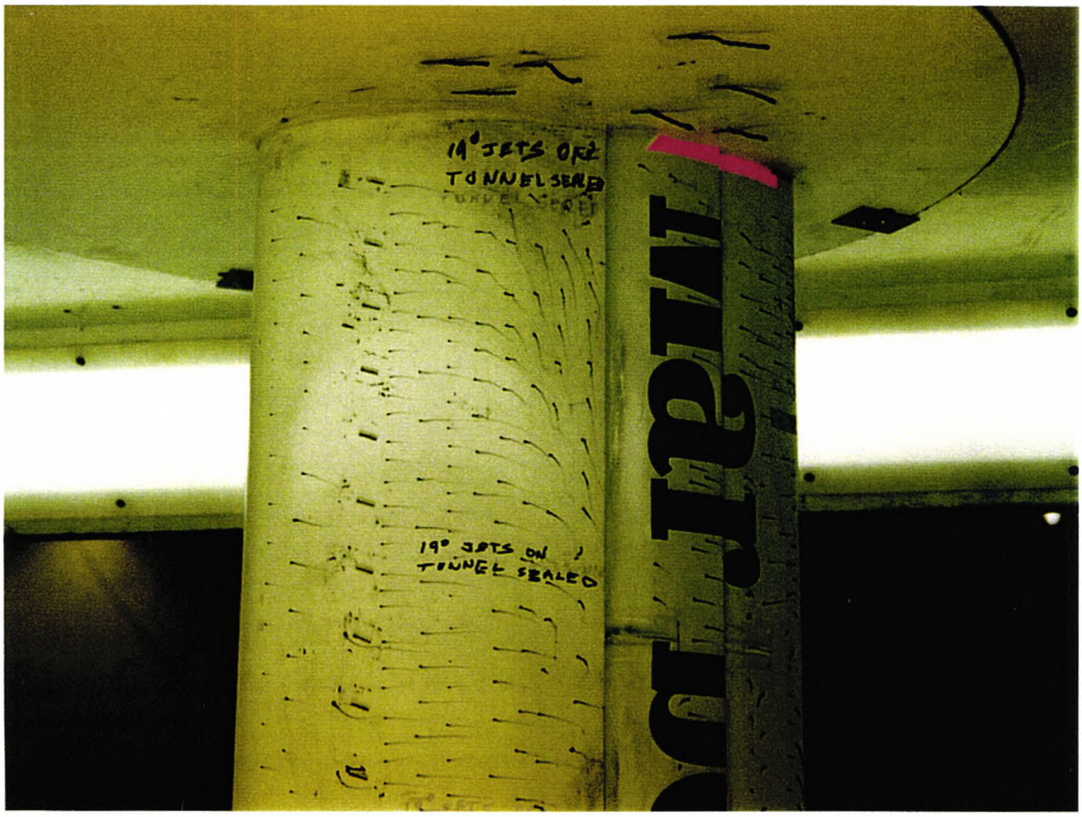

Figure 5.81: Close-up of upper span of wing with AJVGs at 19° incidence.

derived from the experimental and numerical high downforce wings oriented at 19^o angle of incidence.

The clean wing flow shows a measured peak suction C_p on the mainplane of -3.945 very close to the mainplane leading edge at approximately 3.7% chord. Immediately after the peak suction C_p is attained, a significant deceleration in the flow is noted as it negotiates the mainplane lower leading edge. This deceleration of the flow or increase in C_p continues until approximately the 45% chord position up to what is arguably the most noteworthy feature of the pressure distribution about the clean wing high downforce system.

Between 45% chord and the mainplane trailing edge at approximately 60% chord, the pressure distribution about this element shows evidence of an adverse pressure gradient on the lower surface of the mainplane. This is identifiable as the region on the lower surface C_p distribution where $\frac{dC_p}{d(\frac{x}{c})} \approx 0$. After this adverse pressure gradient, the mainplane experiences a trailing edge C_p of -1.215.

The pressure distribution about the vane is consistent with fully attached flow as presented in Figure 5.78. A peak suction C_p of -1.648 was recorded at approximately 63% chord. Thereafter, there is a steady increase in the C_p until the trailing edge where a C_p of -0.525 was measured. That the vane trailing edge C_p is higher than that measured on the mainplane is evidence of the stagewise pressure recovery on each lifting element as discussed by Smith (1975).

The flap pressure distribution exhibits a measured peak suction C_p of -1.154 at approximately 84% chord. There is a steady increase in the pressure after the peak suction C_p is achieved until 90% chord where a sudden but small increase in the C_p or a deceleration in the flow is seen. The trend on increasing C_p continues until the trailing edge where a C_p of -0.35 is measured. The fact that the flap trailing edge C_p is negative is an indication that the Kutta condition is not satisfied at the flap trailing edge and that there is flow separation somewhere on the system. It is known that flow separation occurs on the mainplane from reviewing the flow visualisation that has been presented in Figure 5.78.

5.6.4 Pressure Distribution about Wing with Air Jets at 19^o Incidence

The use of air jets is responsible for significant qualitative and quantitative changes to the lower surface pressure distributions about all of the elements in the high downforce wing. The upper surface C_p on all the elements is effectively constant when compared those measured with the air jets quiescent.

Referring to Figure 5.82, it is seen that the main flow field as modified by the interaction with the air jets produces a peak suction C_p of -4.593 at the 4.7% chord position. After the peak suction is attained on the mainplane, the pressure recovery begins immediately but the C_p measured on the lower mainplane surface are seen to be significantly lower than those measured on the clean wing.

The effects of the adverse pressure gradient at 45% chord on the lower mainplane surface are absent with the use of air jets as the C_p experience continuous recovery to the mainplane trailing edge where a C_p of -1.83 was measured. This is some 53.39% lower than that measured on the mainplane with the air jets quiescent. It indicates that the flow as modified by the air jets allows the mainplane boundary layer to leave the trailing edge with a higher velocity. This is also an indication of increased circulation on this element.

The effect of the air jets on the pressure distribution about the vane can be seen in Figure 5.82 as the vane is subjected to a lower C_p on the entirety of its lower surface. A peak suction C_p of -2.343 is measured on this element at approximately 63% chord. There is not an immediate recovery of the C_p after this peak suction is attained because a relatively flat C_p distribution persists until 67% chord. A steep recovery of the pressure is seen on this element until the trailing edge where a C_p of -0.525 is measured. This is

28.95% higher that the measured C_p at the same location when the air jets were quiescent. This significant increase the vane trailing edge C_p indicates that the vane is now sustaining a greater proportion of the stagewise pressure recovery that is possible without the use of the air jets.

The effect of the air jets on the flap pressure distribution is contrary to that seen on the mainplane and vane in that there is an increase in pressure over the lower flap surface. The use of air jets sees a peak suction C_p of -1.154 measured on the flap. This is some 21.17% higher than that achieved on this element with the air jets quiescent. After the peak suction C_p is attained, an immediate recovery, slightly steeper than that seen without the use of air jets, ensues until the flap trailing edge is reached where a C_p of 0.235 is recorded. This represents an increase of 167.14% over the flap trailing edge C_p with the air jets quiescent. The fact that the flap trailing edge C_p is positive indicates that the Kutta condition is satisfied at the flap trailing edge and that there is no separation on the high downforce system.

5.6.5 Comparing Predicted and Experimental Pressures at 19^o Incidence

The predicted pressure distribution at 19^o incidence about the high downforce wing is included in Figure 5.82. The predicted results can be compared directly to those results derived from the experimental pressure distribution about the clean wing. It is seen in Figure 5.82 that the predicted and experimental clean wing pressure distributions are qualitatively very similar and there is good agreement between the predicted and experimental results on the upper surfaces of all the elements. However, the lower surface C_p on the mainplane are significantly overpredicted including the peak suction C_p of -5.579. The predicted results also fail to capture the severity of the adverse pressure gradient seen in the experimental clean wing pressure distribution. Instead, there is a predicted pressure recovery to the mainplane trailing edge terminating with a C_p of -1.984.

The pressure distribution on the lower surface of the vane is also overpredicted when compared to the clean wing experimental results. A peak suction C_p of -2.171 is predicted at 64% chord on this element, some 31.7% lower than the measured peak suction. After this peak suction is achieved, there is a predicted pressure recovery terminating with a C_p of -0.892 at the vane trailing edge. This is 20.7% lower than the measured C_p at the same location.

In contrast to the mainplane and vane elements, an underprediction of the lower flap surface pressures affected by AJVGs is seen when compared to the clean wing pressure distribution. A peak suction C_p of -1.001 is predicted on this element. This predicted flap peak suction C_p is approximately 39% higher than the experimental peak suction C_p. A flap trailing edge C_p of -0.016 is predicted at the end of the pressure recovery. This is approximately 95% higher than the measured flap trailing edge C_p of -0.35.

A review of the pressure distributions in Figure 5.82, the predicted streamlines in Figure 5.3 and the predicted velocity vectors in Figure 5.4 shows that no flow separation is predicted on the two-dimensional model at 19^o incidence. This explains the overprediction of the lower surface pressures on the mainplane and the vane elements. The underprediction of the pressure distribution on the lower flap surface is due to the suppression of the peak suction by the circulation developed at the vane trailing edge that is in the opposite sense to that generated by the flap.

Table 5.4: Peak suction C_p on each element for clean and AJVG equipped wing.

Element	**Clean Wing**	**AJVGs**	**2D Prediction**
Mainplane Peak Suction C_p	−3.945	−4.953	−5.579
Vane Peak Suction C_p	−1.648	−2.343	−2.171
Flap Peak Suction C_p	−1.64	−1.154	−1.001

Table 5.5: Trailing edge C_p on each element for clean and AJVG equipped wing.

Element	**Clean Wing**	**AJVGs**	**2D Prediction**
Mainplane Trailing Edge C_p	−1.215	−1.830	−1.984
Vane Trailing Edge C_p	−0.739	−0.525	−0.892
Flap Trailing Edge C_p	−0.350	0.235	−0.016

5.6.6 Loads Generated by Wing at 19^o Incidence

The use of the air jets is seen to have a profound effect on the forces generated by the high downforce wing at 19^o incidence. These forces are presented in Tables 5.6, 5.7 and 5.8. The possibility of inaccuracies in the estimation of C_x and c_d as previously discussed

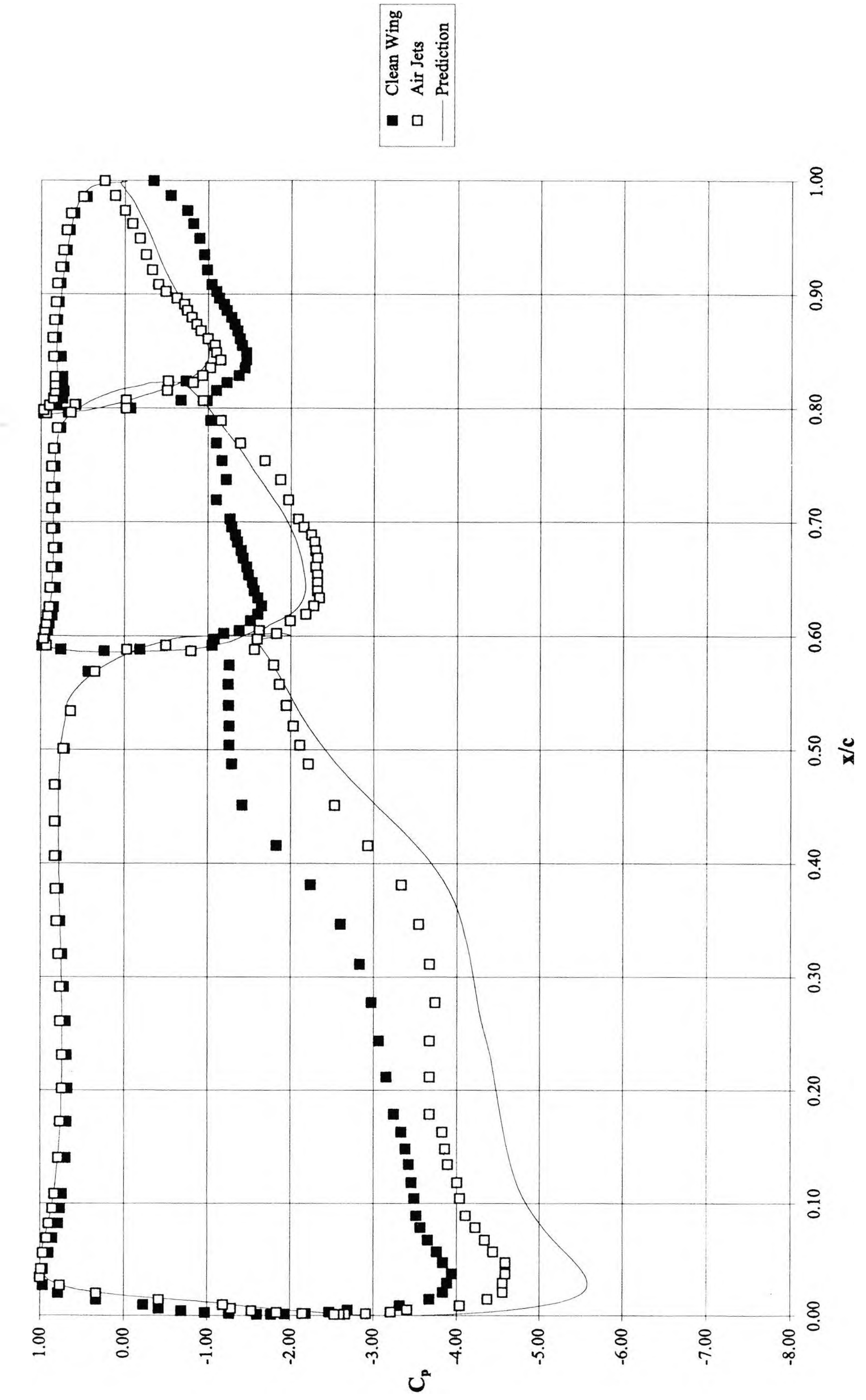

Figure 5.82: Pressure distributions about high downforce wing at 19^o incidence.

in Section 1.2.4 means that the trends in these parameters are more certain than the absolute values. The predicted forces derived from the two-dimensional high downforce calculations are also included in these tables so that direct comparisons can be made with the experimental values.

The C_n presented in Table 5.6 are arguably the most important useful aerodynamic force. It is seen that at 19^o incidence, the use of air jets increases the C_n generated by the mainplane and the vane elements but their use is accompanied by a decrease in the C_n generated by the flap. Despite the decrease in the flap C_n, the clean wing assembly generates a C_n of -2.858 and the use of AJVGs increases the assembly C_n to -3.317. This represents an increase of some 16.06%. It is seen that the predicted C_n for the assembly is -3.748 represents an overprediction of 31.14% when compared to the experimental, clean wing C_n. This overprediction is not unexpected when the C_p distributions in Figure 5.82 are reviewed.

Table 5.7 shows some experimental and predicted C_x at 19^o incidence. The experimental and predicted results all show that the mainplane experiences a negative C_x or a thrust at this angle. It is possible that this thrust is over predicted when compared to the experimental results but the possibility of inaccuracies could be decreased by the higher level of discretisation around the leading and trailing edge regions of the mainplane. This could also be the case for the predicted C_x on the vane and the flap.

The estimates of c_l and c_d derived from the experimental and predicted results are presented in Table 5.8. The estimated, experimental, clean wing c_l is -2.809. This is accompanied by a c_d of 0.674. The use of air jets is estimated to increase the c_l by 17.76% to -3.308 while bringing about a reduction of 1.78% in the c_d. While the magnitude of the reduction in c_d may be in doubt, it is highly likely that the use of the air jets does bring about some reduction in c_d because their use was seen to decrease the size of the wake immediately behind the high downforce wing.

The predicted c_d is estimated to be 0.166. This is 75.37% lower than the experimental clean wing estimate. This substantial difference between the prediction and experiment can be partly explained by the difference in the pressure distributions. It is also possible that the higher level of aerofoil surface discretisation in the numerical model plays a role in reducing the estimate of the predicted c_d.

Table 5.6: Normal force coefficients for high downforce wing at 19^o Incidence.

Element(s)	**C_n Clean Wing**	**C_n AJVGs**	**C_n 2D Prediction**
Mainplane	−3.309	−4.054	−4.729
Vane	−1.973	−2.498	−2.418
Flap	−1.692	−1.187	−1.228
Assembly	−2.858	−3.317	−3.748

Table 5.7: Axial force coefficients for high downforce wing at 19^o Incidence.

Element(s)	**C_x Clean Wing**	**C_x AJVGs**	**C_x 2D Prediction**
Mainplane	−0.275	−0.285	−0.401
Vane	0.255	0.111	0.052
Flap	0.015	0.030	0.019
Assembly	0.420	0.616	0.434

Table 5.8: Sectional lift and drag coefficients for high downforce wing at 19^o Incidence.

Case	c_l	c_d	$\frac{l}{d}$
Clean Wing	−2.809	0.674	4.167
AJVGs	−3.308	0.662	4.997
Prediction	−3.745	0.166	22.560

Conclusion

Numerical and experimental investigations have been conducted on an isolated high downforce rear wing using the upper rear wing of a contemporary Ferrari Formula One racing car. Through these investigations, it was established that the application of air jet vortex generators to such a rear wing could bring about an increase in the downforce generated.

The high downforce system comprised a mainplane, vane and flap elements with substantial aft camber. Some modifications were made to this model to facilitate its testing in the City University Low Speed T2 Wind Tunnel. These modifications included the installation of the air jet array at the 19% chord position on mainplane, the installation of static pressure orifices to all three elements and the addition of endplates to the model to allow it to be placed in the wind tunnel. There was not enough time to install boundary layer control devices on these endplates. This would have provided the facility to maintain a consistent nominal two-dimensional flow field at the wing-endplate junctions.

A Two-dimensional numerical study was performed on the high downforce model between the 3^o and 29^o angles of incidence in 2^o increments. The results from this study included predicted flow visualisation, pressure distributions, and estimated forces.

There was no predicted flow separation on any of the elements in the high downforce wing at any of the angles investigated. Instead, the streamlines and velocity vectors at 3^o, 19^o, and 29^o showed evidence of an increase in the severity of adverse pressure gradients about the wing with respect to an increasing angle of incidence.

A comparison of the predicted and measured pressure distributions and estimated forces for the 19^o case constituted a validation of the numerical results. There is good qualitative agreement between the predicted and measured pressures about the wing, but the quantitative agreement is characterised by an overprediction of the lower surface pressures on the mainplane and vane elements. This is accompanied by an underprediction of the pressures on the lower flap surface. It is also seen that the severity of the adverse pressure gradients on all elements is underpredicted.

While no flow separation is predicted about the high downforce model, the predicted flap trailing edge C_p is negative after 19^o angle of incidence. The predicted flap trailing edge C_p are seen to decrease further with increasing angle of incidence until α_{max} of 29^o. According to Smith (1975), it can be inferred from these predictions that $\alpha c_{l\,max}$ is approximately 19^o angle of incidence and that the predicted downforce decreases between approximately 19^o and 29^o.

The estimated forces derived from the two-dimensional numerical results are typical of high downforce wings. The predicted downforce curve exhibits a non-linear relationship with respect to the angle of incidence. There is a constant rate of increase in the predicted downforce between 3^o and 21^o. This represents a 2^o difference between the predicted $\alpha c_{l\,max}$ as inferred by the flap trailing edge C_p and the estimated forces. After 21^o, a progressive decrease in the downforce generated is predicted until α_{max} of 29^o.

Flow visualisation shows that increasingly adverse pressure gradients and not flow separation are responsible for this decrease in downforce. The drag is predicted to increase over the angle of incidence range in non-linear manner. The validation performed at 19^o incidence suggests that there is a general overprediction of the downforce and an underprediction of the drag.

All numerical three-dimensional models of the high downforce wing were oriented at 29^o angle of incidence. This angle of incidence was known to produce the greatest amount of flow separation on the mainplane in the experiments. The models used in the study were the 810 mm span clean wing, 240 mm span clean wing and the 240 mm span wing incorporating air jets.

The 810 mm span clean wing model was used as the three-dimensional grid refinement study to demonstrate that CFX-4.2 was capable of providing a grid independent solution. The predicted pressures and skin friction derived from these solutions show good agreement. No incipient flow separation was predicted on any of the wing elements. The only predicted flow separation occurred at the junctions formed by the mainplane and the test section walls of the virtual wind tunnel. These separated regions were caused by the interaction of the boundary layers on the mainplane and the test section walls under the influence of the adverse pressure gradients acting on the mainplane.

Due to limited resources, the air jets were only incorporated in the 240 mm span numerical high downforce models. The air jets were modelled with three values of the blowing pressure, P_{ajvg}. These were P_{ajvg} = 1.01 x 10^5 Pa, 1.11 x 10^5 Pa and 1.16 x 10^5 Pa. The results from the models with AJVGs were compared with a 240 mm span clean wing model. Separated regions at the mainplane-wall junctions were predicted on the 240 mm span clean wing. No incipient flow separation was predicted on any of the 240 mm span wing elements. Surface flow visualisation showed that the use of AJVGs was predicted to reduce but not eliminate the flow separation on the mainplane in these models. No flow separation was predicted on the vane and the flap elements. The size of the separated regions on the mainplane incorporating AJVGs was predicted to be inversely proportional to P_{ajvg}.

The application of AJVGs to the wing with different values of P_{ajvg} was predicted to increase the C_L generated when compared with that of the clean wing. These increases in C_L were achieved because the AJVGs were able to increase the skin friction over the lower mainplane surface to levels above those seen on the clean mainplane. The increase in skin friction was caused by enhanced mixing in the boundary layer adjacent to the lower surface of the mainplane. This mixing had its origins in the discrete vortices created by the interaction of air jet effluxes with the air flowing adjacent the lower surface of the mainplane. The resulting increased kinetic energy in this near-wall flow field aided in the suppression of the flow separation on the lower surface of the mainplane by allowing the boundary layer to be better able to negotiate the adverse pressure gradient.

The degree of enhancement of the shear stress was seen to be proportional to the increases in P_{ajvg}. However, due to the interaction of the AJVG effluxes with the boundary layers on the mainplane and the bounding walls, none of the models with AJVGs succeeded in eliminating the predicted flow separation on the mainplane. The predictions show that within the context of these models, the enhancement of the C_f is not uniform across the mainplane span. It is seen that a sudden reduction in C_f originates from interaction of the AJVG flow with the local flow field, the domain walls and the mainplane surface itself.

The solution derived from the clean 240 mm span wing predicted a C_L of -3.312 and a C_D of 0.923. The highest increase of C_L was predicted to occur on the AJVG equipped wing with $P_{ajvg} = 1.15P_{atm}$ with a C_L of -3.789 and a C_D of 0.954. This represents a 14.4% increase in the C_L for a 3.35% increase in drag. With the exception of the case with $P_{ajvg} = 1.10P_{atm}$, increases in P_{ajvg} were predicted to progressively increase the aerodynamic efficiency of the wing.

Experiments were focused on the clean wing and the wing incorporating AJVGs at 19^o angle of incidence. Flow visualisation with oil droplets reveals that the AJVGs eliminate the incipient separation seen on the mainplane when the AJVGs are quiescent. The use of AJVGs was also seen to bring about significant improvements in the pressure distribution about the high downforce wing. These improvements took the form of reduced pressures on the lower surfaces of the mainplane and the vane accompanied by improved lower surface pressure recovery on these two elements. The use of AJVGs was accompanied by a flap trailing edge C_p of 0.235 compared to -0.35 that was measured when the AJVGs are quiescent. This positive flap trailing edge C_p implies that the AJVGs eliminate the flow separation on the mainplane at this angle of incidence.

A comparison with the clean wing shows that at 19^o angle of incidence, the use of AJVGs increases the c_l and reduces the c_d. This is consistent with the results of the flow visualisation and the measured pressures. At 19^o angle of incidence, the clean wing c_l and c_d are estimated to be -2.809 and 0.674 respectively. The AJVGs increase the c_l by 17.76% to 3.308 while reducing the c_d by 1.78% from 0.674 to 0.662. This results in an improvement in $\frac{l}{d}$ from 4.167 with the clean wing to 4.997 when the AJVGs are in use.

The numerical and experimental results presented show that AJVGs may be capable of increasing the downforce produced by Formula One style high downforce rear wings. It may also be the case that greater benefits could be realised if the AJVGs are considered as an integral part of the high downforce design from the concept stage. This suggests that any wing designed with integral AJVGs would be inoperable without them.

Future Work

There is much scope for future numerical and experimental investigations into the application of AJVGs to Formula One high downforce rear wings. It is possible to conduct useful investigations on isolated models provided there is an appreciation for the operating environment for which such a wing is intended.

In any numerical study involving high lift and vortex generators, it is imperative that the prediction of flow separation be accurate and consistent. In Navier-Stokes fluid flow solvers, it would be beneficial to carry out numerical investigations on high lift devices incorporating AJVGs using other turbulence models. Investigations using low Reynolds number turbulence models such as the Spalart-Allmaras Turbulence Model and the Menter Shear Stress Transport (SST) model could improve the accuracy of the solutions. Such models forego the use of wall functions and in so doing are capable of resolving the near-wall velocity profiles. In the numerical investigations of Rumsey et al. (1998), the Spalart-Allmaras model is noted for its realistic predictions of the performance of multi-element, high lift aerofoils and wings up to $\alpha C_{L\,max}$ while the Menter SST model is capable of accurate and realistic predictions past $\alpha C_{L\,max}$.

The use of higher order turbulence models such as the differential Reynolds Stress model might be considered in an effort to address the excessive numerical dissipation for which the standard $k-\epsilon$ model is known. The dissipative nature of a turbulence model has a direct impact on the prediction of vortex persistence and the calculation of drag. Further improvements in the the estimation of drag might be realised by performing an integration of the velocity profiles in the predicted wakes downstream of the high downforce wing.

Any investigations involving a Navier-Stokes solution for a high lift flow must take in account the effect of streamline curvature on the performance of the turbulence model used for closure. Bradshaw (1973) and more recently Rumsey & Gatski (2001) discuss the need to modify turbulence models to account for significant changes to shear layers brought about by the presence of convex and concave surfaces.

The use of unstructured grids was not necessary for this type of study due to the simplicity of the model. However the recent investigation into the use of adaptive meshes by Habashi et al. (1998) has shown promise and it is only possible to use such techniques with unstructured tetrahedral grids. Such an approach would decrease the likelihood of grid dependent solutions.

Further experiments should be conducted with boundary layer control endplates on the model perhaps with the facility to vary the endplate distance from the first and last air jets. It would also be useful to perform some studies of the effects of different chordwise positions for the AJVGs as well as changes in pitch and skew angles. In addition, a parametric study of the effect of different blowing pressures should be investigated because it is highly likely that air from the engine exhausts could be used as blowing pressure for the AJVGs if they are used on the lower rear wing of a Formula One car.

The use of a wake rake that is better suited to the severe buffeting experienced throughout the angle of incidence range would be beneficial as this would allow more accurate measurements of the drag at all angles of incidence usng a method similar to that suggested for the numerical results.

BIBLIOGRAPHY

Bibliography

Abbott, I. H. & Von Doenhoff, A. E. (1959), *The Theory of Wing Sections*, Dover Publications Inc., New York, NY USA.

Agoropoulos, D. & Squire, L. C. (1988), 'Interactions between turbulent wakes and boundary layers', *AIAA Journal* **26**(3), 1194–1200.

Akanni, S. D. & Henry, F. S. (1995), Numerical calculations for air jet vortex generators in turbulent boundary layers, *in* 'Proceedings of the Royal Aeronautical Society Conference on High-Lift and Separation Control', The Royal Aeronautical Society, pp. 16.1–16.12. ISBN 1 85768 061 8.

Alderton, J. H. & Wilkes, N. S. (1988), 'Some applications for new finite difference schemes for fluid flow problems', *AERE-R 13234*.

Alston, R. P. (1935), 'Wing flaps and other devices as aids to landing', *Journal of the Royal Aeronautical Society* **39**, 637–650.

Anderson, J. D. Jr. (1995), *Computational Fluid Dynamics, The Basics with Applications*, McGraw-Hill Inc., London UK.

Anderson, W. K. & Bonhaus, D. L. (1993), 'Navier-stokes computations and experimental comparisons for multielement airfoil configurations'. AIAA Paper 93-0645.

Atkinson, K. B. (1996), *Close Range Photogrammetry and Machine Vision*, Whittles Publishing., Caithness, Scotland.

Bartsch, P., Nitsche, W. & Britsch, M. (1993), 'Navier-stokes computations of turbulent flow around high-lift configurations'. AGARD CP-515, Paper 6.

Bradshaw, P. (1973), 'Effects of streamline curvature on turbulent flow'. AGARD AG-169,.

Cao, H. V., Kusunose, K., Spalart, P., Ishimitsu, K., Rogers, S. E. & McGhee, R. (1994), 'Study of wind tunnel wall interference for multi-element airfoils using a navier-stokes code'. AIAA Paper 94-1993.

Castro, I. P. & Jones, J. M. (1987), 'Studies in numerical computations of recirculating flows', *International Journal of Numerical Methods in Fluid Mechanics* **7**, 793–823.

CFX-International (1995), *CFX-4.2 User Manual*, AEA Industrial Technology, Oxfordshire, UK.

Claus, R. W. & Vanka, S. P. (1992), 'Multigrid calculations of a jet in crossflow', *Journal of Propulsion and Power* **Vol. 8, No. 2**, 425–431.

Compton, D. A. & Johnston (1992), 'Streamwise vortex production by pitched and skewed jets in a turbulent boundary layer', *AIAA Journal* pp. 640–647.

Courant, R., Issacson, E. & Rees, M. (1952), 'On the solution of non-linear hyperbolic differential equations by finite differences', *Comm. On Pure and Applied Math* **Vol. 5**, 243–255.

Demirdzic, I. & Muzaferija, S. (1997), *Introduction to Computational Fluid Dynamics*, Mechanical Engineering Faculty, University of Sarajevo, Sarajevo, Bosnia and Herzegovina.

Duddy, R. R. (1949), 'High lift devices and their uses', *Aeronautical Journal (53)* **Vol. 71**, 860–883.

Fage, A. & Sargent, R. F. (1944), Design of suction slots, Technical Report ARC-R/M-2127, HMSO.

Fejtek, I. (1997), 'Summary of code validation results for a multiple element airfoil test case'. AIAA Paper 97-1932.

Foster, D. N., Irwin, H. P. A. H. & Williams, B. R. (1970), 'The two-dimensional flow around a slotted flap'. Aeronautical Research Council, Reports and Memoranda No. 3681.

Freestone, M. M. (1995), Inviscid theory applied to vortex-induced mixing, *in* 'Proceedings of the Royal Aeronautical Society Conference on High-Lift and Separation Control', The Royal Aeronautical Society, pp. 15.1–15.14. ISBN 1 85768 061 8.

Fritz, W. (1993), 'Calculation of maximum and high lift characteristics of multi element airfoils'. AGARD CP-515.

Gentry, R. A., Martin, R. E. & Daly, B. J. (1966), 'An eulerian differencing method for unsteady incompressible flow problems', *Journal of Computational Physics* 1, 87–118.

Habashi, W. G., Dompierre, J., Bourgault, Y., Fortin, M. & Vallet, M. G. (1998), 'Certifiable computational fluid dynamics through mesh optimization', *AIAA Journal* **36**(5), 703–711.

Hamidy, E. (1998). Private Communication.

Harvey, C. (1980), *Great Marques*, Octopus Books, Hong Kong.

Henry, F. S. & Pearcey, H. H. (1994), 'Numerical model of boundary layer control using air-jet generated vortices', *AIAA Journal* pp. 2415–2425.

Horton, H. P. (1971), 'Fundamental aspects of flow separation under high-lift conditions'. AGARD LS-43. Paper 4.

Innes, F. (1995), An Experimental Investigation into the Use of Vortex Generators to Improve the Performance of a High Lift System, PhD thesis, The City University, London.

Innes, F., Pearcey, H. H. & Sykes, D. M. (1995), Improvements in the performance of a three element high-lift system by the application of air jet vortex generators, *in* 'Proceedings of the Royal Aeronautical Society Conference on High-Lift and Separation Control', The Royal Aeronautical Society, pp. 25.1–25.11. ISBN 1 85768 061 8.

Johnston, J. & Nishi, M. (1989), Vortex generator jets - a means for passive and active control of boundary layer separation, *in* '27^{th} Aerospace Sciences Meeting', The American Institute of Aeronautics and Astronautics, pp. 25.1–25.11. AIAA Paper 89-00564.

Jones, I. (1998). Private Communication.

Katz, J. (1995*a*), 'Integration of computational methods into automotive wind tunnel testing', *SAE Journal* pp. 2415–2425. SAE Paper 890601.

Katz, J. (1995*b*), *Race Car Aerodynamics (Designing for Speed)*, Bentley Publishers, Cambridge MA USA.

Katz, J. & Dykstra, L. (1989), 'Study of an open-wheel racing-car's rear-wing aerodynamics', *SAE Journal* pp. 2415–2425. SAE Paper 890600.

Kim, A. & Benson, T. (1992), 'Calculation of a circular jet in a crossflow with a multiple-time-scale turbulence model', *International Journal of Heat and Mass Transfer* **35**(10), 2357–2365.

Krus, H. (1998). Private Communication.

Küpper, C. (1999), A Study of the Application of Air-Jet Vortex Generators to Intake Ducts, PhD thesis, The City University, London.

Larsson, T. & Arlinger, B. G. (1997), 'On the prediction of flows around airfoils at high lift conditions', *Notes on Numerical Fluid Mechanics* **58**, 241–252.

Leonard, B. P. (1979), 'A stable and accurate convective modelling procedure based on quadratic upstream interpolation', *Computational Methods and Applied Mechanical Engineering* **19**, 59–98.

Lewington, N. (2002), Enhancing Lift on a Three Element High Lift System by Installing Air Jet Vortex Generators, PhD thesis, The City University, London.

Liebeck, R. H. (1978), 'Design of subsonic airfoils for high lift', *Journal of Aircraft* **15, No. 9**, 547–561.

Lin, J. C., Robinson, S. K., McGhee, R. J. & Valarezo, W. O. (1994), 'Separation control on high-lift airfoils via micro-vortex generators', *Journal of Aircraft* **31, No. 6**, 1317–1323.

Ljungstrom, B. L. G. (1972), Boundary layer studies on a two-dimensional high lift wing, Technical Report Report AU 862, Flygtekniska Försöksanstalten, Bromma, Sweden.

Lonsdale, G. & Schueller, A. (1993), 'Multigrid efficiency for complex flow simulations on distributed memory machines', *Parallel Computing* **19**(1), 23–32.

Luo, S. C. & Gan, T. L. (1992), 'Flow past two tandem circular cylinders of unequal diameter', *Aeronautical Journal* pp. 105–114.

Maskew, B. (1983), Vsaero, a computer program for calculating the non-linear aerodynamic characteristics of arbitrary configurations, Technical Report CR-166476, NASA.

Milliken, W. F. & Milliken, D. L. (1995), *Race Car Vehicle Dynamics*, Society of Automotive Engineers, Warrendale, Pensylvania, USA.

Mullarkey, S. M. (1998). Private Communication.

Nakayama, A., Kreplin, H. P. & Morgan, H. L. (1990), 'Experimental investigation of flow field about a multielement airfoil', *AIAA Journal* **28, No. 1**, 14–21.

Nash, J. F. & Hicks, J. G. (1968), An integral method including the effect of upstream history on turbulent shear stress, Technical Report CR-166476, Lockheed Georgia Research Laboratory, Marietta, Georgia, USA.

Papadakis, M. & Miller, L. S. (1992), 'Experimental and computational investigation of wind tunnel effects on airfoil flow fields'. AIAA Paper 92-0672.

Patankar, S. V. (1980), *Numerical Heat Transfer and Fluid Flow* 1^{st} *Edition.*, McGraw Hill, New York, NY, USA.

Patankar, S. V. & Spalding, D. B. (1972), 'A calculation procedure for heat, mass and momentum transfer in three dimensional parabolic flows', *International Journal of Heat and Mass Transfer* **15**, 1787–1806.

Pauley, W. R. & Eaton, J. K. (1988), 'Experimental study of the development of longitudinal vortex pairs embedded in a turbulent boundary layer', *AIAA Journal* **26, No. 7**(7), 816–823.

Peake, D. J., Henry, F. S., Lush, P. A. & Pearcey, H. H. (1998), Flow control with air-jet vortex generators, *in* 'Proceedings of the Royal Aeronautical Society Conference on Passive and Active Flow Control', The Royal Aeronautical Society. Paper No. 10.

Pearcey, H. H. (1961), *Shock-Induced Separation and its Prevention by Design and Boundary Layer Control*, Pergamon Press, Oxford.

Rhie, C. M. & Chow, W. L. A. (1983), 'Numerical study of the turbulent flow past an airfoil with trailing edge separation', *AIAA Journal* **21**, 1525–1532.

Rodi, W. (1952), The use of airjets for boundary layer control, appendum to aeronautical technical note no. 110 (n-34736), Technical report, Aeronautical Research Laboratories, Australia.

Rumsey, D. & Gatski, T. B. (2001), Isolation curvature effects in computing wall-bounded turbulent flows, *in* '39^{th} AIAA Aerospace Sciences Meeting and Exhibit', AIAA.

Rumsey, D., Gatski, T. B., Ying, S. X. & Bertelrud, A. (1998), 'Prediction of high-lift flows using turbulent closure models', *AIAA Journal* **36**(5), 765–774.

Runchal, A. K. & Wolfstein, M. (1969), 'Perspective: Selected benchmarks from commercial codes', *Journal of Mechanical Engineering and Science* **11**(5), 445–453.

Shi-Ying, Z. & Fan, L. (1987), Experiments about the air jet vortex generator, Technical Report A87.462.33, Nanjing Aeronautical Institute, People's Republic of China.

Smith, A. M. O. (1975), 'High-lift aerodynamics', *Journal of Aircraft* **12, No. 6**, 501–530.

Smith, G. D. (1985), *Numerical Solution of Partial Differential Equations: Finite Difference Methods, 3rd Edition*, Clarendon Press, Oxford, England.

Spalding, D. B. (1972), 'A novel finite-difference formulation for differential expressions involving both first and second derivatives', *International Journal of Numerical Methods Engineering* **4**, 551.

Stokes, G. G. (1845), 'On the theories of the internal friction of fluids in motion', *Trans. Cambr. Phil. Soc.* **8**, 287–305.

Sykes, D. (1998). Private Communication.

Thompson, J. F., Warsi, Z. U. A. & Mastin, C. W. (1985), *Numerical Grid Generation Foundations and Applications*, North Holland, New York, USA.

Toet, W. (1998). Private Communication.

Valarezo, W. O. & Mavriplis, D. J. (1993), 'Navier-stokes applications to high-lift airfoil analysis'. AIAA Paper 93-3534.

Van Doormal, J. P. & Raithby, G. D. (1984), 'Enhancements of the simple method for predicting incompressible fluid flows', *Numerical Heat Transfer* **7**, 147–163.

Versteeg, H. K. & Malalaskera, W. (1995), *An Introduction to Computational Fluid Dynamics, The Finite Volume Method*, Longman Group Limited, Harlow, UK.

Wallis, R. A. (1956), A preliminary note on a modified type of airjet for boundary layer control, Technical Report CP-513, Aeronautical Research Laboratories, Australia.

Wallis, R. A. & Stuart, C. M. (1958), On the control of shock-induced boundary layer separation with discrete airjets, Technical Report 19865, Aeronautical Research Laboratories, Australia.

Wehner, G. (1998), *The P-Cube Manual*, ICEM-CFD, Hannover, Germany.

Wright, P. G. (1982), 'The influence of aerodynamics on the design of formula one racing cars', *International Journal of Vehicle Design* **3**(4), 383–397.

Ying, S. X. & Spaid, F. W. (1998), 'Investigation of confluent boundary layers in high-lift flows'. AIAA Paper 98-2622.

Appendix

Appendix A

Additional Experimental Results

Some additional experimental results are presented in this chapter. These results are known to have been compromised by an air leak between the high downforce wing and the wind tunnel test section. The effect of this leakage was to exacerbate the flow separation experienced on the mainplane. This effect was seen to be proportional to the angle of incidence. Despite this problem, these additional results are included in this appendix so as to give as complete a record as possible of the experimental proceedings. While they do not constitute rigorously scientific data, they do show the ability of the air jets to decrease extent of flow separation seen on the mainplane with the air jet quiescent.

Flow visualisation of the model at 3^o, 19^o and 29^o are presented with quiescent and active air jets. The detailed data comprise pressure distributions and integrated force calculations. Also discussed is the variation and position of the peak suction C_p and the trailing edge C_p at each angle of incidence on each element. In keeping with Smith (1975), measurements of C_p at the trailing edge of the mainplane, vane and flap are used as an indication of the circulation generated by each element and of flow separation on the model.

A.1 Discussion of Additional Experimental Results

In the wind tunnel testing of high downforce wings, flow separation is expected and where wall effects are significant, some type of boundary layer control at the wing-wall interfaces is normally employed to encourage a nominal two dimensional flow. It has been shown that two dimensional flow fields can provide a good insight into the mechanisms of more complex three dimensional flow fields. Such was the case in the numerical and experimental work on a high downforce system carried out by Agoropoulos & Squire (1988), where they investigated the mixing of turbulent wakes with the boundary layers about a circulation control model. This model consisted of an elliptic main element with a leading edge slat. Endplates were used to increase the effective aspect ratio of the system and to promote two-dimensional flow conditions.

Papadakis & Miller (1992) conducted an experimental and computational investigation to account for the wind tunnel effects on the flow field about a NACA 0011 aerofoil. They also used endplates to ensure a two-dimensional flow field about this aerofoil. In their experimental work on separation control of high downforce aerofoils via micro-vortex generators, Lin et al. (1994) used a boundary layer control system to reduce the effects three-dimensional boundary layers to allow for better analysis of the effects of the vortex generators.

At high angles of incidence, flow separation, corner flows and leakage resulted in complex three-dimensional flow fields. This had a significant detrimental influence on the correlation between the experimental and the numerical results. Other experiments carried out by the author have shown similar flow separation can exist on the rear wings of a Formula One car at high angles of incidence due to incipient flow separation and corner flows. Thus, the presence of separation on the model was not unexpected.

The buffeting associated with this flow separation also affected the experiments in two significant ways. First, it was not possible to perform any wake surveys for fear of destroying the wake rake. Another effect of this buffeting was to force a reduction in the test section speed from 40 m/s to 35 m/s for the later experiments to relieve the stresses imposed on the wind tunnel structure.

A.2 Clean High Downforce Wing

The results discussed in this section were obtained from experiments performed on the clean wings in both experimental sessions. The results from the incorporation of the AJVGs into the high downforce system were performed exclusively is the second series of experiments. The tests were performed with a freestream velocity of 40 m/s in the first series of experiments and 35 m/s in the second series. Apart from the aerodynamic buffeting this 5 m/s difference in velocity did not produce any significant change the flow fields. This allows direct comparisons to be made between both experiments.

An angle of incidence range of 3^o to 29^o was used to establish the performance of the isolated high downforce system for the purposes of this investigation. Such highly cambered, multi-slotted components as found in this high downforce model would never be used at the lowest angles of incidence at any racing venue. A dedicated low or medium downforce design would be required on the race car.

A.2.1 Clean Wing Surface Flow Visualisation

The surface flows at three angles were investigated at 3^o, 19^o and 29^o. Only three angles were chosen due to the limited time available. The 3^o angle of incidence was used to confirm flow attachment on all the elements. The 19^o angle of incidence was examined because it was αC_{lmax} and $\alpha_{\frac{l}{d}max}$. Visualisation was performed at 29^o to directly investigate the worst case flow separation on the mainplane.

The surface flow field at 3^o is illustrated in Figure A.1. The mainplane is operating with completely attached flow except for a small section at the upper mainplane-tunnel wall junction. In this region, a flow pattern consistent with corner flow separation is present. On the lowest part of the span, the flow is completely attached.

The flow on the vane was attached except for an area of occluded oil that in all probability was caused by a separation bubble. This flow pattern is in evidence mostly on the lower span. The upper span on the vane and flap were obscured by sponsors lettering. Several oil traces are visible amongst these letters and their development is consistent with a separation bubble and flow reattachment which persists to the vane trailing edge.

In all likelihood, the flap was operating with fully attached flow. The oil traces all approach the trailing edge to within 2 to 3 mm and those with enough fluidity then turn downwards under the force of gravity. It is unlikely that this is due to flap trailing separation at 3^o incidence. It is more likely due to the low momentum of the air flow near the flap trailing edge. There were areas of disturbed flow on the flap in the vicinity of the slot gap spacer and unexpectedly near the upper test section wall.

Figure A.2 shows the surface flow field on the wing at 19^o incidence. There is an asymmetric flow separation pattern in evidence on the mainplane. At the model-ceiling junction, it extends from approximately 4% chord to the mainplane trailing edge at 60% chord. However, there is complete flow attachment by approximately the half span position on the mainplane and this is maintained until the lower extremities of the model.

Figure A.2 also shows that the vane and flap elements are operating with completely attached flow. There is some asymmetry in the flow on the vane. It is quite possible that a laminar separation bubble was formed on the vane just downstream of the mainplane trailing edge. This region covered by this bubble would experience comparatively lower velocities when compared to the local freestream. The oil drops would then be more

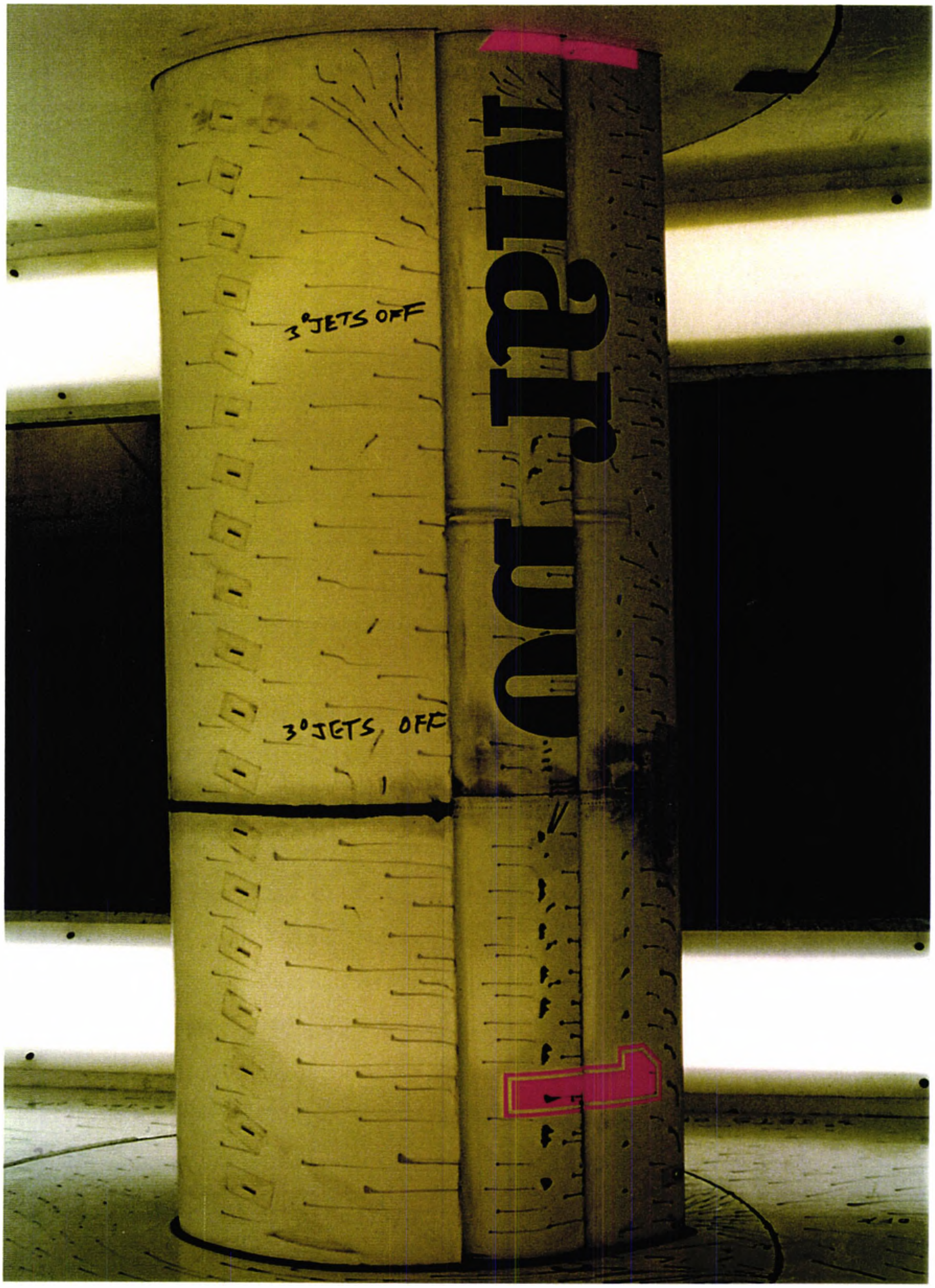

Figure A.1: Flow visualisation on clean wing, $\alpha = 3^o$.

affected by gravity and tend to flow down the vane towards the tunnel floor as is seen in Figure A.2. Generally, the flow reattaches downstream forming a turbulent boundary layer and this attachment is maintained until the element's trailing edge.

The flow on the flap was also completely attached but the pattern shown in Figure A.2 is not of good quality. Some of the oil drops near the slot were stagnant or flowed vertically under gravity. This was probably due to the separation bubble formed on the flap. Some smaller oil drops placed along the flap span do develop traces to the trailing edge while other larger drops remain stagnant. This is an area of pressure recovery and the velocities are decreasing towards the trailing edge. This being the case, there might not be enough momentum in the air flow to carry these larger oil drops to the flap trailing edge. Evidence of complete flap flow attachment for this angle is therefore intermittent along the span.

Figure A.3 shows the surface flow visualisation results on the model's pressure side at 29^o. The visualisation near the mainplane pressure side are not very clear because this area experiences very low velocities and so there is very little if any development of the oil traces. This was the case for all the positions tested. One interesting area on the model was the development of the oil traces in the area close to the pressure side of the vane and the flap. This is an area of higher velocity as the flow accelerates towards the flap trailing edge. Photographs of the pressure side of the wing were made they are not very compelling. Most efforts concentrated on the suction side of the wing.

Figure A.4 shows the suction side of the wing at 29^o. The large scale flow separation on the mainplane can be seen with the oil traces flowing down its span. This downward component imparted to the oil traces is induced by the air leak between the mainplane and the wind tunnel ceiling. The source of the leakage is the space between the wing and the turntable as enclosed in the dashed ellipse in Figure A.4. The separated region covers the entire mainplane span. On the upper part of the mainplane, it extends from approximately 4% chord to the mainplane trailing edge at 60% chord. On the lower part of the span, the separated region is significantly smaller, extending from approximately 50% chord to the trailing edge. The flow pattern assumes a more two-dimensional nature as the bottom of the model is approached.

The corner separation at both ends of the mainplane is not unusual because of the high angle of incidence and the lack of boundary layer control at the test section ceiling and floor. However, the extent of asymmetry in the flow separation pattern raised some concerns despite the fact that when separation occurs, even in controlled experiments, it

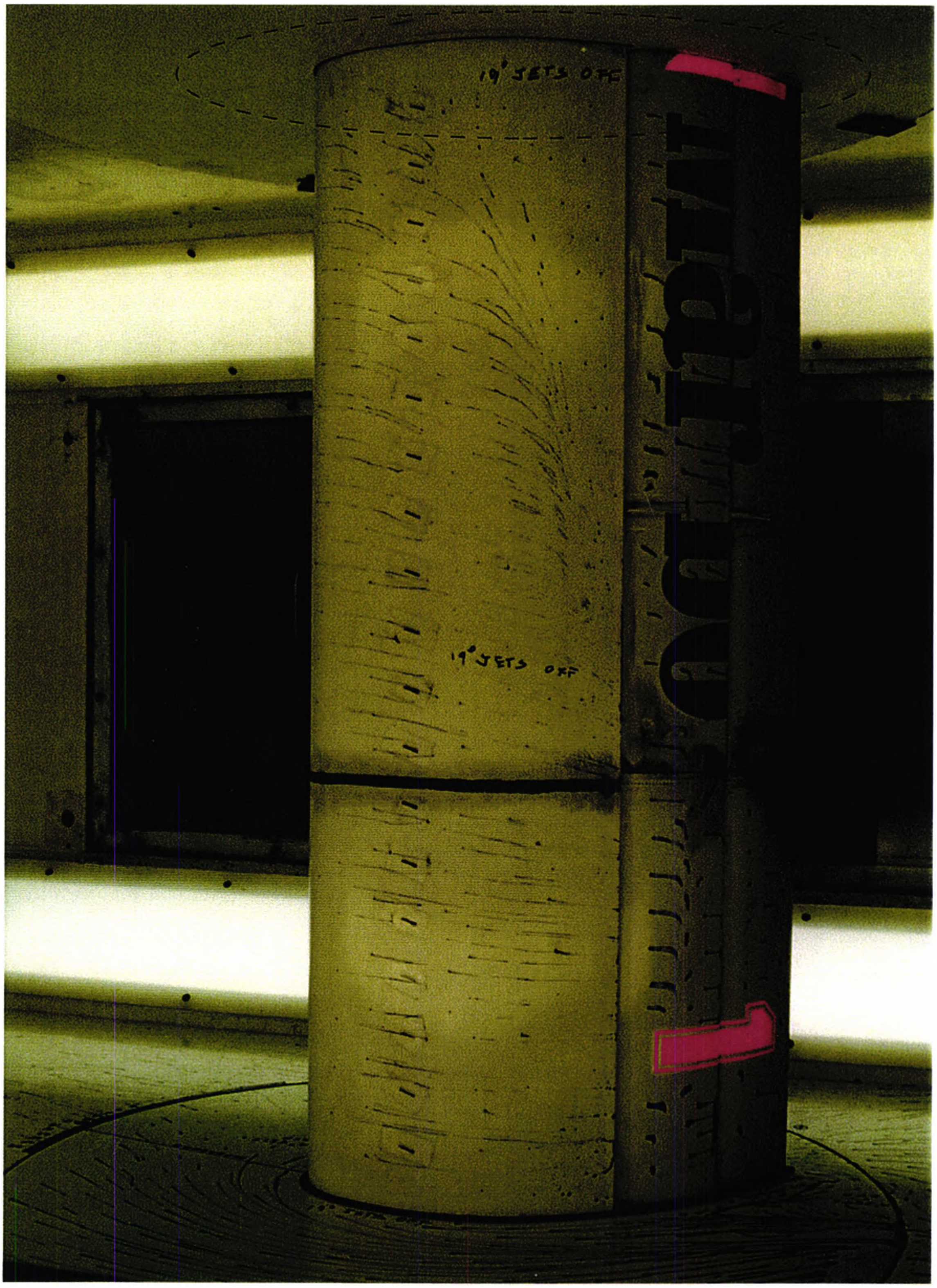

Figure A.2: Flow visualisation on clean wing at 19^o.

seldom occurs in a symmetrical manner. The model was later found to be affected by air leakage at the upper model-turntable junction.

Figure A.4 also shows that despite the separated flow on the mainplane, the flows on the vane and the flap are completely attached. These elements are benefiting from the effects of the slotted flows. These two elements did not demonstrate any separated flow in the corners formed with the tunnel walls.

A.2.2 Additional Pressure Distributions

The measured pressure distributions of the high downforce wing demonstrates the similar characteristics as the predicted pressure distributions discussed in Section 5.2.2. The pressure distributions for the 3^o, 9^o, 15^o, 19^o, 23^o and 29^o angles of incidence can be seen in Figures A.5 through A.7. The main differences are that the lower surfaces pressures are overpredicted when compared to the experimental results and the severity of the adverse pressure gradients is underpredicted. The reasons for this overprediction can be found in the numerics of CFX-4.2 in that it fails to correctly resolve the boundary layer in the face of an adverse pressure gradient.

Over the angle of incidence range, it experiences a peak suction ΔC_p of approximately -1.86. By comparison, the vane and the flap elements are less sensitive to changes in α with the flap being the least sensitive. Between 3^o and 29^o, the vane exhibits a peak suction ΔC_p of approximately 0.75 and the flap has a peak suction ΔC_p of approximately -0.36.

Between 3^o and 19^o, there is a general decrease in the lower mainplane surface pressures and in peak suction. At 21^o, the lower surface pressures on the mainplane begin to increase. The peak suction C_p also follow this trend. This increase is accompanied by a reduction in the pressure gradient on the lower mainplane surface between 45% chord and the mainplane trailing edge at 60% chord. This suggests the onset of trailing edge separation on the mainplane. Further increases in the angle of incidence cause further reductions in the pressure gradient which are localised between 45% and 60% chord. The extent of the region where this adverse pressure gradient occurs increases with increasing incidence so that by the α_{max} of 29^o, the separated region on the mainplane extends from 35% chord to the trailing edge at 60% chord.

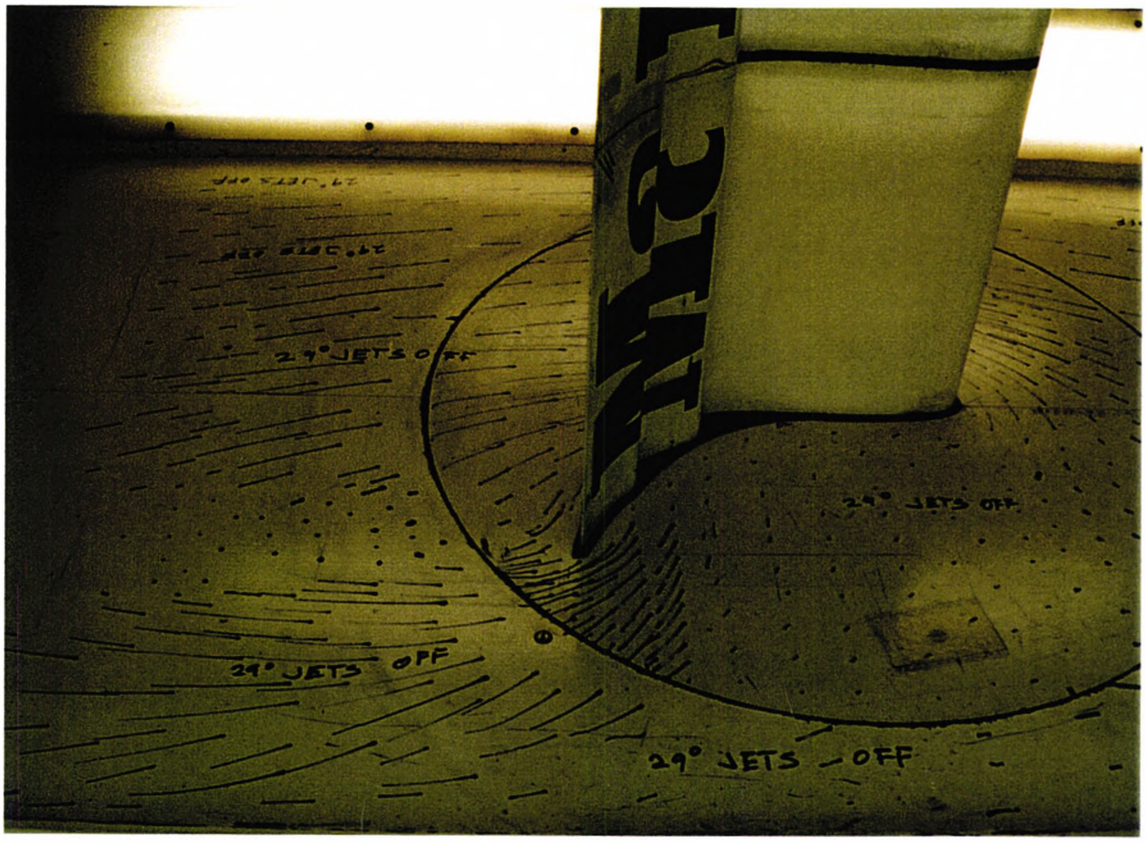

Figure A.3: Flow visualisation of sidewall at $\alpha = 29^o$.

A.2.3 Clean Wing Trailing Edge C_p versus Angle of Incidence

The monitoring of the element trailing edge C_p is important when studying the behaviour of high downforce systems. Figure A.9 shows the measured trailing edge C_p for each element with respect to angle of incidence. The *dumping* effect is evident at the mainplane and vane trailing edge C_p. The flap trailing edge C_p are indicative of a successful pressure recovery with attached flow on all the elements. When the Kutta condition is satisfied at the flap trailing edge, a positive C_p value is recorded there. A negative trailing edge C_p indicates that the Kutta condition is not satisfied at the flap trailing edge and that separated flow is in evidence on some element in the high downforce system.

A review of the element trailing edge C_p values in Figure A.9 shows that the mainplane C_p values are consistently lower than those at the vane trailing edge. Most of the vane trailing edge C_p are lower than the flap as the latter element is the final opportunity for pressure recovery in the system. The trend of increasing trailing edge C_p from the mainplane to the vane to the flap is an indication of the pressure recovery occurring in stages as discussed in Section 3. The flap C_p are all positive but decreasing between 3^o and 19^o, indicating attached flow. At 21^o, a negative flap trailing edge pressure is measured

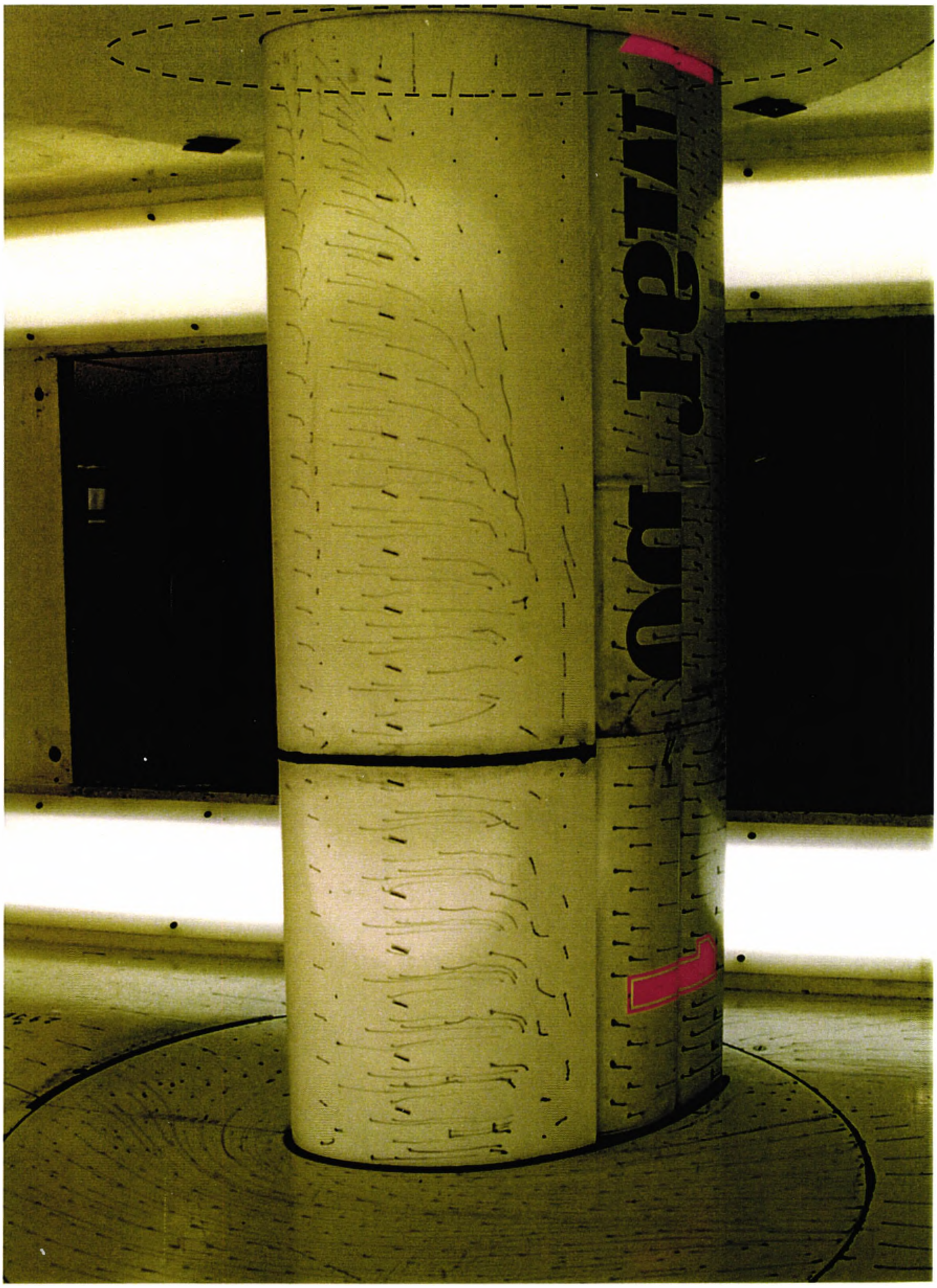

Figure A.4: Flow visualisation of clean model suction surfaces at $\alpha = 29^o$.

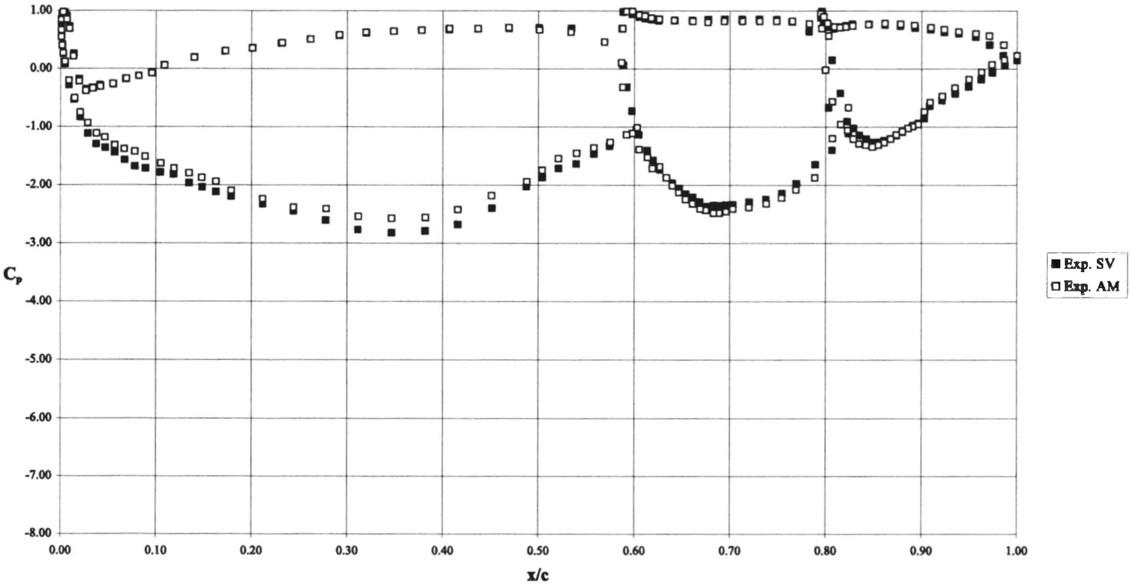

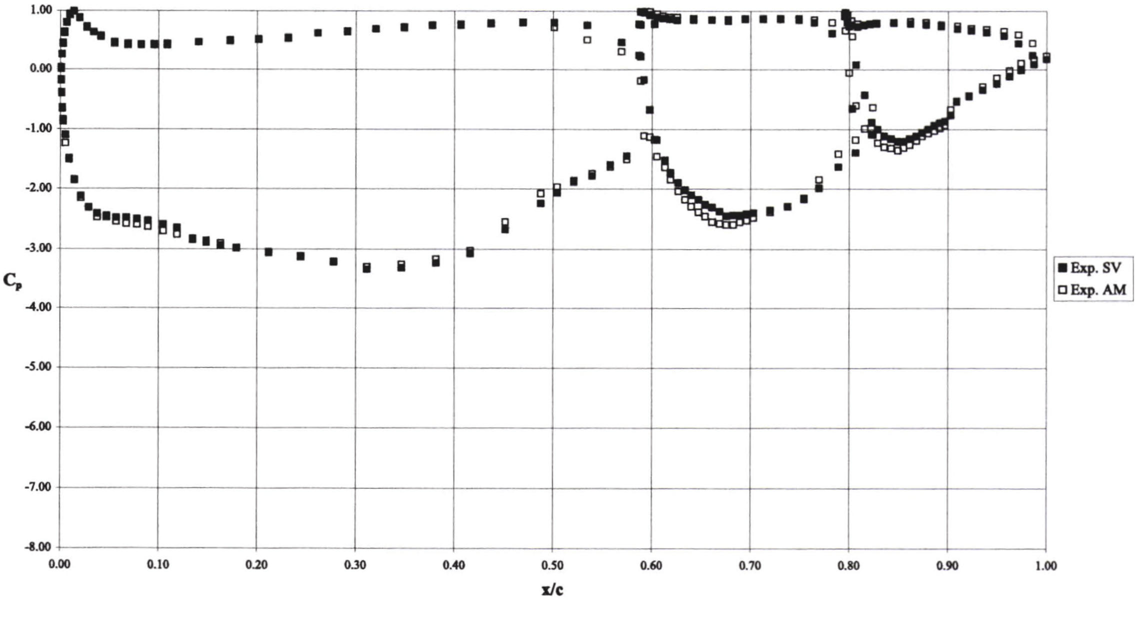

Figure A.5: Pressure distributions for $\alpha = 3^o$ (top) and 9^o (bottom).

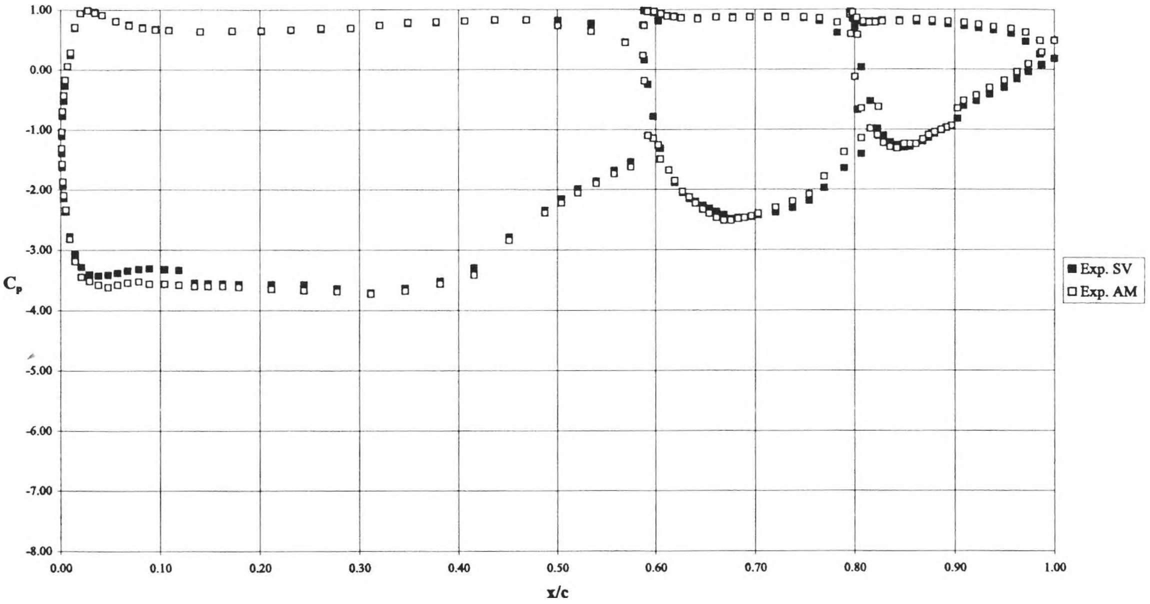

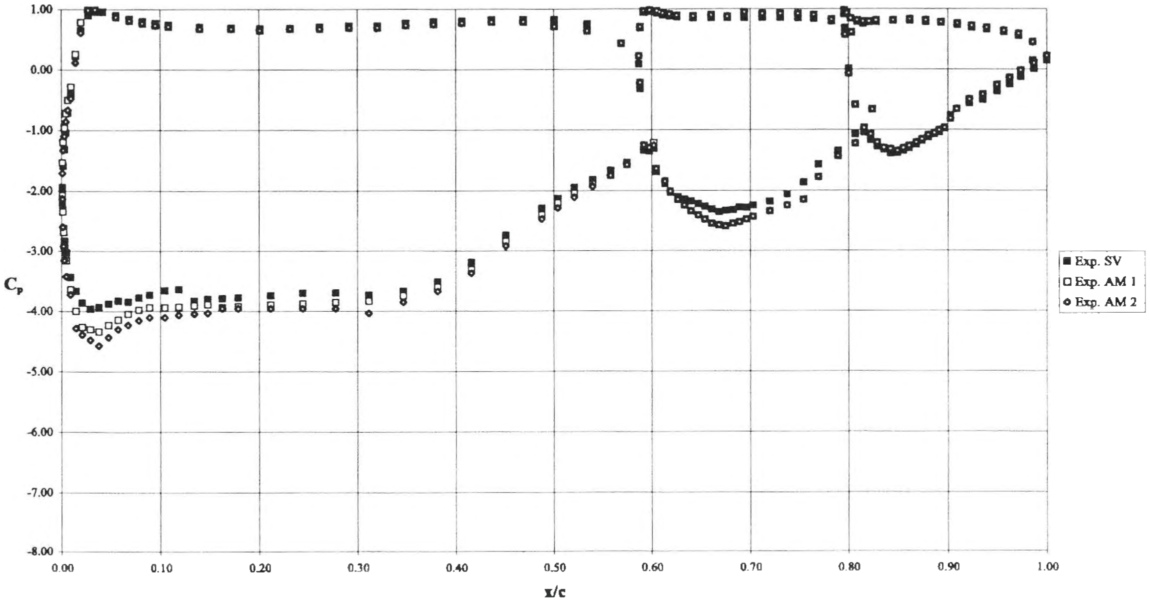

Figure A.6: Pressure distributions for $\alpha = 15^o$ (top) and 19^o (bottom).

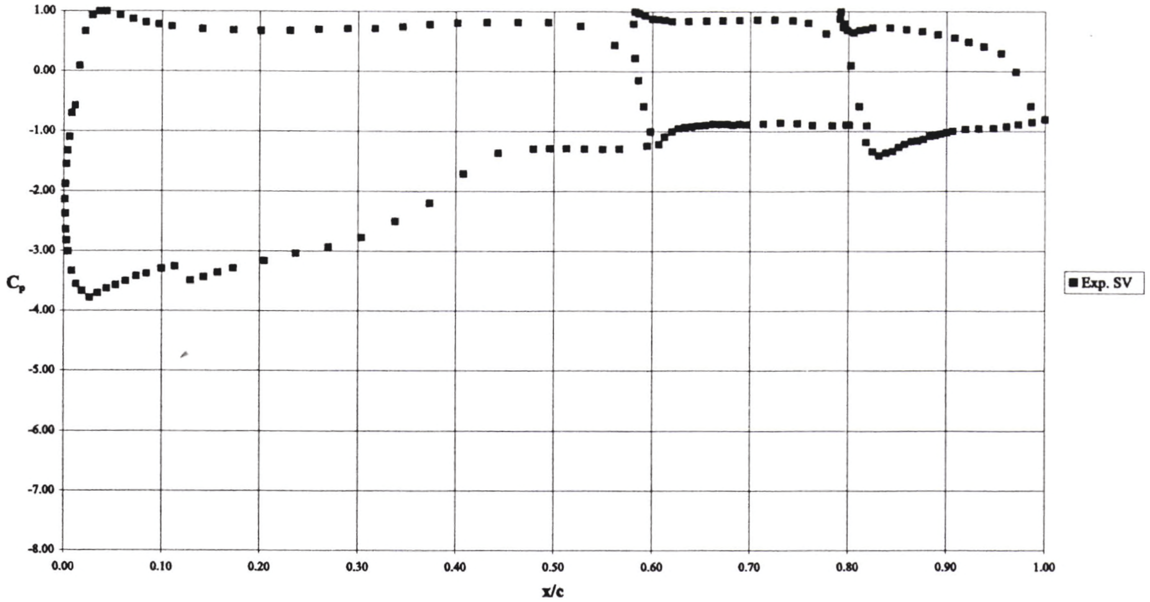

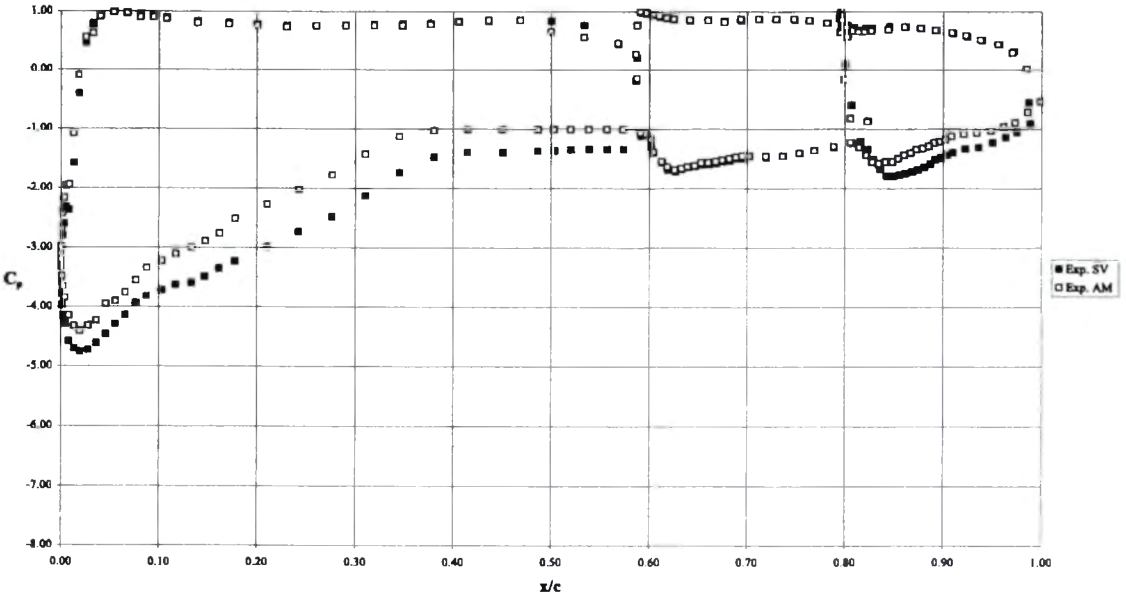

Figure A.7: Pressure distributions for $\alpha = 23^o$ (top) and 29^o (bottom).

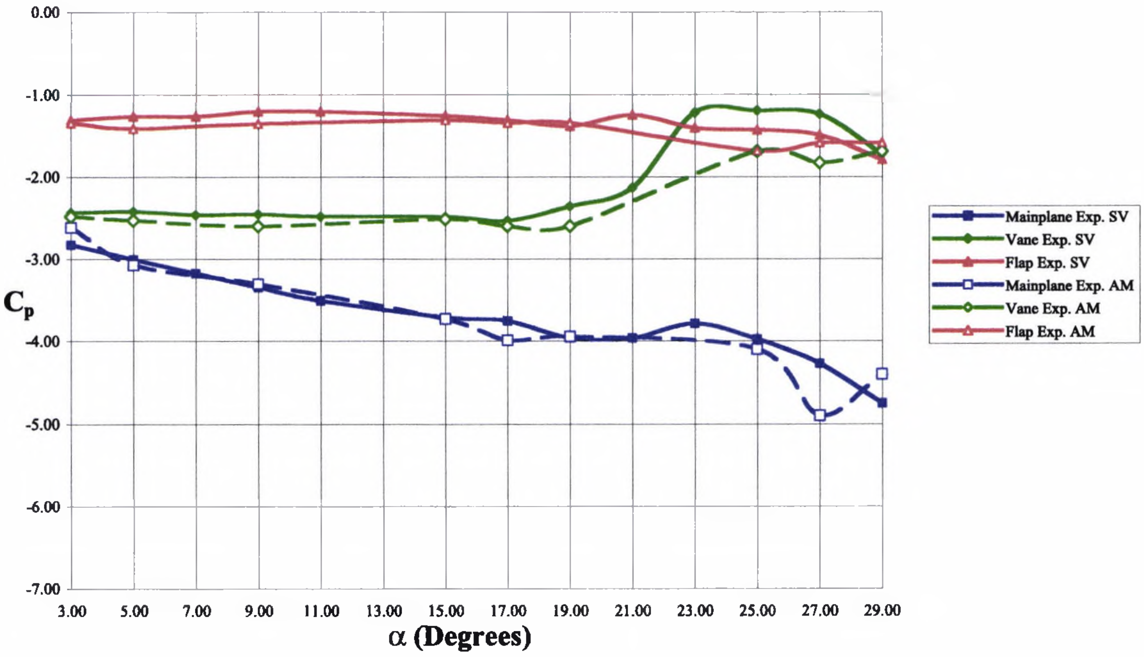

Figure A.8: Peak suction C_p versus α.

for the first time indicating separated flow somewhere on the model. From 21^o onwards, flow separation is in evidence on the mainplane.

All angles of incidence higher than 21^o produce a more negative flap trailing edge C_p, indicating that the flow separation worsens with increasing incidence. This is consistent with the pressures measured about the aft suction side region on the mainplane. The pressures indicate an increasing mainplane trailing edge flow separation with increasing incidence. The decrease in the pressure gradient and the negative, decreasing flap trailing edge C_p are both indicative of a decrease in aerodynamic loading generated by the high downforce model with increasing angle of incidence past 21^o.

A.3 Experimental Integrated Forces for Clean Wings

A.3.1 Clean Wing Normal Forces versus Angle of Incidence

Figure A.10 shows the calculated normal forces for the clean wings. The mainplane is the dominant element in terms of the normal forces at all angles except 3^o. At this angle, the vane generates an average C_n of -2.60. The mainplane generates an average C_n of -2.25. This is not surprising because this type of mainplane was not designed to be used at such an angle.

The mainplane possesses the largest surface area and this is the primary reason why its performance dominates the behaviour of the system. It is also the thickest element and

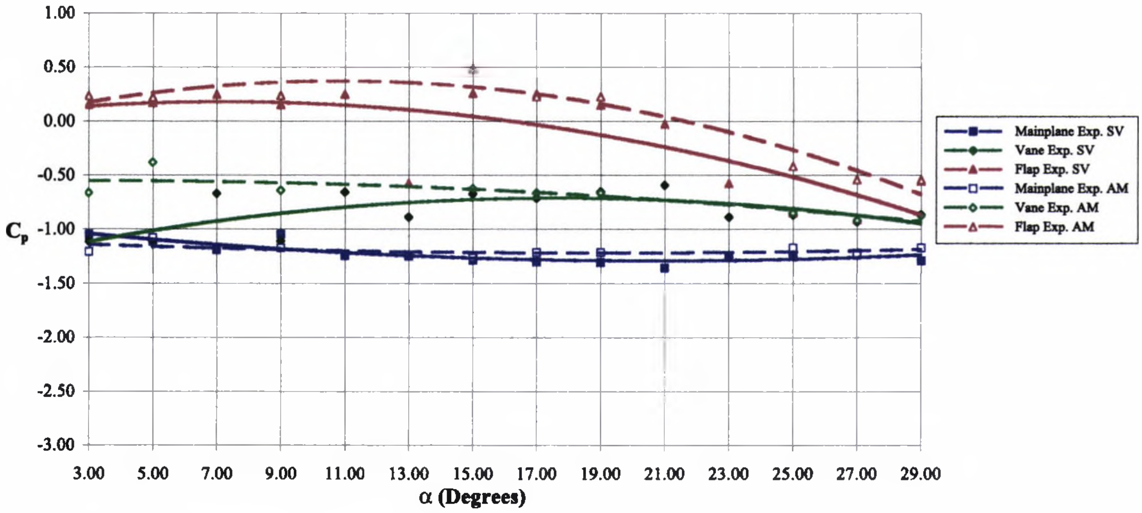

Figure A.9: Clean wing trailing-edge C_p versus α.

it has the largest leading edge radius. These are also features which contribute to a high circulation and therefore a high C_n.

Between 3^o and 15^o, the normal force generated by the mainplane increases in linear fashion with the maximum average C_n of -4.07 occurring at 19^o. Further increases in the angle of incidence result in a non-linear decrease in the mainplane C_n with a minimum average value of -3.16 recorded at α_{max} of 29^o.

At 23^o and 25^o, lower values of the C_n are calculated for all the elements. This part of the C_n versus α curve is characterised by a sudden decrease in C_n followed by a relatively constant C_n up to α_{max}. This behaviour is observed in both series of experiments for the mainplane, and vane. Horton (1971) observed similar behaviour of high lift systems at post stall angles of incidence in his experimental investigations.

With the exception of 3^o, the vane is consistently the second most highly loaded element in this high downforce model. A review of the C_n generated by the vane will show that the average maximum C_n of -2.93 is generated at approximately 17^o. Thereafter, the C_n decreases with increasing incidence.

In terms of C_n, the flap is the least loaded element. This is consistent with this element being the final stage of pressure recovery in the high downforce system. From 3^o, the average C_n generated by the flap show a steady load increase from -1.22 to a maximum of -1.73 at α_{max}.

In terms of normal forces, the behaviour of the assembly is largely dictated by the mainplane. This is reflected in the summation of the component C_n and the assembly C_n trendlines. It can be seen from Figure A.10 that the assembly C_n and the mainplane C_n

is intimately linked. They have the same gradient and their maxima and minima occur at the same angles.

A.3.2 Clean Wing Axial Forces versus Angle of Incidence

The axial forces for the clean wing experiments are presented in Figure A.11 and they show some noteworthy performance features for the system. Again, these are derived from the behaviour of the mainplane. The measured mainplane C_x and the corresponding trendline show a steady increase with increasing angle of incidence. The average mainplane C_x at 3^o is -0.34. This shows that the pressure distribution about the mainplane produces a net thrust. This thrust decreases with increasing incidence. It persists until approximately 15^o where positive values for C_x are calculated. A positive C_x of 0.14 was also recorded at 9^o, but given the trendline, it is more likely that this measurement is in error. The C_x of -0.17, recorded in second experiment is a more accurate indication of the axial force on this element at 9^o because it is more consistent with the trend of the forces.

An examination of the axial force on the vane shows that it also experiences a small thrust, albeit a decreasing one, between 3^o and 15^o. The average vane C_x at 3^o is -0.076 and a value of -0.048 is recorded at 15^o. Thereafter, the vane C_x demonstrates small positive values that are insensitive to changes in incidence. A review of Figure A.11 shows that there is a very small increase in the vane C_x. The only exception to this is the anomalous value of 0.164 that was measured at 9^o. This is in conjunction with a similarly high C_x that was recorded for the mainplane at this angle. Interestingly, there is nothing unusual about the normal forces that could help to explain these axial force values.

The average axial force on the flap at 3^o is small and positive with a value of 0.019. The axial forces on this element tend to decrease until approximately 15^o whereupon they maintain values consistent with a small thrust. They are also rather insensitive to angle of incidence. It would appear that this is an accurate representation of this element's behaviour despite anomalous C_x values of -0.394 and -0.365 at 17^o derived from both experiments.

The axial force characteristics of the high downforce system are once again dominated by the mainplane performance. A comparison of the axial force trends of the assembly and the mainplane reveals that the characteristics of the assembly possess minima, maxima and gradients the same as those of the mainplane. The forces generated by the vane and the flap do contribute to the overall performance, but it is clear that their effect on the system as a whole is not as profound as that of the mainplane.

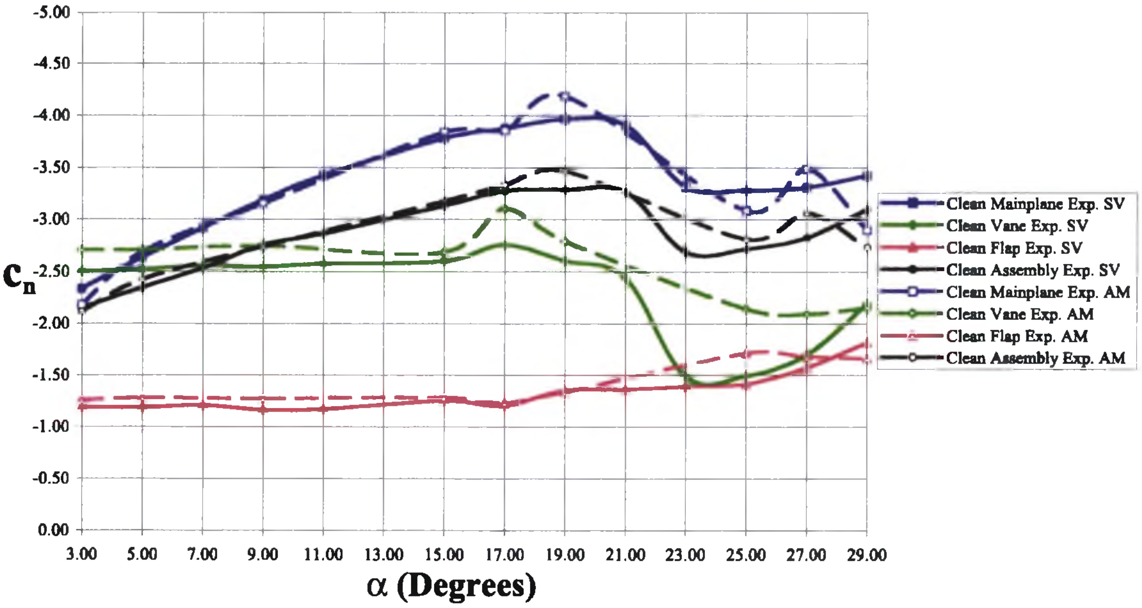

Figure A.10: C_n versus α for clean wings.

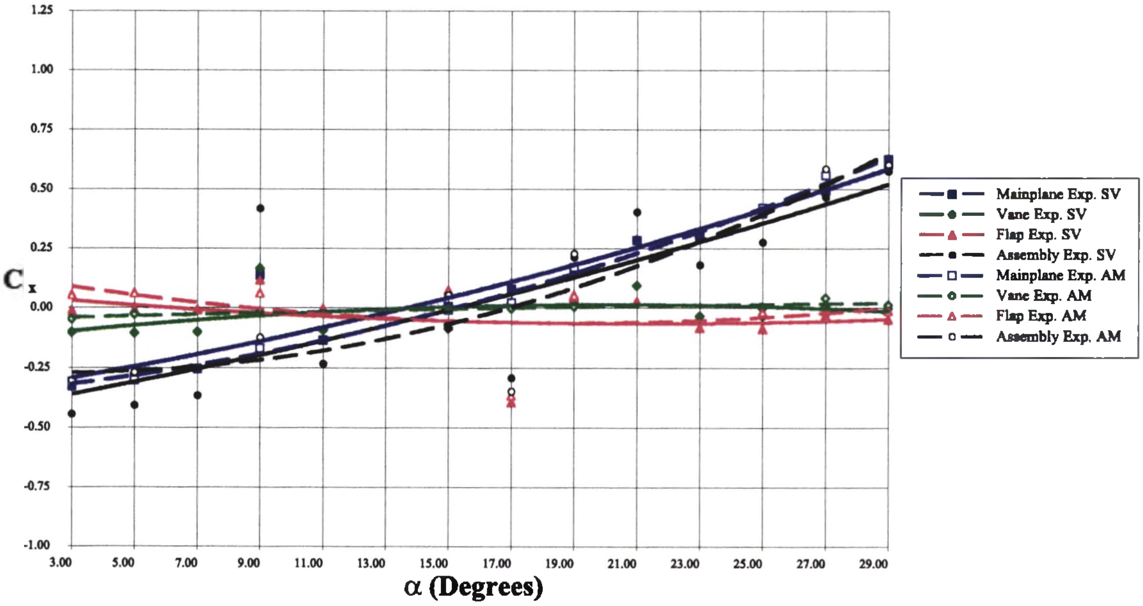

Figure A.11: C_x versus α for clean wings.

A.3.3 Clean Wing Downforce versus Angle of Incidence

The non-dimensional forces C_n and C_x provide valuable insight into the performance of individual elements and how they interact as a system. However, it is more meaningful to speak in terms of c_l and c_d because for the most part, Formula One aerodynamicists analyse their cars and high downforce systems in terms of lift and drag coefficients.

The c_l data are presented in Figure A.12. The increase in downforce is in evidence between 3^o up to 19^o (Exp. SV) and 17^o (Exp. AM). At these angles, the high downforce system produces a $c_{l\,max}$ of -3.45 and -3.33 respectively. Due to experimental variance in the measurements, one can only make an approximation of the $\alpha c_{l\,max}$ when reviewing the forces derived from the distributed pressure about the wings. However, the trailing edge C_p in Figure A.9 show that the last positive flap trailing edge pressure is recorded at 19^o. The model was not run at 21^o in the second series of experimental and a negative flap trailing edge C_p of -0.026 (Exp. SV) is recorded for this angle. Therefore the high downforce model has experienced flow separation and a reduction in downforce. This implies that $\alpha c_{l\,max}$ is 19^o.

After 19^o incidence, there is a progressive reduction in c_l up to α_{max} of 29^o. There is a sudden loss of downforce as the mainplane stalls at 23^o (Exp. SV). This lower level of downforce is also seen at 25^o (Exp. SV and Exp. AM). An examination of the Exp. SV c_l curve shows a small post stall increase in the downforce up to α_{max} of 29^o. After stalling, the Exp. AM c_l curve shows some fluctuations but the c_l never increases to the point where they are an improvement on $c_{l\,max}$. The post stall characteristics of the c_l curve are similar to those discussed in Horton (1971).

A.3.4 Clean Wing Drag versus Angle of Incidence

The author has some reservations about the accuracy of the estimation of drag at the higher angles of incidence. These reservations are based in part on the author's own experiences and on the findings of Larsson & Arlinger (1997). In their numerical and experimental work on high lift aerofoils, Larsson & Arlinger (1997) found that the computation of drag through the integration of surface pressures can be in error by as much as 50% even though both the predicted pressure and skin friction distributions can show excellent agreement with experiments. In performing an integration, small errors in the surface pressure can produce relatively large errors in the drag. This is especially true of the leading and trailing edge areas.

During the experiments conducted with the high downforce wing, it was not possible

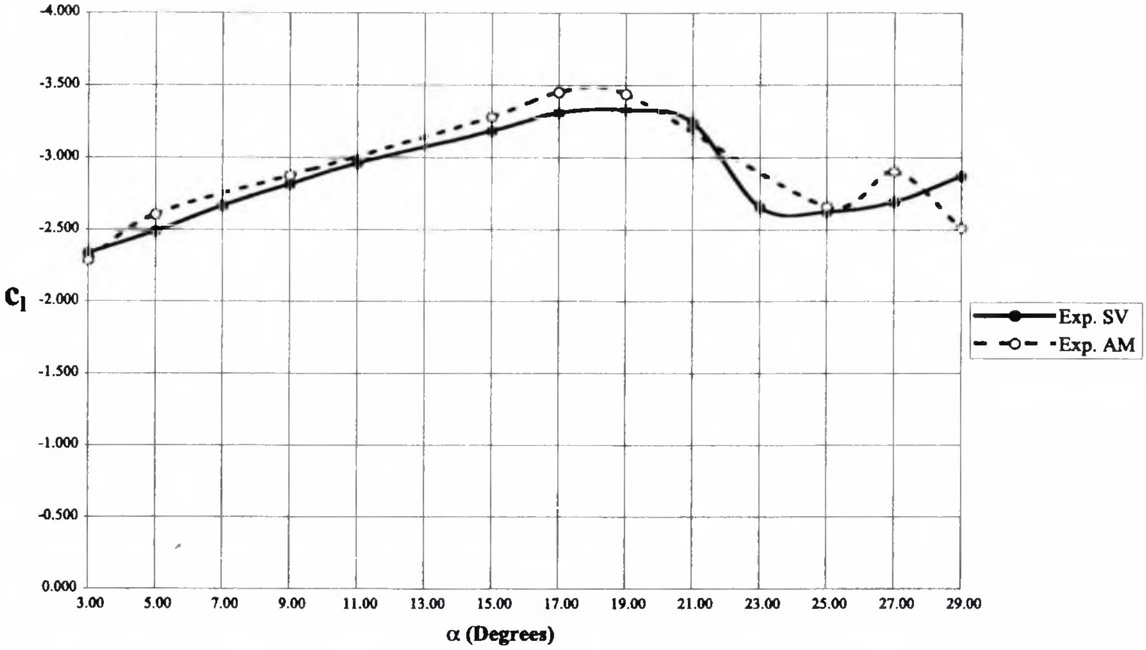

Figure A.12: Experimental clean wings c_l versus α.

to use the wake rake provided by the laboratory staff because it was subjected to severe buffeting between 19^o and 29^o. It is highly unlikely that the instrument would have survived any prolonged testing. Measurements with the wake rake would have allowed the calculation of drag through the integration of the momentum loss downstream of the high downforce model. In their work on high lift models Innes (1995) and Lewington (2002) successfully used the wake integration technique to estimate the drag.

This c_d versus α curve is shown in Figure A.13 for the two series of experiments carried out on the clean wing. This figure shows a trend of increasing c_d with increasing angle of incidence. The data shows reasonably good agreement between 3^o and 21^o with $c_{d\,min}$ of 0.090 (Exp. SV) and 0.097 (Exp. AM) being recorded at 3^o. At angles of incidence greater than 21^o degrees, the data are contradictory with the Exp. AM data showing a consistently higher c_d than Exp. SV data between 21^o and 27^o. At 29^o, the Exp. SV data shows a $c_{d\,max}$ of 0.659 compared to 0.552 (Exp. AM). This difference is not surprising given the differences in C_p shown in Figure A.7.

A.3.5 Clean Wing Downforce to Drag Ratio versus Angle of Incidence

Despite the lift having a negative sign, it is convention in Formula One aerodynamics to define the aerodynamic the efficiency as $\frac{|l|}{d}$ thus effectively ignoring the negative sign. The author follows this convention. The experimental lift to drag ratio of the clean wing is shown in Figure A.14. With the exception of the highest value of 32.33 at 5^o (Exp. AM),

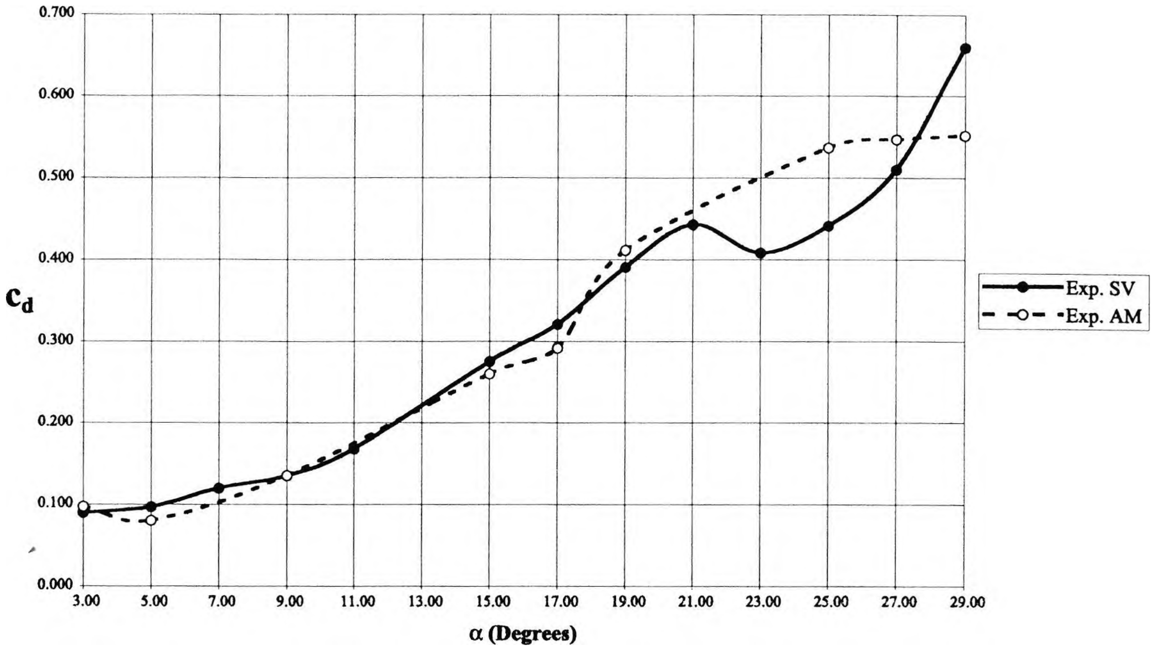

Figure A.13: Experimental clean wings drag curve.

there is reasonably good agreement between the data from the two experiments on the clean wing.

Figure A.14 shows a trend of decreasing $\frac{|l|}{d}$ with increasing angle of incidence. The wing is most efficient at the lowest angles of attack with an $\frac{|l|}{d}$ of 26 (Exp. SV) at 3^o and 32.33 (Exp. AM) at 5^o. The efficiency reaches its minimum at 29^o with values of 4.35 (Exp. SV) and 4.54 (Exp. AM).

A.4 High Downforce Wing Equipped with AJVGs

Experiments on the wing with AJVGs were made exclusively in the second experimental series using the alcohol manometer system to measure the pressures about the wing elements. In certain graphs the reader will find legends denoting the use of air jets on the high downforce system. These labels are 'Mainplane with Air Jets', 'Vane with Air Jets', 'Flap with Air Jets', and 'Assembly with Air Jets'. The AJVG array was only applied to the mainplane element of the model. This notation is used when the vane, flap and assembly performance were affected by the use of the air jets. The label 'Clean Wing' is used to denote the high downforce wing without the AJVGs or with the AJVGs quiescent.

The use of alcohol manometers was significantly less efficient than the electronic system and the entire angle of incidence range could not be covered in a reasonable time. Thus the high downforce system equipped with the AJVGs was examined at 3^o, 5^o, 9^o, 15^o,

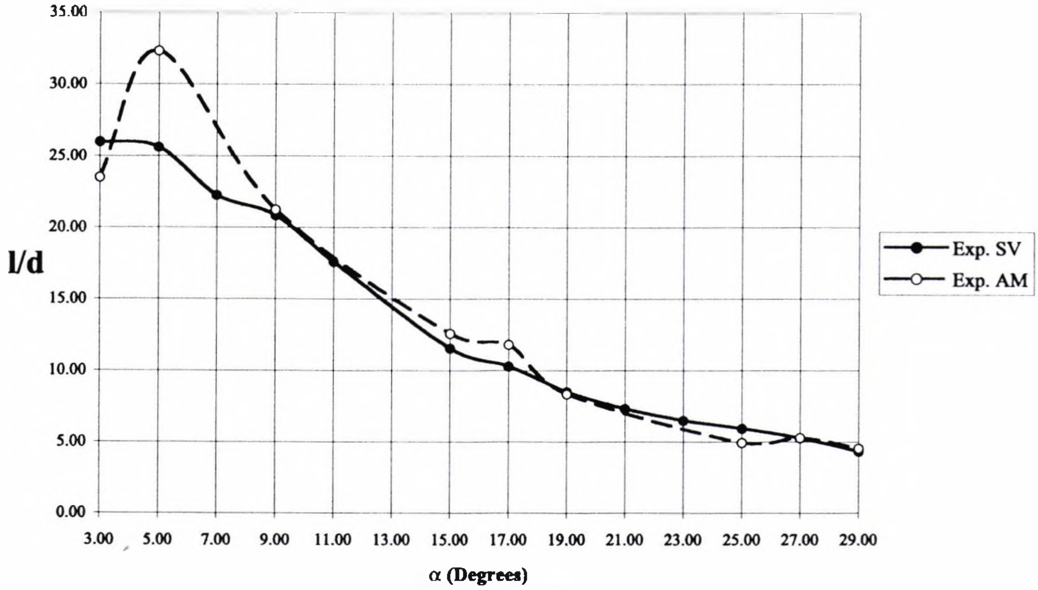

Figure A.14: Experimental clean wings $\frac{l}{d}$ versus α.

17^o, 19^o, 25^o, 27^o and 29^o. These angles were chosen to give a good indication of the performance throughout the angle of incidence range.

A.4.1 Flow Visualisation with Air Jets

A view of the lower surfaces of the wing with AJVGs at 29^o is presented in Figure A.15. This model can be compared directly with a similar experiment on the clean mainplane high downforce model in Figure A.3. The AJVGs have a profound and beneficial effect on the mainplane boundary layer. This is seen in Figure A.15 as smaller regions of flow separation on the mainplane. This is significant given that they have to counter the adverse flow effects created by the leakage through the wall seal. The vane and flap do not exhibit any signs of flow separation. The effect of the leakage which was misinterpreted as an asymmetric stall, can be seen as a strong, downwards spanwise flow. This separated flow pattern dominates the upper part of the mainplane. However, in the region of the pressure taps, (the black stripe on the mainplane), the extent of this flow is sufficiently weak to allow a nominal two-dimensional flow to exist.

It is possible that a nominal two-dimensional separated flow on the mainplane would bear a close resemblance to the flow pattern on the lower part of the mainplane. The flow separation in this lower region is significantly less than that seen on the upper span of this element. The flow patterns on the clean wing in Figure A.3 and those on the wing with AJVGs in Figure A.15 show the effects of the faulty seal. This leakage introduces more adverse conditions on the mainplane that the AJVGs must overcome in order to increase the loading on the element. It is promising that the AJVGs were able to achieve an increase in the downforce. It is possible that further increases in the downforce would have been measured if these leaks had been identified at an earlier stage.

A.4.2 Measured Pressure Distributions with Air Jets

Between 3^o and 19^o, the pressure distributions about the high downforce model with AJVGs are qualitatively similar to the clean wing pressure distributions. This can be seen by reviewing Figures A.16 and A.17. The variance in the measurements notwithstanding, the pressure distributions are also quantitatively similar. The author defines an improvement as an increase in the area enclosed by the points of a pressure distribution for a given element of the wing. At the lower angles of incidence, there is no significant improvement in the pressure distributions when AJVGs are employed over and above those of the clean wings. This is contrary to the findings of Innes (1995) where it was found that the use of AJVGs increased the total normal force coefficient, C_n, at all angles below the stall incidence. This improvement in C_n was attributed to a reduced displacement effect of the shear layers above the main wing.

Innes et al. (1995) employed a source of compressed air to power the air jet array used in his investigations. In all experiments, a blowing pressure 60% above the freestream stagnation pressure was used. A ram air jet array is dependent on the ambient local pressures about the mainplane. This may be the reason for the failure of the AJVGs to effect an increase in C_n at the lowest angles of incidence for this installation. The high pressure that drives the AJVGs is the ambient atmospheric pressure and it is constant. The lower pressure that provides a favourable pressure gradient for the AJVG efflux is determined by the local pressure at 19% chord on the mainplane suction surface. At the angles of incidence below $\alpha_{C_{l\,max}}$, it would appear that this pressure difference is not effective at producing a jet efflux that is strong enough to increase C_n.

The first significant sign of an improvement in the pressure distribution about the high downforce model with AJVGs is noted at an incidence of 25^o. No tests were performed for the model with AJVGs at 21^o or 23^o , but it is likely that an improvement would have been seen at these angles of incidence had they been investigated. Improvements are also recorded for 27^o and 29^o.

The pressure distribution for the model at 25^o, 27^o and 29^o can be reviewed in Figures A.18, A.19 and A.20 respectively. These figures show that for 25^o and 27^o, there is a significant reduction in the pressures on the lower mainplane surface due to the presence

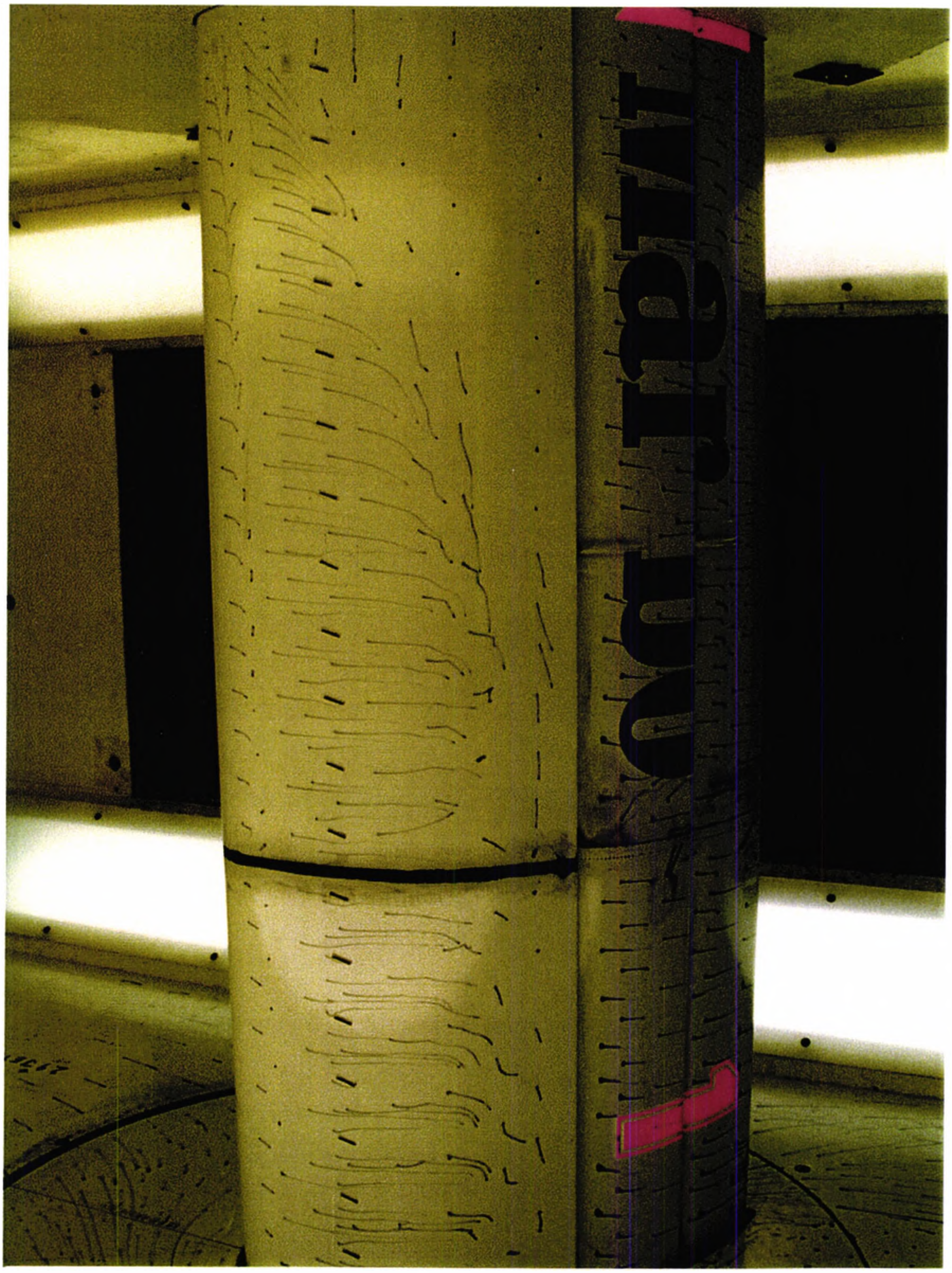

Figure A.15: High downforce model with AJVGs at 29^o incidence.

of the AJVGs. Between 25^o and 29^o, there is a decrease in the effectiveness of the AJVGs and this is seen in the figures as a reduction in the ΔC_p between the AJVG and the clean wing cases at each angle of incidence. Despite the use of two different measuring systems, the pressures produced by the use of AJVGs are clearly lower than those of the clean wings at 25^o and 27^o. However at 29^o, the mainplane lower surface, the clean wing pressures (Exp. SV) and the AJVG influenced pressures (Exp. AM) are nearly identical after x/c = 0.10. However the AJVG effected pressures on the mainplane (Exp. AM) are all clearly lower than those clean wing pressures (Exp. AM).

In Figure A.20, the pressure distribution on the mainplane at 29^o incidence shows that $\frac{dC_p}{d(\frac{x}{c})} \approx 0$. This is similar to the clean mainplane pressure distribution but with lower pressures. The region where $\frac{dC_p}{d(\frac{x}{c})} \approx 0$ on the mainplane extends from x/c = 0.45 to the mainplane trailing edge at x/c = 0.60. There is an increase in the aft aerodynamic load carried by the mainplane and it bears this increased loading with trailing edge flow separation albeit to a lesser extent than with the clean wing case.

To aid clarity, the peak suction C_p generated on the AJVG equipped high downforce model are illustrated separately in Figures A.21 and A.22. These figures show that the effect of the AJVGs is to decrease the mainplane peak suction C_p with increasing incidence. However, their ability to effect this decrease only starts at 17^o. Below 17^o, the measured results and the trendlines show that there is little or no change. In both Figures A.21 and A.22, there is a clear reduction in the peak suction between 9^o and 29^o. It can also be seen that $\Delta C_{p\,peak}$ increases with increasing incidence. At 29^o, the use of AJVGs produces a peak suction C_p of -5.23 compared to -4.75 (Exp. SV) and -4.40 (Exp. AM) measured on the clean wings.

The pressures about the vane are not significantly affected by the presence of the AJVGs until the higher angles of incidence. Figures A.16 and A.17 show that the behaviour of the pressure distribution for this element is not unlike that of the mainplane. There is no real change in the magnitude of measured pressures until after 19^o. At 25^o and 27^o, the presence of the AJVGs produces a significant reduction in the C_p on the entire lower surface of the vane. Figures A.21 and A.22 show an AJVG effected peak suction C_p of -2.075 (Exp. AM) compared to clean vane peak suctions of -1.72 (Exp. SV) and -1.69 (Exp. AM). At 29^o, lower C_p are only seen up to x/c = 0.70. Thereafter, a recovery ensues and the measured C_p are all higher than both the clean wing values.

Throughout the angle of incidence range, the lower surface C_p measured about the flap do not demonstrate any significant decrease. This is not unusual given that it is the final stage of pressure recovery. In Figures A.16 to A.20, a comparison of the flap pressures show that there is very little difference between the clean wing measurements (Exp. SV) and those with the AJVGs. A comparison of the clean wings pressures (Exp. AM) shows a very small improvement. In absolute terms, it can be said that the AJVGs effect a change in the pressure distribution first and foremost on the mainplane, then the vane and finally, the flap.

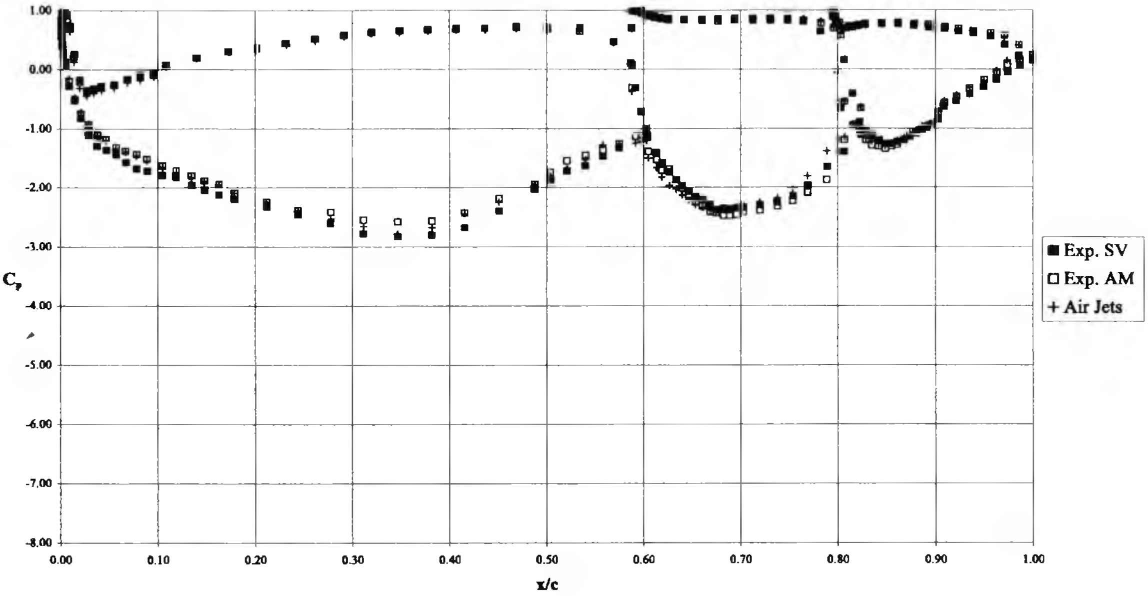

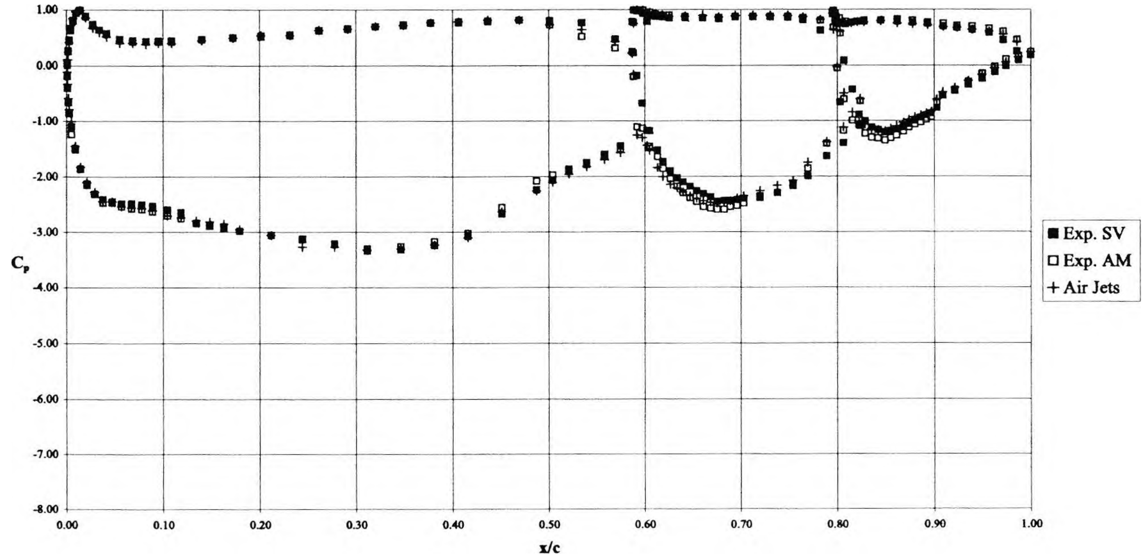

Figure A.16: Air jet C_p distributions at $\alpha = 3^0$ (top) and 9^0 (bottom).

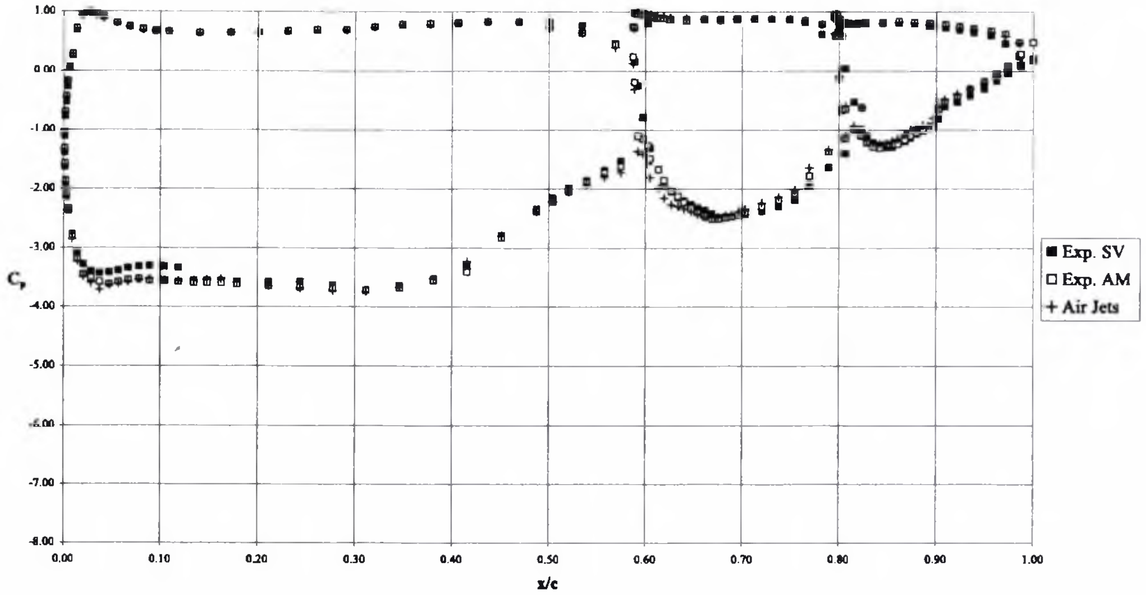

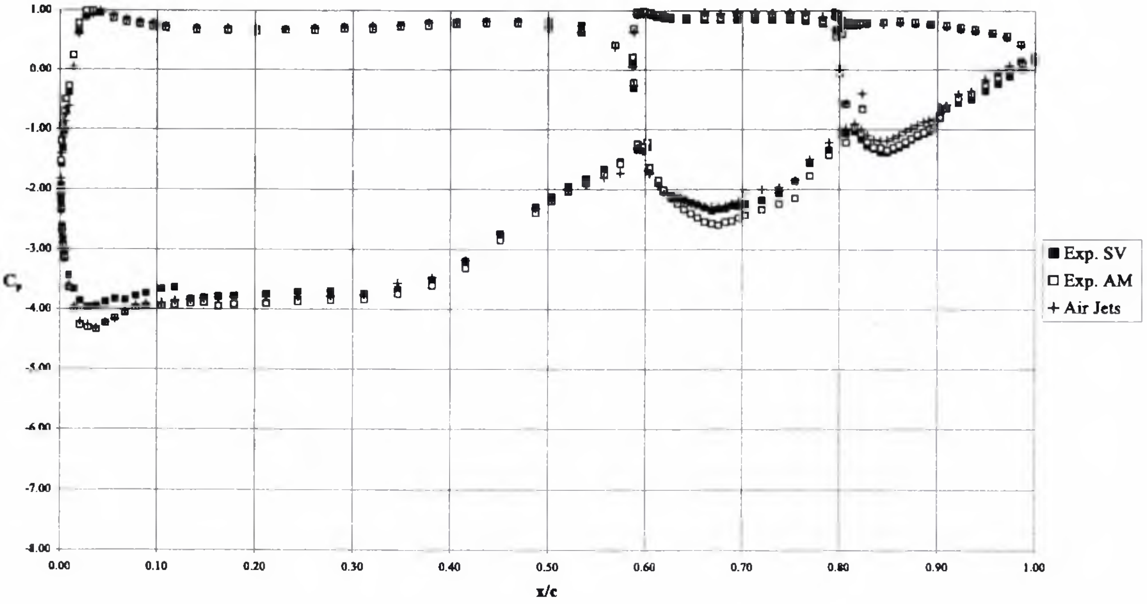

Figure A.17: Air jet C_p distributions at $\alpha = 15^0$ (top) and 19^0 (bottom).

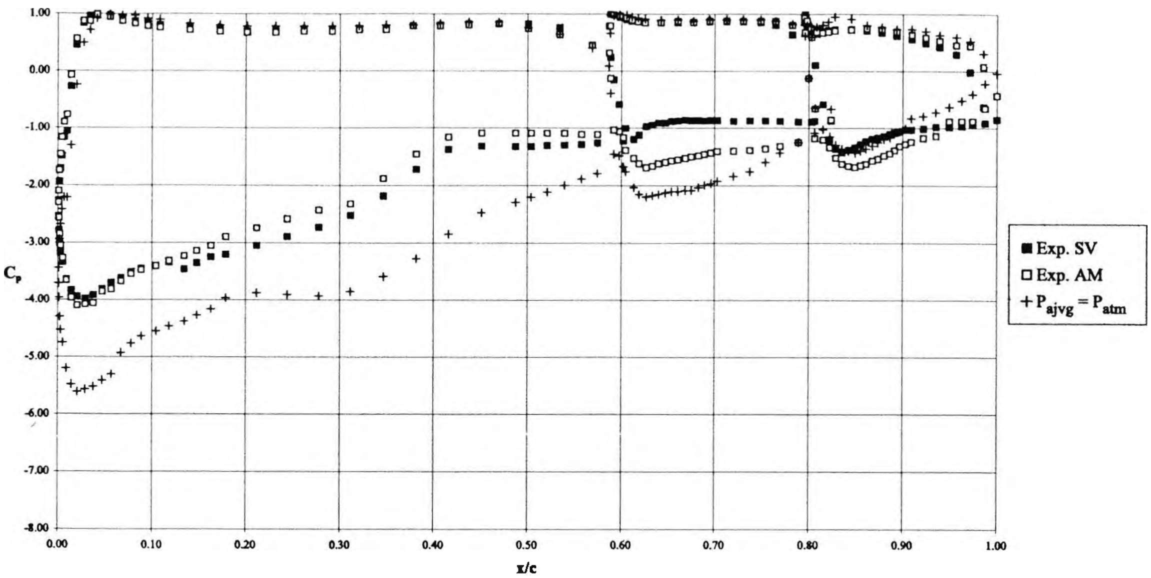

Figure A.18: Air jet C_p distributions at $\alpha = 25^0$.

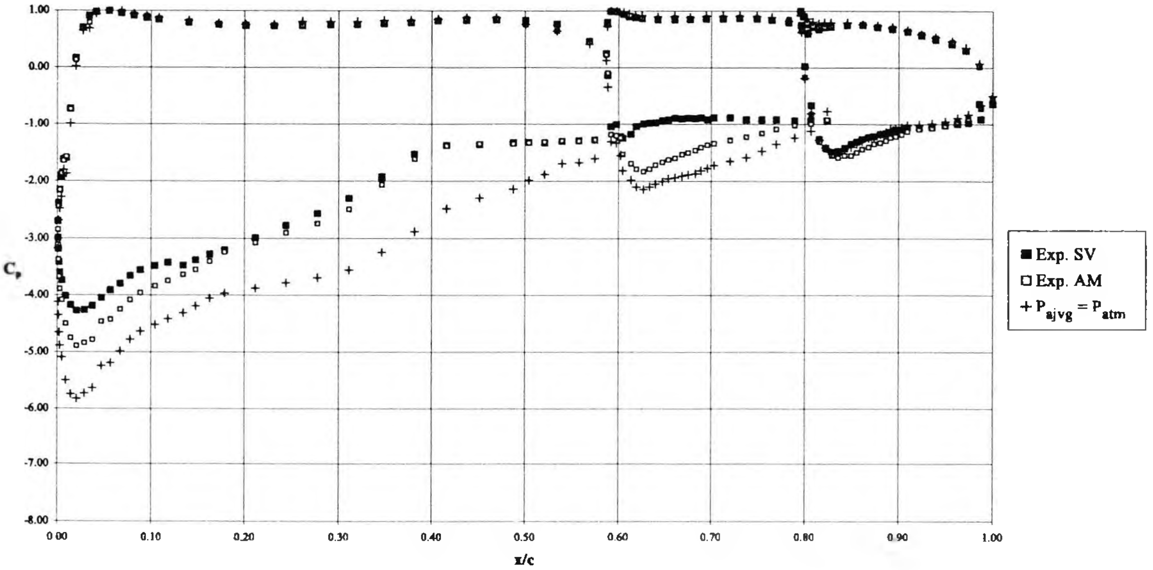

Figure A.19: Air jet C_p distributions at $\alpha = 27^0$.

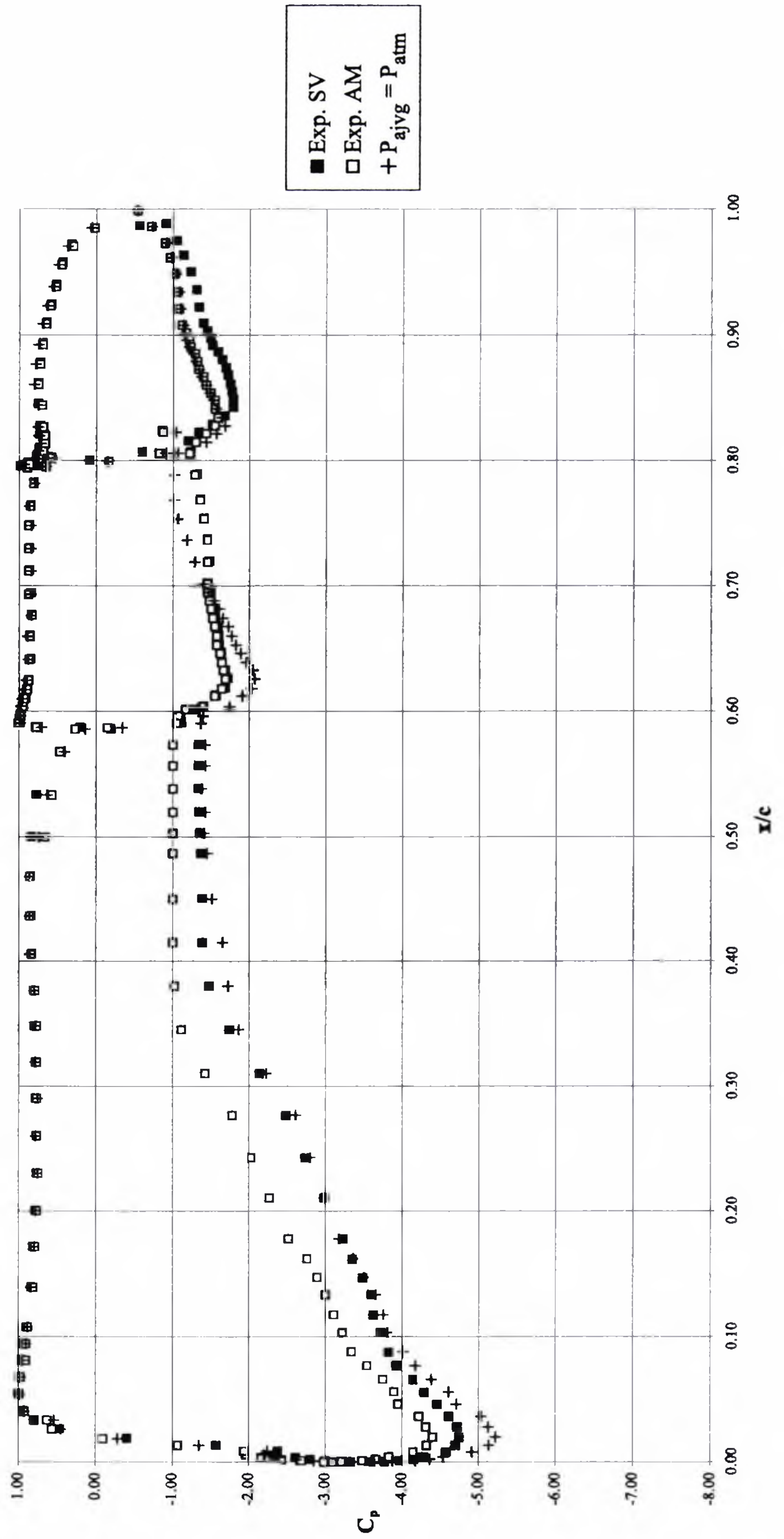

Figure A.20: Air jet C_p distributions at $\alpha = 29^0$.

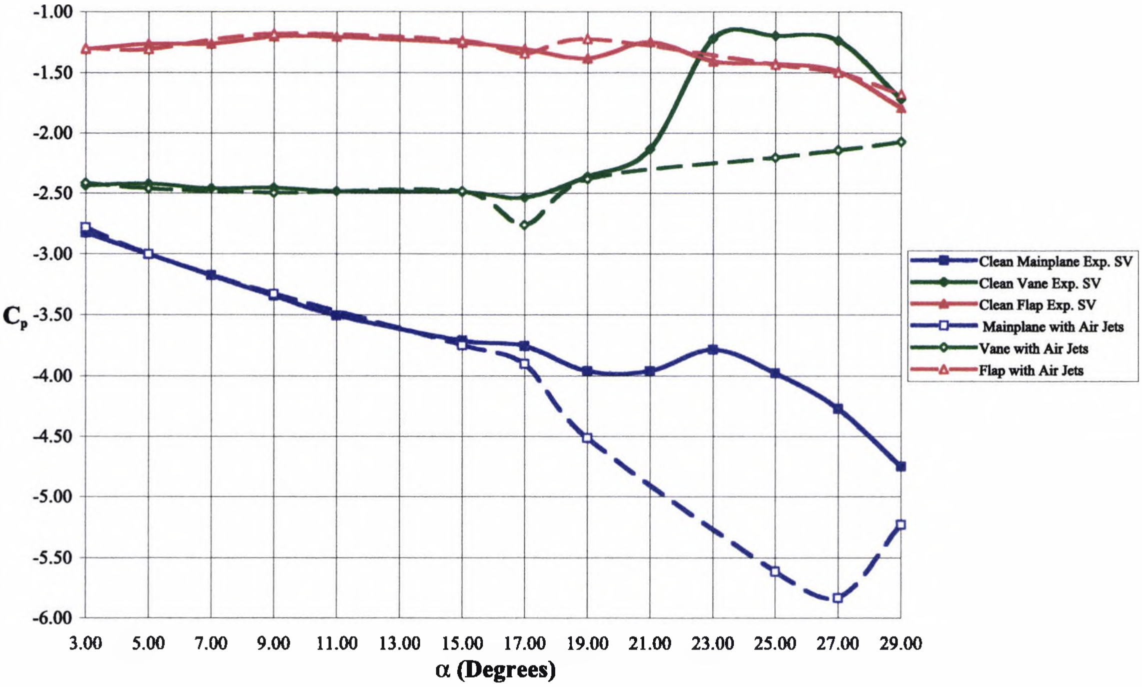

Figure A.21: Air jet and clean wing (Exp. SV) peak suction C_p versus α.

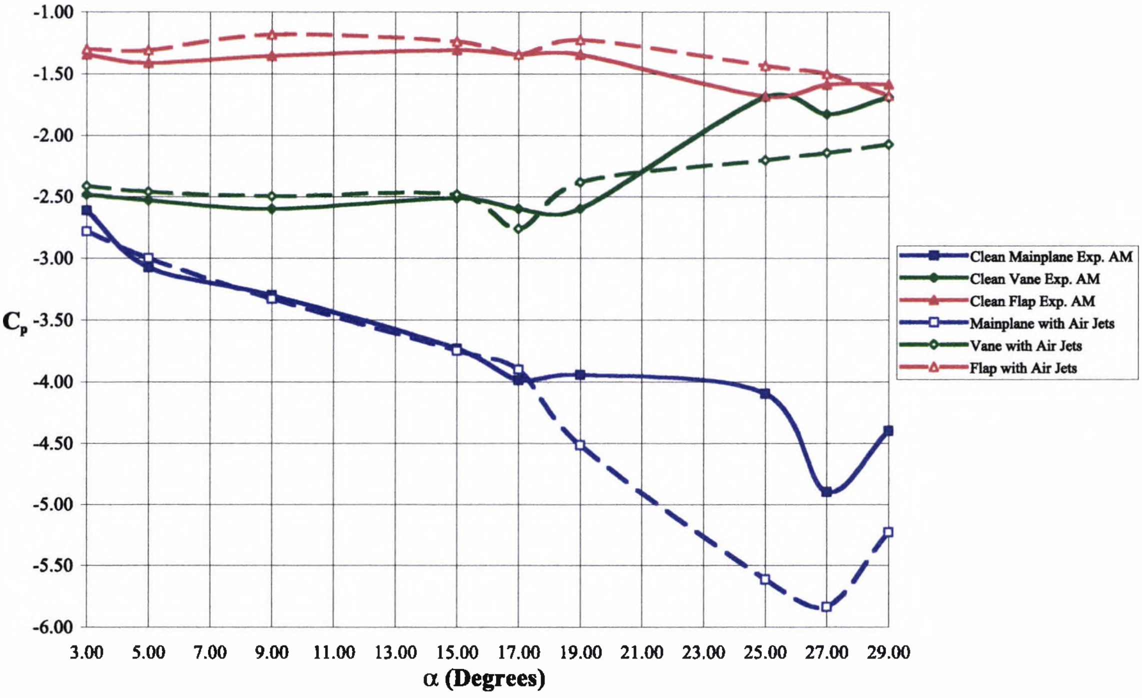

Figure A.22: Air jet and clean wing (Exp. AM) peak suction C_p versus α.

A.4.3 Trailing Edge C_p versus Angle of Incidence with Air Jets

It will be seen that without exception, the AJVGs have an beneficial effect on the performance of the high downforce system at every angle of incidence with the mainplane performance being the most affected. This discussion is aided through the use of Figures A.23 and A.24. These figures show the clean wing and AJVG influenced trailing edge C_p on each element throughout the angle of incidence range.

The use of the AJVGs consistently reduce the mainplane trailing edge C_p at every angle of incidence. This is an indication of an increased *dumping* velocity of the mainplane boundary layers on to the vane when compared to the clean wing cases. The effect on the mainplane trailing edge C_p is marginally greater in the middle of the angle of incidence range. Figures A.23 and A.24 show that at 3^o on the mainplane, the AJVG influenced trailing edge C_p is -1.209 compared to -1.046 (Exp. SV) and -1.15 (Exp. AM) for the clean wings. There is a gradual reduction in this C_p with increasing angle of incidence as the wing produces greater circulation. Using the trendline, the minimum trailing edge C_p of -1.65 occurs at 17^o. The clean wing C_p at this angle are -1.30 (Exp. SV) and -1.215 (Exp. AM). Between 17^o and 29^o, there is a gradual increase in the mainplane trailing edge C_p. However the figures show that the use of the AJVGs produces a C_p of -1.448 compared to -1.238 (Exp. SV) and -1.17 (Exp. AM). The trailing edge C_p at this, the highest angle indicates that the mainplane with AJVGs has a higher circulation than the clean mainplane.

Figures A.23 and A.24 show that with the use of AJVGs, the vane trailing edge C_p are consistently greater than those of the clean wing vane trailing edge C_p (Exp. SV). According to Figure A.23, when AJVGs are used, the vane trailing edge C_p is always greater than that of the vane as part of a clean mainplane system. However, Figure A.24 shows that the AJVGs decrease the vane trailing edge C_p between 3^o and 7^o. At 9^o the AJVG and clean vane trailing edge C_p are equal at -0.571 (Exp. AM). Between 9^o and 29^o, the vane trailing edge C_p associated with the AJVGs are higher than those of the clean vane but there is a decreasing trend that sees the two converge to -0.944 at 29^o. The use of the AJVGs create lower pressures about the mainplane which means that a larger proportion of the pressure recovery has to occur on the other elements in the system. One indication of this is the higher vane trailing edge C_p. The flap is the final stage of pressure recovery. Figure A.23 shows that the AJVG influenced flap trailing edge pressures, with the exception of 3^o incidence, are greater than those of the clean flap. However Figure A.24 shows that this improved recovery only occurs from 17^o up to α_{max}

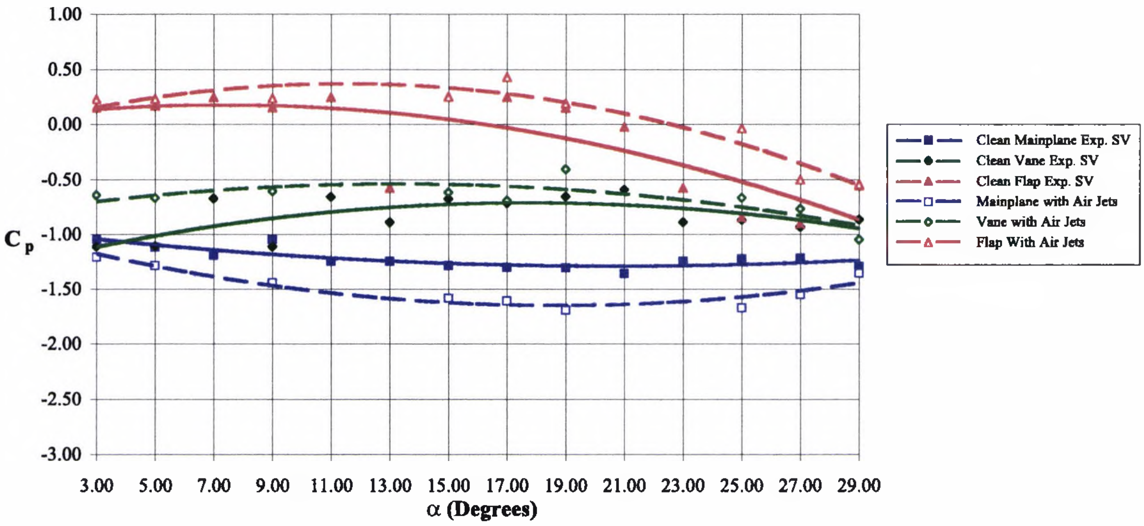

Figure A.23: Air jet and clean (Exp. SV) trailing edge C_p versus α.

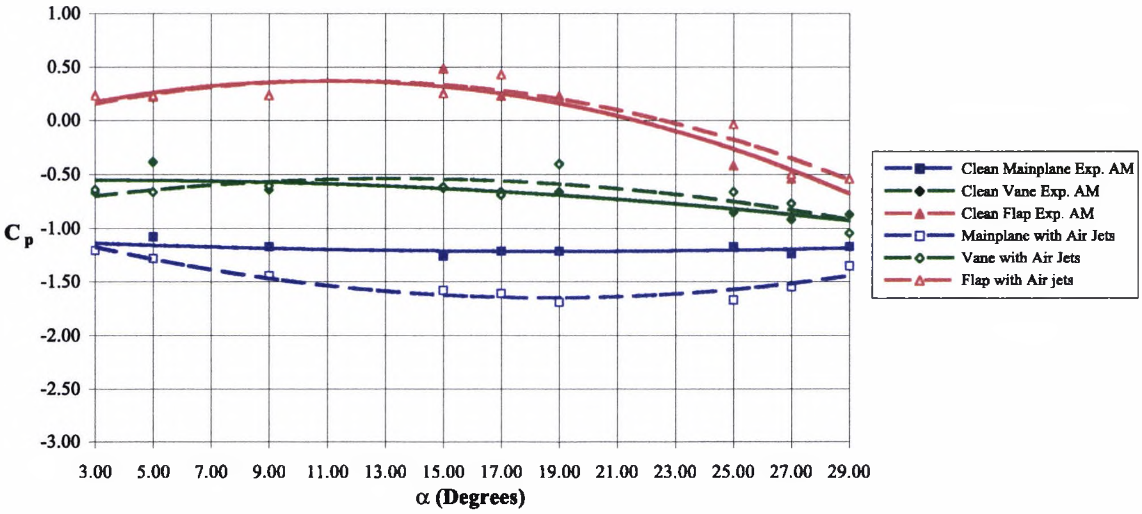

Figure A.24: Air jet and clean (Exp. AM) trailing edge C_p versus α.

of 29^o. At approximately 23^o, the flap trailing edge C_p with the use of AJVGs is -0.05. These C_p become more negative up to 29^o where a value of -0.544 is measured compared to -0.696 (Exp. AM) for the flap as part of a clean mainplane system. The fact that the AJVG trailing edge C_p are greater than those of the clean flap suggests that while the flow separation has not been eliminated, the extent of flow separation is reduced compared to the clean wings.

A.5 Experimental Integrated Forces with Air Jets

A.5.1 Normal Forces versus Angle of Incidence with Air Jets

Figures A.25 and A.26 show that the relationship between the normal forces versus angle of incidence for high downforce system with the AJVGs. On comparing the mainplane C_n clean and with AJVGs, between 3^o and 13^o, there is no improvement. There is not a large enough pressure difference about the mainplane to drive the AJVGs. At the lower angles of incidence, the C_n curve for the mainplane with AJVGs also shares a similar slope with the clean mainplane C_n curve. This is more the case when a comparison is made between the results measured with the alcohol manometers. The clean mainplane C_n curve (Exp. SV) shows that the use of AJVGs degrades the mainplane C_n between 3^o and approximately 9^o. However, at these lower angles, there is some degree of uncertainty in this comparison given the two different sets of instrumentation used.

There are definite increases in the mainplane C_n as the angle of incidence increases. An increase in the angle of incidence creates lower pressures on the mainplane that is beneficial to jet performance. The curves from Figures A.25 and A.26 show that at 11^o (Exp. SV) and 15^o (Exp. AM), there begins an AJVG related increase in the load on the mainplane. At angles of incidence between 11^o (Exp. SV), 15^o (Exp. AM) and 29^o (Exp. AM), the AJVG mainplane C_n is always greater than that of the clean wing values. With the AJVGs, the mainplane has a $C_{n\,max}$ of -4.427 at an $\alpha C_{n\,max}$ of 23^o. This compares to -3.961 (Exp. SV) and -4.176 (Exp. AM) at $\alpha C_{n\,max}$ 19^o for the clean wing cases.

At 29^o, α_{max}, the loading for the mainplane with AJVGs has decreased to a C_n of -3.541. This is only relevant within the context of this isolated model. At 29^o, it is important that the AJVG equipped mainplane C_n is greater than the clean mainplane C_n of -3.421 (Exp. SV) and -2.895 (Exp. AM). There is an increase in the vane C_n over the clean wing vane with increasing angle of incidence. Figure A.25 suggests that the vane C_n as part of the high downforce model with AJVGs, is always superior to that of the

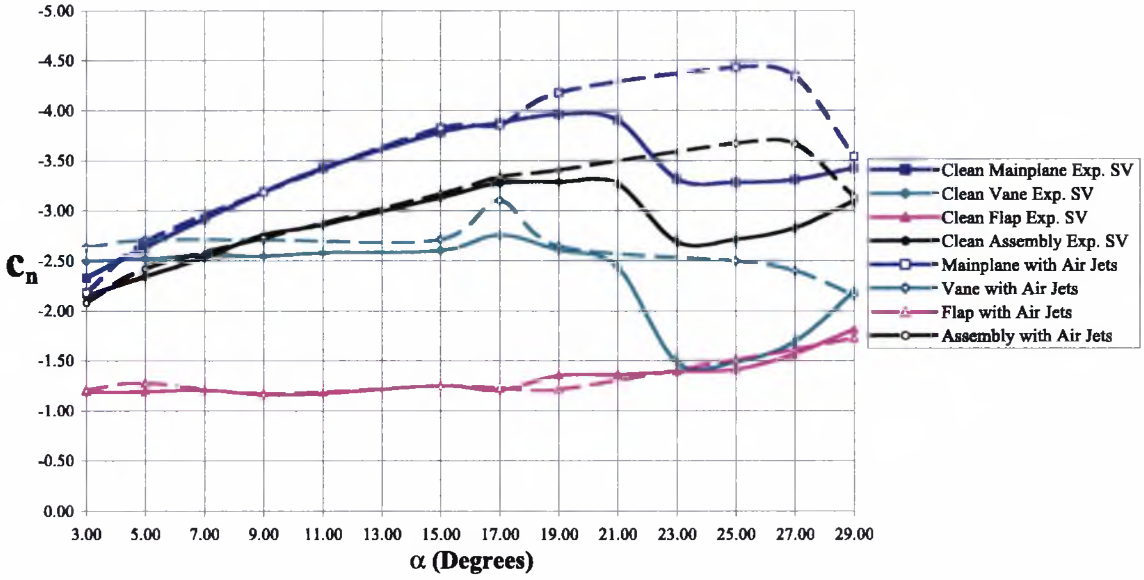

Figure A.25: Air jet and clean wing (Exp. SV) C_n versus α.

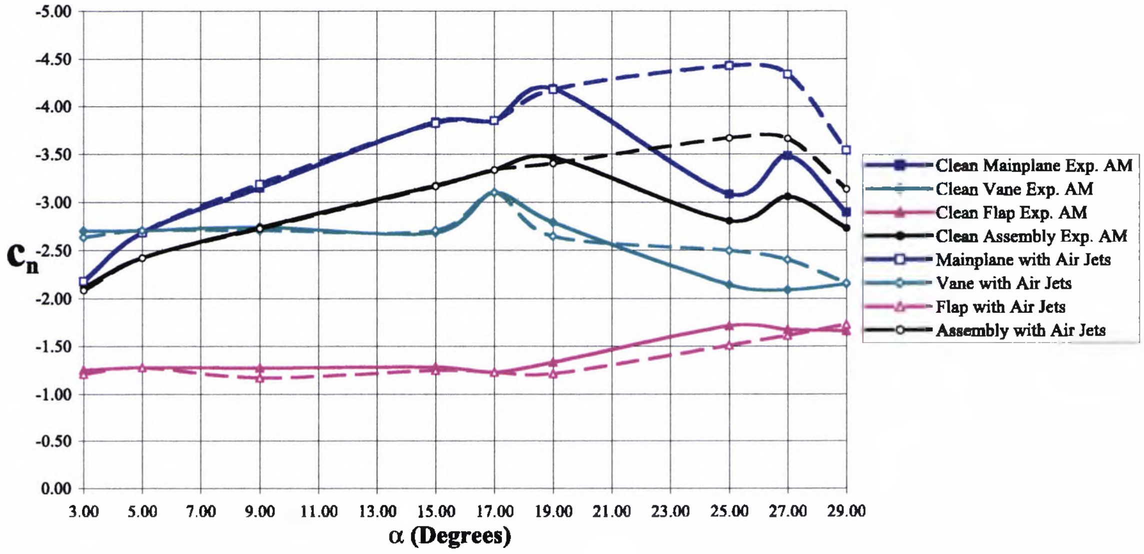

Figure A.26: Air jet and clean wing (Exp. AM) C_n versus α.

clean model cases (Exp. SV). Figure A.26 which compares results measured entirely with the alcohol manometers, suggests that this is not the case. Between 3^o and 15^o, the clean wing vane C_n (Exp. AM) is marginally greater than that of the AJVG influenced vane C_n (Exp. AM).

There is a clear increase in the AJVG influenced vane C_n at angles of incidence greater than 13^o. The $C_{n\,max}$ of the vane occurs at approximately 13^o for all cases. At this incidence, a vane C_n of -2.71 (Exp. AM) produced by the use of AJVGs compares with the clean vane C_n of -2.60 (Exp. SV) and -2.68 (Exp. AM). The effect of the AJVGs on this element is increasingly present up to α_{max}, 29^o, with a C_n of -2.154. The clean wing vane C_n (Exp. SV) is -2.186 and -2.154 (Exp. AM), the latter being the same as the AJVG value. However, the best fit curves show that the AJVG influenced C_n of the vane is approximately -2.21, while the values on the clean wing vane curves at this angle are -1.627 (Exp. SV) and -2.00 (Exp. AM). As with the mainplane at angles of incidence greater than $\alpha C_{n\,max}$, the loading on the vane does decrease with increasing incidence but, the load generated with the use of AJVGs is always higher than that of the clean wing.

In relative terms, when the clean and AJVG affected loads are compared, the behaviour of the flap is not significantly altered by the use of AJVGs on the mainplane. Figure A.25 shows that the clean (Exp. SV) and AJVG influenced loads on the flap are essentially the same throughout most of the angle of incidence range. Figure A.26, shows that the flap C_n (Exp. AM) generated with a clean mainplane is higher than those generated through the use of AJVGs. The only exceptions being at 3^o and 29^o. According to the best fit curves, the C_n with and without AJVGs is essentially equal at 3^o incidence. The curves then diverge as the incidence increases with a $\Delta C_{n\,max}$ occurring at approximately 17^o. Between 17^o and 29^o, the curves begin to converge. Once again at 29^o, the C_n with and without AJVGs, are approximately equal at -1.725 (Exp. AM).

The use of AJVGs on the mainplane acts to decrease the C_n of the flap at nearly all angles of incidence. However, the net effect of the AJVGs is to redistribute an increased circulation about the high downforce model, resulting in an increased C_n on the mainplane and the vane. The increase in C_n on these two elements is much greater that the decrease seen on the flap and the improvement for the system as a whole is clear even when one refers to Figure A.25 where the results are derived from two separate instrumentation systems.

For the assembly, the AJVGs increase $C_{n\,max}$ to -3.50 (Exp. AM) from -3.15 (Exp. SV) and -3.48 (Exp. AM). The use of AJVGs also increases $\alpha C_{n\,max}$ to 23^o, compared to

19^o for the clean assembly. At 29^o, the angle that the highest downforce configurations would use, the use of AJVGs produces an assembly C_n of -3.49 compared to -2.77 (Exp. SV) and -2.80 (Exp. AM). In discussing the pressure distributions, it was noted that the AJVGs did not completely eliminate the flow separation of the flap. However, further evidence that they have improved the loading on the high downforce system can be seen in the $\frac{\delta C_n}{\delta \alpha}$ for the assembly. A study of Figures A.25 and A.26 shows that the clean wing C_n decrease more rapidly than the AJVG equipped system. The difference is more pronounced in Figure A.26.

A.5.2 Axial Force versus Angle of Incidence with Air Jets

The axial force data for each element and the assembly are presented in Figures A.27 and A.28. The trendlines for the mainplane with AJVGs show that there is a consistent increase in C_x from 3^o to 29^o. Between 3^o and 15^o, there is a net thrust on the mainplane. Figure A.27 shows that this thrust is enhanced by the use of AJVGs. From the trendline, at 3^o the mainplane C_x with AJVGs is -0.318 compared to -0.20 (Exp. SV) and -0.303 (Exp. AM). It is more likely that any increase in thrust is similar to the differences measured entirely with the alcohol manometers, that is to say negligible. At the lower angles of incidence the author places greater fidelity in the comparisons made entirely between results from the alcohol manometers. However the author believes that comparisons between the clean wings C_x (Exp. SV) and the AJVG influenced C_x (Exp. AM) are valid between the mid to highest angles of incidence because the differences between the clean mainplane and the mainplane with AJVGs are significant. The experimental variance cannot produce ambiguous results as can be the case at the lowest angles.

The thrust on the mainplane decreases with increasing incidence, with $C_x = 0$ measured at approximately 15^o. The trendlines for the clean mainplane (Exp. SV) and (Exp. AM) show that at 14^o (not measured) and 15^o, respectively, $C_x = 0$. Thus the AJVGs have a negligible impact on the axial force characteristics below 15^o.

For angles of incidence higher that 15^o. the mainplane C_x with AJVGs diverges from those of the clean mainplane and is always greater that the clean mainplane measurement. It is also at 15^o and higher, that the C_n on the mainplane with AJVGs shows an increased loading over the clean mainplane. According to the trendline, The $C_{x\,max}$ for the mainplane with AJVGs is 0.75 and occurs at 29^o. This compares to a C_x of 0.575 (Exp. SV) and 0.637 (Exp. AM).

The use of AJVGs on the mainplane causes an increase in the vane C_x across the entire angle of incidence range. The magnitude of the change is not as dramatic as on the mainplane itself. The vane C_x curve associated with the mainplane with AJVGs remains relatively flat with a very small change between 3^o and 29^o. However, the C_x curve for the vane with AJVGs is always greater than that of the clean vane. Figures A.27 and A.28 show that at 3^o, the vane in the AJVGs system has a C_x of 0.00 compared with a C_x of -0.103 (Exp. SV) and -0.048 (Exp. AM). At 29^o, the vane with AJVGs has a C_x of 0.072 compared to -0.001 (Exp. SV) and 0.011 (Exp. AM). This shows that with or without AJVGs in the system, the vane bears very little of the axial load with its C_x being very close to zero.

The flap differs from the mainplane and the vane in that $C_{x\,max}$ occurs at 3^o. The flap C_x curve has a value of approximately 0.10 at 3^o. At 3^o, the clean flap has a C_x of -0.015 (Exp. SV) and 0.10 (Exp.AM), the latter being the same as the AJVGs C_x at this angle. All curves for the flap show that the C_x decreases with increasing incidence to minimum of -0.05 at 17^o. Between 17^o and 29^o, all the flap C_x curves show a small increase. At 29^o, the flap with AJVGs has a C_x of -0.006. This compares to a clean wing C_x of 0.050 (Exp. SV) and -0.013 (Exp. AM). This would suggest that the axial loading on the clean flap is slightly higher that those of the clean flap.

The axial forces on the assembly show trends that are strongly linked to those of the mainplane. The high downforce model equipped with AJVGs produces a thrust between 3^o and 15^o. This thrust decreases with increasing angle of incidence. Between 17^o (Exp. SV), 9^o (Exp. AM) and 29^o, the AJVG equipped assembly C_x curve continues to increase with increasing angle of incidence. The gradient of this curve is also higher than those of the clean assembly. However a review of Figures A.27 and A.28 shows that the difference in gradients is greater when compared to the clean assembly (Exp. SV) as opposed to the clean assembly (Exp. AM). While it is clear that this trend is actually occurring, the author believes that a comparison of those results in Figure A.28 is more representative of the difference between the clean assembly (Exp. SV) and the AJVG equipped assembly C_x (Exp. AM).

A.5.3 Downforce versus Angle of Incidence for Wing with Air Jets

In the discussion of the downforce performance of the AJVG equipped high downforce model, the author refers the reader to Figure A.29. When comparing the AJVG influenced c_l curve and that of the clean wings, it is apparent that there is no benefit in using the AJVGs at the lower angles of incidence. In fact, the benefit of the AJVGs is not seen until

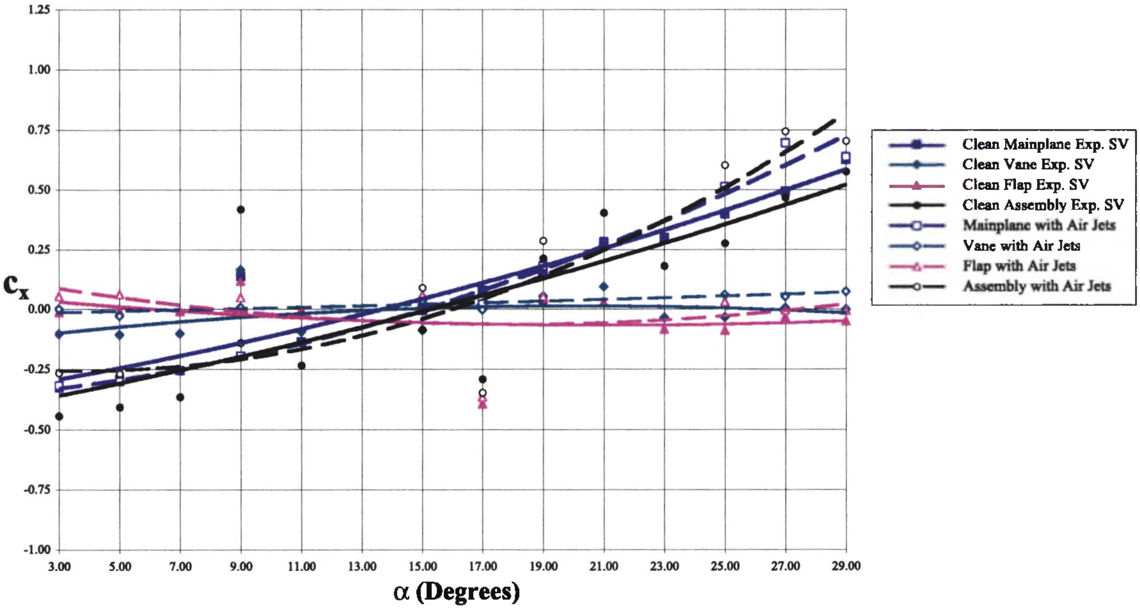

Figure A.27: Air jet and clean wing (Exp. SV) C_x versus α.

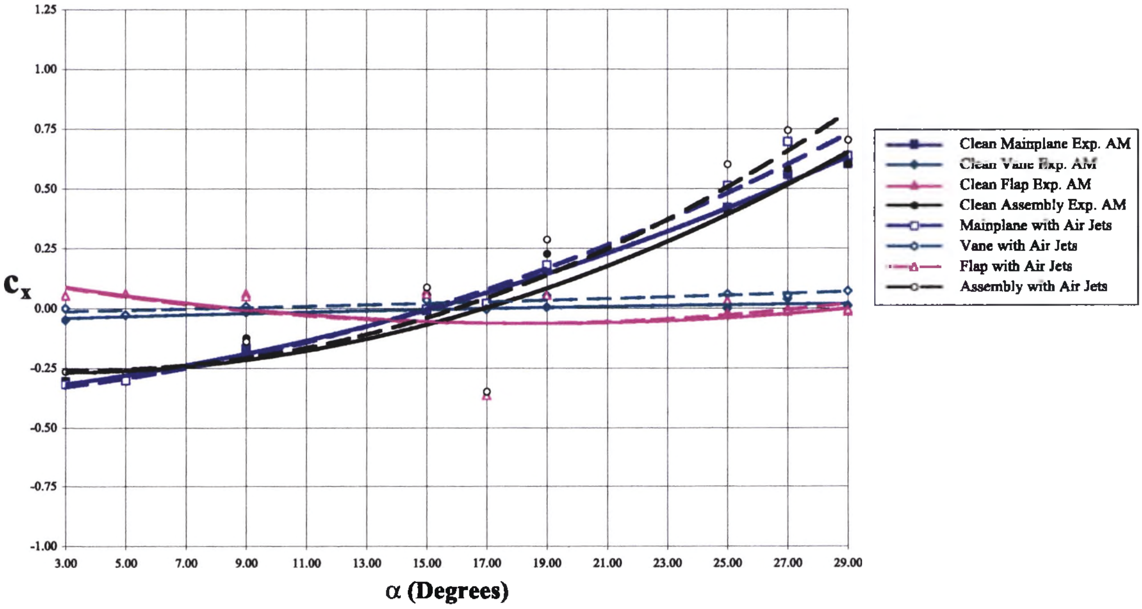

Figure A.28: Air jet and clean wing (Exp. AM) C_x versus α.

after the clean wing has stalled at 19^o.

This is unlike the behaviour of the high lift system investigated by Innes (1995) where the powered AJVGs produced an increase in c_l across the entire angle of incidence range. Air jets using a ram air system are unlikely to produce any significant benefit at lower angles because the pressures generated on the lower mainplane surface are not low enough to produce a favourable pressure gradient of sufficient magnitude to produce a strong enough AJVG efflux. The mainplane also operates in attached flow from 3^o up to 19^o so there is no real need to have the AJVGs active in this range.

Figure A.29 shows that the use of the AJVGs does not bring about a significant increase in $c_{l\,max}$ over that of the clean wing. The $c_{l\,max}$ produced by the clean wing is estimated at -3.33 (Exp. SV) and -3.45 (Exp. AM). The high downforce model equipped with AJVGs produces a $c_{l\,max}$ of -3.60. Thus, the main effect of the AJVGs is to extend the useful angle of incidence range of the wing with a marginal increase in $c_{l\,max}$. Figure A.29 shows that the use of the AJVGs increases $\alpha c_{l\,max}$ to 25^o. At 27^o, the wing experiences a very sudden stall similar to what is seen at 19^o (Exp. SV).

A.5.4 Drag versus Angle of Incidence for Wing with Air Jets

The estimated drag coefficient, c_d, of the high downforce model equipped with AJVGs is very similar to the c_d estimates derived from the experiments with the clean wing. Figure A.30 shows that the drag is comparable between 3^o and 15^o. The range of this agreement could have extended to 17^o but for the c_d of 0.36 from the air jet influenced c_d that deviates from the trend.

Figure A.30 shows that the use of the AJVGs on the high downforce system produces lower drag between 19^o and 21^o when compared to the Exp. SV data and between 19^o and 23^o when compared to the Exp. AM data. When reviewing the estimated c_d of the clean wing and AJVG equipped system derived from the Exp. AM data, it is seen that the AJVGs equipped system has a higher drag than the clean wing at angles of incidence greater than 25^o. A maximum c_d of 0.63 for the high downforce model incorporating the AJVGs occurs at 27^o and not α_{max} of 29^o. Based on a comparison with the c_d (Exp. AM) where the drag increases marginally between 25^o and 29^o, the use of the AJVGs creates a small decrease in drag from a $c_{d\,max}$ of 0.63 at 27^o to 0.62 at 29^o. However, the Exp. SV and Exp. AM data contradict each other at the highest angles of incidence. Further experiments would be required to produce results with better agreement.

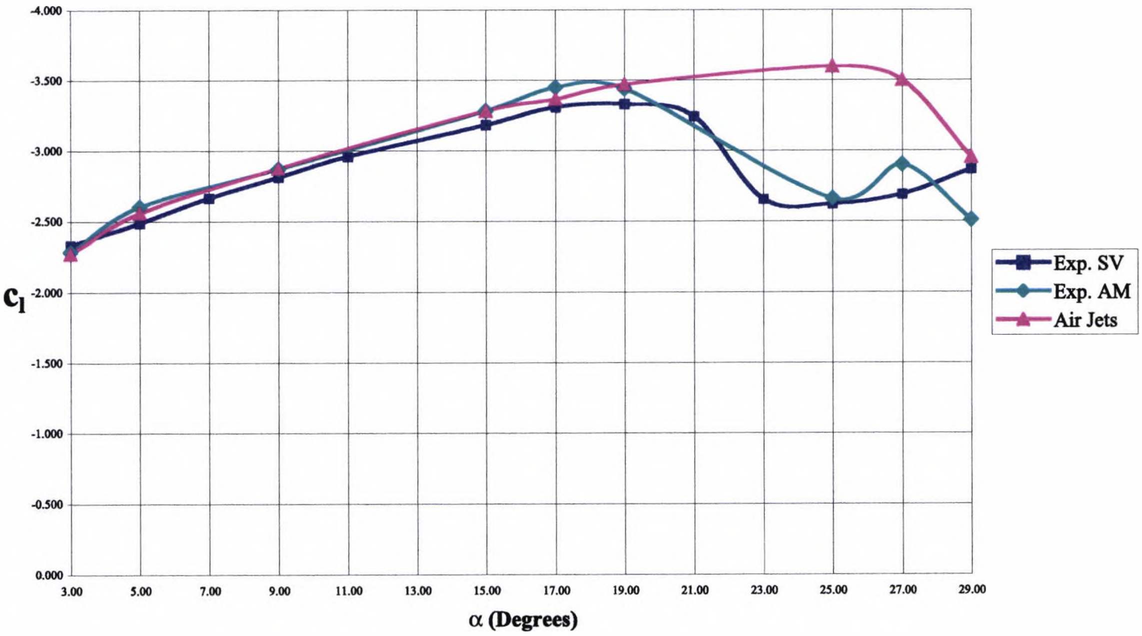

Figure A.29: c_l versus α for high downforce wing with air jets.

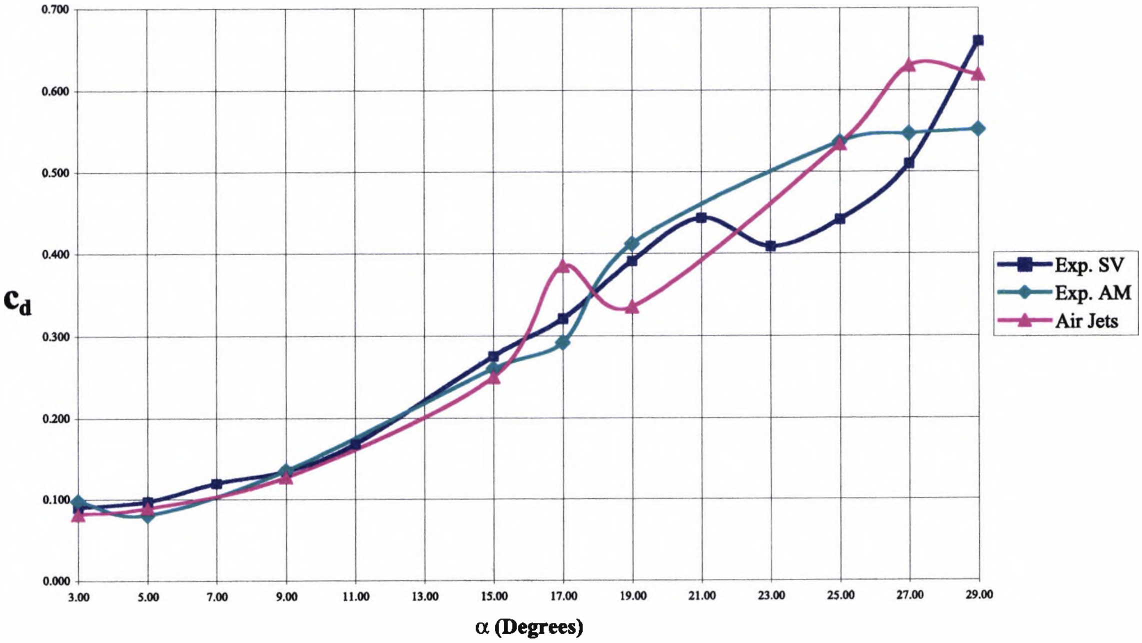

Figure A.30: c_d versus α for high downforce wing with air jets.

A.5.5 Downforce to Drag Ratios for Wing with Air Jets

The lift to drag ratio of the AJVG equipped wing is presented in Figure A.31. As with the clean wing high downforce model, the AJVG equipped system is most efficient at the lowest angles of incidence with a maximum lift to drag ratio of 28.74 occurring at 5^o. But as previously stated, it is highly unlikely that this type of wing would be used at such a low angle of incidence. The $\frac{l}{d}$ of the AJVG equipped system decreases as the angle of incidence increases.

With the exception of the $\frac{l}{d}$ of 8.73 at 17^o which is lower than the trend at that point, the model equipped with the AJVGs is seen to have a slightly higher $\frac{l}{d}$ than the clean wing model. The aerodynamic efficiencies of the AJVG equipped wing and the clean wing is seen to converge as the angle of incidence increases. Figure A.31 shows that at the 27^o and 29^o angles of incidence, the AJVG equipped wing and clean wing lift to drag ratios are essentially the same. The systems share similar lift to drag ratios because the increase in downforce accompanying the use of the AJVGs is also accompanied by an increase in drag.

Given the performance of the clean wing and AJVG equipped high downforce systems, the argument for the use of AJVGs would be based on the fact that the lift to drag ratio has remained essentially constant while an increase in downforce has been achieved. The Monaco and Hungarian Grands Prix are two venues where increased downforce can improve the performance of some Formula One cars even when the increase in downforce incurs $\frac{L}{D}$ penalties as high as 1:1.

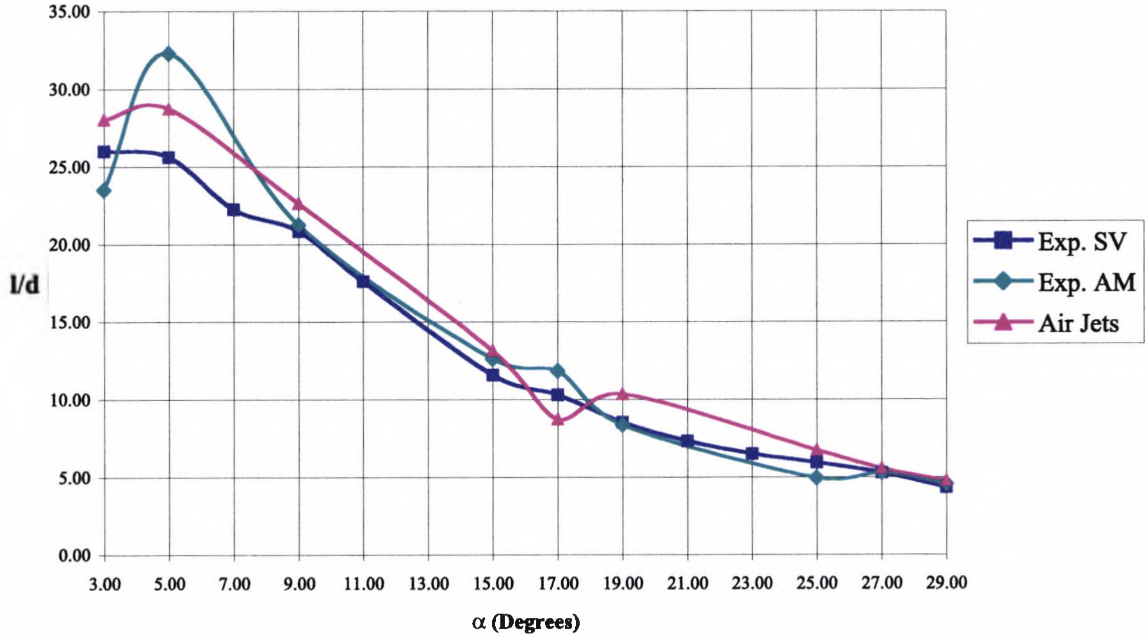

Figure A.31: $\frac{l}{d}$ versus α for high downforce wing with air jets.

A.6 Three-Dimensional CFX-4.2 Command File

The listing below is representative of a command file used for to specify flow and boundary conditions for a three dimensional problem.

```
>>CFXF3D
  >>SET LIMITS
    TOTAL INTEGER WORK SPACE 200000000
    TOTAL REAL WORK SPACE 200000000
    TOTAL CHARACTER WORK SPACE 100000
    MAXIMUM NUMBER OF BLOCKS 60
    MAXIMUM NUMBER OF PATCHES 400
    MAXIMUM NUMBER OF INTER BLOCK BOUNDARIES 400
  >>OPTIONS
    THREE DIMENSIONS
    BODY FITTED GRID
    TURBULENT FLOW
    INCOMPRESSIBLE FLOW
    USER SCALAR EQUATIONS 4
  >>VARIABLE NAMES
    USER SCALAR1 'X SHEAR STRESS'
    USER SCALAR2 'Y SHEAR STRESS'
    USER SCALAR3 'Z SHEAR STRESS'
    USER SCALAR4 'YPLUS'
>>MODEL TOPOLOGY
  >>INPUT TOPOLOGY
    READ GEOMETRY FILE
>>MODEL DATA
  >>DIFFERENCING SCHEME
    U VELOCITY 'HIGHER UPWIND'
    V VELOCITY 'HIGHER UPWIND'
    W VELOCITY 'HIGHER UPWIND'
    K 'HYBRID'
    EPSILON 'HYBRID'
  >>SET INITIAL GUESS
```

```
>>SET INITIAL GUESS
  >>SET CONSTANT GUESS
    U VELOCITY 40.0
    V VELOCITY 0.00
    W VELOCITY 0.00
    PRESSURE 1.0100E+05
    END
  >>TITLE
    PROBLEM TITLE '240 MM SPAN, 5 JETS, ALPHA = 29 DEGREES, P_AJVG 0 P_ATM.'
  >>PHYSICAL PROPERTIES
    >>STANDARD FLUID
      FLUID 'AIR'
      STANDARD FLUID REFERENCE TEMPERATURE 3.1316E+02
    >>FLUID PARAMETERS
      VISCOSITY 1.9100E-05
      DENSITY 1.1200E+00
>>SOLVER DATA
  >>PROGRAM CONTROL
    MAXIMUM NUMBER OF ITERATIONS 500
    MASS SOURCE TOLERANCE 1.0000E-06
    ITERATIONS OF TURBULENCE EQUATIONS 1
  >>DEFERRED CORRECTION
    K START 501
    K END 501
    EPSILON START 501
    EPSILON END 501
  >>UNDER RELAXATION FACTORS
    U VELOCITY 5.0000E-01
    V VELOCITY 5.0000E-01
    W VELOCITY 5.0000E-01
    PRESSURE 1.0000E+00
    VISCOSITY 1.0000E+00
    K 5.0000E-01
    EPSILON 5.0000E-01
```

```
>>MODEL BOUNDARY CONDITIONS
  >>SET VARIABLES
    #CALC
    UINL=35.0;
    TEINL=0.002*UINL*UINL;
    CH=0.395;
    EPSINL=TEINL**1.5/(0.3*CH);
    #ENDCALC
    PATCH NAME 'IN'
    U VELOCITY #UINL
    V VELOCITY 0.0000E+00
    W VELOCITY 0.0000E+00
    K #TEINL
    EPSILON #EPSINL
  >>SET VARIABLES
    PATCH NAME 'J1'
    PRESSURE 1.0100E+05
  >>SET VARIABLES
    PATCH NAME 'J2'
    PRESSURE 1.0100E+05
  >>SET VARIABLES
    PATCH NAME 'J3'
    PRESSURE 1.0100E+05
  >>SET VARIABLES
    PATCH NAME 'J4'
    PRESSURE 1.0100E+05
  >>SET VARIABLES
    PATCH NAME 'J5'
    PRESSURE 1.0100E+05
  >>SET VARIABLES
    PATCH NAME 'OUT'
    PRESSURE 1.0100E+05
>>OUTPUT OPTIONS
  >>FRONTEND PRINTING
```

```
    NO FRONTEND PRINTING
  >>DUMP FILE FORMAT
    UNFORMATTED
>>STOP
```

A.7 Co-ordinates of Static Pressure Orifices at 29^o Incidence

Mainplane

Port Number	X-co-ordinate	Y-co-ordinate
1-29	1016.360	588.621
1-30	1009.324	580.948
1-31	1004.698	576.877
1-32	999.608	572.547
1-33	994.431	568.264
1-34	989.684	564.388
1-35	985.021	560.617
1-36	974.537	552.641
1-37	963.950	545.490
1-38	953.149	539.366
1-39	941.623	533.997
1-40	929.644	529.356
1-41	917.573	525.666
1-42	905.122	522.640
1-43	892.822	520.383
1-44	879.974	518.705
1-45	873.562	518.159
1-46	867.522	517.816
1-47	861.870	517.584
2-01	854.970	517.751
2-02	848.893	517.963
2-03	841.895	518.518
2-04	836.888	519.145
2-05	831.798	519.870
2-06	826.883	520.778
2-07	822.097	521.853
2-08	817.109	523.282
2-09	812.435	524.955
2-10	807.569	527.204
2-11	803.320	529.713

Mainplane continued ...

Port Number	X-co-ordinate	Y-co-ordinate
2-12	799.245	532.570
2-13	795.636	535.651
2-14	793.525	537.670
2-15	791.986	539.482
2-16	790.334	541.629
2-17	788.934	543.653
2-18	787.576	545.858
2-19	786.547	548.070
2-20	785.504	550.484
2-21	784.655	552.949
2-22	784.168	555.156
1-01	784.000	557.560
1-02	784.216	560.273
1-03	785.311	562.389
1-04	787.176	564.401
1-05	789.191	565.978
1-06	791.485	567.197
1-07	796.115	569.217
1-08	800.807	570.732
1-09	805.792	571.920
1-10	810.846	572.881
1-11	815.970	573.687
1-12	828.534	575.103
1-13	841.658	575.903
1-14	853.639	576.430
1-15	866.324	576.522
1-16	879.212	576.328
1-17	892.209	575.894
1-18	904.805	575.352
1-19	917.340	574.785
1-20	929.785	574.293

Mainplane continued . . .

Mainplane Port Number	X-co-ordinate	Y-co-ordinate
1-21	942.228	574.030
1-22	955.217	573.924
1-23	968.450	574.750
1-26	980.851	576.341
1-27	993.203	579.355
1-28	1005.091	583.882

Vane

Vane Port Number	**X-co-ordinate**	**Y-co-ordinate**
1-28	1067.793	657.072
1-27	1064.782	650.234
1-26	1061.323	643.930
1-23	1057.108	637.112
1-22	1053.787	632.105
1-21	1049.871	627.067
1-20	1045.588	621.977
1-19	1041.176	617.330
1-18	1039.330	615.588
1-17	1037.500	613.861
1-16	1035.702	612.343
1-15	1033.638	610.615
1-14	1031.735	609.142
1-13	1029.526	607.510
1-12	1027.351	606.125
1-11	1025.319	604.855
1-10	1023.054	603.562
1-09	1021.001	602.456
1-08	1018.787	601.413
1-07	1016.187	600.316
1-06	1014.135	599.725
1-05	1010.976	598.878
1-04	1008.096	598.595
1-03	1005.603	598.796
1-02	1003.607	599.528
1-01	1002.197	600.867
1-45	1001.457	602.914
1-44	1001.490	605.256
1-43	1002.655	607.668
1-42	1004.379	609.851

Vane continued ...

Vane Port Number	**X-co-ordinate**	**Y-co-ordinate**
1-41	1005.868	611.506
1-40	1007.814	613.167
1-39	1009.978	614.675
1-38	1015.091	617.897
1-37	1020.871	621.178
1-36	1026.101	624.071
1-35	1031.541	627.014
1-34	1037.180	630.432
1-33	1042.555	633.931
1-32	1047.909	637.881
1-31	1052.266	641.621
1-30	1056.937	646.410
1-29	1062.142	652.008

Flap

Port Number	X-co-ordinate	Y-co-ordinate
1-28	1094.384	734.704
1-27	1093.489	727.484
1-26	1091.797	721.167
1-23	1090.276	715.753
1-22	1088.507	709.749
1-21	1086.415	703.297
1-20	1084.285	697.384
1-19	1082.277	691.931
1-18	1081.310	689.291
1-17	1080.324	686.865
1-16	1079.371	684.669
1-15	1078.444	682.619
1-14	1077.308	680.171
1-13	1076.101	677.775
1-12	1074.955	675.680
1-11	1073.520	673.338
1-10	1072.186	671.416
1-09	1070.796	669.590
1-08	1069.200	667.476
1-07	1067.511	665.513
1-06	1065.705	663.880
1-05	1063.891	662.485
1-04	1061.908	660.977
1-03	1058.977	659.730
1-02	1056.331	659.376
1-01	1054.140	660.141
1-45	1052.774	661.840
1-44	1052.231	664.581

Flap continued . . .

Port Number	**X-co-ordinate**	**Y-co-ordinate**
1-43	1052.690	666.696
1-42	1053.899	669.062
1-41	1055.237	671.055
1-40	1056.763	672.857
1-39	1058.505	674.746
1-38	1062.903	679.537
1-37	1066.884	684.468
1-36	1070.495	689.545
1-35	1073.834	694.788
1-34	1077.220	700.580
1-33	1080.078	705.763
1-32	1083.075	711.302
1-31	1086.503	717.840
1-30	1089.160	723.613
1-29	1091.690	729.367